Brain-state dependent activity and selective cortical innervation of identified GABAergic medial septal neurons



Minas Nabil Aziz Salib

Brasenose College,

University of Oxford

A thesis submitted for the degree of

Doctor of Philosophy (DPhil)

Trinity, 2019

“The mind loves the unknown.

It loves images whose meaning is unknown,

since the meaning of the mind itself is unknown”

René Magritte

Abstract

Brain-state dependent activity and selective cortical innervation of identified GABAergic medial septal neurons

Minas Salib
Brasenose College, University of Oxford
Thesis submitted for the degree of Doctor of Philosophy, Trinity Term, 2019

Rhythmicity facilitates the coordination of neuronal activity, and these rhythms are detected as oscillations of different frequencies, such as 5-12 Hz theta oscillations. Degradation of these rhythms, e.g. through neurodegeneration, causes cognitive deficits including memory impairment. Temporally ordered firing sequences of cortical principal cells such as 'place cells' support spatial navigation. These temporal sequences are distributed across different regions of the temporal cortex and are coordinated by rhythmic inhibition from presynaptic cortical GABAergic interneurons. However, it is not clear how the diverse temporal specificity of interneurons is coordinated to govern the excitability of these pyramidal cell assemblies. Subcortical GABAergic neurons of the medial septum innervate cortical interneurons, but the rules of innervation of identified types of cortical cells in different cortical regions are largely unknown.

For my DPhil, I have hypothesized that specialized, distinct types of medial septal GABAergic neurons contribute to brain-state dependent network activity through selective cortical connectivity in targeted areas. To address my hypothesis, I have used *in vivo* extracellular recordings of single medial septal cells in head-restrained awake drug-free mice followed by juxtacellular labelling of recorded cells. I have found the following: (1) In *Chapter 3*, I demonstrate the diversity of the medial septal neuronal population. I combined electrophysiological, anatomical and immunohistochemical methods to identify and define single medial septal neurons; (2) Based on these initial characterisations, in *Chapter 4*, I have established that two identified subpopulations of GABAergic high-rhythmic firing neurons (HRNs), *Teevra* and *Orchid* cells, selectively target interneurons in restricted regions of the cortex. *Teevra* cells are short burst firing GABAergic medial septal neurons that selectively innervate axo-axonic cells in hippocampal area CA3, bypassing CA1, CA2, and the dentate gyrus (Joshi, **Salib** *et al.*, 2017). *Orchid* cells, however, are long burst firing GABAergic medial septal neurons primarily innervating the entorhinal cortex and the presubiculum and target distinct subpopulations of GABAergic interneurons (Viney, **Salib** *et al.*, 2018). (3) After identifying HRNs, in *Chapter 5* I present my novel observations and definitions of GABAergic low-rhythmic firing neurons (LRNs) of the medial septum that preferentially target interneurons in the dentate gyrus and CA3. As a population, LRNs strongly reduce their firing during sleep-related hippocampal sharp-wave ripple oscillations and have a low burst incidence in contrast to HRNs (**Salib** *et al*, 2019). (4) In addition, I have documented several individual HRNs with novel firing patterns and cortical projections including neurons innervating the entorhinal cortex, parasubiculum and ventral subiculum. (5) I have also recorded multi-unit activity with chronically implanted electrodes in the medial septum of freely moving mice with the aim to investigate previously defined HRNs across the sleep-wake cycle.

Overall, my results demonstrate the existence of a diverse and dynamic medial septal neuronal population that includes three distinct subgroups of identified GABAergic cortically-projecting neurons. My findings suggest specialised functional roles of these projections in the coordination of cortico-cortical circuits. While the two defined subgroups of HRNs are likely to coordinate the temporal dynamics of glutamatergic inputs to CA1 via CA3 and the entorhinal cortex, LRNs likely contribute to the modulation of neural circuits during mnemonic processes such as dentate gyrus-dependent memory discrimination.

Acknowledgments

First and foremost, I would like to express my special thanks to my supervisors Professor Peter Somogyi, Dr Tim Viney and Professor Vladyslav Vyazovskiy, who gave me this great opportunity to fulfil this project. I cannot thank you enough for your input in my scientific development. I thank Professor Peter Somogyi for the immense support, trust, mentorship and endless lessons over the past years; Dr Tim Viney for the daily supervision, support, discussions, trouble-shootings and scientific discoveries! My achievements and scientific contributions would not have been possible without your abundant patience when introducing me to scientific work, starting from lab work, analysis, microscopy, and surgeries up to electrophysiological recordings and allowing me to work independently. Thank you Professor Vyazovskiy for allowing me to be part of your group, weekly discussions, for the exciting joint project introduction and using a novel approach!

Special thanks to the continuous advice, involvement and support of Professor Elspeth Garman, Professor Russel Foster, Professor David Dupret and Professor Grant Churchill throughout my DPhil ensuring continuity of my research.

Many aspects of my PhD would not have been possible without the seamless support of Mary! As an African proverb says, "*If you want to go fast, go alone; if you want to go far go together*"; in this environment 'together' was the only way forward, by all means, this environment is pushing frontiers! Great team spirit and great minds have inspired me which immensely affected my time in Oxford within and outside the department. I wish to thank current and past colleagues for your contributions, support and everything I learned from you. Many thanks to Dr Linda Katona, Dr Abhilasha Joshi, Dr Gunes Unal, Dr Istvan Lukacs and Dr Laura Lefevre. Thank you to Kristina Wagner, Naomi Berry, Dr Katja Hartwich, Michael Howarth, Ben Micklem and Amar Sharma for ensuring a great research environment, for your support and advice, especially during my long recording hours! Big thanks to Linda, Colin, Naomi, Vitor, Tugrul, Stephanie and Laura for the great friendship, lunchbreaks and endless amounts of caffeinated beverages, my DPhil time would have not been as great without you! Special mention to Abhilasha for being the best lab partner, providing great personal support since my arrival and introducing me to amazing people: Arun, Amogh, Usha, Huma, Priyam. I would like to express sincere appreciation to all members of the Pharmacology department for a great environment to work in. In addition, I would like to thank Brasenose College, for all kinds of support and the right platform for the perfect work-life balance.

Oxford became a second home thanks to valuable experiences, projects, discussions and personal growth. I was privileged to share this experience with exceptional people whom, I feel blessed to be surrounded by every day: Mina, Nermeen, Eddie, Crescente, Josef, Virginia, Nada, Florence, Jiorgos, Christian, Mehroz, Alvaro, Mate, Will and Grigory. Especially Edmond Toma, thank you for involuntarily coping with my daily drama, I am grateful having you be a part of this journey, you are exceptional! I wouldn't have known and lived the true meaning of '*the city of dreaming spire*' had I not met my close friend and work partner Mina Bekheet, showing me the ability to transform dreams into reality by being persistent and believing in oneself. The numerous others who I came across during this journey and started great projects with, including every member and alumni of the Science Innovation Union team, you guys did the impossible, thank you all! Most importantly, I want to express my gratitude to my entire family. My parents and my brothers, John and Bishoy, for their strong trust and robust support throughout. Finally, I wish to thank the one person closest to me, my best friend and partner Maryam for her incredible love, support, patience and belief in me. I am blessed to have you be a part of this journey.

Contents

Abstract **3**

Acknowledgments **4**

Chapter 1: General introduction **12**

1.1 Introduction 13

1.2 The intrinsic hippocampal circuit 14

1.3 Contextual spatial representation in the brain 15

1.4 Cortical network oscillations 16

1.5 The septal-diagonal band complex 19

1.6 Functions of the septo-hippocampal system 25

1.7 GABAergic neurons coordinate cortical network activity 26

1.8 Neurodegeneration involves the septo-hippocampal system 28

1.9 Aims 29

Chapter 2: Methods and experimental procedures **30**

2.1 Experimental subjects 31

2.2 Surgical procedures 31

2.2.1 Head plate implantation 31

2.2.2 Chronic silicon probe implantation 33

2.2.3 Virus injections 35

2.3 Electrophysiological recordings 36

2.3.1 Chronic freely-moving MUA recordings 36

2.3.2 Chronic freely-moving recordings technical specifications 37

2.3.3 Awake head-fixed single cell recordings 38

2.3.4 Awake head-fixed recording technical specifications 40

2.3.5 Single unit identification 41

2.3.6 Juxtacellular labelling 42

2.4 Tissue processing 43

2.4.1 Intracardial perfusion 43

2.4.2 Brain sectioning and tissue processing for imaging 43

2.4.3 Immunohistochemical analysis 45

2.4.4 Diamino-benzidine-based HRP reaction and embedding 47

2.5 Imaging and reconstruction 51

2.5.1 Wide-field epifluorescence microscopy 51

2.5.2 Confocal laser scanning microscopy 52

2.5.3 2D and 3D single cell reconstruction 53

2.6 Electrophysiological data analysis 54
2.6.1 Statistical analysis and quantification 54
2.6.2 Spike train analysis 55
2.6.3 Theta network oscillations analysis 56
2.6.4 Rhythmicity Index 57
2.6.5 Sharp wave ripple network oscillations analysis 58

Chapter 3: Diversity of medial septal cells recorded in awake mice based on physiological parameters during different brain states 62

3.1 Introduction 63

3.2 Results 65
3.2.1 In vivo extracellular recordings in awake head-fixed mice 65
3.2.2 Diversity of medial septal neurons based on spike train dynamics 68
3.2.3 Novel medial septal cells projecting to extra-hippocampal areas 73
3.2.4 Medial septal cells silenced after air puff presentation and during sharp wave ripples (SWRs) 78
3.2.5 Subcortically projecting medial septal cell 78
3.2.6 Viral tracing of medial septal cells targeting the DG/CA3 80
3.2.7 Chronic MUA recordings in the MS of freely moving mice 82

3.3 Discussion 86
3.3.1 Roles of subcortical GABAergic neurons governing cortical network activity 86
3.3.2 Dual subcortical and cortical projection from the medial septum 88
3.3.3 The role of the septo-hippocampal system in contextual memory consolidation during REM sleep 90

Chapter 4: Two identified subpopulations of high-rhythmic firing medial septal neurons targeting specific cortical areas with distinct spike train dynamics and molecular profiles 92

4.1 Introduction 93

4.2 Results 96
4.2.1 Identifying high-rhythmic firing medial septal neurons 96
4.2.2 Electrophysiological parameters of labelled Teevra and Orchid cells 97
4.2.3 Cortical target areas of labelled Teevra and Orchid cells 106
4.2.4 Molecular profiles of identified Teevra and Orchid cells 109
4.2.5 GABAergic Teevra cells preferentially innervate axo-axonic cells in CA3 111
4.2.6 GABAergic Orchid cells project to multiple extra-hippocampal regions 117
4.2.7 Preferential synaptic targets of Orchid cells 120
4.2.8 Medial septal neurons projecting to the entorhinal cortex 127

4.3 Discussion 129
4.3.1 Orchid cells are a subpopulation of Komal neurons 129

4.3.2 Orchid cells modulate the firing dynamic of spatially-modulated neurons 131
4.3.3 Orchid cells support indirect rhythmic coordination of CA1 pyramidal cell assemblies 132
4.3.4 Teevra cells enable CA3 pyramidal cell activation via disinhibition 133

Chapter 5: GABAergic medial septal neurons with low-rhythmic firing innervating the dentate gyrus and hippocampal area CA3 136

5.1 Introduction 137

5.2 Results 139
5.2.1 Identifying low-rhythmic medial septal neurons 139
5.2.2 Electrophysiological parameters of labelled low-rhythmic neurons 146
5.2.3 Low-rhythmic neurons are suppressed during sharp-wave ripples 156
5.2.4 LRNs innervate select regions of the hippocampal formation with a bias towards the DG and CA3 160
5.2.5 Majority of LRNs are PV- GABAergic neurons 164
5.2.6 The dentate gyrus receives less PV+ septal innervation than CA3 165
5.2.7 Postsynaptic targets of low rhythmic PV–/CB– septo-hippocampal neurons 169

5.3 Discussion 172
5.3.1 LRNs provide variable cortical network control 172
5.3.2 Modulation of LRNs during SWRs 173
5.3.3 Specialization of medial septal low-rhythmic firing neurons 175

Chapter 6: General discussion 178

6.1 Thesis outline 179

6.2 Subcortical-cortical GABAergic modulation via disinhibition 184
6.2.1 Teevra cells facilitate temporal coding in CA1 184
6.2.2 Orchid cells participate in the rhythmic entrainment of spatially-modulated projection neurons in the PrSd and EC via disinhibition 185
6.2.3 LRNs participate in memory discrimination on select theta cycles 186

6.3 Rhythmic activity in the basal forebrain 188

6.4 Technical limitations 189

6.5 Concluding remarks 191

6.6 Outlook 192

References 194

Appendix 213

Figures

Figure 1-1 Septal nuclei organisation and connectivity with hippocampus and hypothalamus. 24

Figure 2-1 Awake head-fixed recording setup with circular plate. 38

Figure 2-2 Awake head-fixed recording setup with wheel. 39

Figure 2-3 Recording hardware and software for single unit identification. 40

Figure 2-4 Coronally sectioned mouse brain sections in a 24-well-plate. 45

Figure 3-1 Schematic overview of innervated cortical regions of recorded and labelled single medial septal neurons. 67

Figure 3-2 Diversity in physiological features of identified medial septal neurons. 71

Figure 3-3 Preferred firing phase during CA1 theta oscillation and ripple-related activity of identified medial septal neurons. 72

Figure 3-4 Firing patterns, molecular profile and innervated cortical region of an identified medial septal neuron. 77

Figure 3-5 Single medial septal cell MS13c reacts to external air puff presentation. ... 79

Figure 3-6 Medial septal neurons simultaneously innervate the CA3 and supra-mammillary area. 81

Figure 3-7 Medial septal cell recorded in head-restrained mouse during REM sleep... 84

Figure 3-8 Chronic MUA recordings in the MS of freely moving mice 85

Figure 4-1 Ripple-related activity of *Orchid* cells and putative *Orchid* cells..... 105

Figure 4-2 Schematic representation *Teevra* and *Orchid* cells. 108

Figure 4-3 Firing patterns, molecular profile, and CA3 target neurons of *Teevra* neuron MS90g..... 115

Figure 4-4 Identification of a target neuron of *Teevra* neuron MS90g in CA3. 116

Figure 4-5 Firing patterns and molecular profile of *Orchid* neuron MS14i projecting to the EC. 119

Figure 4-6 Firing patterns, 3D reconstruction and cortical target regions of a GABAergic medial septal *Orchid* cell (TV58g). 124

Figure 4-7 Postsynaptic GABAergic target neurons of *Orchid* cell, TV58g.....125

Figure 5-1 Co-firing of high-rhythmic and low-rhythmic medial septal neurons. 143

Figure 5-2 LRNs are distinct from HRNs recorded in awake mice.....145

Figure 5-3 LRN and HRN firing patterns and their recording locations. 152

Figure 5-4 Theta-skipping properties high- and low-rhythmic neurons. 155

Figure 5-5 Low-rhythmic neuron is suppressed during SWRs.....157

Figure 5-6 Firing probability densities LRNs relative to SWRs during immobility. ..159

Figure 5-7 Synaptic targets of a GABAergic LRN mainly targeting the DG.....163

Figure 5-8 Differential input of DG/CA3 by GABAergic and PV+ MSDB axons. 168

Figure 5-9 Cortical target neurons of LRN TV78l. 171

Figure 6-1 Conceptual framework of identified subgroups of the mouse medial septum 183

Tables

Table 2-1 List of primary antibodies.....49

Table 2-2 List of secondary antibodies 51

Table 2-3 Distress Scoring Table.....60

Table 2-4 Recording sheet 61

Table 3-1 Electrophysiological parameters of recorded and labelled ‘unclassified’ cells. 75

Table 4-1 Electrophysiological parameters of identified *Teevra* neurons. 102

Table 4-2 Electrophysiological parameters of identified *Orchid* cells. 103

Table 4-3 Electrophysiological parameters of putative *Orchid* cells.....104

Table 4-4 Immunohistochemical profiles of *Teevra* and *Orchid* cells. 110

Table 4-5 Subcortical and cortical synaptic target neurons of a *Teevra* cell, MS90g. 113

Table 4-6 Cortical target neurons of *Orchid* cell TV58g.....126

Table 5-1 Properties of identified low-rhythmic neurons 148

Table 5-2 Properties high- and low-rhythmic neurons 153

Table 8-1 Single recorded medial septal neurons 215

List of abbreviations

A
AAC, axo-axonic cells
AAV, adeno-associated virus
AP, action potential
AD, Alzheimer's disease
AIS, axon initial segment

B
BDA, biotinylated dextran amine
BI, Burst incidence

C
CA1, Cornu Ammonis 1
CA2, Cornu Ammonis 2
CA3, Cornu Ammonis 3
CA1d, dorsal CA1
CB, calbindin
CCK, cholecystokinin
CDF, cumulative distribution function
ChAT, choline acetyltransferase
CR, calretinin
Cy3, cyanine 3
Cy5, cyanine 5

D
DAB, 3,3'-diaminobenzidine
DB, diagonal band of Broca
DG, dentate gyrus

E
EC, entorhinal cortex
EEG, electroencephalography
EDF, European Data Format
FFT, Fast Fourier Transform
EM, electron microscopy

G
GABA, gamma-Aminobutyric acid
$GABA_A$, gamma-Aminobutyric acid type A receptor

H
HRN, how-rhythmic neurons
HRP, horseradish peroxidase enzyme

I
IM, immobility
IR, immunoreactivity
ISI, inter-spike intervals
IQR, inter quartile range

L
LFP, local field potential
LIA, large amplitude irregular activity
LRN, low-rhythmic neurons

M
M, mobility
MAC, minimum steady-state anaesthetic concentration
mGluR1α, metabotropic glutamate receptor 1a
MS, medial septum
MSDB, medial septum and the vertical and horizontal diagonal band nuclei
MUA, multi-unit activity

N
NHS, normal horse serum
NOS, nitric oxide synthase

P
PB, phosphate buffer
PFC, prefrontal cortex
PrS, presubiculum
PrSd, dorsal presubiculum
PRV, pseudorabies virus
PV, parvalbumin

R
RI, rhythmicity index

S
s.d., standard deviation
SATB1, special AT-rich sequence-binding protein 1
SOM, somatostatin
SuB, Subiculum
SuM, supramammillary nucleus
SWR, sharp wave associated ripple

T
TBS-TX, tris buffered saline with Triton X-100®

V
VGAT, vesicular GABA transporter

Chapter 1

General introduction

1.1 Introduction

Much of the neuronal activity in the cortex and subcortex is rhythmic, and this activity is coordinated by various behaviour-dependent network oscillations. The hippocampus is a key structure involved in learning and memory, yet little is known about the mechanisms of how subcortical inputs influence the many different kinds of hippocampal neurons within the network. In investigating neuronal activity, the major focus has been the study of excitatory elements of the brain. However, inhibitory elements are critical components of neuronal networks and inhibition plays an important role in shaping network activity. Subcortical GABAergic medial septal neurons selectively target GABAergic interneurons within the hippocampal formation (dentate gyrus, CA3, CA2, CA1, subiculum) and extra-hippocampal areas such as presubiculum (PrS) and entorhinal cortex (EC), but the relationship firing activity of medial septal neurons and their postsynaptic targets is unknown. Thus, investigating the septo-hippocampal relationship of single medial septal neurons and revealing their connectivity in the targeted areas as well as their brain-state dependent activity during different network oscillations on a single cell basis will contribute to our contemporary understanding of the coordination of cortical brain activity and the generation of brain network oscillations.

I have investigated the role of subcortical GABAergic projection neurons in shaping network activity in the cortex. Using *in vivo* extracellular recordings of single medial septal cells in head-restrained awake drug-free mice on a circular treadmill followed by juxtacellular labelling of recorded cells, I have achieved the following:

In *Chapter 3*, I introduce and explore the diversity of the medial septal (MS) population. I further introduce a strategy of how I combined electrophysiological, anatomical and immunohistochemical methods to characterise and identify single medial septal neurons.

Based on selected parameters I have initially grouped recorded and labelled medial septal neurons with similar characteristics such as cortical target area and behaviour dependent firing activity. Based on my initial characterizations, in *Chapter 4*, I contributed to the hypothesis that two identified subpopulations of GABAergic high-rhythmic firing MS neurons (HRNs), *Teevra* and *Orchid* cells, selectively target interneurons in restricted regions of the cortex. After identifying HRNs, in *Chapter 5*, I identified and delineated a third novel group of low-rhythmic firing MS neurons (LRNs) with distinct firing characteristics and cortical innervation areas compared to HRNs. LRNs will be the focus of this thesis. In addition, I documented (*Chapter 3*) several single high-rhythmic firing MS neurons with unmatched firing patterns and projection characteristics targeting extra-hippocampal areas such as retrosplenial cortex, entorhinal cortex, amygdaloid piriform cortex or the ventral subiculum. Lastly, I have recorded septal multi-unit activity with chronically implanted electrodes in freely moving mice with the aim to match and investigate known identified medial septal neurons across the sleep-wake cycle.

1.2 The intrinsic hippocampal circuit

A central theme in brain research is to understand how memories and actions are dynamically represented in real time by the firing patterns of neurons. The hippocampus and its associated areas has been studied as a major system for its involvement in episodic memory and spatial navigation in rodents (O'Keefe and Dostrovsky, 1971; O'Keefe and Nadel, 1978; Morris *et al.*, 1982) and in humans (Burgess, Maguire and O'Keefe, 2002). Located in the medial temporal lobe (temporal cortex in rodents) it is part of the hippocampal formation, including the subiculum, presubiculum, parasubiculum and entorhinal cortex (EC). The hippocampal formation itself has three main subdivisions of the Cornu Ammonis, the CA3, CA2 and CA1 in addition to the DG and SUB. Together with its connections to other areas of the temporal lobe and the prefrontal cortex (PFC),

the hippocampus contributes to the encoding, association, consolidation, and recall of representations of the external and internal world in the combined firing rates and spike timing of glutamatergic pyramidal and principal cells (Somogyi and Klausberger, 2018). Most connections within the regions of the cerebral cortex are reciprocal. The intrinsic glutamatergic hippocampal circuit includes the perforant path from the EC towards the DG and CA3. The mossy fibres, unmyelinated axons of granule cells, and the glutamatergic hilar mossy cells connect the principal cells of the DG (Scharfman and Myers, 2013) with the pyramidal cells and interneurons of CA3 (Acsády *et al.*, 1998). The CA3 pyramidal cells in turn project a major input to the CA1 hippocampal field through the Schaffer collateral axons. The CA1 field projects to the subiculum, the entorhinal cortex and the prefrontal cortex as well as to several subcortical areas. The hippocampal formation projects to its main outputs the entorhinal, perirhinal and prefrontal cortices, the amygdala, ventral striatum, the hypothalamus and the lateral septum (Andersen, 2007). External as well as internal glutamatergic hippocampal inputs segregate to different parts of the dendritic tree of pyramidal cells and some in parallel to GABAergic interneurons (van Strien, Cappaert and Witter, 2009).

1.3 Contextual spatial representation in the brain

The hippocampal formation provides a very detailed representation of an animal's current location and heading. Spatial navigation and contextual representation remain the foundation and profound model to our growing understanding of the mechanisms of spatial cognition in mammals, including humans. With the discovery of place cells by O'Keefe & Dostrovsky (1971) in freely behaving rat, they firstly showed behaviour-related firing patterns of individual hippocampal cells. So called ‘place cells’ increased their firing rate characteristically within a certain region of an environment, the place field (O’Keefe and Dostrovsky, 1971). Thus, monitoring the firing rates of a population

of ‘place cells’ over a period of time, the animals’ location can be accurately be reconstructed (Wilson and McNaughton, 1993; Zhang *et al.*, 1998). Later the phase correlation between these hippocampal place cells and theta rhythm was discovered (O’Keefe and Recce, 1993). Hippocampal neurons including those place cells are organized in time into ‘neuronal assemblies’, whereas their activity can reflect both external sensory input and internal cognitive processes (Harris *et al.*, 2003). Since then more spatially-modulated cells contributing to navigation were discovered. Within the hippocampal formation, ‘head-direction cells’ were discovered by recording neurons in the presubiculum (PrS) of freely moving rats (Taube, Muller and Ranck, 1990; Brandon *et al.*, 2013), while ‘grid cells’ and ‘border cells’ were characterised in the entorhinal cortex (Hafting *et al.*, 2005; Solstad, 2008). Such representations in the PrS, EC and hippocampal regions are facilitated by interconnected glutamatergic cortico-cortical projections (Swanson and Cowan, 1977) and relatively sparse long-range GABAergic connections (Melzer *et al.*, 2012). These findings suggest an involvement of a wide network of different cell types with key roles for spatial cognition, especially when new spatial locations are being encoded for memory guided behaviours within the hippocampal formation. In addition, recent studies also show an internal representation of time by ‘time cells’ (Pastalkova *et al.*, 2008; Eichenbaum, 2014). All mentioned representations suggests an underlying mechanism for temporal coordination of activity across brain structures. This raises the question whether such a system requires an external input to govern it.

1.4 Cortical network oscillations

One of the major challenges in neuroscience is to establish how temporally coordinated sequences of neuronal assemblies create cognitive functions. The computations require flexible and effective communication structures that can work on the cortical circuit

structures. Such communication can be delivered by rhythmic synchronization of neurons on various time scales as reflected by network oscillations. Neurons in the brain discharge action potentials, or spikes, with enormous variability in both resting and active states (Shadlen and Newsome, 1994; Stein, Gossen and Jones, 2005; Faisal, Selen and Wolpert, 2008). In general, synchronous oscillations reflect a spatio-temporal structure of neural assemblies within and across networks (Schomburg *et al.*, 2014). Neural assemblies was first described by Donald Hebb (Hebb, 1949) as strongly interconnected group of active neurons representing a distinct cognitive entity. This concept is based on two facts; firstly, activated neuronal groups have the intrinsic properties to oscillate (Llinas, 1988), and secondly that those oscillations constitute rhythmic modulations in neuronal excitability, affecting the output of the neuronal assemblies as well as its sensitivity to their synaptic input. As a result, it creates temporal windows that open and close rhythmically for neuronal assemblies to effectively communicate (Fries, 2005). Such network oscillations can be observed by recording local field potentials (LFPs) that represent the sum of extracellular voltage changes due to currents flowing in the vicinity of the recording electrode. Most of the neuronal activity is rhythmic in the brain. This rhythmicity facilitates local and global interactions and enables the representation of temporal sequences. As part of this thesis I will focus on hippocampal oscillations and its subcortical influences, as I point out three most studied major network oscillations that dominate the hippocampal system. These are oscillations in theta (5–12 Hz), gamma (30–130 Hz), and sharp wave ripple (SWR; 130–230 Hz) frequency range in the temporal cortex of rodents. Different states of the hippocampus are defined by oscillatory patterns. The “theta state” is associated with exploratory movement behaviour and REM sleep (Kramis, Vanderwolf and Bland, 1975; Buzsáki, Leung and Vanderwolf, 1983; Lapray *et al.*, 2012), gamma oscillations (~30 – 120 Hz) which are phase-amplitude coupled to

theta (Colgin *et al.*, 2009; Bieri, Bobbitt and Colgin, 2014; Schomburg *et al.*, 2014; Lasztóczi and Klausberger, 2016), and hippocampal sharp waves ripple oscillations (SWR; 130–230 Hz) which occur during immobility, consummatory behaviour and slow wave sleep (O'Keefe and Nadel, 1978; Buzsáki, 1986; Buzsáki *et al.*, 1986). Hippocampal theta rhythms correlate with intake of sensory information during movements i.e. whisking and sniffing in rats. This process allows temporal segmentaion of samples of stimuli from the environment, with each theta cycle providing a discrete unit for sensory information processing in the brain (Colgin and Moser, 2010). In the hippocampus, gamma oscillations exhibit their largest amplitude when they are nested within the slower theta oscillations (Leung, Lopes da Silva and Wadman, 1982; Buzsáki, Lai-Wo S. and Vanderwolf, 1983; Bragin *et al.*, 1995). Despite their co-occurrence, hippocampal theta and gamma rhythms appear to be independently generated (Leung, 1992). Gamma oscillations occur in bursts at particular times within the theta cycle (Soltesz, Deschênes and Deschenes, 1993; Bragin *et al.*, 1995; Canolty *et al.*, 2006; Colgin *et al.*, 2009) and have been proposed to select particular cell assemblies for processing at those times. Further, oscillation like 'theta' are not confined to a single behavioural state. For instance as mentioned above, theta oscillations are the dominant rhythmic of REM sleep, and SWRs take place during slow wave sleep and awake states (Jadhav *et al.*, 2012; Lapray *et al.*, 2012). While during immobility and large amplitude irregular activity (LIA) a wide spectral content, including gamma oscillations dominates the hippocampal field potential (O'Keefe and Nadel, 1978), theta oscillations are most prominent during locomotion (Vanderwolf, 1969; Buzsáki, 2002). Theta oscillations are thought to provide temporal windows for local circuit computation in the entorhinal-hippocampal loop (Buzsáki and Draguhn, 2004; Mizuseki *et al.*, 2009). These windows during theta oscillation provide temporal packaging and transfer of neuronal sequences

(Skaggs *et al.*, 1996; Hasselmo, Bodelón and Wyble, 2002; Hasselmo, 2005; Dragoi and Buzsáki, 2006; Sirota *et al.*, 2008) that are critical for synaptic plasticity (Pavlides *et al.*, 1988; Huerta and Lisman, 1995). Moreover, theta oscillations coordinate the encoding and retrieval of episodic and spatial memories (Hasselmo, 2005; Jensen and Lisman, 2005; O'Keefe and Burgess, 2005) as disruption the rhythm results in behavioural deficits (Winson, 1978).

The origin and cellular mechanisms of these oscillations in the hippocampal formation requires further clarification. In particular, do theta oscillations facilitate neuronal coordination, and if so, through what *mechanisms*? Subcortical structures and in particular the medial septum (MS) play a crucial role in providing rhythmic inputs at theta frequency to the hippocampus and related areas (Vertes and Kocsis, 1997). However, the synaptic mechanisms underlying theta rhythmogenesis are still not known. Furthermore, it is not known how the populations of neurons phase-modulated by theta oscillations are interconnected nor how specific connections govern action potential (AP) synchronization and contribute to the generation of rhythmic activity required for coordination of cortical neuronal activity.

1.5 The septal-diagonal band complex

The septal area is divided into two main anatomical areas: the medial septal complex and the lateral septum. Specific immunohistochemical and anatomical connectivity is characterizing each of these areas (Amaral and Kurz, 1985; Freund and Antal, 1988; Pepeu and Blandina, 1998; Hajszan, Alreja and Leranth, 2004; Lecourtier *et al.*, 2011). Further, the medial septum complex is composed of two subnuclei: the dorsally located medial septum nucleus (MS) and the ventrally located nucleus of the diagonal band of Broca (DB). The lateral septum is divided into rostral, caudal and ventral subregions

(Risold and Swanson, 1997) (Figure 1-1). The diagonal band of Broca consists of large myelinated fibre bundles in the ventral forebrain between the medial septum and the anterior hypothalamus (Brashear, Zaborszky and Heimer, 1986).

Immunohistochemistry defines the major differences between the medial and lateral septal nuclei. The medial septum is mainly characterized by GABAergic, cholinergic and glutamatergic neurons (Amaral and Kurz, 1985; Brashear, Zaborszky and Heimer, 1986; Freund and Antal, 1988; Colom *et al.*, 2005). Wei et. al 2012 described the septal-diagonal band complex as an onion skin-like structure composed of five groups of neurons. These neurons are parvalbumin (PV), choline acetyltransferase (ChAT), neuronal nitric oxide synthase (nNOS), calretinin (CR) and calbindin (CB) immunoreactive. From medial to lateral, the septum is layered by PV+-ChAT+-nNOS+-CR+-CB+ neurons, forming a laminated structure where each layer may correspond to an independent role in brain circuits (Wei *et al.*, 2012). Within the septum-diagonal band complex cholinergic neurons were estimated to be about two times more numerous than GABAergic neurons. GABAergic cells are scattered throughout the nucleus of the vertical limb of the diagonal band, whereas cholinergic neurons are more numerous medially and are distributed in groups corresponding to the dorsal and ventral aspects of the nucleus. In the rostral parts of the nucleus of DB, cholinergic cells tend to be located medially. The majority of GABAergic neurons remain in a more ventral and lateral position within DB (Brashear, Zaborszky and Heimer, 1986; Tsanov, 2018).

The hippocampal formation receives noradrenergic, dopaminergic, serotonergic, histaminergic, cholinergic, glutamatergic, and GABAergic subcortical inputs. Over the last decades, the medial septum, has been in focus for its key involvement for the proper function of the hippocampus and memory formation. My DPhil thesis will be mainly focusing on the projections from the basal forebrain, in particular from the septal-

diagonal band complex (MSDB). The septal nuclei are reciprocally connected to the hippocampus by GABAergic neurons (Raisman, 1966; Takács, Freund and Gulyás, 2008) in addition to cholinergic and glutamatergic neurons (Kimura *et al.*, 1980; Freund, 1989; Hajszan, Alreja and Leranth, 2004; Colom *et al.*, 2005), with various developmental origins (Wei *et al.*, 2012). Aside from innervating the entire temporal cortex, MSDB neurons also innervate the prefrontal cortex, parietal cortex, supramammillary nucleus, and ventral tegmental area (Wyss, Swanson and Cowan, 1979; Gonzalez-Sulser *et al.*, 2014; Unal *et al.*, 2015; Fuchs *et al.*, 2016; Agostinelli, Geerling and Scammell, 2019). Hippocampal pyramidal neurons project to GABAergic lateral septum neurons in a topographical manner (Risold and Swanson, 1997). In terms of medial septal inputs to the hippocampus, the cholinergic input innervates both interneurons and pyramidal cells, while GABAergic septal neurons preferentially innervate GABAergic interneurons (Freund and Antal, 1988; Unal *et al.*, 2015), and most of their extra-hippocampal cortical postsynaptic neurons are also GABAergic cells in rat and mouse (Freund and Buzsáki, 1998; Gonzalez-Sulser *et al.*, 2014; Unal *et al.*, 2015). Nevertheless, it has been recently shown that all cholinergic medial septal neurons also co-transmit GABA (Takács *et al.*, 2018) in addition to a recent tracing study demonstrating medial septal GABAergic neurons innervating CA1 excitatory cells (Sun *et al.*, 2014).

The human septal nuclei is located in the rostra1 telencephalon between the two hemispheres and is bordered dorsally by the corpus callosum, laterally by the ventricle, rostrally by the subcallosal gyrus, hippocampal continuation and genu of the corpus callosum, rostroventrally by the nucleus accumbens and subcallosal gyrus and caudoventrally by the anterior commissure, preoptic area and anterior hypothalamus (Andy and Stephan, 1968). It has been the focus of relatively few human neuroimaging

studies, mainly due lack tools for accurately quantifying this region. The relatively small region (~290 mm^3) located the base of the brain, in between the ventricles, is difficult to image as it is prone to artefacts in magnetic resonance imaging (MRI) studies, especially those that use automated processing (Butler *et al.*, 2014). In rodents, the septal nuclei are strongly interconnected with hippocampi via the fimbria/fornix and are critical for generating the hippocampal theta rhythm needed for learning and memory (Winson, 1978; Stewart and Fox, 1990; Huerta and Lisman, 1993; Buzsáki, 2002; Hangya *et al.*, 2009). Similar to animals studies, lesioning the septal nuclei in humans impaired memory (Alexander and Freedman, 1984; Fujii *et al.*, 2002).

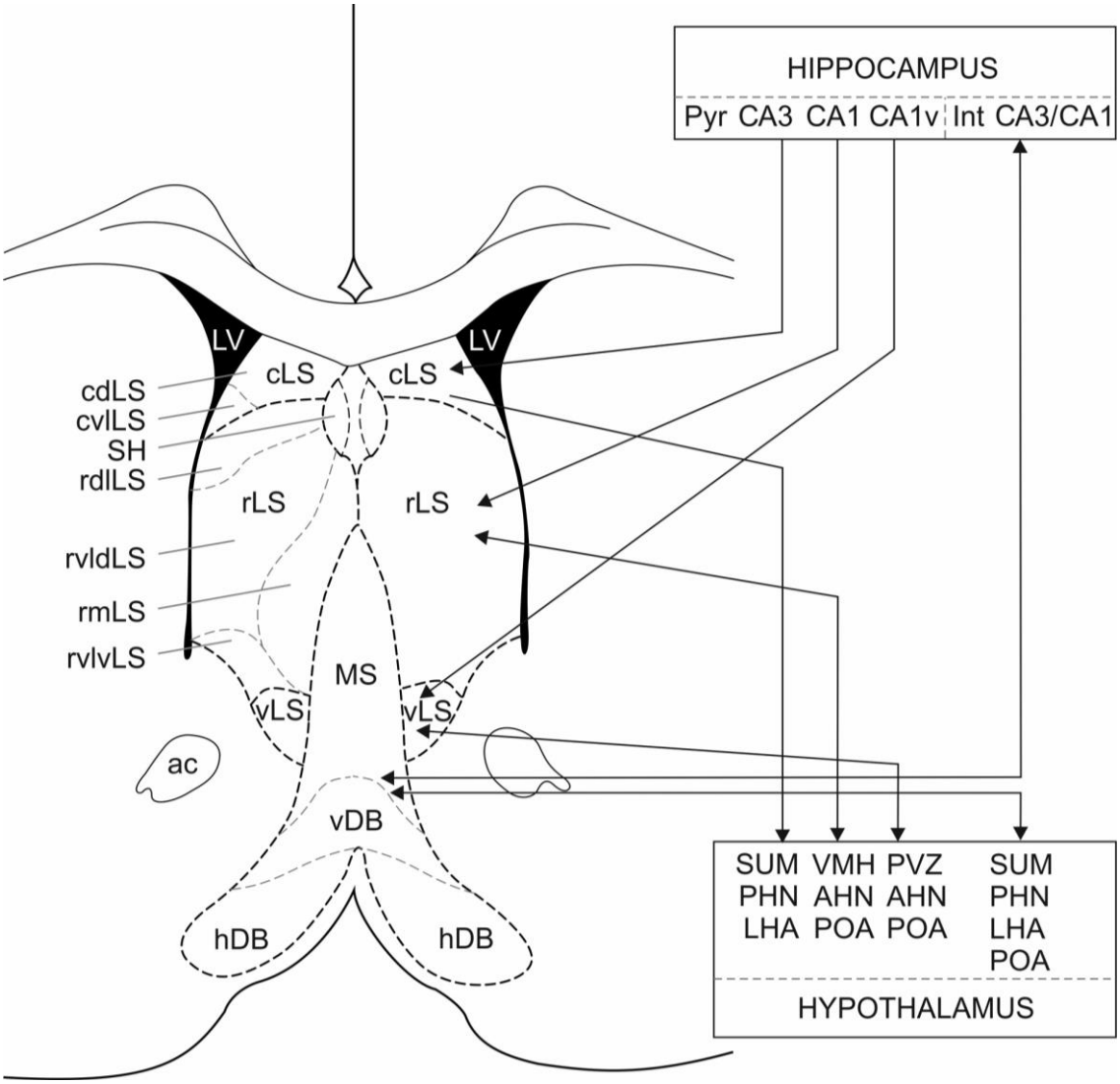

HIPPOCAMPUS
Pyr CA3 CA1 CA1v Int CA3/CA1
LV
LV
cLS
cLS
cdLS
cvlLS
SH
rdlLS
rLS
rLS
rvldLS
rmLS
rvlvLS
MS
vLS
vLS
ac
vDB
hDB
hDB
SUM PHN LHA
VMH AHN POA
PVZ AHN POA
SUM PHN LHA POA
HYPOTHALAMUS

Figure 1-1 Septal nuclei organisation and connectivity with hippocampus and hypothalamus.

Schematic representation of the medial and lateral septal nuclei organisation. Representative intraseptal subregions are separated with grey dashed lines. Arrows indicate the main connections of medial and lateral septal nuclei with the hippocampus and hypothalamic areas. Cortical medial septal projections also include extra/hippocampal areas e.g. presubiculum (PrS) and entorhinal cortex (EC) (Viney et. al. 2018). ac, anterior commissure; AHN, anterior hypothalamic nucleus; cdLS, dorzal zone of caudal lateral septum; cvlLS, lateral region of ventral zone of caudal lateral septum; dLS, dorsal lateral septum; hDB, horizontal limb of diagonal band of Broca; Int CA3/CA1, interneurons in hippocampal areas CA3 and CA1; LHA, lateral hypothalamic area; LV, lateral ventricle; MS, medial septum; PHN, posterior hypothalamic nucleus; POA, preoptic area; PVZ, periventricular zone of hypothalamus; Pyr CA3, CA1, CA1v, pyramidal neurons in hippocampal cornu ammonis area CA3, CA1 or ventral CA1; rdlLS, dorsolateral zone of rostral lateral septum; rLS, rostral lateral septum; rmLS, medial zone of rostral lateral septum; rvldLS, dorsal region of the ventrolateral zone of rostral lateral septum; rvlvLS, ventral region of the ventrolateral zone of rostral lateral septum; SH, septo-hippocampal nucleus; SS, superior sagittal sinus; SUM, supramammillary nucleus; vDB, vertical limb of diagonal band of Broca; vLS, ventral lateral septum; VMN, ventromedial hypothalamic nucleus. Schematic overview taken from (Tsanov, 2018).

1.6 Functions of the septo-hippocampal system

Rhythmically burst-firing 'theta cells' recorded in the MSDB have been hypothesized to provide rhythmic entrainment of hippocampal target neurons (Petsche, Stumpf and Gogolak, 1962; Ford, Colom and Bland, 1989; Borhegyi, 2004; Simon *et al.*, 2006). This hypothesis was extended to provide such rhythmic entrainment via disinhibition of principal cells (Freund and Antal, 1988). Even during the absence of theta oscillations in the hippocampal LFP, the rhythmic activity of these cells suggested their role as "pacemakers" (Brücke *et al.*, 1959; King, Recce and O'Keefe, 1998a). Further, it been suggested that the 'pacemaker' of hippocampal theta may act as a set of functionally differentiated components rather than as a single homogenous unit (Nerad and McNaughton, 2006). This has brought the medial septum further in focus as a key relay for subcortically-generated theta oscillations (Brücke *et al.*, 1959; Vertes and Kocsis, 1997; Wang, 2002; Varga *et al.*, 2008; Hangya *et al.*, 2009).

Over the last decades a considerable amount of research has been done on the correlation of theta rhythm with learning and memory (Berry and Thompson, 1978; Winson, 1978; Givens and Olton, 1990; Vertes and Kocsis, 1997; Berry and Seager, 2001). Disruptions and selective inactivation of septal inputs and fornix resulted in loss of theta power and impaired performance in memory-dependent spatial learning tasks (Winson, 1978; Rawlins, Feldon and Gray, 1979; McNaughton, Ruan and Woodnorth, 2006; Pang *et al.*, 2010). Spatial memory impairment was caused by disrupted spatial firing fields of entorhinal grid cells and hippocampal place cell sequences (Jeffery *et al.*, 1995; Leutgeb and Mizumori, 1999; McNaughton, Ruan and Woodnorth, 2006; Brandon *et al.*, 2011; Wang *et al.*, 2015; Zutshi *et al.*, 2018).

1.7 GABAergic neurons coordinate cortical network activity

Network oscillations enable the representation of rhythmic temporal sequences. Further, neuronal assemblies, such as sequences of place cells, are controlled by a network of local GABAergic neurons. These interneurons control the excitability of principal cells by a mechanism of temporal and specific somato-dendritc inhibition over various time scales reflected by underlying network oscillations (Cobb *et al.*, 1995; Ylinen *et al.*, 1995; Somogyi and Klausberger, 2018). A network with over 21 GABAergic cell types identified in CA1 target distinct subcellular domains of principal cells, each cell type preferentially firing during specific phases of network oscillations, which together contribute to a temporal redistribution of inhibition from the axon initial segment to the soma, and all the way to the distal dendrites of principal cells (Somogyi and Klausberger, 2005; Klausberger and Somogyi, 2008; Varga, Golshani and Soltesz, 2012; Somogyi *et al.*, 2014). For instance, parvalbumin (PV)-immunopositive bistratified cells terminate on pyramidal cell dendrites, while axo-axonic cells (AACs) preferentially innervate the axon-initial segment of pyramidal cells (Somogyi *et al.*, 1983; Klausberger *et al.*, 2004; Viney *et al.*, 2013). Further, ACCs lack the transcription factor SATB1 (Viney *et al.*, 2013). During movement, AACs and bistratified cells fire with similarly high frequencies. However, while AACs preferentially fire during the peak of dorsal hippocampal CA1 (CA1d) theta oscillation, bistratified cells are inactive but have their maximal firing probability during the trough of CA1d theta cycles on complementary temporal segments of the descending slope of theta cycles. In addition, AACs are suppressed during hippocampal SWRs while bistratified cells are active (Klausberger *et al.*, 2004; Klausberger and Somogyi, 2008; Viney *et al.*, 2013). Classification of novel cell types is still a major challenge in systems neuroscience and, thus, several definitions may exist. One definition by (Peter Somogyi, 2010) states the following: "*Two individual*

neurons belong to the same cell type if they deliver the same neuroactive substances to the same range of postsynaptic targets in the same temporal patterns in a brain state-specific manner". I will apply this definition to the characterisation and identification of medial septal neurons in this thesis. If the concept temporal redistribution of inhibition is taken across the hippocampal formation, and given the diversity of GABAergic cell types coordinating the output of principal cells, it remains unclear which underlying circuits and neurons are responsible for their coordination. Looking at subcortical projections to the hippocampal formation, the medial septum and diagonal band of Broca (MSDB) in the basal forebrain becomes the focus of attention. As mentioned above septal GABAergic cells preferentially target cortical GABAergic neurons. Taking into account that distinct types of hippocampal GABAergic interneurons target different subcellular domains of pyramidal cells and show preferred-firing phases during theta network oscillations, *how do septal inputs influence the coordination of the firing of the many types hippocampal interneuron?* To answer this question, it first becomes necessary to define how single septal neurons contribute to the hippocampal network both in terms of behaviour-dependent activity and their postsynaptic target regions and cells. In particular, it is necessary to define septal presynaptic inputs which may be responsible for coordinating the activity of identified hippocampal interneurons. Yet, the contribution of the different firing patterns of individual GABAergic septo-hippocampal neurons to hippocampal network activity, and to the coordination of principal cell assemblies, has not been well established. This coordination may occur through local interactions in the MSDB, the target regions, interneurons in hippocampus or a dynamic process combining all possibilities. *Yet, given this cortical interneuron diversity, what is the relationship between firing patterns, target brain regions and synaptic target neurons of subcortical projection neurons? Further, considering the cortical temporal redistribution of*

inhibition through a network of cortical GABAergic cell types, *how diverse is the GABAergic subcortical network?*

1.8 Neurodegeneration involves the septo-hippocampal system

Ever since a patient called Henry Gustav Molaison (HM) developed severe anterograde amnesia following his surgery, the hippocampus has been linked with memory. Following removal of hippocampus due to refractory epilepsy, HM was unable to form new episodic memories (Preilowski, 2009). In medical science, he has been perhaps the most studied medical patient for memory so far. Several mechanisms have been linked to hippocampal atrophy, as it is one of the most consistent features and clinical marker for Alzheimer's disease (AD) (Dhikav and Anand, 2011). Loss of memory and lack of memory formation is a main symptom that relates the septo-hippocampal system to AD (Albert and Moss, 1999). For instance, there is a correlation between the decrease of the septo-hippocampal synchrony and the dramatic decrease in memory formation (Whitehouse *et al.*, 1982; Jyoti *et al.*, 2010; Fonseca *et al.*, 2011; Kim *et al.*, 2012). A study investigated in rats physiological effects of hippocampal amyloid beta injections, and concluded septo-hippocampal dependency. The septo-hippocampal system showed decreased rhythmic GABAergic septal activity and memory-associated theta oscillations (Villette *et al.*, 2010). Further, transgenic mice have shown an accelerated decrease of GABAergic terminals along the septo-hippocampal pathway resulting in decreased theta and gamma oscillations (Rubio *et al.*, 2012). Also other disorders of the central nervous system disorders e.g. schizophrenia and autism spectrum are accompanied by abnormal coordination and synchronization of neuronal activity (Uhlhaas and Singer, 2012). Human autopsy and neuroimaging studies have associated Alzheimer's disease with loss of cholinergic neurons in the nucleus basalis of Meynert, located in the posterior basal

forebrain (Whitehouse et al., 1981; Teipel et al., 2005). However, structural changes of septal nuclei, located in the anterior basal forebrain, have not been well studied in human AD. One study examined healthy subjects that are destined to develop AD in the future. They demonstrated septal nuclei enlargement in healthy subjects prior to the development of Alzheimer's disease. Septal enlargement may reflect neuroplastic compensation, amyloid deposition or inflammation (Butler et al., 2018).

1.9 Aims

During my DPhil, I have attempted to delineate the subcortical role of distinct medial septal GABAergic neurons regarding their cortical connectivity in targeted areas as well as their brain-state dependent activity in relation to different network oscillations. I hypothesise that distinct medial septal GABAergic neurons with similar molecular marker combinations and specific temporal firing activity across different brain states, specifically innervate same cortical areas and have selective synaptic targets. I have mainly used *in vivo* extracellular recordings of single medial septal cells in head-restrained awake drug-free mice on a circular treadmill followed by juxtacellular labelling of recorded neurons.

Chapter 2

Methods and experimental procedures

2.1 Experimental subjects

All procedures involving experimental animals were performed under approved personal and project licences in accordance with the Animals (Scientific Procedures) Act, 1986 (United Kingdom) and associated regulations at the University of Oxford. The experiments were conducted with 8 - 35 weeks old male C57BL/6J (Charles River, UK) mice (27 – 45 g) for *in vivo* extracellular electrophysiological recordings (n=107), retrograde and anterograde virus tracing studies (n=8) and silicon probe recordings (n=4). All animals were housed with littermates until surgical implantation of the head-plate/silicon probe or virus injection, after which they were housed individually on a normal 12/12 h light-dark cycle.

2.2 Surgical procedures

2.2.1 Head plate implantation

Surgical procedures for implantation of the head-plate for head-fixed recordings, craniotomies, duratomies and virus injections were performed under general anaesthesia with the mouse mounted in a stereotaxic frame (Kopf Instruments). All surgical procedures were strictly aseptic including the use of autoclaved tools. General anaesthesia was induced with 4 % isoflurane (IsoFlo, Abbott) in oxygen using an anaesthetic vaporiser (flow rate of carbogen, 2L/min). After clipping the scalp, the animal was placed in the prepared stereotaxic frame and fixed using blunt ear bars covered with Lidocaine (Biomedical Services, Oxford). Buprenorphine (Vetergesic, 0.03 mg kg^{-1}, Biomedical Services, Oxford) was administered subcutaneously peri-operatively to reduce postoperative pain and to reduce the minimum steady-state alveolar anaesthetic concentration (MAC). This had a positive effect on the recovery process. The scalp was

locally treated by subcutaneous injection of Marcaine (Biomedical Services, Oxford). Eyes were covered with Lacri-Lube (ocular lubricant, Biomedical Services, Oxford). Body temperature was maintained at 37°C using a homoeothermic blanket (Harvard Apparatus) throughout the surgery. Prior to incision, the skin was locally sterilized with chlorhexidine. The incision was performed posterior to the eyes anteriorly towards the neck muscles along the midline of the scalp. Underlying tissue was removed from the skull using sterile cotton swabs. During the procedure isoflurane concentration was maintained at the lowest level which shows no response to pinch reflex (typically 1 - 1.5 %). After exposing and cleaning the skull, stereotaxic coordinates relative to Bregma were marked on the skull (for *in vivo* electrophysiological recordings: medial septal craniotomy, hippocampal craniotomy, motor cortex EEG, visual cortex EEG, retrosplenial cortex EEG, ground reference screw, head plate fixation; virus injection: medial septum, hippocampus and entorhinal cortex). Prior to drilling the marked coordinates, a small drop of superglue was applied and scratched on the surface of the skull to increase subsequent head-plate stability. Once the superglue dried, the marked coordinates were drilled leaving the dura intact. To enable EEG recordings two M1 2x3 mm screws (Precision Technology Supplies Ltd) connected to female pins for motor cortex (coordinates relative to bregma: anteroposterior, +1.50 mm; mediolateral, +1.70 mm), visual cortex (coordinates relative to bregma: anteroposterior, -2.10 mm; mediolateral, -2.50 mm) and/or retrosplenial cortex (coordinates relative to bregma: anteroposterior, -2.30 mm; mediolateral, -0.50 mm) were fixed to the skull. Another two M1 2x3 mm screws (one or both with a female pin for ground/reference) were fixed above the dorsal cerebellum for securing the head plate. Once all screws were inserted, a small amount of dental cement (Zimmer Biomet UK Ltd) was used to fix the screws to the skull and in a second round applied to secure the head plate (either a 0.7g or 1.1g version,

custom made at the Department of Physics, Oxford University) as well as the holding the screws and pins in place. Here, the screws are critical for proper adherence of head plate to skull. At this stage the skull was to be positioned horizontal relative to the head of the mouse. For subsequent glass electrode recordings in hippocampal CA1 (coordinates relative to bregma: anteroposterior, -2.50 mm; mediolateral, +1.70 mm) and medial septum (coordinates relative to bregma: anteroposterior, +0.85 mm; mediolateral, 0.00 mm), a craniotomy was performed either immediately after head plate implantation or during a second procedure one-two days prior to the recording day. The craniotomies were prepared using a drill bit (size #4 and #6). The first one above the medial septum, the skull was drilled to a depth whereby the sinus can be clearly seen to each lateral edge through the skull. Once the skull fragment was removed from the craniotomy site, the dura was carefully cut and removed using a modified sterile needle. Open craniotomies were covered with silicon (Smooth-On, Macungie, PA, USA) until the recording day. The typical length of surgery was around one-three hours. To prevent dehydration, 0.5 – 1 ml glucose - saline solution (5 % / 0.9% w/v; s.c.) were administered every 1 hour. Post-op recovery and care was maintained at high standards using a distress scoring system, regularly checks and medication.

2.2.2 Chronic silicon probe implantation

For chronic freely-moving multi-unit activity (MUA) recordings in the medial septum the surgery was performed equivalent to the procedure of the head-plate implantation in 2.2.1. Coordinates for the medial septal craniotomy (relative to bregma: anteroposterior, +0.85 mm; mediolateral, 0.00 mm), hippocampal craniotomy (relative to bregma: anteroposterior, -2.50 mm; mediolateral, -1.90 mm), motor cortex EEG (relative to bregma: anteroposterior, +1.50 mm; mediolateral, +1.70 mm), occipital EEG (relative to

bregma: anteroposterior, -2.50 mm; mediolateral, -2.10 mm), and reference and ground screws (above cerebellum) were taken, drilled and prepared using a #6 and #9 drill bit size. Prior to surgery, a set of M1 2x3 mm screws with a female pin were prepared as well as two EMG wires. In addition, a tungsten wire soldered to a female pin was made to record hippocampal CA1 LFP. For the freely moving setting a separate custom-made head stage (PCB connector 8-Way STR Socket 2ROW solder tail 1.27 mm; Inelco Hunter Limited) was used to link the two EEGs, two EMGs, one tungsten wire and one reference point to one connector. The head stage was prepared with male pins connected to 1-2 cm long wires to efficiently and securely connect each point during the surgery. In addition, the long wires would stabilize the head stage above the head of the animal and provide suspension to avoid any pressure while connecting it. The soldered wires were isolated within the head stage using resin. Next, the EEG screw were placed and a 32Ch zif clip Polytrode (A1x32-Poly3-5mm-25s-177-Z32; one shank, 5mm long, 275 µm contact length, 32 channels, 177 μm^2 contact area per channel, 25 µm distance between contact sides; NeuroNexus) was inserted into the medial septum at 3750 µm and fixed using dental bone cement. A recent study has proven that slow insertion of silicon probes improves the quality of neuronal recordings (Fiáth *et al.*, 2019). Thus, I inserted the silicon probe with a speed of 200 µm/min. For two mice (MS118 and MS119) the probe was connected at this point to monitor multi-unit activity intrasurgically while positioning the probe into the medial septum. After placing the probe, the tungsten wire was inserted at 1000 µm depth into the hippocampus and fixed using dental bone cement. The probe was connected to the ground and reference screws and a second layer of dental cement was applied. Finally, the head stage was connected to the EEG screws and tungsten wire before both EMG wires were inserted into the neck muscles and fixed above the cerebellum. After connecting all parts, dental bone cement was applied to fix the head

stage and to isolate and cover all connected parts. After a recovery period of 10 days, mice were initially habituated and connected to the amplifier (PZ5 NeuroDigitizer pre-amplifier, TDT Alachua FL, USA) in a separate cage (see 1.3.1).

2.2.3 Virus injections

The surgical procedure was initiated and performed as described in 2.2.1 until exposing and cleaning the skull. Coordinates were taken for targeting the hippocampal CA1 or CA3 (coordinates relative to bregma: anteroposterior, -2.50 mm; mediolateral, +1.70 mm), medial septum (coordinates relative to bregma: anteroposterior, +0.85 mm; mediolateral, 0.00 mm) and/or entorhinal cortex (coordinates relative to bregma: anteroposterior, -4.85 mm; mediolateral, +3.10 mm). After performing a small craniotomy, a glass pipette (5µl, Harvard Apparatus LTD) was lowered at a 5° latero-medial angle to 3.75 mm ventral of the dura mater into the MSDB, at 0° latero-medial angle to 1.30–2.50 mm into the CA1/CA3 and/or at 0° latero-medial angle to 1.20–1.90 mm into the caudal EC. An Anterograde Cre-dependent EYFP expressing adeno-associated virus (AAV-EF1a-DIO-hChR2(H134R)-EYFP; 400 nl/mouse; UNC Vector Core) and a monosynaptically-restricted retrogradely transported and non-spreading Cre-expressing virus (PRV HKO146 IE180-null hSyn Cre; 250-400 nl/mouse; Oyibo *et al.*, 2014) was pressure-injected in the medial septum and hippocampus/entorhinal cortex, respectively, using a 1 µl syringe at a rate of ~100 nl/min. The PRV-hSyn-Cre virus, a mutant pseudorabies virus of the alpha-herpes virus subfamily, is non-cytotoxic and highly tropic, resulting in Cre expression only in neurons that directly project to the injection site. Note that the tip diameter varied from the virus type (8–15 µm for AAV and 12–19 µm for PRV). To maintain the titre of the PRV, the virus was stored at -80ºC in a minimum volume of 100 ul aliquots. Prior injection the PRV virus was rapidly

thawed using a 37ºC water bath and kept on ice after. Five minutes after injecting the virus the glass pipette was taken out slowly and the incision sutured (Vet-Tech Solutions Ltd). Mice were perfuse-fixed 4-6 weeks after injections in order to ensure optimal viral expression.

In PV-Cre (1 heterozygous Cre mouse, Jackson Laboratory, stock #008069) and VGAT-Cre (3 heterozygous Cre mice, The Jackson Laboratory, Bar Harbor; stock #016962) mice, an anterograde Cre-dependent adeno-associated virus (AAV) was injected. All Cre-dependent anterograde tracing data from PV-Cre and VGAT-Cre mice analysed in Chapter 4 were obtained from *Unal et al. 2015* and *Salib et al.* 2019. After performing a small craniotomy at 0.86 mm anterior and 0.39 mm lateral of bregma, a glass pipette (tip diameter: 12–20 μm, 5 μl; Harvard Apparatus) was lowered at a 5° lateromedial angle to 3.75 mm ventral of the dura mater into the MSDB. Anterograde Cre-dependent AAV2-CAG-FLEX-ArchT-GFP (n = 4 mice; 400 nl/mouse; UNC Vector Core) or pAAV2-EF1a-DIO-EYFP (n = 3 mice) was pressure injected using a 1 μl syringe at a rate of ∼100 nl/min. Mice were perfuse-fixed >28 d after injections to ensure optimal viral expression.

2.3 Electrophysiological recordings

2.3.1 Chronic freely-moving MUA recordings

After a post-surgical recovery period of 10 days, two implanted mice were placed in separate custom-made clear plexiglass cages (20.3 x 32 x 35 cm) with free access to a running wheel (Campden Instruments, Loughborough, UK, wheel diameter 14 cm, bars spaced 1.11 cm apart inclusive of bars), food and water. Cages were placed in a ventilated, sound attenuated Faraday chamber (Campden Instruments, Loughborough, UK, two cages per chamber) on a standard 12:12 h light–dark cycle. Mice were habituated

to the light-dark cycle without interruption for 3 days and connected to the head stage for an additional day. On the fifth day the Polytrode was connected. Before recording the signals were monitored and verified, two mice (MS118 and MS119) had in addition a sensor connected to the wheel including a video recording device.

2.3.2 Chronic freely-moving recordings technical specifications

Signals from the NeuroNexus Polytrode and head stage were acquired using a Tucker Davis Technology (TDT, Alachua FL, USA) Multichannel Neurophysiology Recording System. Cortical LFP was recorded from frontal and occipital EEG derivations. Signals from EEGs, EMG and tungsten wire were filtered between 0.1-100 Hz, amplified (PZ5 NeuroDigitizer pre-amplifier, TDT Alachua FL, USA) and stored at a sampling rate of 800 Hz. EMG was recorded as a derivation of both implanted EMG wires. Extracellular neuronal spike data derived from the NeuroNexus probe were acquired at a sampling rate of 25 kHz (filtered between 300 Hz - 5kHz). Experimental design, visualization, settings and acquisition were done using the TDT Synapse software. During recordings, an amplitude threshold was applied to the signal derived from the Polytrode using an online spike sorting procedure so that only those spikes that exceeded the threshold were detected and stored for further analysis. The threshold was set for each channel separately. Data was acquired for a period of 24 h for each mouse and split in 12 h recordings. By using custom MATLAB scripts (The MathWorks Inc, Natick, Massachusetts, USA) kindly provided by Dr Vladyslav Vyazovskiy the EEG and LFP data were resampled at a sampling rate of 256 Hz for subsequent processing. Next, the Neurotraces software was used to transform data into European Data Format (EDF). All signals including a selection of Polytrode channels were then visualised offline using the software SleepSign (Kissei Comtec Co, Nagano, Japan) and binned in 4-second epochs.

Each epoch was manually scored into its respective vigilance state. Waking was defined by the presence of 5-12 Hz theta oscillation with a high level or phasic EMG phasic activity. Periods with a signal of a high amplitude and low frequency, as well as the occurrence of EEG slow waves was defined as NREM. REM sleep was defined by the presence of 5-12 Hz theta oscillation as a low voltage, high frequency LFP signal, which was distinguished from waking by absence of EMG activity. SleepSign was used to calculate the power spectra for each 4-second epoch of the scored LPF data, using a Fast Fourier Transform (FFT) routine for 4-s epochs (Hanning window, 0.25 Hz resolution). This process was repeated for each recording period separately.

2.3.3 Awake head-fixed single cell recordings

Recordings typically began 1-3 days after the craniotomies were performed over hippocampal CA1 and medial septum. The typical recording session lasted 2-5 hours. Some mice had several recording days. To habituate the mouse to the circular treadmill (wheel) or flat disc after head plate implantation and recovery, the craniotomy was performed during a second procedure under general anaesthesia. On the first recording day an initial brief head-fixation was carried out followed by a short period in its home cage. Afterwards, the mouse was placed again on the wheel and head fixed firmly for recording. Over the whole procedure the animals were monitored for signs of stress, e.g. vocalization or struggling which was rare. The mice exhibited a variety of natural behaviours, such as grooming, locomotion, whisking and sniffing under head-fixation as they do in the home cage (Viney *et al.*, 2018). An



Figure 2-1 Awake head-fixed recording setup with circular plate.

accelerometer as well as a video recording device was attached to the set-up to monitor behavioural changes while recording (Viney *et al.*, 2018). After securing the mouse under head-restrain the craniotomy sites were exposed and rinsed with sterile saline solution (0.9%) and glass pipettes filled with 3-5 % neurobiotin or 5-10 % biotinylated dextran amine (BDA, 3000 MW, Lysine Fixable, Life Technologies Ltd.) were advanced into the brain using a IVM1000 motorised micromanipulator (Scientifica). The neuronal activity was recorded extracellularly (referenced to cerebellar screw) and simultaneously in the medial septum and in the hippocampal dorsal CA1 area. The local field potential (LFP) and action potentials (0.8–5 kHz; 20 kHz sampling) of individual neurons were recorded by a glass electrode (06 – 17 MΩ, filled with 0.9% saline) in CA1 (10° latero-medial angle) and a second glass electrode (10 – 21 MΩ, filled with 3-5 % neurobiotin or 5-10 % BDA in 0.5 M NaCl) in the medial septum. In the CA1 area, the LFP was always recorded in stratum pyramidale or stratum oriens with a single glass electrode. In some cases, the targeted area could not be found or recorded. Using dorsal CA1 (CA1d) LFP as a cortical reference oscillation, the glass electrode was always positioned in an area of identified electrophysiological characteristics including the occurrence of sharp wave-associated ripples and large-amplitude LFPs. Note, associated ripples are positive in stratum pyramidale or stratum oriens, but negative going deeper into stratum radiatum and stratum lacunosum-moleculare, thus these can be used to identify the different layers. However, ‘sharp waves’ must have ripples too, otherwise these could be mistaken for ‘down states’ in the cortex

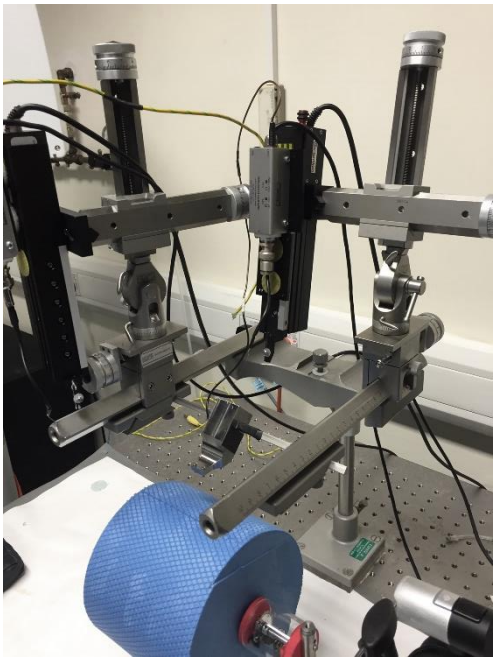


Figure 2-2 Awake head-fixed recording setup with wheel.

above hippocampus, or even dentate spikes if too deep. By always using the same CA1 reference location, recorded LFPs can be compared and referenced to cells recorded in different animals or even different species of rodent (Klausberger *et al.*, 2003). The second glass microelectrode was lowered at the centre of the craniotomy site as close to midline as possible to target the medial septum; often through the sinus. Using the micromanipulator, single cells in the medial septum were slowly approached and recorded until a single stable cell fulfilling the required parameters was found and recorded during different behavioural states (see 2.3.5). After a typical recording period of 3-6 minutes, the cell was attempted for labelling using the juxtacellular labelling technique (see 2.3.6) (Pinault, 1996; Unal *et al.*, 2018). After a recovery and neurotracer diffusion period of 2-48 hours (2-8 h for neurobiotin and 24-48 h for BDA) the mouse was perfused (see 2.4.1) and prepared for tissue processing.

2.3.4 Awake head-fixed recording technical specifications

Intracranial signals were acquired using chlorided silver wires (treated with NaOCl). These were sent to a preamplifier (1x gain), attached to the stereotaxic arms (Heavy-Duty Kopf adapters) or positioned via a clamp next to frame. Following preamplification, signals were carried to the ELC-03M (npi) and 10x amplified before being split and sent to modular amplifiers for 100x gain (BF-48DGX and DPA-2FS, NPI Electronic; total amplification of 1000x) and digitised at 1 or 20 kHz (Power1401 A/D board, Cambridge



Figure 2-3 Recording hardware and software for single unit identification.

Electronics Design). Signals from both glass electrodes were online band-pass filtered according to three different frequency ranges (0.3 Hz – 8/10 kHz, wide-band; 0.3 – 300 Hz (for CA1 LFP), LFP; 0.8 – 5 kHz, action potentials). A 50 Hz noise removing Hum Bugs were used for each channel. In addition, the input to the amplifier for spikes were AC coupled. Signals from the motor cortex, visual cortex and retrosplenial EEG screw were filtered online at 0.3 Hz to 8/10 kHz. All signals were acquired and analyzed using Spike2 software (CED Cambridge UK). All signals were sampled at 20 kHz through an analogue to digital converter (Power 1401, CED Cambridge UK).

2.3.5 Single unit identification

Singe cells within the MSDB were tentatively identified based on their extracellular firing patterns. For the aim of the project it was crucial to ensure the correct placement of the glass pipette within the MSDB, which is surrounded by the lateral septum, which is structurally and functionally distinct from the medial septum. Action potentials of putative MSDB cells were recorded using the extracellular glass electrode filled with 3-5% Neurobiotin or 5-10% BDA. The signal was converted to an audio signal while recording. Once a cell was captured, the cell was recorded during a period of immobility and locomotion to monitor the cell's behaviour during different behavioural states and cortical network oscillations captured by the second glass electrode in the hippocampal pyramidal cell layer or in stratum oriens of CA1. Several criteria were used to ensure the right brain area before selectively targeting different cell types. These initial criteria include the narrow spike width, absence of complex spikes, a feature of lateral septal neurons and the presence high rhythmic burst firing septal cells as known to be GABAergic (King, Recce and O'Keefe, 1998a; Joshi *et al.*, 2017; Viney *et al.*, 2018). Also, the density of cells is a good indicator to be in the medial septum if the depth is

approximately between 2500-4500 μm from the brain surface. Following the experience in recording within the MSDB, many cells, mostly HRNs, had a recognizable firing pattern audio output, e.g. *Teevra* cells had 'sharp sound of bursts' while *Komal* and *Orchid* cells exhibited a 'soft sound of bursts'. Most of my HRNs were included in the analysis used for two published papers (*Teevra*, Joshi *et al.*, 2017; *Orchid*, Viney *et al.*, 2013). Inspired from Hindustani classical music, Dr Abhilasha Joshi gave the them the Sanskrit names *Teevra* for their 'sharp' tone and *Komal* for their 'soft' or 'flat' tone during locomotion. *Orchid* cells were named by Dr Tim Viney after the particular curving shape of the projection axon along with the axon collaterals revealing their unique innervation feature of several brain areas. I identified the LRNs through their inconsistent firing patterns compared to HRNs, low burst incidence and inhibition during hippocampal sharp wave ripples. Overall, I have extracellularly recorded 682 medial septal neurons with meaningful physiology from 107 mice and successfully labelled and recovered 41 neurons in 41 mice. The success rate of 38% reflects the technical difficulty of the performed experiments. Out of the 41 neurons, 8 neurons were HRNs (*Teevra*, n=5; *Orchid* n=4), 11 neurons were LRNs and the rest are either putative extrahippocampal *Komal* cells and/or part of unidentified MSDB groups. Some cells have a unique innervation feature which were, to date, not observed again.

2.3.6 Juxtacellular labelling

The recorded cell was subsequently juxtacellularly labelled once the cell was recorded reliably and for a sufficient amount of time. Juxtacellular iontophoresis is a labelling technique that allows to inject a tracer (3-5% neurobiotin or 5-10% BDA in 0.5 M NaCl) into a single neuron. The tracer is delivered by applying 250 ms cycle pulses of a few nA of current to the recording electrode (Pinault, 1996; Duque and Zaborszky, 2006) to

modulate the firing of the cell. The modulation of the cell varies from different factors, like the diameter of the pipette, neurotracer or distance to the recorded cell. Modulation usually lasted from 30 seconds up to 7 minutes. Best results were achieved once the spike amplitude was > 1 mV. Longer modulation times resulted in the most strongly labelled neurons. After the labelling attempt, the current pulses were stopped, and the electrode was slowly moved away from the cell. After a recovery time of approximately 6-8 h for neurobiotin and 24-48 h for BDA, allowing the neurotracer to diffuse within the cell, the mouse was intracardially perfuse-fixed.

2.4 Tissue processing

2.4.1 Intracardial perfusion

The animal was anaesthetized with 0.1 ml Pentobarbitone (20 % w/v) and intracardially perfused with 0.05 % glutaraldehyde (wt/vol, distilled grade, TAAB Laboratories Equipment Ltd), 4% paraformaldehyde (w/v, Sigma-Aldrich) and 15% of a saturated picric acid solution (v/v, Sigma-Aldrich) in phosphate buffer (PBS 0.1 M, pH 7.4, 4°C) using either an electric pump or 20 ml syringes. Perfused brain was kept in 0.1 M phosphate buffer (PB) with 0.05 % sodium azide and if necessary post-fixed in fixative solution without glutaraldehyde over night at 4°C.

2.4.2 Brain sectioning and tissue processing for imaging

Fixed brains were sectioned at 70-100 μm in the coronal plane using a vibrating microtome (VT1000s vibratome, Leica Instruments) and stainless-steel razorblades. Fixed brain was prepared by cutting off the olfactory bulbs and cerebellum. The left hemisphere was marked by a cut in the cortex. Brain was glued on a small plate and

covered in PBS for sectioning. All sections were stored sequentially (posterior – anterior) in 24 well plates, washed 3 times 10 in PBS and stored in PBS with 0.05 % sodium azide. For further imaging processing and visualization of neurobiotin or BDA filled cells both methods, permeabilising by 0.1 % Trition-X-100® detergent (TBS-TX, 0.3% wt/vol, Sigma-Aldrich) or by freeze/thaw (f/t) with liquid nitrogen, were used. For permeabilization with Trition-X-100® detergent, sections were washed 3 times 10 minutes with tris-buffered saline (TBS) with 0.1 % Trition-X-100® and incubated in TBST-X containing a streptavidin-conjugated-CY3 fluorochrome (1:400) for 24 h at 4°C or for 4 h at room temperature. After incubation, sections were washed 3 times 10 minutes with TBST-X and mounted in an anti-fading medium (Vectashield) on slides. Slides were labelled and covered with a cover slip and sealed with nail vanish. For the f/t method, sections were washed 3 times for 10 minutes in 0.1 M PB and incubated for 3 hours in a 20 % sucrose solution. After incubation the sucrose-cryoprotected sections were treated in 2-5 rounds of freeze and thaw cycle over liquid nitrogen and washed 4 times 10 minutes in 0.1 M PB. Sections were incubated in TBS containing a streptavidin-conjugated-CY3 fluorochrome (1:400) streptavidin-conjugated-488 fluorochrome (1:1000) for 24h at 4°C or for 4 h at room temperature and mounted in anti-fading medium on slides. The f/t method is preferentially used to preserve lipid bilayers for election microscopy (EM), and gives a higher contrast following diamino-benzidine (DAB) based enzyme reaction. For initial observations and fluorescence microscopy, a selection of 12 sections per brain were labelled with a Streptavidin-conjugated fluorescence marker (Cy3 or Alexa488) using the in TBST-X method.

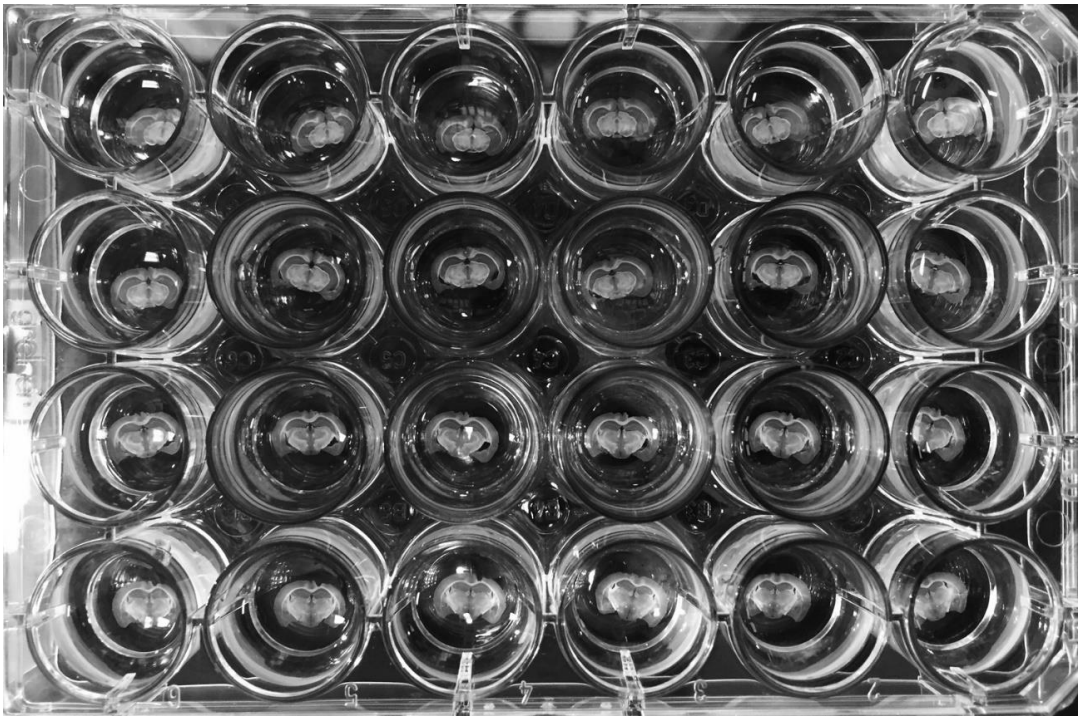


Figure 2-4 Coronally sectioned mouse brain sections in a 24-well-plate.

2.4.3 Immunohistochemical analysis

I used immunohistochemical analysis to test the expression of different peptides, receptors, proteins and transcription factors on *in vivo* labelled cells for characterisation purposes. This method allowed me to detect the expression of cell-type and somato-dendritc specific molecules on individual labelled neurons and control tissue. Therefore, selected sections including a negative and positive control were initially blocked in TBS/TBST-X with a 20 % normal horse serum (vol/vol, NHS) solution for one hour to prevent non-specific antibody binding. Blocked sections were washed 3 times 10 minutes in TBS/TBST-X and incubated with primary antibodies (Table 2-1) for 2-3 days at 4°C, excluding the negative control. Section were then washed again in TBS/TBST-X and incubated overnight at 4°C or for 4 hours at room temperature (RT) with secondary antibodies (Table 2-2) raised in donkey against the immunoglobulins of the host species of the primary antibodies in TBS/TBST-X containing 1% vol/vol NHS. Secondary

antibodies were diluted according to Table 2-2 prior adding to the sections. After incubation, the sections were washed 3 times for 10 minutes in TBS/TBST-X and mounted with Vectashield on slides. Slides were labelled, covered with a cover slip and sealed with nail vanish.

Due to different specificity, I was able to use up to eight primary antibodies, raised in different species, and appropriate secondary antibodies on individual sections. Although I was limited by four fluorescence channels, I used an iterative strategy based on area-dependent marker frequency, subcellular localization, colocalization probability, antibody species, and fluorophore to maximise the number of primary antibodies I can test on one section. Typically, I tested rare markers first, along with non-cytoplasmic markers (e.g. nucleus or cell membrane) to utilize the available subcellular domains for testing. After documenting the first four channels, the sections were demounted, washed 3 times 10 minutes in TBS/TBST-X and prepared for a second IR with different antibodies. Cytoplasmic markers, such as calcium binding proteins, were often tested last. In each round of immunohistochemistry, ‘negative’ controls were included that lacked the primary antibodies, along with ‘positive’ controls from a different brain that included the primary antibodies. In the next round of immunohistochemistry, the previous positive controls became new ‘negative’ controls by lacking the new primary antibodies. Thus, the number of control sections increased with each round of processing, and each control was compared to the test section, along with a comparison of images acquired in the same location before and after each round of immunohistochemistry. Undetectable immunoreactivity within the neuron for a given fluorescence channel was excluded for that particular round if no new signals were present in the vicinity of the neuron of interest.

2.4.4 Diamino-benzidine-based HRP reaction and embedding

In order to obtain light-stable specimens for light microscopic reconstruction, cells were converted using diamino-benzidine (DAB) reaction as follows. Using horseradish peroxidase (HRP) enzyme reaction with diamino-benzidine as chromogen in the sectioned mouse brain, the axon will be followed to determine its innervation area and, if required, reconstructed. An HRP enzyme conjugated to biotin was used. Sections were treated with the freeze/thaw method or with TBS/TBST-X for permeabilising. After 3 times 10 minutes washes, the sections were incubated in TBS or TBS/TBST-X with an avidin-biotin HRP complex (1:100; Vectastain ABC Elite kit, Vector Laboratories) for a minimum of 4 nights at 4°C. After incubation, sections were washed 3 times 10 minutes in TBS/TBST-X and the DAB pre-incubation solution was prepared. Next, sections were incubated in the dark for 10 minutes in a pre-incubation solution containing 2 % nickel ammonium sulphate (Sigma-Aldrich; stock 1% wt/vol), 0.4 % ammonium chloride (Sigma-Aldrich; stock 0.4% wt/vol) in distilled water, 20 % glucose (Sigma-Aldrich) in distilled water, PB and 0.5 mg/ml DAB (Sigma-Aldrich, stock 5 mg/ml). The reaction was initiated by the addition of 1000 U/ml glucose oxidase enzyme (Sigma-Aldrich) in the dark, which catalyses the oxidation of DAB by generating a graduate supply of hydrogen peroxide (H_2O_2). After 15 minutes a sample section per brain was mounted and assessed for the its reaction under the light microscope. Usually visual endogenous biotin throughout the section's thickness is a good indicator for a successful reaction. In some cases, the injected neurotracer, neurobiotin or BDA, was already visible at this stage. After 20 – 40 minutes the reaction was stopped by washing off the sections with 0.1 M PB over 30 minutes. Section were incubated in 0.5 % osmium tetroxide solution (TAAB; 4% wt/vol stock OsO_4) in 0.1 M PB for 40-60 minutes and washed 3 times 10 minutes with 0.1 M PB. Next, dehydration in a series of increasing concentrations of ethanol and

propylene oxide was performed; the sections were treated for 10 minutes each with 50 % and 70 % ethanol and incubated for 35-40 minutes in a solution of 1 % uranyl acetate (TAAB) in 70 % ethanol, which enhances the contrast for electron microscopy by interaction with lipids and proteins. The process was followed by dehydration in 90 %, 95 % and 100 % ethanol (2 times) 10 minutes each. Finally, the sections were immersed 2 times 10 minutes in propylene oxide (VWR International) to enhance resin penetration. Sections were then immersed in epoxy resin (Durcupan ACM Fluka, Sigma-Aldrich) overnight before mounting on slides. The resin mounted slides were polymerized for 24-48 h in an oven at 60 °C.

Table 2-1 List of primary antibodies

Molecule	Host	Dilution	Source	Specificity information	RRID
Calbindin (CB)	Rb	1:5000	Swant, CB-38 (lot 5.5)	No signal in knockout. Mouse knockout: Airaksinen et al. (Proceedings of the National Academy of Sciences, 1997, 94, 1488–1581). Characterization in rat hippocampus: Sloviter (The Journal of Comparative Neurology, 1989, 280, 183–279).	AB_2721225
Calretinin (CR)	Rb	1:500-1:1000	Swant, 7699/3H (lot 18299)	Western blot supplied by Swant. No signal in knockout animals; Swant; Schiffmann et al. (Proceedings of the National Academy of Sciences, 1999, 96, 5257– 5262).	AB_10000321
Calretinin (CR)	Gt	1:1000	Swant, CG1	Antibody does not label the brain of CR knock-out mice (manufacturer's technical information)	AB_10000342
Choline acetyltransferase (ChAT)	Gt	1:500	Chemicon, AB144P	Western blot (manufacturer's technical information)	AB_2079751
Gephyrin	Ms	1:500	Synaptic Systems Cat# 147 021 Lot#	Western blot; band at 93 kDa. No Geph7a signal in knockout. Co-purifies with glycine receptor. Mouse knockout: Feng et al. 1998. Antibody generation: Pfeiffer et al. (Proceedings of the National Academy of Sciences, 1984, 81, 7224–7231).	AB_2232546
GFP	Ck	1:500	Aves Labs, GFP-1020	Antibody does not label the brain of wild-type control mice	AB_10000240
Metabotropic glutamate receptor 1a (mGluR1a)	Gp	1:500-1:1000	Frontier Institute, mGluR1a-GP-Af660	Characterised by Tanaka et al. 2000 *Eur. J. Neurosci.* 12, 781-792	AB_2531897
Muscarinic acetylcholine receptor M2 (M2R)	Rt	1:400	Chemicon, MAB367 lot 2383976	Distinct from other subtypes; characterised by Levey et al. 1991 *J. Neurosci.* 11, 3218-3226	AB_94952
Neuronal Ca^{2+}-binding protein 1 (NECAB 1)	Ms	1:500	Abnova, H00064168-B01P	Western blots; as expected, no cross-reactivity with NECABs 2 and 3. Mouse brain, and antibody generation: Sugita et al. (Neuroscience, 2002, 112, 51–114).	AB_2149170
Neuronal nitrogen oxide synthase (nNOS)	Rb	1:1000	EMD Millipore, AB5380	Does not cross react with iNOS or eNOS. No signal in knockout for rabbit antibody (Zymed/Invitrogen) of same mass. Mouse knockout and similar rabbit antibody: Gyurko et al. (Endocrinology, 2002, 143, 2767–2841).	AB_91824
Parvalbumin (PV)	Rb	1:1000	Swant, PV-28	No signal in knockout, shown by Swant. Similar to other parvalbumin antibodies. Mouse knockout: Schwaller et al. (The American Journal of Physiology, 1999, 276, 403).	AB_2315235
Parvalbumin (PV)	Gt	1:1000	Swant, PVG-214, lot 3.6	No signal in knockout, shown by Swant. Similar to other parvalbumin antibodies. Mouse knockout: Schwaller et al. (The American Journal of Physiology, 1999, 276, 403).	AB_2313848
Parvalbumin (PV)	Gp	1:5000	Synaptic Systems, 195 004, lot 5	Western blot; abolished by pre-absorption with recombinant parvalbumin. Same labeling as Synaptic Systems rabbit antibody 195 002 and Swant monoclonal antibody 235. Rat hippocampus: Kosaka et al. (Brain Research, 1987, 419, 119–149), Sloviter (The Journal of Comparative Neurology, 1989, 280, 183–279). Mouse knockout: Schwaller et al. (The American Journal of Physiology, 1999, 276, 403).	AB_2156476

Molecule	Host	Dilution	Source	Specificity information	RRID
Pro-cholecystokinin (pro-CCK)	Rb	1:500	April 2005 gift (similar to Frontier Institute, CCK-pro-Rb-Af350)	Similar labeling to two non-commercial antibodies characterized by Sloviter and Nilaver (The Journal of Comparative Neurology, 1987, 256, 42–102), Morino et al. (The European Journal of Neuroscience, 1994, 6, 681–773).	AB_2571674
Purkinje cell protein 4 (PCP4)	Rb	1:1000	Santa Cruz, sc-74816, lot G0814	Characterised by San Antonio et al. 2014 *J. Comp. Neurol.* 522, 1333-1354	AB_2236566
Regulator of G-protein signaling 14 (RGS-14)	Ms	1:500-1:1000	NeuroMab, 75-170, clone N133/21	Characterised by manufacturer (see datasheet)	AB_2728538
SATB1 (N-14)	Rb	1:200	Abcam, ab70004	No signal in knockout for a similar rabbit antibody. Western blot, different band to SATB2 at mouse P1. Neuron-specificity shown by NeuN colocalization. Original rabbit antibody: Dickinson et al. (Cell, 1992, 70, 631–1276). Mouse cortex: Huang et al. (Neuroscience Research, 2011, 71, 12–33). Mouse knockout: Balamotis et al. (Molecular and Cellular Biology, 2012, 32, 333–380).	AB_1270545
SATB1 (N-14)	Gt	1:200-1:250	Santa Cruz, sc-5989	Similar labeling to rabbit antibody ab70004. Mouse cortex: Huang et al. (Neuroscience Research, 2011, 71, 12–33). Mouse knockout: Balamotis et al. (Molecular and Cellular Biology, 2012, 32, 333–380).	AB_2184337
Secretagogin	Gt	1:1000	R&D Systems, AF4878 lot CASX0115091	Characterised by Mulder et al. 2009 *Proc. Nat. Acad. Sci. USA* 106, 22492-22497	AB_2269934
SMI32 (neurofilament H non-phosphorylated)	Ms	1:1000	Covance, SMI-32R lot 14835102	Similar to immunoreactivity characterised in primates by Campbell and Morrison 1989 *J. Comp. Neurol.* 282, 191-205 and in rats by Ouda et al. 2012 *Brain Struc. Func.* 217, 19-36	AB_509997
Somatostatin (SOM)	Ms	1:500	GeneTex, gtx71935 clone SOM-018	Same labeling as a rat antibody Chemicon MAB354. No signal in preabsorption test for rat antibody. Mouse hippocampus, rat antibody: Jinno and Kosaka (The Journal of Comparative Neurology, 2000, 428, 377–465). Rat antibody test: Kubota et al. (Cerebral Cortex, 2011, 21, 1803–1820).	AB_383280
Somatostatin (SOM)	Rb	1:50	GenWay Biotech, 18-783-76392	Similar distribution and subcellular localisation as Ms anti-SOM	AB_1027453
Substance P receptor (NK1R)	Rb	1:500	Millipore, AB5060, lot LV1525037	Characterised by Shigemoto et al. 1993 *Neurosci. Lett.* 153, 157-160	AB_2200636
Vesicular Acetylcholine Transporter (VAChT)	Gt	1:1000	Millipore Cat# ABN100 Lot	his antibody recognizes the C-terminus of Vesicular Acetylcholine Transporter (VAChT)	2630394
Vesicular GABA transporter (VGAT)	Gp	1:500	Synaptic Systems, 131 004	Similar to C- and N-terminal fusion protein antibodies. Former gave additional unknown lower mass band in brain extract but same immunoreactivity as specific latter antibody; see rat cortex: Chaudhry et al. (The Journal of Neuroscience, 1988, 18, 9733–9783). Similar rabbit antibody generation: Takamori et al. (The Journal of Neuroscience, 2000, 20, 4904–4915).	AB_887873
Vesicular glutamate transporter 2 (VGLUT2)	Gp	1:2000	Synaptic Systems, 404 lot 135404/16	Similar to immunoreactivity characterised in mouse hippocampus by Herzog et al. 2006 *J. Neurochem.* 99, 1011-1018	AB_887884

Table 2-2 List of secondary antibodies

Primay AB host	Alexa 405	Alexa 421	Alexa 488	CY3	CY5	DyLight647
guinea pig	dk ∩ gp; 1:250	dk ∩ gp; 1:250	dk ∩ gp; 1:1000	dk ∩ gp; 1:250	dk ∩ gp; 1:250	dk ∩ gp; 1:250
goat	dk ∩ gt; 1:250	dk ∩ gt; 1:250	dk ∩ gt; 1:1000	dk ∩ gt; 1:250	dk ∩ gt; 1:250	dk ∩ gt; 1:250
mouse	dk ∩ ms; 1:250	dk ∩ ms; 1:250	dk ∩ ms; 1:1000	dk ∩ ms; 1:250	dk ∩ ms; 1:250	dk ∩ ms; 1:250
rabbit	dk ∩ rb; 1:250	dk ∩ rb; 1:250	dk ∩ rb; 1:1000	dk ∩ rb; 1:250	dk ∩ rb; 1:250	dk ∩ rb; 1:250
rat	dk ∩ rt; 1:250	dk ∩ rt; 1:250	dk ∩ rt; 1:1000	dk ∩ rt; 1:250	dk ∩ rt; 1:250	dk ∩ rt; 1:250
streptavidin	-	-	strep-488; 1:1000	strep-cy3; 1:250	-	-

2.5 Imaging and reconstruction

2.5.1 Wide-field epifluorescence microscopy

The wide-field epifluorescence microscope was used to assess the reactions described in 2.4.3 and 2.4.4, and to identify the labelled cell within the MSDB. After adding a secondary antibody like streptavidin-conjugated-CY3 fluorochrome or streptavidin-conjugated-488 fluorochrome, the signal was visualized using with epifluorescence illumination. Once axonal or dendritic processes were observed, the same processes were traced across sections and documented. In most cases, more sections were processed to identify the labelled cell. The used Leitz DMRB microscope (Leica) is equipped with epifluorescence illumination (Hg arc lamp, HBO, Osram) and PL Fluotar 20x/0.5 and 40x/0.7 lenses. Dichroic mirrors spectrally filtered the light to obtain optimally separated excitation and emission bandwidths for different fluorophores: Alexa405 (excitation: 405/20 nm; emission: 460/50 nm; beam splitter: 425 nm), Alexa488 (excitation: 480/40 nm; emission: 527/30 nm; beam splitter: 505 nm), Cy3 (excitation: 545/30 nm; emission: 610/75 nm; beam splitter: 565 nm) and Cy5 (excitation: 620/60 nm; emission: 700/75 nm; beam splitter: 660 nm). A digital camera (Hamamatsu Photonics ORCA ER) attached to the microscope and controlled by OpenLab software v.5.5.0 (Improvision) was used to capture the reactions by taking images for documentation and qualitative evaluation. Thus, a particular area can be imaged across different fluorescence channels, color-coded,

superimposed and evaluated. The Exposure times varied from reaction to reaction and was individually set for each image. For further verification, greater image resolution and capturing multiple images through the section a confocal laser scanning microscopy was used.

2.5.2 Confocal laser scanning microscopy

An AxioImager.Z1 microscope (Carl Zeiss) equipped with LSM 710 scan head was used to acquire multi-channel fluorescence images operated with ZEN 2008 software v5.0 (Zeiss). The confocal laser scanning microscopy operates by passing a laser beam through a light source aperture, pinhole, which is then focused by an objective lens into a small area on the surface of your sample. Sensors detect only the light passes through the pinhole. This allows to build up an image pixel-by-pixel by collecting the emitted photons from the fluorophores in the sample. In addition, by collecting a series of images through a three-dimensional object, a stack, these images can then be used for a two- or three-dimensional reconstruction. A stack is created along the z-axis of the 70 µm section. DIC M27 Plan-Apochromat 63×/1.4 NA and alpha Plan-Apochromat 100×/1.46 NA oil immersion objectives were used with the following channels (laser and excitation wavelength, fluorophores, beam splitters, emission spectral filter) for detection of: 405-30 solid state 405 nm with attenuation filter ND04, DyLight405, MBS-405, 409–499 nm; argon 488 nm, Alexa Fluor 488, MBS-488, 493–542 nm; HeNe 543 nm, Cy3, MBS-458/543, 552–639 nm; HeNe 633 nm, Cy5/DyLight 649/Alexa Fluor 647, MBS 488/543/633, 637–757 nm. Channels were acquired sequentially with a different dynamic range (4-16 bit), and the pinhole size was set at 1 Airy unit, resulting in 0.6-0.7 µm optical slice thickness, giving all channels the same optical slice thickness. Channels of

secondary antibodies were set in a way to minimize spectral overlap between channels. All confocal image analysis was done using ImageJ (Fiji).

2.5.3 2D and 3D single cell reconstruction

Selected single labelled MSDB cells were reconstructed to reveal their axonal arbour in different targeted brain regions and innervated layers. This technique gives an exclusive insight into the unique morphology of long projection neurons and helps us understand the functional role of single cells by investigating innervation patterns in addition to their postsynaptic targets. Both, 2D and 3D reconstructions techniques were done manually by tracing labelled neuronal processes of a single cell from the medial septum to the entire hippocampal formation. For to enable tracing, section was beforehand converted using the DAB reaction described in 2.4.4. 2D reconstruction were mainly performed on septal sections to reconstruct the soma of the labelled cell including its dendritic and axonal process within the MSDB. Therefore, a drawing tube attached to a light microscope (Leitz Dialux 22 microscope) with an Pl Apo 63x/1.4 oil immersion objective was used. Sections were reconstructed by drawing section-by-section separately and superimposed on a single sheet of transparent paper. After, adding all sections, the 2D image was digitalised and edited using Adobe Illustrator. For digital 3D reconstruction, DAB reacted sections were traced t using Neurolucida system from MBF Bioscience. A Lucivid microdisplay (MBF Bioscience) attached to a Nikon Eclipse 80i transmitted light microscope equipped with a VC Plan Apo 100x/1.4 oil immersion objective was used for digital tracing. The system allowed to superimpose the screen on top of the section displayed by the microscope, thus it was possible to digitally trace an axon using the computer mouse in all three dimensions. In order to align the reconstructed sections using the Neurolucida software, the contours were added for all major boundaries, which

includes the midline and the outline of the whole brain for every section. Hippocampal boundaries which were added to all sections were the axonal process were traced. Differences in cell density were used to identify the boundaries. As most of the sections shrank during tissue processing, mainly due to the dehydration process, a corrected value was added to fit the x-y dimensions. The value was calculated using a DAPI reaction on selected sections and calculating the differences in percentage in refence to the section's thickness value of 70 μm. For visualisation purposes, axon, single buotons and boundaries were colour-coded and in some cases displayed animated to visualize the 3D structure of the neuron.

2.6 Electrophysiological data analysis

2.6.1 Statistical analysis and quantification

Standard functions and custom-made scripts in Spike2 (CED), MATLAB (MathWorks) and Mathematica (Wolfram) were used for all electrophysiological analysis. Based on video recordings, an external accelerometer and the presence theta phases in the recorded hippocampal CA1 LFP, the recorded sessions have been segmented into movement and quite wakefulness phases. Theta oscillatory epochs (5–12 Hz) and SWRs (130–230 Hz) were detected and analyzed using a custom Spike 2 script written by Dr John Tukker. Theta phase relationship analysis were analyzed using a MATLAB script written by Dr Balint Lasztoczi and edited by Dr Abhilasha Joshi. Each recorded and labelled cell has been analysed separately. The analysis included the preferential mean theta phase of firing, firing frequency during movement and quite wakefulness, mean depth of theta modulation, rhythmicity index (RI), burst incidence during movement and quite wakefulness, interburst interval during movement and quite wakefulness as well as the intraburst frequency during movement and quite wakefulness. In addition, I have

performed an in-depth analysis of hippocampal sharp-wave ripples in relation to firing patterns of recorded cells as well as the firing behaviour during theta oscillation. The preferential mean theta phase of firing (circular mean ± circular SD) was determined using Rayleigh's method (Zar, 1999). For comparisons of firing phase preferences of different cell types and groups, a two-sample permutation test was used (Good, 1994; Tukker *et al.*, 2007). To compare two groups and two distributions, the Kruskal-Wallis one-way analysis of variance or Mann Whitney U test and two-sample Kolmogorov-Smirnov tests were used. For the SWR and Rebound Index analysis I used the script developed and adjusted by Dr Linda Katona (Katona *et al.*, 2014). The Rhythmicity index was developed by Dr Robert Stewart. Dr Tim Viney taught me the use of Mathematica and provided great support analysing all parameters regarding the firing pattern of single cells. For all methods p-values and confidence intervals were calculated according to α=0.05.

2.6.2 Spike train analysis

Spike trains of recorded cells were used for all analysis. Spike2 was used to detect and quantify single spike trains. Therefore, the peak of each single action potential was marked, and each peak assigned to a time stamps as an event. All events were extracted in time and used for all firing pattern analysis. Thus, I could determine average firing rates for individual cells during different behavioral and oscillatory network states by counting, for a given state and cell, the total number of spikes and dividing this by the total length of time. Autocorrelograms (AC) were calculated similarly for comparisons between cell types and investigated rhythmicity in their spiking. Mean firing rates were calculated in 1 s windows within each behavioral state. Bursts were defined as a train of >3 spikes with interspike intervals (ISIs) of <20 ms and <40 ms. Burst incidence was

defined by the total number of bursts in 1 s windows. Interburst intervals were calculated by measuring the time elapsed between the first spikes of consecutive bursts (for <40 ms ISIs). Intraburst frequency was calculated from the number of spikes within the duration between the first and last spike of each burst.

2.6.3 Theta network oscillations analysis

To analyse and detect theta oscillations recorded in the LFP of the reference glass electrode within hippocampal CA1, I have digitally band pass filtered the LFP signal (finite impulse response, FIR, Gaussian window, 1024/2048 coefficients, transition gap 2.5 Hz) at delta (2-4 Hz) and theta (5-12 Hz) frequencies offline using Spike2. Based on the theta to delta frequency power ratio using Fast-Fourier transforms (FFT, 1024 points, 2 s Hanning windows) I was able to manually select the theta periods. The script initially suggested a theta periods if the ratio was greater than four in three consecutive windows. I have empirically adjusted the beginnings and ends of theta epochs, based on the regularity of the oscillation. One theta cycle was defined between two consecutives. The mean firing phase preference of each cell during theta oscillation was calculated by detecting all troughs of all theta cycles during the selected periods. Detected troughs were extracted as time stamps. Detected spike time stamps were then sorted in 18° theta-phase bins, cycle-by-cycle. The phase relationship between single cell firing and theta activity was calculated by computing the phase for every spike time (ts) between the preceding (ti) and following (ti+1) theta trough times:

$$phases = [(ts - ti) / (ti+1 - ti)] * 360°$$

As a result, each spike was assigned an instantaneous phase between two troughs (0° and 360°) and plotted on a circular theta phase histogram (18° theta-phase bins). By using the

using Rayleigh's method (Zar, 1999), the depth of theta modulation and preferential mean theta phase of firing was calculated. Therefore, a test of circular uniformity was performed using the mean vector length (r) to describe coupling strength. Phase histograms were smoothed by convolving with a Gaussian. 'Theta off' periods refer to the percentage of theta cycles (trough to trough) that contained zero spikes for a given single neuron recording.

2.6.4 Rhythmicity Index

To calculate the rhythmicity index (RI) for LRNs and some HRNs, I used the script developed by Dr Abhilasha Joshi. For each single cell, data was prepared by calculating the spike time autocorrelogram (bin width 10 ms, maximum lag 500 ms) for spikes defined in periods of movement or quite wakefulness. The autocorrelogram was then normalized by dividing the peak value between 100 and 200 ms (range chosen to match theta frequency first side band), and centre values were clipped so that overall maximum is 1. A linear trend line was fitted to the above and a nonlinear fit was performed (using MATLAB lsqnonlin function) to the detrended data. The fitting function is a Gaussian-modulated cosine function with three parameters: (1) cosine (theta) frequency in Hz (between 4 and 8); (2) the peak value of the Gaussian scaling function (high value indicates strong short-latency theta modulation) and (3) standard deviation (width) of Gaussian scaling function (high value indicates prolonged theta modulation). The solid red lines in the autocorrelograms are the fitted sinusoid functions (oscillatory frequency of the neuron), and the trends are shown by dotted lines. A coefficient of determination is measured at this stage to measure the goodness of fit. After fitting, the rhythmicity index is calculated as follows: (1) for each peak and trough in 50 to 500 ms, the absolute value of the fitted sinusoid is divided by the corresponding trend line value (between zero

and one) and (2) the rhythmicity index is taken as the mean of these trend-normalized peak values.

2.6.5 Sharp wave ripple network oscillations analysis

To analyse and detect sharp wave ripple oscillations recorded in the LFP of the reference glass electrode within hippocampal CA1, I have digitally band pass filtered the LFP signal at 130-230 Hz. The power of the 130–230 Hz band-pass filtered CA1d LFP was used to detect SWRs, with a threshold of at least 4 s.d. above the mean power. I have mainly calculated the firing probability of LRNs during hippocampal SWRs using the script developed by Dr Linda Katona. Low firing rate during of LRNs during hippocampal SWR was a common feature I discovered among this population. For analysis, SWR-related firing rates have been compared to firing rates obtained outside SWR events. Neurons with <20 detected SWRs were excluded from analysis. Firing rates have been calculated for the n detected SWRs. Next, a population of 1000× n "surrogate SWR" time windows were generated sequentially. "Surrogate SWRs" were restricted to "non-theta" periods, when the majority of SWRs occurred. For each of the 1000 sets, individual firing rates were calculated for the n "surrogate SWRs" and their average was derived. Due to the limited recording periods, each spike was included in "surrogate SWRs" repeatedly, but in different time frames. The firing rates during detected SWRs were compared to the average rates during "surrogate SWR" periods using a two-sample Kolmogorov–Smirnov (KS) test. Finally, for each neuron, a SWR index was calculated with values between – 1 (no firing during SWRs) and 1 (firing exclusively during SWRs), with 0 meaning no change in firing rate during SWRs compared to outside these events. Next, the rebound in SWR-related activity of low rhythmic single neurons was quantified by comparing the average firing rate 200 ms before the beginning and 200 ms after the

end of n detected SWRs. For each SWR, a ‘rebound index’ was calculated with values between – 1 (only firing before and not after SWRs) and 1 (only firing after and not before SWRs), with 0 meaning no change in firing rate between before and after SWRs. To statistically test a rebound after SWR-activity of individual single cells a population of 1000× n “surrogate SWR” time windows were generated sequentially like for the mean firing rate comparison. For each of the 1000 sets, individual firing rates 200 ms before and 200 ms after the n “surrogate SWRs” were used to calculate ‘rebound indices’ and their distributions was derived. The median distribution of the 1000× “surrogate SWR” rebound index-distributions was compared to the measured distribution of rebound indexes using a KS test as above.

Table 2-3 Distress Scoring Table

Distress Scoring Table

Name of Investigator: MINAS SALIB **PIL:** xx **PPL:** xx **Contact number:** xx

Animal Identification: MSxxx **Starting weight:** **Species:** mouse **Strain:** BL6C57

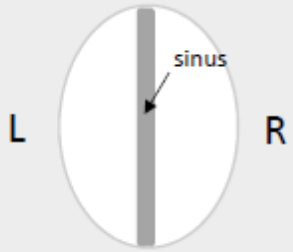
		Day after Treatment						
	Score	0	1st	2nd	3rd	4th	5th	6th
GENERAL APPERANCE								
Normal	**0**							
General lack of grooming	**1**							
Coat staring, ocular & nasal discharges	**2**							
Piloerection, hunched up	**3**							
APPERANCE OF HEAD WOUND								
Normal	**0**							
Slight irritation/inflammation at wound margins	**1**							
Excessive bleeding, local infection or torn sutures	**2**							
SPONTANEOUS BEHAVIOUR								
Normal	**0**							
Minor changes	**1**							
Less mobile and alert, isolated	**2**							
Vocalisation, self-mutilation, restless or very still	**3**							
PROVOKED BEHAVIOUR								
Normal	**0**							
Minor depression of exaggerate response	**1**							
Moderate change in expected behaviour	**2**							
Reacts violently, or very weak	**3**							
WEIGHT (note Take implant into account)								
<-5% starting weight	**0**							
-5% to -10% of starting weight	**1**							
-10% to -15% of starting weight	**2**							
SCORE ADJUSTMENT								
+1 point for each maximum score after first	**1-4**							
TOTAL SCORE	**0-17**							

0-4: 'Normal' **5-9:** 'Mild distress': Monitor carefully; consider analgesics and fluid/energy replacement therapy; seek advice as to possibility of infection.
10-13: 'Suffering': Immediately provide relief. Observe regularly and often over the next 24h; if no improvement over 24h then humanely kill.
14 -17: 'Severe distress': Kill humanely.
If animal's weight is constantly (over a period of 48 hours) lower than 85% of its starting weight, then the animal must be humanely killed.
If no faecal output and signs of overtly bloated abdomen after 48 hours, then terminate.

Table 2-4 Recording sheet

MSxx MS Recordings DD/MM/YYYY

animal: MSxx recording day:	weight: comments:
start: start recording:	end:
Hippocampal CA1 electrode pipette resistance: depth:	**medial septal electrode** pipette resistance: depth:

Task / comments


Juxtacelluar recording

cell	time	depth	area	labelling attempt	comments

Chapter 3

Diversity of medial septal cells recorded in awake mice based on physiological parameters during different brain states

3.1 Introduction

Investigating septo-hippocampal projections at the level of single medial septal neurons and revealing their anatomical connectivity in the targeted area as well their its brain-state dependent activity in different networks will contribute to our contemporary understanding of the temporal and spatial coordination of a wide network involved in memory formation and retrieval. To address this, I have first investigated the diversity of firing of the medial septal population based on their brain-state dependent activity, and second, asked whether single GABAergic septal neurons target restricted or widespread areas of the temporal cortex. Once I have answered these questions I can look for common physiological and anatomical patterns, and investigate further their molecular profiles and post-synaptic targets.

As mentioned above septal GABAergic cells mostly target cortical GABAergic neurons (Sun *et al.*, 2014). From previous studies we know hippocampal GABAergic interneurons with distinct molecular expression profiles target distinct subcellular domains of pyramidal cells and show preferred-firing phases during the theta network state in anaesthetised rats (Klausberger and Somogyi, 2008). This feature has been hypothesized to result in the precise spatio-temporal discharge of pyramidal cells in the hippocampus (Ylinen *et al.*, 1995; Varga *et al.*, 2008, 2014; Varga, Golshani and Soltesz, 2012; Somogyi *et al.*, 2014). In what way does the GABAergic septal input influence the coordination of the diverse types of hippocampal interneurons? The different anatomical and physiological models, as there might be more than one model, behind this circuit is still not revealed. Thus, it is necessary to define how single septal neurons contribute to the hippocampal network both in terms of brain-state dependent activity and their postsynaptic target regions and cells. In particular, it is crucial to find septal presynaptic

inputs to identified hippocampal interneurons which may be responsible for coordinating the activity of the latter neurons.

Most of the available combined neuroanatomical and electrophysiological data have been derived from studies carried out in anaesthetized or head-restrained animals. Regarding the electrophysiology studies only a few investigated the unanaesthetised brain (Simon *et al.*, 2006; Lapray *et al.*, 2012; Varga, Golshani and Soltesz, 2012; Burgalossi, von Heimendahl and Brecht, 2014; Varga *et al.*, 2014; Preston-Ferrer *et al.*, 2016) including an optogenetic tagging study in awake mice which aimed to identify cholinergic neurons in the basal forebrain (Hangya, Sachin P Ranade, *et al.*, 2015). Moreover, It was shown that rhythmic burst behaviour of MS/DBB cells is altered significantly by anaesthesia (Lee, Lamour and Bassant, 1991; King, Recce and O'Keefe, 1998b; Simon *et al.*, 2006). Investigating the firing properties of MSDB neurons has shown a significantly lower percentage of the bursting neurons in the unanaesthetised however, the frequency of the bursts was higher (Lee, Lamour and Bassant, 1991; Sweeney, Lamour and Bassant, 1992). In addition, cortical interneurons appear to have lower firing rates under anaesthesia, and theta frequency is around 4–5 Hz, the low end of the range observed in unanaesthetised animals (Somogyi *et al.*, 2013). Regarding the generation of theta rhythm in rodents it was shown that this is closely linked to voluntary motor activity (Vanderwolf, 1969). Based on these findings and the unknown effects of urethane anaesthesia, all electrophysiological recordings presented in this thesis were performed *in vivo* in awake head-fixed mice on a circular treadmill or similar device.

At the beginning of the project I had the challenge to investigate a brain structure with a heterogenous cell population and hence potentially unknown cell types. As defined in my introduction: "*Two individual neurons belong to the same cell type if they deliver the same neuroactive substances to the same range of postsynaptic targets in the same*

temporal patterns in a brain state-specific manner" (Somogyi, 2010), I will attempt to apply this definition to my characterization and identification of my recorded and labelled single medial septal neurons. In this chapter, I explore the diversity in septal neuronal firing patterns based on *in vivo* extracellular recordings and juxtacellular labelling in awake head-fixed mice running on a circular treadmill.

3.2 Results

3.2.1 *In vivo* extracellular recordings in awake head-fixed mice

I have performed single cell *in vivo* extracellular recordings in head-fixed mice running on a circular treadmill followed by juxtacellular labelling with neurobiotin or BDA. During the entire DPhil project, I have trained, implanted head-plates and recorded from 107 mice. From these 107 mice I have recorded 682 single neurons during different brain states and successfully recorded, labelled and recovered 41 neurons in 41 mice (appendix, Table 8-1). Note, that all 682 recorded neurons are biologically meaningful recordings from the medial septum. Initially, each recorded cell was unique in its firing patters during immobility and locomotion until I started to recognize recurring patterns across the population. A remarkable feature of medial septal cells is their high-firing rate across brain-states and in some cases also their high firing rhythmicity, in particular during locomotion. The action potential waveforms were digitized and converted into an audio-visual signal online. As I will discuss in the next chapter, I used the current knowledge of the firing patterns of neighbouring brain structures such as the lateral septum to identify the medial septum while lowering the glass-electrode. Thus, based on the audio and visual signals I was able to (a) confirm the location of the recording glass-electrode to be in the medial septum and (b) to recognize a diversity of medial septal cells. After the first recordings and labelling attempts, successfully recovered neurons were traced to their

innervation areas. Only once the labelling strength was sufficient for revealing axon with DAB the labelled brain was further processed (not all 41 neurons were traced to their target regions). Once the target area was identified I started to initially group together cells with same cortical innervation pattern (Figure 3-1). In parallel to recording and labelling new medial septal cells I analyzed the physiological parameters of each traceable cell and looked for common features.

In the following chapters I will introduce and discuss three newly identified medial septal cortical projecting cell types with different physiological, molecular and anatomical characteristics. In this chapter I report the existing diversity of neurons within the medial septum and show examples of novel single cells that have not been reported or characterised before, to the best of my knowledge (Table 3-1). Further recording and labelling of single medial septal cells are required to investigate these cells which might form further subgroups with functionally related roles in shaping cortical network activity.

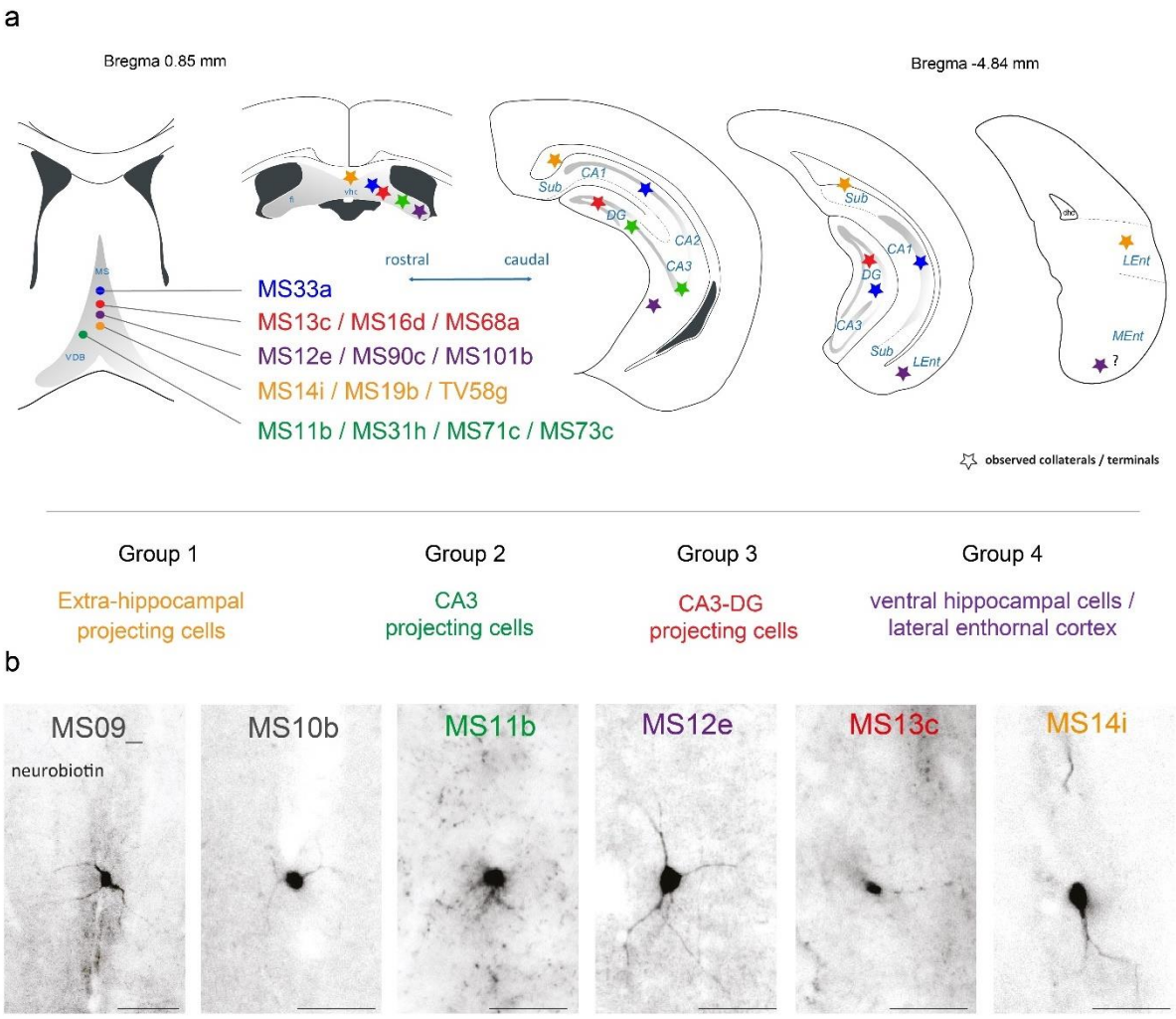


Figure 3-1 Schematic overview of innervated cortical regions of recorded and labelled single medial septal neurons.

a, Identified cortical targets of medial septal neurons. Neurons with similar cortical target region are colour-coded. **b**, Widefield epifluorescence microscopic images of neurobiotin filled and recorded neurons within the medial septum showing the diverse morphology of identified neurons. Scare bars: 50 µm.

3.2.2 Diversity of medial septal neurons based on spike train dynamics

Single medial septal cell recordings were always performed with a reference electrode in dorsal CA1, recording local field potential (LFP). The position of the hippocampal reference electrode has been kept consistent across studies for comparison reasons. Once a stable medial septal cell was identified, I maintained the recordings until I had a sufficient amount of non-movement (immobility) and movement (mobility) periods. Figure 3-2 shows 6 different medial septal cells recorded in 6 different animals referenced to dorsal CA1 LFP. Observing the firing dynamics of each cell, one can see different patterns for each cell, but during different behavioural periods. I attempted to juxtacellular label each of these cells, however the cells MS09a and MS53y were not identified despite several labelling attempts. All cells will be discussed in detail in the following chapters as they are part of the identified medial septal subgroups. The electrophysiological recordings allowed me to analyse the firing patterns in detail in reference to the hippocampal LFP. In particular during movement periods, where hippocampal theta oscillations were prominent, I observed a change in firing patterns in most cases. To quantify and compare the initially selected groups of cells sharing the same cortical projection patterns, a set of physiological parameters was selected and over the time developed with the support of my colleagues working in the laboratory under Professor Peter Somogyi. These include the analysis of e.g. the firing rate during each period, firing rhythmicity, burst patterns (rate, incidence, duration), preferred phase-coupling during hippocampal network oscillations and firing behaviour during hippocampal sharp-wave ripples (SWR) (marked in red Figure 3-2). Figure 3-3a displays the preferred firing phase of cells displayed in Figure 3-2 during hippocampal CA1 theta oscillations. Thus, these cells distinguish themselves not only in their firing rate but also in their firing preference during theta oscillations. However, as it will turn out, each of

these cells also belong to a different subpopulation of medial septal neurons (*Chapter 4*, *Chapter 5*). An example of different labelled cells is shown in Figure 3-1b. In addition, the diversity is represented by their firing probabilities during hippocampal SWRs (Figure 3-2b).

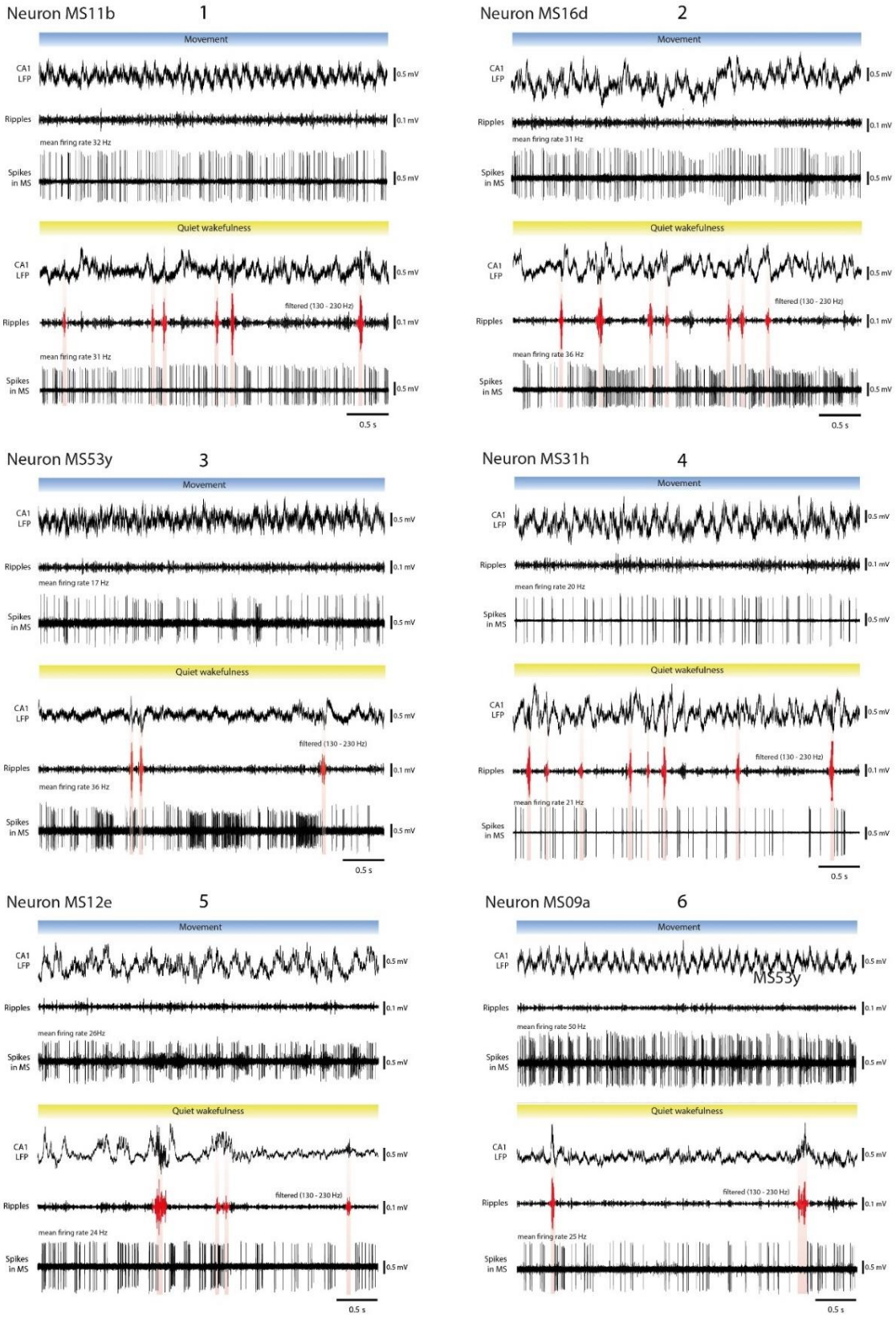

Neuron MS11b
1
Movement
CA1 LFP
0.5 mV
Ripples
0.1 mV
mean firing rate 32 Hz
Spikes in MS
0.5 mV
Quiet wakefulness
CA1 LFP
0.5 mV
filtered (130 - 230 Hz)
Ripples
0.1 mV
mean firing rate 31 Hz
Spikes in MS
0.5 mV
0.5 s
Neuron MS16d
2
Movement
CA1 LFP
0.5 mV
Ripples
0.1 mV
mean firing rate 31 Hz
Spikes in MS
0.5 mV
Quiet wakefulness
CA1 LFP
0.5 mV
filtered (130 - 230 Hz)
Ripples
0.1 mV
mean firing rate 36 Hz
Spikes in MS
0.5 mV
0.5 s
Neuron MS53y
3
Movement
CA1 LFP
0.5 mV
Ripples
0.1 mV
mean firing rate 17 Hz
Spikes in MS
0.5 mV
Quiet wakefulness
CA1 LFP
0.5 mV
filtered (130 - 230 Hz)
Ripples
0.1 mV
mean firing rate 36 Hz
Spikes in MS
0.5 mV
0.5 s
Neuron MS31h
4
Movement
CA1 LFP
0.5 mV
Ripples
0.1 mV
mean firing rate 20 Hz
Spikes in MS
0.5 mV
Quiet wakefulness
CA1 LFP
0.5 mV
filtered (130 - 230 Hz)
Ripples
0.1 mV
mean firing rate 21 Hz
Spikes in MS
0.5 mV
0.5 s
Neuron MS12e
5
Movement
CA1 LFP
0.5 mV
Ripples
0.1 mV
mean firing rate 26Hz
Spikes in MS
0.5 mV
Quiet wakefulness
CA1 LFP
0.5 mV
filtered (130 - 230 Hz)
Ripples
0.1 mV
mean firing rate 24 Hz
Spikes in MS
0.5 mV
0.5 s
Neuron MS09a
6
Movement
CA1 LFP
0.5 mV
MS53y
Ripples
0.1 mV
mean firing rate 50 Hz
Spikes in MS
0.5 mV
Quiet wakefulness
CA1 LFP
0.5 mV
filtered (130 - 230 Hz)
Ripples
0.1 mV
mean firing rate 25 Hz
Spikes in MS
0.5 mV
0.5 s

Figure 3-2 Diversity in physiological features of identified medial septal neurons.

Six different recorded and labelled neurons are shown during mobility (movement) and immobility (quiet wakefulness). Red, examples of detected sharp wave ripples (SWR). LFP, local field potential; MS, medial septum.

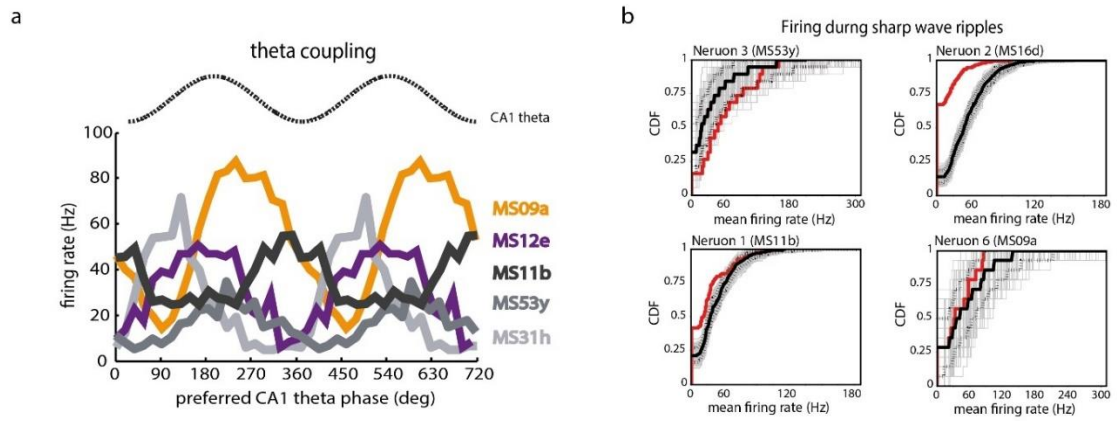


Figure 3-3 Preferred firing phase during CA1 theta oscillation and ripple-related activity of identified medial septal neurons.

a, Firing rate versus CA1 theta phase for five neurons illustrated in Figure 3-2. Black dashed curve, sinusoid representation of two idealised cycles. **b**, Cumulative distribution functions (CDFs) of firing patterns during (red) and outside (gray) SWRs for 4 identified cells. The CDFs show the firing rate distributions during actual ripples (red curves) and for 1000 shuffled distributions (gray). Black curves, median shuffled distributions; dashed curves, 95% confidence intervals. When the red curve falls between the confidence intervals the cell fires during SWRs by chance.

3.2.3 Novel medial septal cells projecting to extra-hippocampal areas

Similar to the diversity of medial septal cell in their firing patterns, I have observed different projection patterns of labelled medial septal neurons projecting cortically. Viral tracing studies have shown a widely distributed innervation area of septal neurons covering the entire temporal cortex (Unal *et al.*, 2015). However, how can we estimate the innervation area of a single neuron? Recovering and reconstructing the labelled projection axon reveals the innervation pattern of single neurons. While grouping labelled cells according to their target area, I have observed different cortical routes of medial septal neurons. Starting from the soma the projection axon goes either straight dorso-caudal towards fimbria or projects initially ventral to turn dorsal towards fimbria. Most medial septal cells target one hemisphere. Early within the medial septum, the axon can be found projecting laterally towards the target hemisphere. In rare cases, I have observed medial septal neurons putatively targeting both hemispheres (MS16d, TV62: not confirmed). The axon of some neurons even split within the MSDB before reaching the fimbira. These observations were confirmed by virus tracing studies that I have conducted. Within the fimbria, the main projection axon can either be seen projecting dorsal towards the dorsal fornix, lateral towards or ventral-lateral towards the targeted hemisphere.

At this point and after recovering several neurons, I can with a high probability predict whether the labelled septal neuron will innervate the hippocampus or extra-hippocampal areas (see *Orchid* and *Teevra* cells, *Chapter 4*). Dorsal projecting neurons tend to innervate the presubiculum and project further to the entorhinal cortex (*Orchid* cells, Viney *et. al*, 2018), while lateral protecting neurons innervate the CA3 (*Teevra* cells, Joshi *et. al*, 2017) and/or DG (Low-rhythmic firing neurons, LRNs, Salib *et. al*, 2019). As I will highlight in the following chapters, the focus of my project was on cells that

shared the same projection patterns and further, the same physiological features during distinct brain states. However, once I came across medial septal cells with unknown or distinct firing patterns, I have attempted to label them. Thus, I have collected a subset of medial septal neurons that distinguished themselves from others by having hitherto uninvestigated projection patterns. Most of these 'unclassified' neurons target extra-hippocampal areas. Yet, unlike the known extra-hippocampal group (*Chapter 4*), these neurons projected cortically by projecting to the lateral fimbria and remain within the ventral fimbria until they reached the ventral presubiculum or entorhinal cortex (Figure 3 1, group 4, purple; Table 3-1). Note that MS104e was identified as an LRN (*Chapter 5*).

One fully analyzed example of these 'unclassified' cells is shown in Figure 3-5 (MS12e). MS12e shared the physiological parameters of high-rhythmic firing neurons (HRNs, *Chapter 4*) with a rhythmicity index (RI) of 0.25, was strongly coupled to dorsal CA1 theta oscillation ($r= 0.33$, $p < 0.005$) and fired during the peak of theta oscillation (Figure 3-5b). Surprisingly, it howed a significant change in firing rate from immobility to mobility (mean firing rate M: 26.7 Hz, mean firing rate IM: 24.5 Hz, Table 3-1). Except for the projection pattern and rate change score (change in mean firing rate from immobility to mobility), it had the criteria of an identified *Orchid* cell (Chapter 4, Viney et. al. 2018). MS12e remains within the ventral fimbria to innervate the lateral entorhinal cortex / amygdalopiriform transition area (Figure 3-5). I could not detect any other collaterals. Immunohistochemical analysis of the soma and dendrites of MS12 lacked immune reactivity (IR) for parvalbumin (PV), ChAT, NK1R and positive IR for Calbindin (CB) and mGluR1a. IR for SATB1 was inconclusive. Differential expression for mGluR1a at the soma (lack of IR) and distal dendrites (positive IR) has been observed before (Joshi et al, 2017). Known *Orchid* cells displayed positive IR for PV, SATB1 and

mGluR1a (Viney *et al.*, 2018). Further investigation and analysis of cells presented in Table 3-1 and newly labelled cells targeting the same area are required to reveal their contributions to the cortical network and define new groups of MSDB cells.

Table 3-1 Electrophysiological parameters of recorded and labelled 'unclassified' cells.

Cell name	**MS12e**	**MS85h**	**MS98d**	**MS101b**	**MS104e**	**MS112l**
Target area	**lEC/ Ata**	**caudal/ ventral Pre/Sub**	**mEC**	**ventral hpc**	**RSg**	**caudal/ ventral Pre/Sub**
Firing rate mobility (Hz)	26.7	u	39.8	60.2	54.1	11.6
Firing rate immobility (Hz)	24.5	u	27.3	38.3	31.4	44.0
Rate change score	0.0	u	0.2	0.2	0.3	-0.6
Rhythmicity Index	0.25	u	0.15	0.22	0.02	0.18
Burst duration mobility (ms)	67.4	u	76.5	47.5	101.8	21.3
Burst duration immobility (ms)	72.1	u	53.7	34.0	63.0	59.6
Pref. theta phase (degree)	171 °	u	102 °	153 °	342 °	31 °
n SWRs	32	u	< 10	< 10	79	43
Mean rate inside (Hz)	18.7	u	n.a.	n.a.	15.6	27.7
Lambda rate outside (Hz)	24.7	u	n.a.	n.a.	31.5	44.2
Poisson *P*-value	0.04	u	n.a.	n.a.	<0.0001	<0.0001
SWR Index	-0.14	u	n.a.	n.a.	-0.34	-0.23

Table 3-1. Electrophysiological parameters of recorded and labelled 'unclassified' cells. Abbreviations: u, unknown/unavailable. Granular retrosplenial cortex, RSg; subiculum, SUB; amygdalopiriform transition area, Ata; Presubiculum, PreSub; medial entorhinal cortex, mEC; Hippocampus, hpc; lateral entorhinal cortex, lEC.

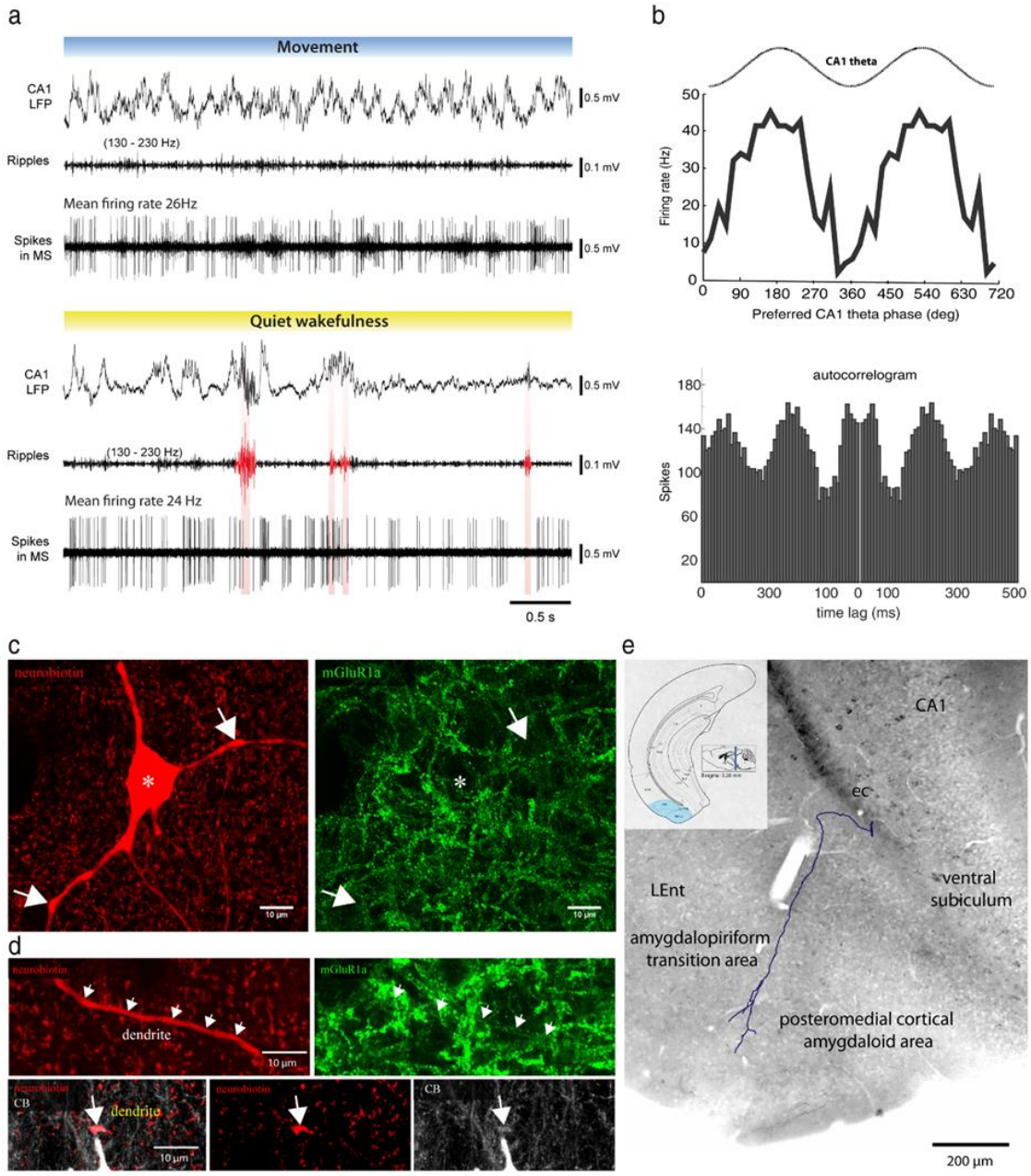

a
Movement
CA1 LFP
0.5 mV
(130 - 230 Hz)
Ripples
0.1 mV
Mean firing rate 26Hz
Spikes in MS
0.5 mV
Quiet wakefulness
CA1 LFP
0.5 mV
Ripples
(130 - 230 Hz)
0.1 mV
Mean firing rate 24 Hz
Spikes in MS
0.5 mV
0.5 s
b
CA1 theta
Firing rate (Hz)
Preferred CA1 theta phase (deg)
autocorrelogram
Spikes
time lag (ms)
c
neurobiotin
mGluR1a
10 µm
d
neurobiotin
dendrite
mGluR1a
CB
e
CA1
ec
LEnt
ventral subiculum
amygdalopiriform transition area
posteromedial cortical amygdaloid area
200 µm

Figure 3-4 Firing patterns, molecular profile and innervated cortical region of an identified medial septal neuron.

a, Rhythmic firing pattern of medial septal neuron MS12e during mobility and immobility. Red, examples of detected sharp wave ripples (SWR). **b**, firing rate versus CA1 theta phase for MS12e neuron. Black, sinusoid representation of two idealised cycles. Autocorrelogram for MS12e during movement periods. **c**, The neurobiotin labelled soma (red). Confocal image of mGluR1a immunoreactivity (green). Labelled neuron lacks IR for mGluR1a at proximal dendrites (arrows). **d**, distal dendrites of MS12e show positive immunoreactivity for mGluR1a and Calbindin (arrows). **e**, reconstructed axon (blue, overlaid onto a reverse contrast light microscopic) of labelled medial septal neuron MS12e targets the amygdalopiriform transition area.

3.2.4 Medial septal cells silenced after air puff presentation and during sharp wave ripples (SWRs)

Recording and labelling single neurons in the medial septum is in particular interesting in head-restrained behaving mice, as their behaviours are immediately reflected by the firing patterns of a single neuron. While neurons usually respond to voluntary behavioural changes, I conducted a small pilot study to investigate whether external stimuli such as light, tone or air puff can affect the firing patterns of medial septal neurons. None of the tested neurons (n=5 animals) reacted to a light or tone representation. Interestingly, one neuron, MS13c (Figure 3-6) showed a change in firing pattern when the animal was introduced to an air puff stimulus towards its whiskers. Immediately (mean 16 ms) after the air puff presentation the cell stopped firing for an average of 18 ms. MS13c was identified as an LRN cell (*Chapter 5*) with a strong suppression during hippocampal SWRs. MS13c displayed a very high firing rate, thus, most of the times the cell stopped firing was either during a SWR or an air puff stimulus (Figure 3-6b). Further investigations and testing are needed to conclude the effect observed in MS13c.

3.2.5 Subcortically projecting medial septal cell

Nearly all of the 41 recovered neurons with an identifiable axon projected cortically. In one case, MS09_, Dr Linda Katona observed a long axon projecting rostro-ventrally instead of the expected cortical projection. Due to a second labelling attempt, I have labelled two neurons in MS09, thus the electrophysiology could not be matched. However, I was able to follow one cortical CA3 and DG projecting axon. To my knowledge, the ventral projecting neuron did not have any other branches projecting cortically. This provides, first evidence for, solely subcortical projecting medial septal

neurons. In the next paragraph I will describe medial septal neurons projecting to both, hippocampus and subcortically.

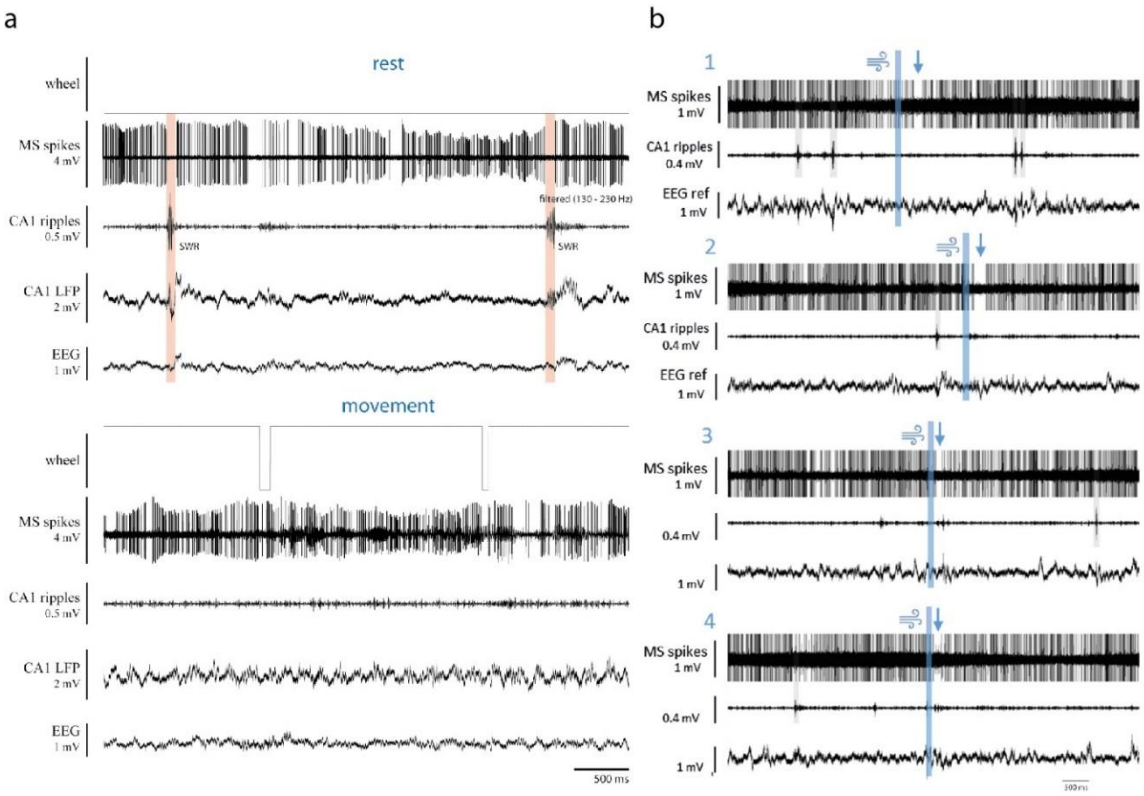


Figure 3-5 Single medial septal cell MS13c reacts to external air puff presentation.

a, Top, firing pattern of MS13c during immobility (rest), SWRs in red columns. Bottom, firing pattern of MS13c during mobility (movement). CA1 LFP, local field potential in SP. **b**, Four different periods during immobility showing MS13c's firing activity after air puff presentation (blue columns). Neuron MS13c stops firing during external air puff stimulation (blue arrows).

3.2.6 Viral tracing of medial septal cells targeting the DG/CA3

I conducted several retrograde viral studies to investigate the projection patterns observed in single cell labelling across a population. In addition, retrograde labelling of septal cells with a virus can be an additional support in revealing the axonal arborization of single juxtacelluary labelled medial septal neurons. Unfortunately, the probability of hitting a viral labelled neuron during juxtacellularly recording was very low, thus I did not succeed in recovering a virus labelled cell. By using an anterograde Cre-dependent EYFP expressing adeno-associated virus (AAV) and a monosynaptically-restricted retrogradely transported and non-spreading Cre-expressing virus (PRV) I was able to visualise medial septal neurons targeting a specific area. The AAV was injected within the medial septum and the PRV injected in the region of interest, resulting in Cre expression only in neurons that directly project to the injection site. Thus, I have investigated medial septal neurons projecting to the entorhinal cortex (*Chapter 4*) as well as neurons targeting the CA3 and DG. Here, I have made two interesting observations. By injecting the virus unilaterally, I could answer the question whether one medial septal neuron only targets one or both hemispheres. Interestingly, a small number of retrogradely labelled medial septal neurons from the CA3 of one hemisphere projected to the same target area on the other hemispheres (Figure 6-3b, Table 8-1, PRV brains). Thus, I have observed the existence of contralateral projecting medial septal cells. In addition, I asked whether cortical projecting medial septal neurons would innervate subcortical areas. Indeed, in a few examples I have observed medial septal neurons projecting to the CA3 and or DG to have also axonal branches projecting to the supramammillary area (SuM, Figure 3-7d).

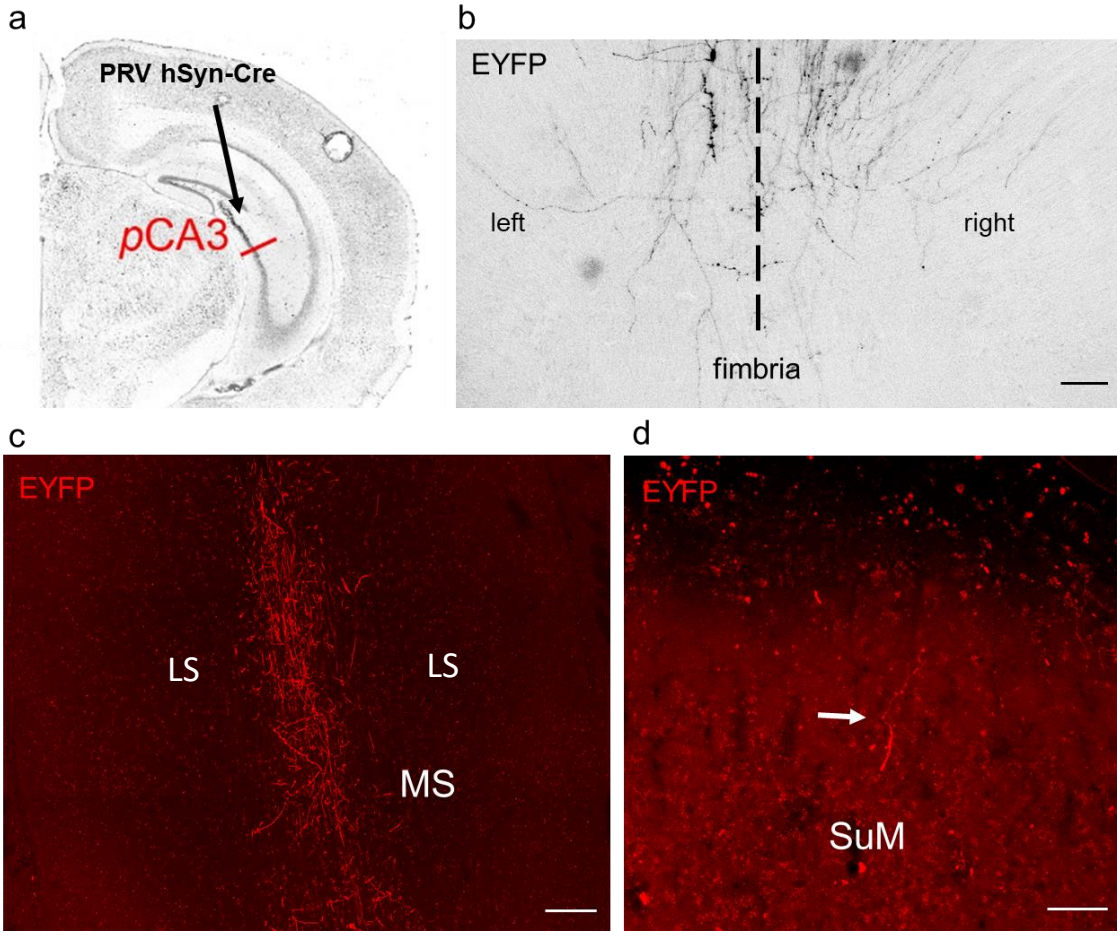


Figure 3-6 Medial septal neurons simultaneously innervate the CA3 and supra-mammillary area.

a, Coronal light microscopy mouse brain hippocampal section showing the viral injection area. **b**, EYFP expression of viral retrogradely labelled medial septal axons in fimbria from CA3 showing axonal projections to both hemispheres. Note that the retrograde PRV was injected unilaterally. **c**, EYFP expression of viral retrogradely labelled medial septal axons from CA3 in the medial septum. Note the lack of viral expression in lateral septum (LS). **d**, EYFP expression viral retrogradely labelled medial septal axons from CA3 detected in the supramammillary area (SuM). Scale (µm), b, c, 100, d, 50.

3.2.7 Chronic MUA recordings in the MS of freely moving mice

All so far observed medial septal neurons in this chapter and identified MS neurons I am introducing in *Chapter 4* and *Chapter 5* are based on awake head-fixed single neuron recordings. Thus, I have explored the diversity of medial septal neurons and observed their distinct behaviour and brain-state related activity across the medial septal population. Knowing the firing characteristics of subgroups of identified medial septal neurons (*Chapter 4, Chapter 5*) during mobility and immobility, I asked how and whether the firing activity of these neurons would change during other behavioural and brain-states such as slow wave sleep and REM sleep under normal conditions. The recording setup for recording and labelling single medial septal cells under head-restrained condition, makes it difficult to record several brain states including REM sleep. In one case, MS49b (only recorded), I succeeded in recording a medial septal neuron during REM sleep. MS49b, a high-rhythmic firing medial septal cell, changes its firing behaviour during REM sleep to rhythmic short bursts (Figure 3-7). As suggested, medial septal cells change their firing behaviour during REM sleep. Especially, as the high-rhythmic firing medial septal neurons (HRNs) are phase-locked to hippocampal theta oscillation during mobility, *I raised the question how the same neurons would fire during theta oscillation occurring during REM sleep*. In addition, behavioural experiments such as sleep deprivation would reveal additional functional characteristics of already identified medial septal neurons, considering their already known target areas (Joshi *et al.*, 2017; Viney *et al.*, 2018; Salib *et al.*, 2019). To address this question, I have chronically implanted NeuroNexus 32 channels Polytrodes (see methods 2.2.2, Figure 3-7b, c) in the medial septum and recorded septal multi-unit-activity (MUA) in freely moving mice (n=4) over a period of 48 h. The aim of this experiment was to perform a baseline recording of MUA in the MSDB in undisturbed animals during spontaneous

home cage behaviours for 24 hours, followed by behavioural experiments the following day e.g. sleep deprivation. For technical reasons, in two out of four mice I was not able to identify MUA of sufficient quality. However, connecting the probe during implantation (see 1.2.2) significantly improved MUA detection in two mice (MS118, MS119, Figure 3-7a). However, MUA was not detected after baseline recording in both cases, thus further behavioural experiments with MUA were not possible. MUA baseline recordings of MS118 and MS119 needs further analysis to initially identify medial septal neurons based on their firing activity and secondly to analyse the firing activity in a freely-movi ng condition during different brain-states.

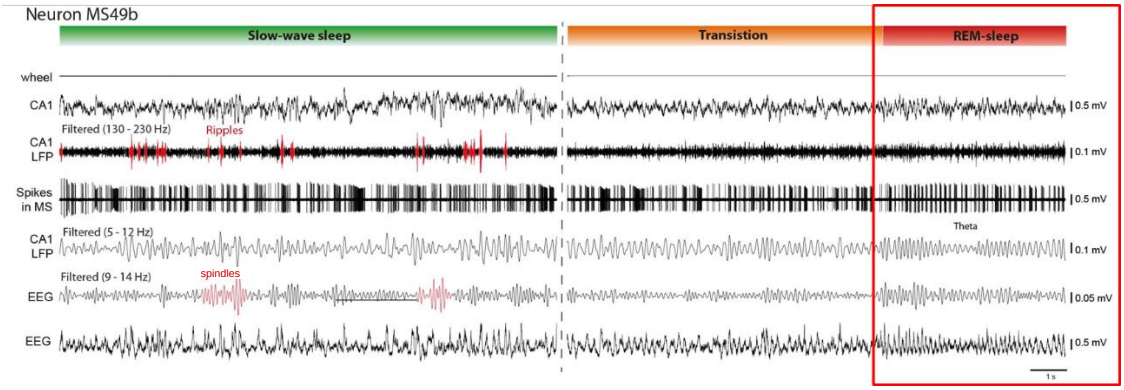


Figure 3-7 Medial septal cell recorded in head-restrained mouse during REM sleep.

Medial septal cell recorded in head-strained setup during several behavioural states (green, slow-wave sleep; orange, transition phase to REM; red, REM sleep). Top to Bottom: Channel monitoring wheel/movement activity; dorsal CA1 LFP (reference electrode); spike activity of MS49b in the MS; filtered CA1 LFP; filtered cortical EEG; cortical EEG; sharp wave ripples and spindles are shown in red.

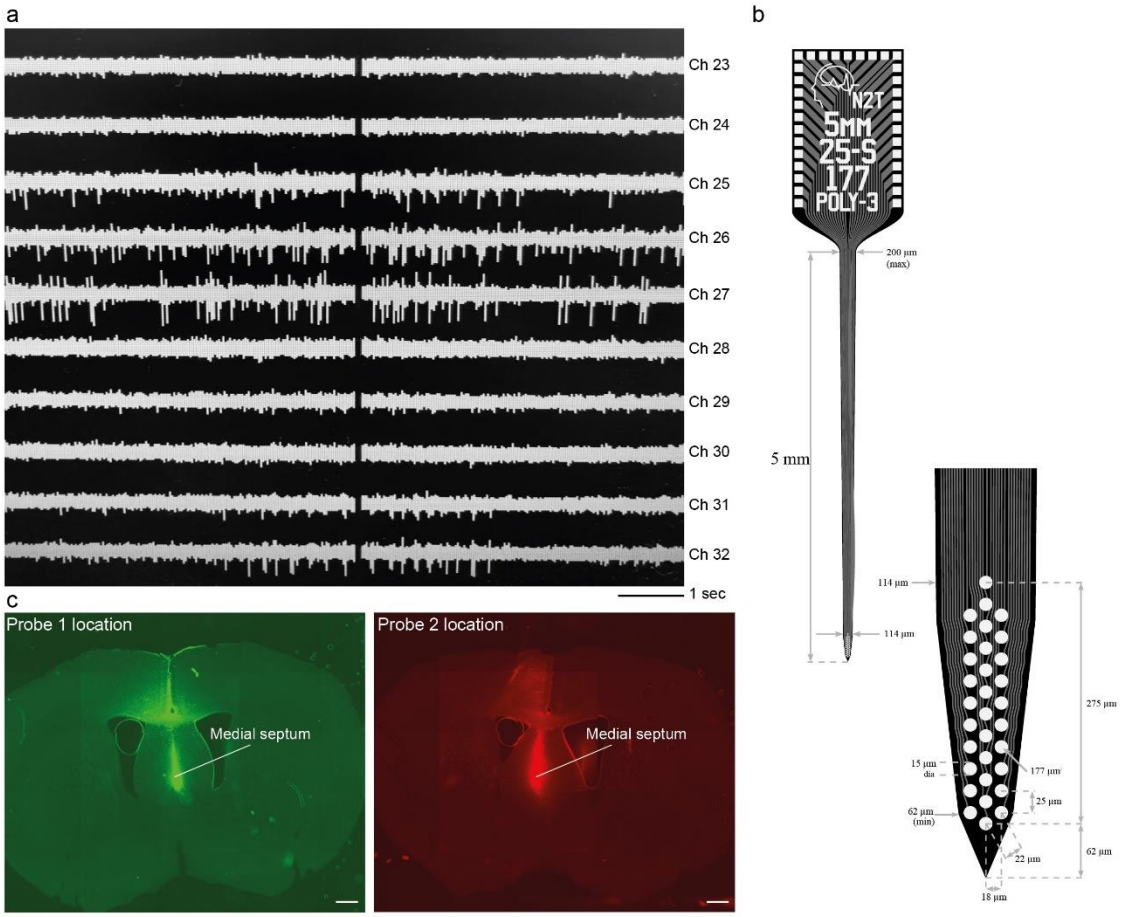


Figure 3-8 Chronic MUA recordings in the MS of freely moving mice

a, Multi-unit-activity (MUA) recorded in the medial septum of a freely moving mouse using a 32 channels Polytrode. Only 10 band-pass filtered channels are shown. **b**, NeuroNexus 32 channels Polytrode. Modified and edited from NeuroNexus. **c**, probe locations of chronically implanted Polytrodes in the medial septum in two different animals. Scale bar: 500 µm.

3.3 Discussion

In this chapter I have introduced the diversity of medial septal neurons as well as the approach to record and label single medial septum neurons in awake head-fixed mice. Based on the observed diversity of firing patterns during distinct behavioural states, immobility and mobility as well as individual neurons having distinct projection patterns, I have grouped neurons with similar projection patterns to further investigate these neurons on a molecular and anatomical level. I am discussing classified groups in *Chapter 4* and *Chapter 5*, thus, the aim of this chapter was to showcase the existence of other subpopulations that needs to be classified for our further understanding of the functional roles of the medial septum.

3.3.1 Roles of subcortical GABAergic neurons governing cortical network activity

Cortical oscillations observed in EEGs represent a temporal reference for information coded by neuronal assemblies. However, the mechanisms and circuits underlying the generation of EEG oscillations are still poorly understood. Rhythmic cortical activity is related to defined behaviours (Buzsáki, Anastassiou and Koch, 2012). Synaptic plasticity is gated by theta oscillations as the timing of stimulus relative to the phase of theta is important in determining the magnitude and direction of synaptic change (Pavlides *et al.*, 1988; Huerta and Lisman, 1993). Therefore, it is assumed that theta oscillations provide a temporal window within the hippocampal circuit responsible for local circuit computation (Lubenov and Siapas, 2009).

Neuronal excitability is governed by intracortical inhibition produced by local GABAergic neurons that are also phase locked to network oscillations (Sik *et al.*, 1995; Klausberger *et al.*, 2003; Ego-Stengel and Wilson, 2007; Czurko *et al.*, 2011). Parallel

with the pyramidal cells a rich diversity of GABAergic interneurons evolved which are able to temporally regulate pyramidal cell activity (Klausberger and Somogyi, 2008). So far 21 types of local GABAergic cells have been defined based on their in vivo firing patterns in dorsal CA1 of the rat hippocampus (Somogyi and Klausberger, 2005; Klausberger and Somogyi, 2008; Somogyi, 2010). This set of interneurons has a differentiated relationship to pyramidal cells and thus to the preferred phase of a theta cycle (Maurer *et al.*, 2006; Hangya *et al.*, 2010). Such organisation ensures that distinct hippocampal GABAergic interneurons innervate pyramidal cells at different subcellular domains and their activity is coordinated in time (Klausberger and Somogyi, 2008). Interestingly, serval PV-expressing GABAergic interneurons innervate distinct subcellular domains of pyramidal cells. For instance, the axon initial segment of all pyramidal cells receives GABAergic innervation from PV positive axo-axonic cells, basket cells target the cell bodies and proximal dendrites, bistratified cells innervate the apical and basal dendrites and oriens-lacunosum molecular (O-LM) interneurons target the distal dendritic apical tuft (Somogyi, 2010). If distinct GABAergic neurons fire at different phases of the theta cycle and innervate different domains of pyramidal cells coordinating their excitability, *what mechanisms underlie the coordination of hippocampal interneurons?* All fields of the hippocampal formation are innervated by medial septal fibres but are most prominent in the dentate gyrus and the CA3 field. So far, there are only limited data on the projection of single labelled GABAergic septal cells to the hippocampus (Viney *et al.*, 2013, 2018; Joshi *et al.*, 2017; Salib *et al.*, 2019). However, as I could show so far, the hippocampus is not the only target of septal GABAergic projections.

The diversity of medial septal population shown in 3.2.2 based on their firing patterns during locomotion and immobility suggests the involvement of the septal-diagonal band

complex in various simultaneous computational activities. While some cells are active with a high-firing rhythm, others are silenced or low-rhythmic firing and correlate to various network oscillation such as theta oscillations or hippocampal sharp-wave ripples. In order to reveal the functional role of a subpopulation of medial septal cells, further single cell anatomical examinations (Chapters 4-5) are needed. Another possibility is to correlate the electrophysiological activity of a single cell by introducing external stimuli. One example is shown in 3.2.4, where an air puff stimulus was presented during recording. Within 16 ms the medial septal cell (MS13c, HRN, targeting the DG) stopped firing for an average of 18 ms. Such a fast respond was shown before in the basal forebrain. Basal forebrain cholinergic neurons were shown to respond to reward and punishment with an unusual speed and precision (18 ± 3 ms) (Hangya, Sachin P. Ranade, *et al.*, 2015). Thus, the medial septum may be involved in processing and relying external stimuli to cortical areas such as the hippocampus.

3.3.2 Dual subcortical and cortical projection from the medial septum

By using a Cre-dependent adeno-associated virus (AAV) and a monosynaptically-restricted retrogradely transported and non-spreading Cre-expressing virus (PRV) I showed dual projecting medial septal neurons to the hippocampus and supramammillary nucleus (SUM) in mice. The SUM of the hypothalamus lies dorsal to the mammillary bodies in the caudal diencephalon (Swanson, 2018) and has strong links with the septum and hippocampus. The bidirectional projection between the SUM and medial septum are known (Vertes, 1988, 1992; Borhegyi and Freund, 1998; Borhegyi *et al.*, 1998; Leranth *et al.*, 1999; Agostinelli, Geerling and Scammell, 2019). However the SUM only sends but does not receive projections from the hippocampus (Amaral and Cowan, 1980; Haglund, Swanson and Köhler, 1984; Saper, 1985; Vertes, 1992; Vertes and McKenna,

2000). SUM sends excitatory projections to both GABAergic and cholinergic cells of MSDB (Leranth and Kiss, 1996; Borhegyi *et al.*, 1998). SUM fibres projecting to the hippocampus predominantly target two regions of the hippocampus; the dentate gyrus throughout the hippocampus and the CA2/CA3a region of the dorsal hippocampus (Wyss, Swanson and Cowan, 1979; Haglund, Swanson and Köhler, 1984; Saper, 1985; Vertes, 1992; Vertes and McKenna, 2000).

Studies have shown that the SUM is directly involved in the modulation of the theta rhythm of the hippocampus (Vertes, 1986; Bramham and Srebro, 1989; Vertes and Kocsis, 1997; Kirk, 1998). It has been demonstrated that stimulation of the SUM region generates theta (Oddie *et al.*, 1994), moreover the reversible blockade of SUM with procaine disrupts spontaneous theta as well as the bursting discharge of the MSDB (Kirk and McNaughton, 1993; Bland *et al.*, 1994; Oddie *et al.*, 1994). Also electrophysiological recordings have shown SUM neurons to fire phasically in bursts synchronous with hippocampal theta oscillations (Kirk and McNaughton, 1991; Kocsis and Vertes, 1994; Bland *et al.*, 1995). Thus, the SUM appears to represent a vital role in modulating the MSDB and hippocampus regarding the generation of theta oscillation. In conclusion the SUM projects strongly to the MSDB as well as to the dentate gyrus. Interestingly, a subpopulation of SUM neurons (5–10%) sends dual projections to the MSDB and DG of the hippocampus (Vertes and McKenna, 2000). My tracing study however showed dual projections from the medial septum to the DG/CA3 and SUM. These dual projecting neurons might have a parallel hippocampal disinhibitory role and a strong subcortical inhibitory role within the SUM. Further electrophysiological and anatomical investiagtions are needed to understand the role of these dual projecting neurons as my tracing studies showed only a few descending MSDB axons to the SUM suggesting a small subpopulation of dual projecting MSDB neurons.

Overall, single septal GABAergic cells show a high degree of specialisation and are likely to contribute to the modulation/generation of cortical theta oscillations via their synaptic GABAergic target cells in the cortex and to coordinating neuronal activity across functionally-related cortical areas required for learning and memory. In addition, the subcortical input to the medial septum and hippocampus needs further investigation as it has a strong influence on the medial septal output.

3.3.3 The role of the septo-hippocampal system in contextual memory consolidation during REM sleep

I observed modulatory changes in firing activity of single medial septal neurons in head-restrained and chronic freely behaving mice during REM sleep. Such an observation implicates that the MSDB is actively involved during REM sleep. However, the functional role is not known. Rapid-eye movement (REM) sleep is characterized by rapid eye movements, muscle atonia and prominent theta rhythm in the hippocampus and cortex (Saper *et al.*, 2010). During this state, mice and rats display a prominent ~7-Hz theta oscillation observed LFP recordings from cortical structures, including the hippocampus (Buzsáki, 2002). The REM sleep generator was initially suggested to be located in the pons (Jouvet, M. 1962). Here, reciprocal inhibition between cholinergic neurons and serotonergic neurons from raphe nuclei and noradrenergic neurons from locus coeruleus were originally hypothesized to gate REM sleep (Hobson, McCarley and Wyzinski, 1975; McCarley and Hobson, 1975; McGinty and Harper, 1976; Aston-Jones and Bloom, 1981; Pace-Schott and Hobson, 2002). Recently, GABAergic and glutamatergic neurons were integrated into the brainstem circuitry that is critical for the onset of REM sleep (Boissard *et al.*, 2003; Lu *et al.*, 2006; Verret *et al.*, 2006; Sapin *et al.*, 2009). Thus, REM sleep correlates with neuronal activity in the brainstem, basal

forebrain and lateral hypothalamus. Further has REM state been linked with spatial and emotional memory consolidation (Stickgold and Walker, 2005; Diekelmann and Born, 2010). During REM sleep hippocampal theta rhythms may contribute to memory consolidation by providing a mechanism for strengthening place cells activated during prior wakefulness (Louie and Wilson, 2001; Lecourtier *et al.*, 2011). Although the medial septum is not directly involved in REM sleep generation, the generation of theta rhythm requires an intact medial septum (Mitchell *et al.*, 1982; Brown *et al.*, 2012). Rhythmic MS GABAergic neurons are thought to be involved in hippocampal theta generation (Petsche, Stumpf and Gogolak, 1962; Kiss *et al.*, 1990; K Tóth, Freund and Miles, 1997; Simon *et al.*, 2006). To test whether MS GABAergic neuronal activity is required for memory consolidation during REM sleep, MS GABAergic neurons were optogentically silenced during REM sleep without disrupting sleeping behaviour. Silencing of these neurons selectively during a REM erased subsequent novel object place recognition and impaired fear-conditioned contextual memory. This study demonstrated that MS GABAergic activity, specifically during REM sleep, is required for normal memory consolidation (Boyce *et al.*, 2016). The chronic MUA recordings aimed to provide an insight into the firing behaviour of identified medial septal cells (Chapters 4-5). Further analysis is required to identify whether MSDB neurons involved in coordinating hippocampal spatially modulated cells are active in the same manner during REM sleep as they have shown to be during awake theta oscillation.

Chapter 4

Two identified subpopulations of high-rhythmic firing medial septal neurons with distinct firing properties and molecular profiles target specific cortical areas

4.1 Introduction

Network oscillations provide a framework for temporal coordination, as represented by theta oscillations (5-12 Hz) which are prominent during movement and REM sleep (Kramis, Vanderwolf and Bland, 1975), gamma oscillations (30-120 Hz) which are phase-amplitude coupled to theta (Soltesz, Deschênes and Deschenes, 1993; Colgin *et al.*, 2009; Schomburg *et al.*, 2014; Lasztóczi and Klausberger, 2016), and hippocampal sharp wave ripples (SWRs, 130-230 Hz) which occur during slow wave sleep, awake immobility and consummatory behaviour (Buzsáki, 1986). These oscillations enable the representation of rhythmic temporal sequences. A network of local GABAergic neurons controlling the excitability of principal cells by a mechanism of temporal and specific somato-dendritic inhibition over various time scales reflected by underlying network oscillations (Cobb *et al.*, 1995; Ylinen *et al.*, 1995; Somogyi and Klausberger, 2018). Over 21 GABAergic cell types have been so far identified in CA1 targeting distinct subcellular domains of principal cells, each cell type preferentially firing during specific phases of network oscillations. Together they contribute to a temporal redistribution of inhibition from the axon initial segment to the soma, and all the way to the distal dendrites of principal cells (Somogyi and Klausberger, 2005; Klausberger and Somogyi, 2008; Varga, Golshani and Soltesz, 2012; Somogyi *et al.*, 2014). It remains unclear which underlying circuits and neurons are responsible for their coordination. Looking at subcortical projections to the hippocampal formation, the medial septum and diagonal band of Broca (MSDB) is the focus of attention in this thesis.

In the previous chapter I have introduced the septo-hippocampal pathway, including its components and its involvement in spatial learning. Several studies suggest that the medial septal input to hippocampus plays a crucial role, in particular in coordinating the hippocampal theta rhythm and associated mnemonic processes. Importantly, it is known

that medial septal GABAergic neurons preferentially target hippocampal and extrahippocampal GABAergic interneurons (Freund and Antal, 1988; Unal *et al.*, 2015). There, I focused on the GABAergic MSDB neurons. However, the variety of potential post-synaptic innervation of different cortical GABAergic cells, given their known diversity, makes the existence of only one type of septal GABAergic cell very unlikely. Until recently, the functional role of the MSDB has been investigated *in vivo* at the population level, and with network effects mostly being studied in the dorsal CA1 region of the hippocampus (Buzsáki, Lai-Wo S. and Vanderwolf, 1983; McNaughton, Ruan and Woodnorth, 2006; Boyce *et al.*, 2016; Tsanov, 2017; Korotkova *et al.*, 2018). However, it has been shown that most MSDB GABAergic septal afferents to the hippocampus extensively target interneurons in CA3 and the dentate gyrus (DG) compared to CA1 (Freund and Antal, 1988). It remains unclear how diverse the septal neuronal population is. Therefore, I address the question, whether distinct septal GABAergic cell types selectively target distinct cortical interneuron types in a spatio-temporal manner in the hippocampal formation area during network oscillations. To answer this question, I analyzed the MSDB at the single cell level by performing single-neuron glass extracellular recordings and juxtacellular labelling in head-fixed awake mice.

In this chapter, I will introduce two groups of high-rhythmically firing neurons in the MSDB named ‘T*eevra*’ and ‘*Komal*’ gorups, initally recorded using silicon probes in the mouse medial septum and classified by clustering (Joshi *et al.*, 2017). This clustering is supported and confirmed by my observations of single labelled and identified medial septal neurons and contributed to the identification of two new cell types, *Teevra* (Joshi *et al.*, 2017) and *Orchid* (Viney *et al.*, 2018) neurons, each with distinct physiological features and specific cortical innervation areas, as I present in this chapter.

In summary, simultaneously recorded medial septal cells in Joshi et al. 2017 exhibited varying burst duration and extent of rhythmicity. Moreover, the preferential mean firing phase of the individual cells, collectively, covered the entire theta cycle as referenced to ongoing LFP theta oscillations in the pyramidal layer of CA1. Across the population, these cells could either increase, decrease or not change their mean firing phase between locomotion and immobility. An unsupervised hierarchical clustering algorithm was used to cluster the simultaneously recorded population based on the calculated rate change score and burst durations. Four main clusters with distinct correlation to the selected parameters were identified (Joshi et al., 2017).

I have, in *Chapter 3*, discussed the characteristic firing patterns of medial septal neurons and how I established a strategy to locate and confidently record single medial septal neurons in awake head-fixed mice. Using electrophysiological parameters of known medial septal cells to confirm the recording area, the focus was initially on the highly rhythmic cells observed in the multi-channel extracellular probe recordings (Joshi *et al.*, 2017), also considering rhythmic medial septal cells have been previously reported and not only considered to be a characteristic feature of MS GABAergic neurons (Dragoi *et al.*, 1999; Borhegyi, 2004; Simon *et al.*, 2006). In addtion, these cell has been also linked to a ‘pacemaking’ functional role within the medial septum (King, Recce and O’Keefe, 1998). For an initial characterisation of highly rhythmic medial septal neurons I referred to the multi-channel silicon probe recordings for two main reasons. Firstly, to estimate the diversity of high rhythmic neurons by clustering the population-based defined parameters. In *Chapter 5*, I used this population analysis to characterise the low-rhythmic firing neurons. Secondly, I aimed to rule out any technical and behavioural biases regarding changes in firing patterns across MSDB neurons during recordings. Having just the spike trains of a population of medial septal neurons during different behavioural

states (locomotion, immobility) and cortical LFP in dorsal CA1, parameters like the burst duration, firing rate during each behavioral state, rhythmicity index, preferred firing phase during ongoing theta oscillations and the changes in firing rate can be calculated.

4.2 Results

4.2.1 Identifying high-rhythmic firing medial septal neurons

I observed and recognized single medial septal neurons that matched the features of *Teevra* and *Komal* neurons during my *in vivo* juxtacellular recordings. *Teevra* and *Komal* neurons differed in their burst duration during locomotion and in their firing rate change score (Joshi *et al.*, 2017). Further, I have shown the diversity of the medial septal population in their network-state related activity and based on select parameters shown initial clustered groups of high rhythmic active septal cells during locomotion. The two largest clusters previously described, the *Teevra* and *Komal* cells, are both highly rhythmic and have distinct distinguishable parameters. These quantifiable results set the basis for the electrophysiological characterization of the *in vivo* extracellularly recorded and juxtacellularly labelled medial septal cells in this chapter (Table 4-1, Table 4-2, Table 4-3) with the aim to characterise the different identified clusters. Firstly, I asked whether *Teevra* and *Komal* cells have the same molecular profiles, innervate the same cortical areas and, finally, whether they have specific post-synaptic targets.

For clarification, *Teevra* cells will be established as a novel medial septal high-rhythmic firirng cell type as I will introduce and discuss within this chapter. *Komal* cell, however, will remain a high-rhythmic firing cell population with one so far identified cell type, the *Orchid* cells. Thus, a group of cells with common physiological features can be further distinguished based on further anatomical and molecular profiles and cortical target

regions. Consequently, in this chapter, I will discuss two kinds of GABAergic medial septal neurons: *Teevra* and *Orchid* cells.

4.2.2 Electrophysiological parameters of labelled *Teevra* and *Orchid* cells

Linking the two identified clusters, the *Teevra* and *Komal* cells, to my identified i.e. single-neuron recording and labelling cells, I recognised that the rhythmicity of the single neurons I recorded with glass electrodes during both immobility and movement, as well as the sound of the spike bursts during these states were likely to match the *Teevra* and *Komal* units from the silicon probe recordings. The sound of the spike trains during locomotion was the primary indicator for targeting a high-rhythmic firing medial septal neuron (HRNs, see methods 2.3.5). Out of 107 mice and 682 single neurons, I have successfully recorded, labelled and recovered 41 neurons in 41 mice from which 12 (*Orchid* cells: 3 labelled, 4 unlabelled; T*eevra* cells: 5) were classified as HRNs. Dr Abhilasha Joshi labelled, further 11 HRNs (*Orchid* cells: 3, *Teevra* cells: 8) and Dr Tim Viney 6 HRNs (*Orchid* cells: 2 labelled, 4 unlabelled) that I have only included for calculation and comparison purposes. Thus, a total of 21 HRNs recorded and labelled medial septal neurons in 21 mice were pooled for characterization. All “MSxx” (Minas Salib) cells were recorded, labelled, processed and analyzed by me.

The degree of rhythmicity of activity displayed by medial septal neurons during locomotion and immobility may indicate their diverse modulation of their postsynaptic target neurons in the cortex, but also locally in the MSDB. According to the calculated RI and the hierarchical clustering presented in Joshi et al 2017, both, *Teevra* and *Orchid* cells displayed an RI above 0.1 during locomotion. I have calculated the RI for all of my identified medial septal neurons using the methods from Joshi et al. 2017 and classified

neurons with an RI above 0.1 as HRNs (Table 4-1, Table 4-2, Table 4-3). Note that two HRNs with an RI below 0.1, MS14i and MS11b, were considered as HRNs based on their molecular and axonal parameters. Since both neurons were recorded in untrained (not trained to run in head-restrained setup) animals a valid comparison of their RI and burst duration with the identified groups of recorded *Orchid* and *Teevra* neurons was not possible.

Next, the question was whether during dorsal CA1 theta oscillations the mean firing preference of my single recorded HRNs show a clear peak or trough. In addition, I calculated the rate change score of my identified cells. Out of my 12 identified HRNs, 5 preferentially coupled to the trough (75° ± 50.8°, n=5) and did not change the mean firing rate from immobility to locomotion (Table 4-1). The other 7 showed a preferential peak (n=3 labelled; 4= unlabelled, 176° ± 28.6°, n=7) and displayed a comparable higher rate change score, where the mean firing rate increased during locomotion (Table 4-2, Table 4-3). These observations are consistent with the *Teevra* neurons (37.5° ± 53.5°, n=13) in Joshi et al 2017 and *Orchid* neurons (178.6° ± 39.1°, n=8) in Viney et al. 2018.

CA1d theta trough firing HRNs were identified as *Teevra* cells, indicated by their very low rate-change-score (Table 4-1) indicating a constant mean firing phase from immobility to locomotion. CA1d theta peak firing *Orchid* cells displayed a comparable higher rate change score, where the mean firing rate increased during locomotion (Table 4-2). However, both groups of HRNs displayed a comparable high firing rate to known medial septal neurons (King, Recce and O'Keefe, 1998) during both immobility (*Teevra* cells: 40.7 ± 15.8 Hz, n = 13 including MS31h, MS11b, MS71c, MS73c and MS90g; *Orchid* cells: 39.8 ± 8.1 Hz; n = 8 including MS14i, MS19b, MS74b) and locomotion (*Teevra* cells: 37.2 ± 13.5 Hz, n = 13 including MS31h, MS11b, MS71c, MS73c and MS90g; *Orchid* cells: 55.2 ± 14.1 Hz, n = 8 including MS14i, MS19b, MS74b) (Table 4-

1, Table 4-2, Table 4-3). In addition, a group of unlabelled HRNs (n=8 including MS17k, MS58i, MS24a, MS84f, Table 4 3) were classified as putative *Orchid* cells, as they displayed matching physiological parameters. All 8 neurons had different mean firing rates during locomotion and immobility (locomotion 61.7 ± 18.0 Hz versus immobility 43.4 ± 8.9 Hz; n = 8, t7 = 3.80, p=0.0067, paired t-test). As with the labelled neurons, most putative *Orchid* cells showed a phase preference close to the peak of CA1d theta oscillations (group mean phase (circular mean ± circular s.d.): identified, 178.6° ± 39.1°, n = 8; putative, 183.3° ± 38.5°, n = 8; difference = 4.7°; p=0.8143, permutation test; Table 4-2, Table 4-3).

I have observed an additional feature of the HRNs. All display a unique consistent burst activity, during both locomotion and immobility. Unlike the fully trained animals running on the jet ball used for the silicon probe recordings, I recorded in mostly untrained animals that had many immobility periods. Here, I have observed different kind of bursts across HRNs during immobility periods. Interestingly, once the animal initiated locomotion/movement, the burst firing behaviour of the cells became more rhythmic and, in some cases, changed their pattern, i.e. *Teevra* cells exhibited short bursts during locomotion (Figure 4-3). Thus, In addition to the firing frequency and preferred mean firing phase during dCA1 theta oscillations, I looked at the burst properties of my 12 HRNs, *Teevra* and *Orchid* cells, and compared them to all identified *Teevra* and *Orchid* groups. All HRNs showed a high burst incidence during both locomotion and immobility (>3.0 Hz, Table 4-1, Table 4-2, Table 4-3) with *Orchid* cells having a higher burst incidence (mobility: 4.98 ± 1.30 Hz; immobility: 4.24 ± 0.74; 40 ms, n =8) than *Teevra* cells (mobility: 4.40 ± 1.56 Hz; immobility: 3.56 ± 1.23; 40 ms, n =13). However, *Teevra* cells mostly exhibited short duration bursts during locomotion (median <50 ms, Table 4-1, Figure 4-3) while *Orchid* cells displayed long duration bursts during locomotion and

immobility (median >50 ms, Table 4-2, Table 4-3, Figure 4-5). Figure 4-3a and Figure 4-5a show the firing patterns of two of my recorded and labelled HRNs, with MS90g (Figure 4-3) being a *Teevra* cells and MS14i (Figure 4-5) an *Orchid* cell.

Finally, I asked whether the identified HRNs were modulated during hippocampal sharp-wave ripple (SWR) oscillations, especially, as all my recorded HRNs had sufficient immobility periods to capture hippocampal SWRs. Previous studies have shown that GABAergic MSDB neurons can be active or supressed during SWRs (Dragoi *et al.*, 1999; Borhegyi, 2004; Viney *et al.*, 2013). During immobility periods, most HRNs did not change their firing rate during CA1d theta SWR events. However, not all identified neurons (10/21 labelled HRN neurons, 5/8 unlabelled *Orchid* neurons; Table 4-1, Table 4-2, Table 4-3) had sufficient detectable SWR events to support this conclusion. However, one labelled and two unlabelled (putative) Orchid cells (MS19b: $p<0.0001$, SWR index: -0.75; TV78d: $p<0.0001$, SWR index: -0.83, TV86b: $p<0.0001$, SWR index: -0.81, Figure 4-1) showed a significant drop in firing activity during SWRs (Table 4-1, Table 4-2, Table 4-3).

To conclude, analysing the physiological parameters of identified HRNs, the common features are: (1) both, *Teevra* and *Orchid* cells, have a high rhythmicity index (RI > 0.1) during locomotion; (2) both exhibit a high burst incidence during both locomotion and immobility; (3) both have a high mean firing rate during both locomotion and immobility; (4) both did not show a significant change in their firing rate during CA1d theta SWR events.

Investigating the differences between *Teevra* and *Orchid* cells, the unique features of each cell are: (1) *Teevra* cells display short burst durations while *Orchid* cells have long burst durations during locomotion and immobility. (2) *Teevra* cells do not change their

mean firing rate from immobility to locomotion while *Orchid* cells increase their mean firing rate. (3) *Teevra* cells fire preferentially during the trough of dCA1 theta oscillations while *Orchid* cells preferentially fire during the peak of dCA1 oscillations, both with strong coupling to the hippocampal theta network oscillation (mean vector length > 0.2).

At this stage I want to summarize that the common physiological features described above are sufficient to calssify Teevra and Orchid cells as HRNs, while the further splitting and analysis (e.g. molecular profiles and postsynaptic targets) of these HRNs will lead to putative candidates for characterising cell types.

Table 4-1 Electrophysiological parameters of identified *Teevra* neurons.

Teevra cells	Cell name	MS31h	MS11b*	MS71c^{L}	MS73c^{L}	MS90g*
Firing activity	RI	0.3	0.01	0.14	0.23	0.29
	Firing rate M	20.6	39.7	49.4	34.6	32.7
	Firing rate IM	20.5	31.8	47.6	52.5	36.3
	Rate change score	0	0.1	0	-0.2	0.05
	Burst incidence IM	1.7	3.3	4.8	4.2	3.3
	Burst duration M	39.1	56	42.3	36	44.5
CA1d theta (5 – 12 Hz)	Pref. theta phase	115	320.3	34.1	75	138.6
	Mean vector length (*r*)	0.49	0.15	0.33	0.05	0.52
	Mean ang. dev. (°)	58.0	74.5	64.5	67.8	56.6
	SWR Index	0.10	-0.16	0.07	-0.08	0.11

Table 4-1. Electrophysiological parameters of identified *Teevra* neurons. Spike burst defined as >3 spikes with ISIs <40 ms. Firing rates and burst incidence (Hz) are expressed as mean of 1 s bins ± s.d.; burst duration (ms) are expressed as median and interquartile range. Abbreviations: RI, rhythmicity index; M, locomotion; IM, immobility. Superscripts denote location of soma and axonal terminal in the right $^{(R)}$ or left $^{(L)}$ hemisphere. *Animal was not trained.

Table 4-2 Electrophysiological parameters of identified *Orchid* cells.

Orchid cells	Cell name	**MS14i^{L}**	**MS19b^{L}**	**MS74b^{R}**
Labeling strength		++	++	+
Firing activity	Max speed (cm/s)	6.3	18.8	u
	RI	0.05	0.11	0.20
	Firing rate M	67.8 ± 12.9	43.4 ± 9.3	55.0 ± 11.0
	Firing rate IM	48.2 ± 10.0	31.9 ± 5.2	37.6 ± 16.0
	Rate change score	0.2	0.2	0.2
	Burst incidence M	3.8 ± 1.7	4.4 ± 0.9	5.2 ± 1.3
	Burst incidence IM	4.9 ± 0.9	4.5 ± 1.3	3.5 ± 0.9
	Burst duration M	121.0, 193.0	96.2, 57.5	80.1, 40.1
	Burst duration IM	81.1, 48.9	100.0, 57.3	97.0, 75.0
CA1d theta (5 – 12 Hz)	LFP measurement	upper SP	SP	SP
	Pref. theta phase	152°	167°	233°
	Mean ang. dev. (°)	70.8	69.2	73.0
	Mean vector length (*r*)	0.23	0.27	0.34
	Rayleigh *P*-value	<0.0001	<0.0001	<0.0001
	Total *n* spikes	6659	5143	578
	Spikes per cycle (mean ± s.d.)	8.7 ± 4.2	7.2 ± 3.4	8.1 ± 3.2
CA1d mid-gamma (55 - 80 Hz)	Pref. gamma phase	164°	158°	u
	Mean vector length (*r*)	0.04	0.25	u
	Rayleigh *P*-value	0.0008	<0.0001	0.47
	Total *n* spikes	3553	2052	437
CA1d SWRs (130 – 230 Hz)	*n* SWRs	57	58	16
	Mean rate inside (Hz)	57.71	4.88	u
	Lambda rate outside (Hz)	48.96	33.16	u
	Poisson *P*-value	0.0238	<0.0001	u
	SWR Index	0.22	-0.75	-0.02

Table 4-2. Electrophysiological parameters of identified *Orchid* cells. Spike burst defined as >3 spikes with ISIs <40 ms. Firing rates and burst incidence (Hz) are expressed as mean of 1 s bins ± s.d.; burst duration (ms) are expressed as median and interquartile range. Abbreviations: RI, rhythmicity index; M, locomotion; IM, immobility. KS, Kolmogorov-Smirnov; SP, stratum pyramidale; SO, stratum oriens, u, unknown/unavailable. Superscripts denote location of soma and axonal terminal in the right $^{(R)}$ or left $^{(L)}$ hemisphere.

Table 4-3 Electrophysiological parameters of putative *Orchid* cells.

Orchid cells*	Cell name	MS17k	MS58i	MS24a	MS84f
Firing activity	Max speed (cm/s)	9.9	u	16.8	u
	Firing rate M	51.6 ± 25.5	80.9 ± 20.2	48.7 ± 10.7	65.2 ± 7.5
	Firing rate IM	44.6 ± 13.8	52.1 ± 14.7	33.7 ± 8.8	48.4 ± 9.2
	Burst incidence M	3.3 ± 2.2	6.6 ± 1.0	5.3 ± 1.4	5.1 ± 1.5
	Burst incidence IM	4.3 ± 1.2	4.9 ± 1.1	3.3 ± 1.2	4.8 ± 1.1
	Burst duration M	86.7, 115.8	70.2, 22.0	57.4, 36.8	86.4, 111.8
	Burst duration IM	84.4, 67.7	76.7, 57.4	94.1, 73.0	94.3, 69.9
CA1d theta (5 – 12 Hz)	Pref. theta phase	176°	133°	178°	177°
	Mean vector length (r)	0.29	0.42	0.43	0.31
	Rayleigh P-value	<0.0001	<0.0001	<0.0001	<0.0001
	Total n spikes	727	2869	3287	4624
	Spikes per cycle (mean ± s.d.)	9.0 ± 3.7	7.6 ± 3.9	6.8 ± 3.9	8.8 ± 2.7
CA1d mid-gamma (55 - 80 Hz)	Pref. gamma phase	u	u	155°	u
	Mean vector length (r)	u	u	0.321	u
	Rayleigh P-value	0.1919	0.6089	<0.0001	0.087
	Total n spikes	1003	1032	284	1227
CA1d SWRs (130 – 230 Hz)	n SWRs	24	6	55	0
	Mean rate inside (Hz)	69.35	u	27.47	u
	Lambda rate outside (Hz)	46.33	u	36.92	u
	Poisson P-value	0.0004	u	0.0176	u
	SWR Index	0.20	u	-0.15	u

Table 4-3. Electrophysiological parameters of putative *Orchid* cells. Spike burst defined as >3 spikes with ISIs <40 ms. Firing rates and burst incidence (Hz) are expressed as mean of 1 s bins ± s.d.; burst duration (ms) are expressed as median and interquartile range. Cells are classified as putative *Orchid* cells due to insufficient labelling strength. *Soma was not recovered. Abbreviations: RI, rhythmicity index; M, locomotion; IM, immobility. KS, Kolmogorov-Smirnov; u, unknown/unavailable.

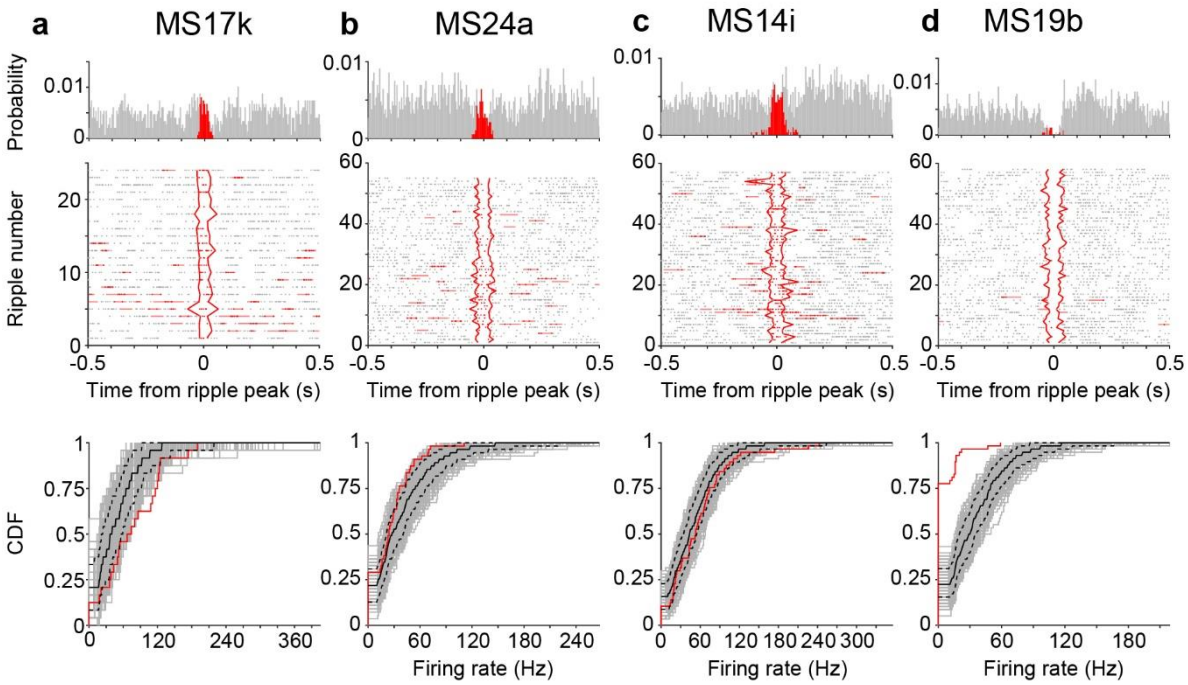


Figure 4-1 Ripple-related activity of *Orchid* cells and putative *Orchid* cells.

a-d, Firing probability density (top), spike raster (middle) and cumulative distribution functions (CDFs, bottom) of firing patterns during (red) and outside (grey) SWRs for 4 identified *Orchid* cells. In the raster plot, continuous staggered lines delineate start and end of aligned ripples, horizontal lines delineate ripples within 0.5 s of an aligned ripple. The CDFs show the firing rate distributions during actual ripples (red curves) and for 1000 shuffled distributions (grey). Black curves, median shuffled distributions; dashed curves, 95% confidence intervals. When the red curve falls between the confidence intervals the cell fires during SWRs by chance. MS19b is inhibited during most SWRs, whereas TV58g is activated during SWRs with high firing rates. e-h, Same as a-d but for putative *Orchid* cells. MS17k is activated during SWRs, with SWRs mostly occurring on the second half of individual rhythmic bursts (e, top). MS17k and MS24a are classified as putative *Orchid* cells due to insufficient labelling strength.

4.2.3 Cortical target areas of labelled *Teevra* and *Orchid* cells

Having established the common parameters of HRNs and distinguishable physiological features of labelled and identified *Teevra* and *Orchid* cells, in agreement with the parameters of neurons recorded labelled by Dr Abhilasha Joshi and Dr Tim Viney, I investigated in the next step their molecular profiles and axonal target regions. Revealing the anatomical structure of a single medial septal neuron is a major aim of my project adding the greatest value and insights to the functional role of septo-cortical cells, especially when knowing their physiological and molecular profiles. Note that grouping the cells discussed above strongly linked to their cortical innervation patterns and molecular profiles i.e. the firing patterns predicted their axonal target regions and even molecular profiles. As most of the cells were part of the initial database discussed in *Chapter 3*, the same strategy was used to group single recorded and labelled medial septal neurons. Once the septal projection axon was recovered and traced to its target area(s), post-synaptic target analysis revealed the potential functional role of the identified cell by predicting its effect on the postsynaptic targets e.g. disinhibiting principal cells. Moreover, linking the network-state dependent activity of the identified medial septal cell to the known network-state dependent activity of the targeted cell type will extend our contemporary understanding of the functional role of the medial septum on a single cell level. Defining GABAergic medial septal cell types based on distinct behaviour-related activity and cortical innervation patterns provides insights into the range of cell types that contribute to the coordination of neuronal activity in the cortex.

I initially questioned whether distinct GABAergic cell types selectively target distinct cortical interneuron types in a spatio-temporal manner. As hypothesised, I found that cell groups with common unique physiological features share the same cortical innervation patterns. As described earlier, cells with common physiological features form a cell group

and further splitting them into sub-groups based on unique features lead to putative cell types like the *Teevra* and *Orchid* cells. Thus, the question is whether these putative cell types share the same unique anatomical features?

My results of 9 recorded and labelled HRNs (including my analysis of TV58g) show clear cortical target area preferences. While my labelled *Teevra* cells selectively targeted the hippocampal CA3 region (n=5, Figure 4-3, 4-4, Table 4-2), *Orchid* cells largely avoided the hippocampus to target extra-hippocampal areas including the presubiculum and entorhinal cortex (n=3, Figure 4-5. 4-6, Table 4-3). These results are consistent with the *Teevra* and *Orchid* groups published in Joshi et at. 2017 and Viney et al. 2018. In addition, to date, all additionally discovered putative *Komal* cells and 'non-*Orchid* cells' targeted extra-hippocampal cortical areas (*Chapter 3*, Table 3-1; n=6/6 cells).

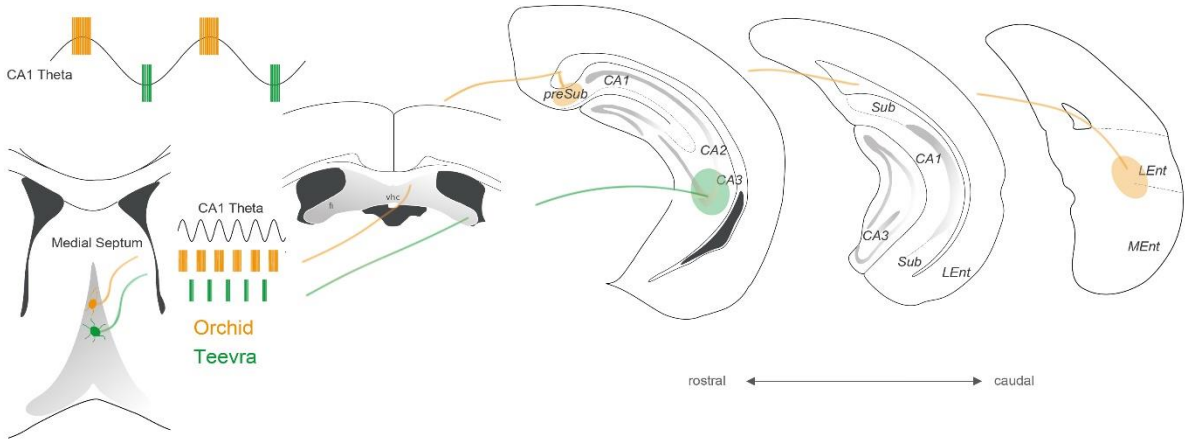


Figure 4-2 Schematic representation *Teevra* and *Orchid* cells.

Medial septal *Teevra* and *Orchid* cells projecting to distinct cortical areas share common physiological parameters as indicated by their phase coupling to CA1d theta oscillations (idealised schematic, 2 theta cycles) and innervation areas (orange: presubiculum and entorhinal cortex; green: CA3). Note the different burst lengths of the two groups (*Orchids*, orange; *Teevra*, green). Schematic coronal brain sections representing the rostral-caudal extent of the mouse brain at five different levels. Left, medial septum; middle, fimbria; right, hippocampus up to entorhinal cortex. *Orchid* cells; orange; *Teevra* cells; green.

4.2.4 Molecular profiles of identified *Teevra* and *Orchid* cells

The molecular profiles of all recorded and labelled somata were tested for their immunoreactivity to a specific set of molecules to firstly confirm their functional origin and secondly to test whether all HRNs have the same molecular profiles or not. I tested my labelled high-rhythmic cells for SATB1, PV, mGluR1α, VGAT, nNOS, ChAT, Calbindin and Calretinin. In addition, *Orchid* cells had further molecules tested such as NK1R, PCP4, SMI32, (Viney et al 2018). As *Orchid* cells were initially tested before *Teevra* cells, the list of molecules tested was increased until a conclusive set was selected (Table 4-4).

Orchid cells that I have tested were immunopositive for the calcium binding protein parvalbumin (PV, n =4/4 tested cells), the transcription factor SATB1 (n=3/4 tested), and mGluR1α in the somatic plasma membrane (n=3/4 tested), and their terminals were immunoreactive for VGAT (n=1/4 tested; Table 4-4). In addition, they lacked detectable immunoreactivity for calbindin (4/4 tested) and calretinin (3/4 tested). Teevra cells that I have tested were immunopositive for PV (n=3/5 tested), SATB1 (n=3/5 tested), but lacked detectable immunoreactivity for mGluR1α on the somatic plasma membrane (n=4/5 tested, Table 4-4). These results are consistent with the *Teevra* and *Orchid* groups published in Joshi et at. 2017 and Viney et al. 2018. Unfortunately, none of my labelled *Teevra* cells could be tested for VGAT at the axon terminals due to weak labelling. However, like *Orchid* cells, axon terminals of *Teevra* cells tested for VGAT at the target areas were immunopositive (n=4/4 tested, Joshi et al 2017). These results confirm the GABAergic origin of both subpopulations of the medial septum. In addition, note that both are PV+ and SATB1+. A differentiating feature is mGluR1α, which showed only positive immunoreactivity in *Orchid* cells.

Table 4-4 Immunohistochemical profiles of *Teevra* and *Orchid* cells.

Teevra cells	Cell name	MS31h	MS11b*	MS71c^{L}	MS73c^{L}	MS90g*
Immunoreactivity	Target Area	CA3^{L}	CA3^{L}	CA3^{L}	CA3^{L}	CA3/(CA1)^{R}
	PV	u	u	s+	s+	a+
	SATB1	u	u	n+	n+	n+
	mGluR1a	u	d-	s-	s-	s-
	VGAT	u	u	u	u	u

Orchid cells	Cell name	MS14i^{L}	MS19b^{L}	MS74b^{R}	TV58g^{R}
Immunoreactivity	Target Area	SUBd PrSd EC	SUBd PrSd EC	u	SUBd FC RSg AB PrSd EC
	PV	ds+	a+	a+	ad+
	SATB1	n+	n+	u	n+
	mGluR1a	d+	s+	u	d+
	VGAT	u	u	u	t+
	NK1R	u	s-	u	d-
	PCP4	ds+	u	u	d+
	SMI32	u	u	u	d+
	Calbindin	d-	ad-	a-	d-
	Calretinin	d-	ad-	u	d-
	ChAT	u	u	u	sd-
	nNOS	u	u	u	sd-

Table 4-4. Immunohistochemical profiles of *Teevra* and *Orchid* cells. Positive (+) or negative (-) immunoreactivity observed within subcellular domain: s, soma; n, nucleus; d, proximal dendrite; a, axon; t, axon terminals; u, unknown (unavailable or inconclusive). MS74b: soma was not recovered; dendrites were beaded indicative of a cell damaged during labelling. Granular retrosplenial cortex, RSg; dorsal subiculum, SUBd; dorsal presubiculum, PrSd; AB, angular bundle; entorhinal cortex, EC; fasciola cinereum, FC. Superscripts denote location of soma and axonal terminal in the right $^{(R)}$ or left $^{(L)}$ hemisphere.

4.2.5 GABAergic *Teevra* cells preferentially innervate axo-axonic cells in CA3

Based on their physiological parameters and molecular profiles, *Teevra* and *Orchid* cells comprise distinct neuron subpopulations of the medial septum. This raises the question whether the projection and innervation patterns of subpopulations also represent distinct cell types according to the previous physiological classification. It has been known that medial septal GABAergic neurons innervate all hippocampal regions and extra-hippocampal cortices (Freund and Antal, 1988; Unal *et al.*, 2015). However, it is not known whether single neurons innervate one or multiple cortical areas. I will firstly discuss the *Teevra* cells.

All *Teevra* cells I have identified projected septo-temporal to the hippocampus through the dorsal fornix or the fimbria (n=4/4, Table 4-4), either to the left or right hemisphere (Table 4-4). Across the septo-temporal axis, *Teevra* cells entered the hippocampus and preferentially innervated the CA3 region (Figure 4-2). I have not observed any terminals of my labelled cells in the DG and CA2 region. The main projection axon was observed in the CA3, including axonal branches with collaterals innervating a restricted area of the septo-temporal CA3 region. As terminals were not visible in fluorescence due to weak labelling, I used light microscopic methods such as DAB processing to visualise axon terminals in CA3 (Figure 4-3, 4-4). Note that no branches were observed in the retrosplenial cortex, subiculum, pre- and para-subiculum, or the entorhinal cortex. Thus, *Teevra* cells exclusively innervate one functional area of the hippocampus, the CA3 (Joshi *et al.*, 2017). Although technical limitations such as incomplete labelling attempts of *Teevra* cells could possibly lead to incomplete axonal visualisation, all cells with sufficient labelling strength showed the same innervation pattern. My observations are

consistent with all reported *Teevra* cells in Joshi et al 2017. Note, that in MS90g, a branch was observed in CA1.

Strongly labelled cells with visible boutons at the target area allow the testing of synaptic targets. One of my recorded *Teevra* cells (MS90g) was sufficiently labelled to be tested for targets. However, despite the good labelling, the labelling strength at the target area(s) was too weak to be identified in fluorescence. Nevertheless, after processing the section with DAB, I was able to identify axons and boutons of MS90g in CA3 due to the enhanced DAB signal. Thus, selected sections were reacted for immunohistochemistry and captured before being processed for DAB reaction. In total the molecular profiles of cellular targets of MS90g (n=6, Table 4-5, Figure 4-3, Figure 4-4) were tested. All target cells (n=6/6) of MS90g were PV+. Interestingly, all PV+ cells were lacking immunoreactivity for SATB1 (Table 4-5, Figure 4-3, Figure 4-4). These results provide a strong indication that MS90g target axo-axonic cells in CA3, consistent with other Teevra cells (Joshi *et al.*, 2017). Axo-axonic cells have been shown to be PV+ and SATB1- (Viney *et al.*, 2013). In addition, 4 targeted cells identified by Dr Abhilasha Joshi in CA3 were CCK+ interneurons and proven to lack PV, SATB1, somatostatin and calbindin (CB), indicating the molecular profile of CCK basket cells (Lasztoczi *et al.*, 2011). An estimation has shown that only 30% of all PV+ cells in CA3 are axo-axonic cells. The target profiles of MS90g match the rest of the *Teevra* group in Joshi et al 2017 which led to the conclusion that *Teevra* cells selectively target axo-axonic cells in CA3, including CCK+ cells.

Table 4-5 Subcortical and cortical synaptic target neurons of a *Teevra* cell, MS90g.

Cell ID	Target ID	Target Location	Domain	PV	SATB1	Endo-biotin	CCK	CB	SM
MS90g	s28_s1	CA3	s	s+	n-	s+	s-	u	u
	s29_s1	CA3	s	s+	n-	s+	s-	u	u
	s30_s1	CA3	s	s+	n-	s+	s-	u	u
	s30_s2	CA3	s	s+	n-	s+	s-	u	u
	s31_s2	CA3	sd	s+	n-	s+	s-	u	u
	s32_s1	CA3	s	s+	n-	s+	s-	u	u

Table 4-5. Subcortical and cortical synaptic target neurons of a *Teevra* cell, MS90g. Molecular expression profiles of postsynaptic neurons, based on close apposition of septal terminals. '+' detectable positive immunoreactivity or signal; '-' undetectable immunoreactivity or signal in vicinity of immunopositive signals observed within subcellular domain: s, soma; n, nucleus; d, dendrite; u, unknown.

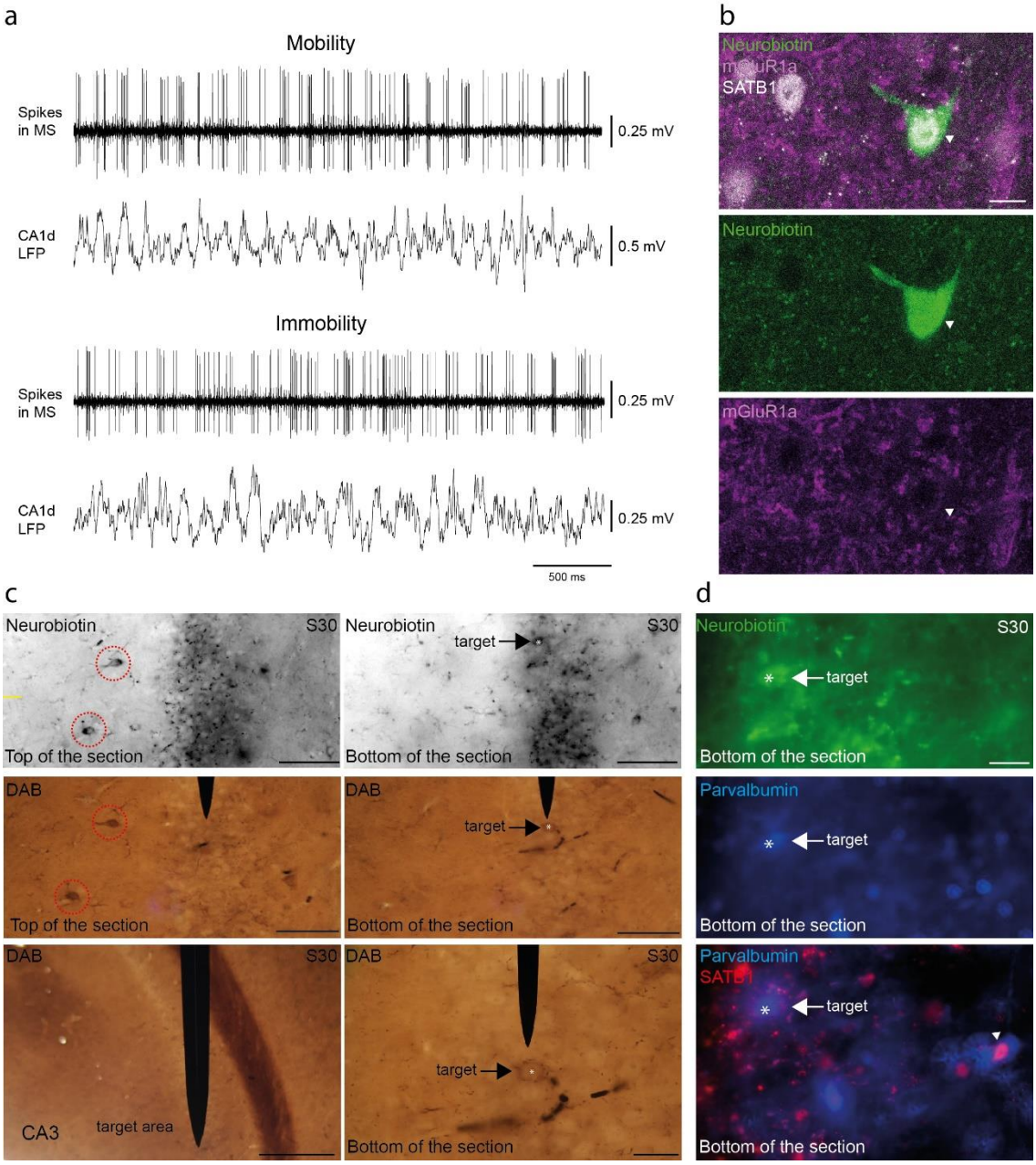

a
Mobility
Spikes in MS
0.25 mV
CA1d LFP
0.5 mV
Immobility
Spikes in MS
0.25 mV
CA1d LFP
0.25 mV
500 ms
b
Neurobiotin
mGluR1a
SATB1
Neurobiotin
mGluR1a
c
Neurobiotin
S30
Top of the section
Neurobiotin
target
S30
Bottom of the section
DAB
Top of the section
DAB
target
Bottom of the section
DAB
S30
CA3
target area
DAB
S30
target
Bottom of the section
d
Neurobiotin
S30
target
Bottom of the section
Parvalbumin
target
Bottom of the section
Parvalbumin
SATB1
target
Bottom of the section

Figure 4-3 Firing patterns, molecular profile, and CA3 target neurons of *Teevra* neuron MS90g.

a, Top, rhythmic short burst firing during locomotion. CA1d LFP in dorsal SP. Bottom, rhythmic short burst firing during immobility. **b**, Confocal image of MS90g soma in the medial septum. Streptavidin-Cy3 for neurobiotin (green), mGluR1a (magenta, somato-dendritc membrane) and SATB1 (white, nuclei) immunoreactivity. MS90g shows positive IR for SATB1 (arrowhead) and lacks detectable IR for mGluR1a. **c**, Top row, widefield fluorescence microscopic images of the target area of MS90g (asterisk) in CA3. Section 30 of 80 (S30) was captured at the top and bottom of the section (thickness: 70 μm). Middle row, same section (S30) after DAB processing captured at the top and bottom of the section showing the identical location shown in top row. Bottom row, DAB light microscopic images of the target area (left) and target neuron shown (asterisk) in **d**. Due to weak labelling I used this matching strategy to identify the target neuron in DAB to then match it to the previously captured fluorescence and IR images in **d**. **d**, Confocal image of an MS90g target (arrow, asterisk) in CA3 matched to the same fluorescence and DAB section from **c** (S30, asterisk). Streptavidin Cy3 (neurobiotin, green), Parvalbumin (blue) and SATB1 (red) immunoreactivity. Target of MS90g shows positive IR for PV (arrow) and is lacking detectable IR to SATB1 (arrow). Example of an SATB1 positive neuron is shown nearby (arrowhead). Scale bars: **b, d,** 50 μm; **c**, top, middle, 200 μm; bottom left, 100 μm, right, 50 μm.

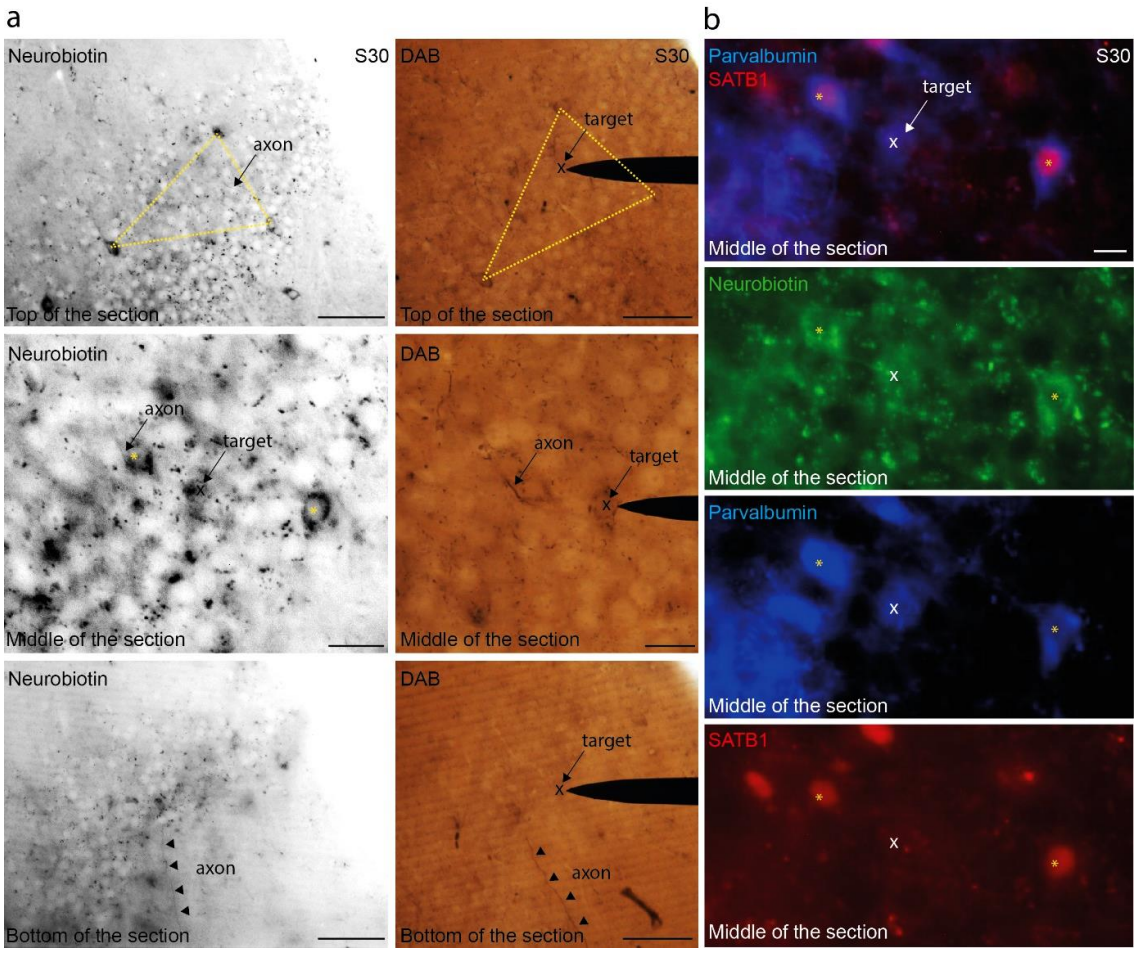


Figure 4-4 Identification of a target neuron of *Teevra* neuron MS90g in CA3.

a, Left column, fluorescence microscopic images of the target area of MS90g in CA3. A different region of section 30 (S30) to Figure 4-3 was captured at the top, middle and bottom of the section (thickness: 70 µm). Identified target neuron in **b** is shown in the middle section. Right column, same section (S30) after DAB processing captured at the top, middle and bottom of the section showing the identical location shown in the left column. Due to weak labelling of MS90g I used this 'matching' strategy to identify the target neuron in DAB to then match it to the previously captured fluorescence and IR images in **b**. **b**, Confocal image of an MS90g target (arrow, asterisk) in CA3 matched to the same fluorescence and DAB section from **a** (section 30). Streptavidin Cy3 (neurobiotin, green), Parvalbumin (blue) and SATB1 (red) immunoreactivity. Target of MS90g shows positive IR for PV (asterisk) and is lacking SATB1 (asterisk). Note the PV and SATB1 positive neurons (yellow asterisks) nearby, also to find in **a** (middle left) by the visible endogenous biotin (yellow asterisks). Scale bars: **a**, top (left and right) bottom (left and right), 200 µm; middle (left and right) 50 µm; **b**, 10 µm.

4.2.6 GABAergic *Orchid* cells project to multiple extra-hippocampal regions

After elucidating the area and postsynaptic selectivity of *Teevra* cells within the CA3, I next will report my observations of innervation patterns of the identified *Orchid* cells (Table 4-2, Table 4-4 and how this group of HRNs contrast to *Teevra* cells. All my recorded and labelled *Orchid* cells (n=4/4 including TV58g recorded by Dr Tim Viney) projected septo-temporally from the medial septum dorsally through the dorsal fornix to innervate select cortical areas. At the level of the dorsal fornix, *Orchid* cells primarily start innervating extra-hippocampal areas within the hippocampal formation. Interestingly, and this was the first time to observe such a phenomenon for single labelled neurons, the main projection axon did not end there but continued to project more caudal to reach the entorhinal cortex to branch out again (Figure 4-2, Figure 4-6a). Most of my cells (n=3/4) were sufficiently labelled to confirm innervation in the EC, based on observed axonal branches and terminals. Thus I am proposing the EC to be the main target area of *Orchid* cells. Outside the EC, most terminals were identified in the dorsal presubiculum (n=3/4, PrSd, Table 4-4, Figure 4-6a). However, across all cells reported in Viney et al. 2018, other innervation areas included also the retrosplenial cortex, dorsal subiculum, fasciola cinereum and angular bundle. In addition, I have not observed any branches in the hippocampus, except in one case, MS14i, where a collateral was observed in CA1. Thus, *Orchid* cells target multiple extra-hippocampal areas and, unlike *Teevra* cells, mostly avoid the hippocampus.

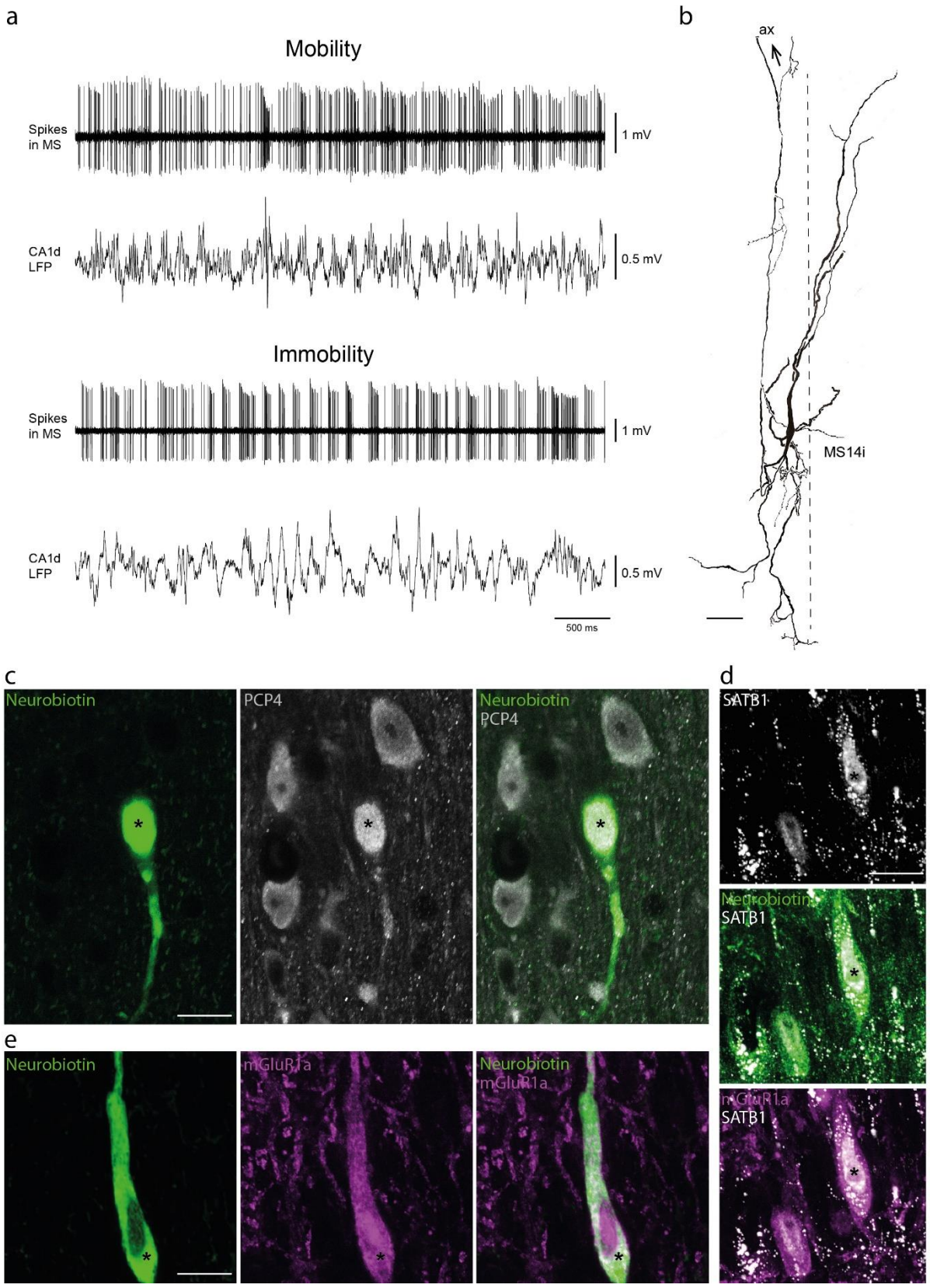

a
Mobility
Spikes in MS
1 mV
CA1d LFP
0.5 mV
Immobility
Spikes in MS
1 mV
CA1d LFP
0.5 mV
500 ms
b
ax
MS14i
c
Neurobiotin
PCP4
Neurobiotin
PCP4
d
SATB1
Neurobiotin
SATB1
mGluR1a
SATB1
e
Neurobiotin
mGluR1a
Neurobiotin
mGluR1a

Figure 4-5 Firing patterns and molecular profile of *Orchid* neuron MS14i projecting to the EC.

a, Top, rhythmic burst firing during locomotion. CA1d LFP in dorsal SP. Bottom, rhythmic burst firing during immobility. **b**, Reconstruction of MS14i soma in medial septum with support of Amar Sharma. **c**, Confocal image of streptavidin CY3 (green), PCP4 (grey) immunoreactivity of a cut soma of MS14i in the medial septum. MS14i shows positive IR for PCP4 (asterisk). **d-e**, Confocal image of the other half of the MS14i soma (different section). Streptavidin CY3 (green, neurobiotin), mGluR1a (magenta) and SATB1 (grey) immunoreactivity of a cut soma of MS14i in the medial septum. MS14i shows positive IR for mGluR1a (e, d, asterisk). and SATB1 (d, asterisk). Scale bars: b-e, 50 μm.

4.2.7 Preferential synaptic targets of *Orchid* cells

I have fully analyzed and reconstructed the first identified Orchid cell, recorded and labelled by Dr Tim Viney, TV58g (Figure 4-6) to elucidate its innervation pattern extra-hippocampally. This cell provided the initial insights of a multiple extra-hippocampal innervation pattern which could be linked to its behaviour-related firing activity (Figure 4-6b). Importantly, postsynaptic target analysis in extra-hippocampal areas gave me the primary insight of the target selectivity of *Orchid* cells. Like all *Orchid* cells, the main projection axon of TV58g projected dorsally along the midline of the medial septum to reach the dorsal fornix. At the beginning of the dorsal fornix the axon started branching to innervate the presubicular area of the hippocampal formation. Within the presubiculum, terminals were exclusively in presubicular layers 5-6, defined by differential calbindin immunoreactivity (41.6% of cortical varicosities); other cells additionally innervated more superficial layers (n = 5 cells). Further, I observed axon terminals at high density clustered in PrSd 'hot spots'. The SUBd was also innervated by 3 other cells (Table 4-4). The axon of TV58g subsequently extensively innervated caudo-dorsal EC (45.6% of cortical varicosities, Figure 4-6a) preferentially in layer 6. I have observed terminals from 4 other *Orchid* cells including AJ50 at a similar location (Table 4-4). In order to gain insight into the role of high-rhythmic GABAergic input from *Orchid* cells to cortical circuits, I followed the collaterals of TV58g to synaptic targets at the innervated area. I identified 13 targeted cells in different brain sections mainly in the dorsal presubiculum by using a different set of molecular markers using confocal microscopy. Further, electron microscopy images (Figure 4-6e) performed by Prof. Peter Somogyi and Kristina Wagner in the laboratory were used to test the reliability of predicting synaptic connections from light microscopy. The dorsal presubiculum starts approximately at the point where the CA1 pyramidal cell layer is tapering out, identifiable

by the absence of the stratum oriens. Figure 4-6d and Figure 4-7a show examples of innervated cells within the PrSd and layer 6 of RSg surrounded by many boutons of the labelled cell.

By using a carefully chosen and tested selection of molecular markers, I identified different putative targeted postsynaptic neuronal profiles, based on the combination of molecular markers within the dorsal presubiculum and axonal boutons originating from TV58g apposed to somato-dendritic locations, confirmed by confocal microscopy (Figure 4-6). All identified cells were targeted by the same axonal branch of TV58g. Most of the selected markers were studied in detail in rat hippocampus (Somogyi and Klausberger, 2005), hence, less is known about the different cell types within the dorsal presubiculum. Unlike in the CA1-CA3 regions where for instance axo-axonic cells (AACs) lack detectable SATB1 immunoreactivity (Viney et al., 2013), all identified cells in the presubiculum so far were SATB1 positive. Interestingly, some PV positive cells in the presubiculum showed positive immunoreactivity for neuronal nitric oxide synthase (nNOS), which is shown to be lacking in PV positive cells in the hippocampus except a small portion in the hilus of the dentate gyrus (Jinno and Kosaka, 2002). However, the co-expression of PV and nNOS was shown before to exist in the mouse cortex (Perrenoud *et al.*, 2012).

To characterize the molecular pattern of the selected targets, I used up to seven molecular markers on a single section (example TV58g, section 44, Figure 4-6d). As there are only four spectrally-distinct secondary antibody-conjugated fluorophores available, I took advantage of the different subcellular localization of each antibody to use the same secondary antibody for more than one molecular marker. Thus, in case the immunoreactivity was negative I was able to use the same channel again for another primary antibody. Some markers are so abundant, e.g. PV, thus, adding an addtional

antibody on top of it would not work, because all new primary antibodies would bind to the abundant PV secondary. Thus, I selected ‘rare’ or ‘less likely’ primaries such as CCK before testing for calcium-binding proteins. Thus, I sequentially tested the targeted cells for NPY, CCK, SATB1, mGlur1α, calbindin (CB), nNOS and PV. All markers were previously tested on control mouse brain sections. The immunoreactivity for CCK, SATB1, mGlur1α, calbindin, nNOS and PV immunoreactivity was tested consistently in all three sections.

In the dorsal presubiculum, I tested targets (5/5) of TV58g which were PV+ and 3/7 tested were nNOS+ interneurons, including 1 PV+ cell (Table 4-6). In the electron microscopic study by Prof Peter Somogyi, all 11 tested boutons formed synapses with interneurons; 6 (55%) of them dendrites (Figure 4-6ei,ii), and 5 somata (Figure 4-6eiii), including a PV+/SATB1+/mGluR1a+ interneuron (Figure 4-6d) receiving 4 synapses (Figure 4-6ei). I observed that somata and proximal dendrites of GABAergic interneurons received an extensive innervation. Moreover, targets in three regions (PrSd, RSg and FC) were SATB1+ (n=13/13; Table 4-6), but CCK– (n=0/10, Table 4-6). Nearby interneurons with different molecular profiles were not targeted, indicating target selectively of TV58g. Further 4 *Orchid* cells had axon terminals apposed to some cortical neurons with high levels of endogenous biotin (Table 4-6), suggesting that these are interneurons with high metabolic activity, such as ‘fast spiking’ neurons. These data suggest that GABAergic PV+ *Orchid* cells influence extra-hippocampal regions, via rhythmic modulation of distinct cortical GABAergic interneurons. To conclude, based on the shared cortical target regions, similarity in rhythmic burst firing patterns, strong theta coupling, overlapping molecule profiles, and the resemblance of the axon to Phalaenopsis orchids (Figure 4-6a), these GABAergic PV+ neurons were named *Orchid* cells (Salib, 2015; Viney *et al.*, 2018).

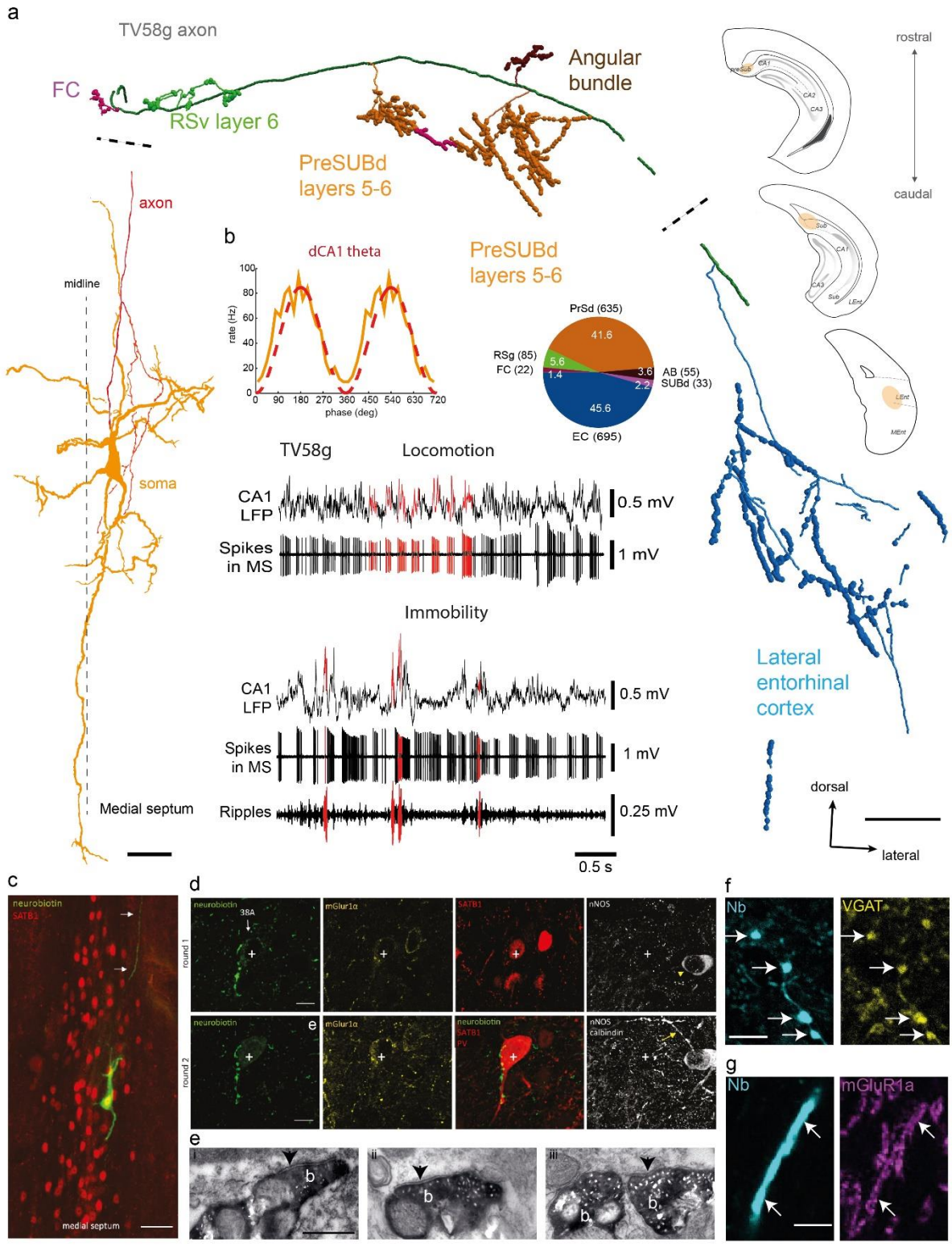

a
TV58g axon
FC
RSv layer 6
Angular bundle
PreSUBd layers 5-6
axon
midline
soma
Medial septum
rostral
caudal
b
dCA1 theta
rate (Hz)
phase (deg)
PreSUBd layers 5-6
PrSd (635)
41.6
RSg (85)
FC (22)
5.6
1.4
3.6
2.2
AB (55)
SUBd (33)
45.6
EC (695)
TV58g
Locomotion
CA1 LFP
0.5 mV
Spikes in MS
1 mV
Immobility
CA1 LFP
0.5 mV
Spikes in MS
1 mV
Ripples
0.25 mV
0.5 s
Lateral entorhinal cortex
dorsal
lateral
c
neurobiotin
SATB1
medial septum
d
neurobiotin
38A
mGlur1α
SATB1
nNOS
round 1
round 2
calbindin
PV
e
i
ii
iii
b
f
Nb
VGAT
g
Nb
mGluR1a

Figure 4-6 Firing patterns, 3D reconstruction and cortical target regions of a GABAergic medial septal *Orchid* cell (TV58g).

a, Reconstruction of part of the axon of neuron TV58g axon (cortical regions color-coded). Black dashed line, rostral (left) and caudal (right) innervation zones. Pie chart, number (parentheses) and proportion (%) of axonal varicosities. Projection axon enters the cortex via the dorsal fornix (left, black dashed line). left, reconstruction of the soma and dendrites (orange) and axon (red) of TV58g in the tip of dorsal MS. Black dashed line, midline. Local axon collateral in red. Right, schematic coronal mouse brain sections visualizing the target areas of TV58g. **b,** Top, rhythmic burst firing during locomotion. CA1 LFP, local field potential in SP. Red, examples of detected peaks of CA1 theta oscillations and associated MS neuron spikes. Note preferential coupling of bursts to theta peak. Bottom, rhythmic burst firing during immobility with some spikes during some SWRs (red; ripples, 130-230 Hz filtered CA1 LFP). **c**, Anatomical localization the soma of TV58g in the medial septum was SATB1+ (red, nuclei) and PV+ (not shown), neurobiotin in green. **d,** Confocal standard deviation projection (36-38 optical sections, 11.96 - 14.89 μm-thick z-stack) of streptavidin CY3 (green,), SATB1 (red), nNOS (grey) and mGlur1α (yellow) immunoreactivity. Targeted cell shows positive IR for SATB1 and mGlur1α (cross on targeted cell) and negative immunoreactivity for nNOS (yellow w arrowhead). PV antibody was added after imaging SATB1 immunoreactivity using the same primary antibody host and same secondary dye Alexa488. Targeted cell of TV58g shows positive IR for PV. Calbindin antibody was added after imaging nNOS immunoreactivity using the same primary antibody host and same secondary dye Alexa647 (arrow). Targeted cell of TV58g shows negative IR for calbindin. **e,** Electron micrographs of synapses (arrows) made by boutons (b) of TV58g on interneurons in the PrSd with the proximal dendrite of a PV+ cell (i, b11 in **d**), (ii) the dendrite of an unknown interneuron and (iii) soma of another interneuron. **f**, Presubicular terminals of TV58g (cyan) were VGAT+ (yellow, arrows). **g,** Dendrites of TV58g (cyan) were mGluR1a+ (magenta, arrows). Nb, neurobiotin. FC, fasciola cinereum, AB, angular bundle, LS, lateral septum, vDB, vertical diagonal band. Images (z-thickness in μm and z-projection type): **f,** 2.61, maximum, **g,** 0.37, single optical section. Scale bars (μm): **a,** 500, **c**, 50, **d**, 10, **e,** 0.5 (applies to *i/ii/iii*), **f**, **g**, 5, inset, 500, soma, 10. Data in **c**, **d**, **f**, **g** obtained during my MSc Thesis (Salib, 2015). **e**, images taken by Professor Peter Somogyi and Kristina Wagner.

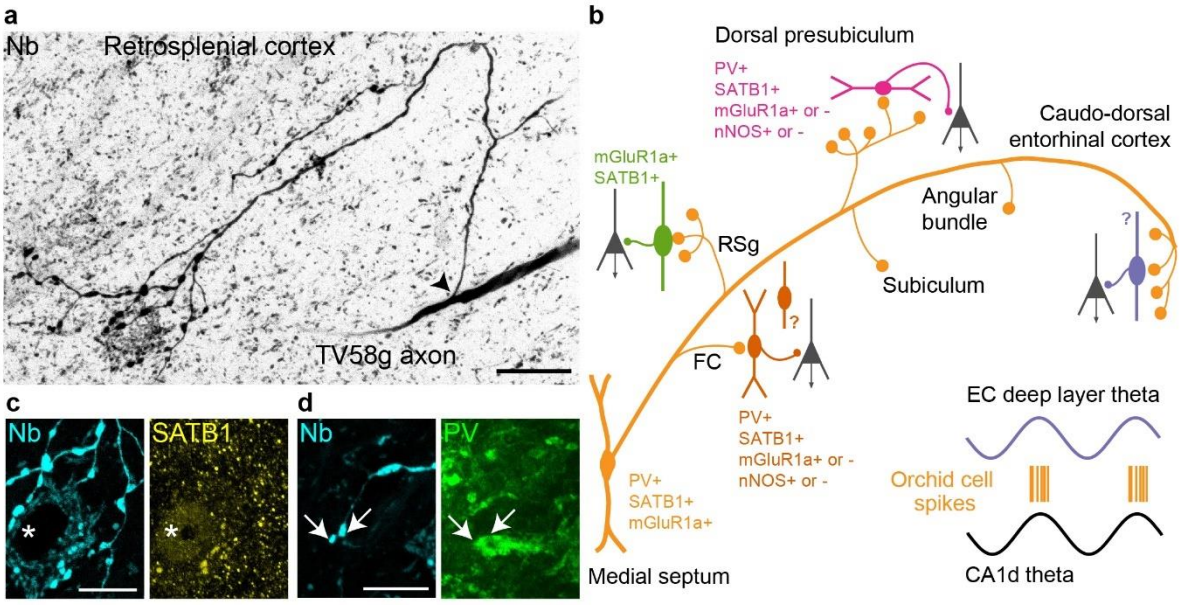


Figure 4-7 Postsynaptic GABAergic target neurons of *Orchid* cell, TV58g.

a, Main axon and collateral (arrow, branch point) of TV58g along with terminals surrounding a neuron in layer 6 of RSg (reverse contrast, confocal microscopic image). The target neuron contains a high level of endogenous biotin (high background), revealed by the streptavidin-conjugated fluorophore signal. **b**, Schematic summary of the data presented in Figure 4-5 and Table 4-4. Immunoreactivity of synaptic target neurons is color-coded based on innervated cortical region. Bottom right, two idealized theta cycles with representative *Orchid* cell spike bursts at the peak of CA1d theta and EC theta. **c,** The target neuron soma (asterisk) innervated by multiple terminals (cyan) from **a** showed nuclear immunoreactivity for SATB1 (yellow). **d,** The dendrite of the target showed positive immunoreactivity for PV (green); arrows highlight two terminals in close apposition**.** Nb, neurobiotin**.** Images (z-thickness in µm and z-projection type): **a**, 22.09 standard deviation, **c,** 2.8 maximum, **d,** 2.88 maximum. Scale bars: **a,** 20 µm, **c,d,** 10 µm. Data modified from Viney et. al, 2018.

Table 4-6 Cortical target neurons of *Orchid* cell TV58g.

Target ID	Location	PV	SATB1	mGluR1a	Endobiotin	CCK	CB	nNOS
S45A	FC	–	+	+	–	–	–	–
S45B		u	+	u	–	–	u	–
S45D		+	+	–	+	–	–	+
S45G		+	+	–	+	–	–	+
S44A	RSg L6	–	+	+	–	–	–	–
S44B		u	+	u	–	–	u	–
S38A	PrSd L5-6	+	+	+	+	–	–	–
S38C		+	+	u	+	–	–	–
S38I		u	+	+	(+)	–	u	+
S38J		u	+	u	–	–	+	+
S36A		+	+	u	+	u	u	u
S34A		+	+	u	+	u	u	–
S34C		+	+	–	(+)	u	u	+
Total +		**7**	**13**	**4**	**8**	**0**	**1**	**5**

Table 4-6. Cortical target neurons of *Orchid* cell TV58g. Molecular profiles of presumed postsynaptic neurons, based on close apposition of septal terminals; +, detectable positive immunoreactivity or signal; –, undetectable immunoreactivity or signal in vicinity of immunopositive signals; u, unknown (unavailable or inconclusive). Parentheses indicate weak immunoreactivity or signal. Endobiotin, endogenous biotin (detected with streptavidin-conjugated fluorophore) may indicate high metabolic activity due to a high density of mitochondria, such as in “fast spiking” neurons. Data extended from (Salib, 2015; Viney *et al.*, 2018).

4.2.8 Medial septal neurons projecting to the entorhinal cortex

Once the *Orchid* cell groups were identified to project to the PrSd and EC, I next quantified the medial septal population projecting to the EC and asked whether other medial septal cell types project to extra-hippocampal areas. Therefore, I injected a monosynaptically-restricted retrograde viral tracer, PRV-hSyn-Cre (Oyibo *et al.*, 2014), into the caudo-dorsal EC and a Cre-dependent adeno-associated virus encoding EYFP into the MSDB. The PRV-hSyn-Cre virus, a mutant pseudorabies virus of the alpha-herpesvirus subfamily, is non-cytotoxic and highly tropic, resulting in Cre expression only in neurons that directly project to the injection site. After ≥2 weeks of incubation, strong Cre-dependent EYFP expression in neurons was mainly in the rostral part of the dorsal medial septum, representing 60.5% of the retrogradely-labelled neurons (n = 129 cells from six mice; mean ± s.d. 21.5 ± 11.7 total EYFP+ neurons/mouse, Viney et al 2018). Within the EC, virally labelled medial septal neurons with extensive terminals were observed in all layers of the EC (n=4 mice). Like *Orchid* cells, EC-projecting axons also gave dense collaterals in other extra-hippocampal regions where they formed terminals. As reported in Viney et. al 2018, the distribution of axonal collaterals in hippocampal and extra-hippocampal cortical regions was quantified. The proportion of axonal branches in the dorsal presubiculum and granular retrosplenial cortex (median: 37%) was substantially greater than in CA1, the dentate gyrus and the dorsal subiculum (SUBd) (median: 5%), where only rare axonal collaterals were observed**.** These confirm the results from the *Orchid* cells that a large subpopulation of GABAergic EC-projecting MSDB neurons innervate other extra-hippocampal areas, primarily the PrSd and RSg (Viney *et al.*, 2018).

Interestingly, not all EC projecting MSDB neurons shared the same molecular profiles of PV+/SATB1+/mGluR1a+ as *Orchid* cells. Thus, within the MS, 21.0% of EC-projecting

(EYFP+) neurons were triple immunopositive for PV, SATB1, and mGluR1a, while 37.1% showed no detectable signal for these 3 molecules (n=62 tested neurons, 6 mice, Viney et al., 2018). These data match with my data presented in *Chapter 3*, where the 8 identified extra-hippocampal projecting medial septal neurons might account for the rest of the population targeting the EC. Moreover, neurons found nearby as PV+/SATB1+/mGluR1a– did not project to the EC, consistent with the profile of CA3-projecting *Teevra* cells (Joshi *et al.*, 2017). Only 2/13 of the EYFP+ neurons were ChAT+/PV–/mGluR1a–, 1/13 was only mGluR1a+, and 10/13 lacked detectable immunoreactivity (ChAT–/PV–/mGluR1a–). Most likely, the PV– and ChAT– MSDB neurons comprise both GABAergic and glutamatergic EC-projecting neurons (Gonzalez-Sulser *et al.*, 2014; Fuchs *et al.*, 2016; Justus *et al.*, 2017; Viney *et al.*, 2018).

4.3 Discussion

In this chapter I have introduced two subpopulations of high-rhythmic firing medial septal neurons targeting specific cortical areas with distinct spike trains and molecular profiles, the *Teevra* and *Orchid* cells.

I have recorded, labelled and analyzed 8 HRNs that match the *Teevra* and *Orchid* cells reported in Joshi et al 2017 and Viney et al 2018. Further, I have shown that both are distinct cell types based and their physiological parameters, molecular profiles, cortical target areas and post-synaptic target selectivity. *Orchid* cells represent a high-rhythmic firing medial septal GABAergic population of PV+/SATB1+/mGluR1a+ neurons with a strong coupling to the peak of CA1d theta oscillations, high burst incidence and long burst durations during both locomotion and immobility, that specifically target GABAergic cells in multiple extra-hippocampal areas but mainly the presubiculum and entorhinal cortex. *Teevra* cells represent a high-rhythmic firing medial septal GABAergic population of PV+/SATB1+/mGluR1a- neurons with a strong coupling to the trough of CA1d theta oscillations, high burst incidence and short burst durations during both locomotion and immobility, that specifically target axo-axonic and CCK+ interneurons in CA3.

4.3.1 *Orchid* cells are a subpopulation of *Komal* neurons

Initially, four major clusters of highly rhythmic medial septal neurons were defined (Joshi *et al.*, 2017). The *Teevra* cell cluster had short burst durations during locomotion and did not significantly change their mean firing rate between locomotion and rest periods, whereas the *Komal* cell cluster had long burst durations and increased their firing during locomotion compared to rest periods. Juxtacellular labelling of medial septal cells with

firing properties of both clusters revealed that (1) *Teevra* cells targeted CA3 but no extra-hippocampal areas, and (2) Komal cells targeted multiple extra-hippocampal areas but not the hippocampus. These CA3-projecting neurons preferentially fired at the trough of CA1d theta oscillations. *Komal* cells preferentially fired around the peak of CA1d theta oscillations. In contrast to *Teevra* cells, rhythmically bursting *Komal* cells increase firing during locomotion, have long duration bursts, fire preferentially at the peak of CA1d theta oscillations, and innervate the PrSd and EC. Thus, it seems likely that *Orchid* cells represent a distinct subpopulation of *Komal* cells defined by their theta phase firing preferences and synaptic target regions. Another subpopulation of *Komal* cells preferentially fire at the theta trough (Joshi *et al.*, 2017; Viney *et al.*, 2018) remain to be defined using juxtacellular labelling in awake animals, as I have focussed on theta peak firing cells. Interestingly, the 'unclassified' population I have reported in *Chapter 3* comprised up five high-rhythmic firing medial septal neurons projecting to extra-hippocampal areas such as the EC, including MS112l that preferentially fired during the trough of CA1d theta oscillations and was strongly inhibited during SWRs (Table 3-1, *Chapter 3*). Although they differ in their target areas this shows the potential for other Komal-type neurons in additional to *Orchid* cells. Nevertheless, studies have shown that a large proportion of MSDB projections target extra-hippocampal areas, including the EC (Jeffery *et al.*, 1995; Gonzalez-Sulser *et al.*, 2014; Unal *et al.*, 2015; Fuchs *et al.*, 2016; Justus *et al.*, 2017; Viney *et al.*, 2018). However, the virus tracing study (Viney et al 2018) has revealed that only 21% of the EC projecting MS neurons share the molecular profiles of *Orchid* cells. Within the MS, neurons with a molecular profile of PV+/SATB1+/mGluR1a+ and PV+/SATB1+/mGluR1a- compromised only <7% of the total septal population (Viney *et al.*, 2018). The cellular organization of these circuits may be more diverse than previously anticipated, as identities of neurons within the other

groups of the cluster in Joshi et al 2017, and with different cortical projecting and molecular profiles remain to be determined.

4.3.2 *Orchid* cells modulate the firing dynamic of spatially-modulated neurons

The shared extra-hippocampal target regions of single *Orchid* cells demonstrate that *Orchid* cells provide strong GABAergic input to presubicular, retrosplenial, and entorhinal interneurons at the peak of CA1d/EC theta cycles during locomotion (Viney *et al.*, 2018). Spatially-modulated neurons such as 'head-direction cells' were discovered by recording neurons in the presubiculum of freely moving rats (Taube, Muller and Ranck, 1990; Brandon *et al.*, 2013), while 'grid cells' and 'border cells' were characterised in the entorhinal cortex (Hafting *et al.*, 2005; Solstad, 2008). Thus, as described earlier, a wide network of different cell types with key spatial-related roles exists within the temporal cortex. Hence, a multi-area innervation e.g. extra hippocampal areas by medial septal cells is likely to support the firing dynamics of spatially-modulated neurons, including grid cells, which lose their spatial periodicity upon MS inactivation (Brandon *et al.*, 2013). As *Orchid* cells are most rhythmic and phase-modulated during CA1d/EC theta oscillation it raises the question about the postsynaptic effect of *Orchid* cells within the targeted areas. A model suggested that the theta rhythm allows the hippocampal formation to alternate rapidly between conditions that promote memory encoding, and conditions that promote memory retrieval (Hasselmo, Bodelón and Wyble, 2002). Memory encoding involves strong synaptic input from entorhinal cortex to areas CA3 and CA1 while memory retrieval relies on strong synaptic input from CA3 to CA1 (Hasselmo, Bodelón and Wyble, 2002). That model predicted that the preferred theta phase of CA1 spiking should differ for information being encoded versus information

being retrieved. Further, encoding of information takes place preferentially at the theta peak (Manns *et al.*, 2007), coincident with the preferential firing of layer 3 EC principal neurons that project to CA1d (Mizuseki *et al.*, 2009). Therefore, disinhibition of EC glutamatergic neurons by *Orchid* cells around the theta peak may facilitate the transfer of temporal sequences relating to navigation to the hippocampus (Koenig *et al.*, 2011; Schlesiger *et al.*, 2015).

4.3.3 *Orchid* cells support indirect rhythmic coordination of CA1 pyramidal cell assemblies

Orchid cells target cortical neurons, including PV+ and nNOS+ neurons (Viney *et al.*, 2018). Previous studies have shown that cortical PV+ neurons are considered to be 'fast spiking' basket and axo-axonic cells, and display rhythmic modulation at theta frequency (Preston-Ferrer *et al.*, 2016). Within the dorsal presubiculum, some PV+ neurons are immunopositive for nNOS, which is also expressed by other interneuronal types. Unlike the hippocampus, the *in vivo* firing patterns of interneurons in those regions including the FC, SUB and RSg are unknown (Henriksen *et al.*, 2010) except for 'theta' cells recorded in the vicinity of PrSd head direction cells (Taube, Muller and Ranck, 1990; Preston-Ferrer *et al.*, 2016). However, 'fast spiking' neurons recorded in more caudal regions of PrS do not show strong theta modulation (Tukker *et al.*, 2015), suggesting a topographical change in theta modulation across the PrS. Like the work done by (Klausberger and Somogyi, 2008) on CA1 interneurons, visualization of interneuron axon terminals in extra-hippocampal areas is required to define their target cortical layers as well as their target subcellular domains on postsynaptic principal cells. However, based on the high density of GABAergic MSDB terminals around somata and dendrites of PV+ cells in PrSd, I hypothesize that postsynaptic targets of *Orchid* cells will be strongly theta

modulated, supporting the rhythmic coordination of pyramidal cell assemblies. Thus, Orchid cells are the first to describe specialized subcortical GABAergic input to specific extra-hippocampal regions that are functionally-related and converge to the caudo-dorsal EC. Their movement-related theta-rhythmic burst firing, and similarly strong rhythmic bursting during immobility, likely serve as a mechanism - via target interneurons - for the temporal coordination of cortico-cortical neurons. These cortico-cortical principal neurons project from 'upstream' areas (PrSd) to 'downstream' areas (RSg, EC) forming transient assemblies involved in mnemonic processes representing sequential information, such as routes of navigation.

4.3.4 *Teevra* cells enable CA3 pyramidal cell activation via disinhibition

Unlike *Orchid* cells, *Teevra* cells' targeted area, the CA3, is well studied. Their selective termination in restricted spatial domains along the septo-temporal axis of CA3, largely avoiding other hippocampal areas is remarkable and, as discussed above, a major differentiator compared to *Orchid* cells. Postsynaptic target analysis revealed an unexpected sophistication in the spatio-temporal organization of septo-hippocampal projection. Based on the molecular profiles of targeted cells in CA3, *Teevra* cells most likely specialise in innervating CA3 interneurons, such as axo-axonic cells and CCK basket cells (Lasztoczi *et al.*, 2011; Somogyi *et al.*, 2014). Both interneurons types preferentially fire around the peak of CA1 theta oscillations.

Pyramidal cells are known to fire at the highest rate during the trough of CA1 theta oscillations in anesthetized rats (Lasztoczi *et al.*, 2011). In anaesthetised rats, identified axo-axonic cells in CA3 fired bursts of action potentials at the peak of CA1d theta oscillations (Viney *et al.*, 2013; Varga *et al.*, 2014). Moreover, axo-axonic cells exclusively innervate the axon initial segment of pyramidal neurons, which is particularly

well developed in CA3 with up to 150 synapses on a single axon initial segment (Kosaka, 1980). $GABA_A$ receptors mediate where the action potential is generated (Buhl *et al.*, 1994) with fast inhibitory postsynaptic currents in their synaptic targets (Ganter *et al.*, 2004). Not only that, axo-axonic cells form synapses with several hundred pyramidal cells at the site where their rhythmic input does not have to be integrated with other inputs on the soma and dendrites. Since one axo-axonic cell would influence a large number of pyramidal cells in the same way, they are likely to have a crucial role in rhythmic activity in the hippocampus (Somogyi *et al.*, 1983). Consequently, the subcortical inhibitory input to axo-axonic cells at the trough of theta oscillation would lead to the disinhibition of CA3 pyramidal cell assemblies (Katalin Tóth, Freund and Miles, 1997). As a result, this will drive pyramidal cell firing in CA1 at the trough of theta in the pyramidal layer.

Nevertheless, not all subcortical inputs to axo-axonic cells are *Teevra* cells. I have recorded and labelled one medial septal neuron, MS94h, targeting axo-axonic neurons in CA3 with a very low rhythmicity index (RI = 0.06) compared to *Teevra* cells. Due to labelling difficulties the identified cell cannot be matched confidently to the recovered soma. However, despite a very weak coupling to theta oscillation (r = 0.13) the preferred firing phase is during the trough of theta oscillations. All other firing properties match the profile of *Teevra* cells. Even the molecular profile matches as it is immunopositive for SATB1 and lacking mGluR1a. Such a cell, if correctly linked to the recorded physiology, might play a variable modulatory role in parallel to *Teevra* cells. The second targeted interneuron type by *Teevra* cells, CCK+ cells, which may be basket cells, also fire action potentials at around the peak of CA1 theta oscillations (Lasztoczi *et al.*, 2011). The temporally coordinated circuit during retrieval of stored contextual associations around the theta trough (Hasselmo, Bodelón and Wyble, 2002) may be provided by *Teevra* cells through disinhibition by enabling the CA3 pyramidal cell output to

contribute to temporal coding in the CA1 ensemble (Middleton and McHugh, 2016; Fernández-Ruiz *et al.*, 2017). The coordination proposed for *Teevra* and *Orchid* cells may be the crucial input for mediating theta oscillatory activity in CA1 (Winson, 1978) as inactivating this input through the medial septum affects theta oscillation in CA1 and leads to impairment in memory (Chrobak, Stackman and Walsh, 1989; McNaughton, Ruan and Woodnorth, 2006). Thus, based on the discussed results, both the *Teevra* and *Orchid* cells likely modulate and coordinate the timing of converging glutamatergic inputs to CA1; *Teevra* cells act through modulating CA3 and *Orchid* cells through modulating the EC input to CA1.

Chapter 5

GABAergic medial septal neurons with low-rhythmic firing innervating the dentate gyrus and hippocampal area CA3

5.1 Introduction

In the previous chapter, I presented data on two distinct high-rhythmic medial septal cell groups (HRNs), the *Teevra* and *Orchid* cells. HRNs account for a high portion of the medial septal GABAergic cell population, and make up almost half of the recorded medial septal population using acute silicon probe recordings (Joshi *et al.*, 2017). Almost half of the recorded medial septal population shown by Joshi *et al.*, 2017 had a rhythmicity index (RI) above the defined cut-off for high and low rhythmicity. The distinguishable firing pattern of HRNs, especially compared to the lateral septal cells (Stewart and Fox, 1990), is a signature characteristic of the medial septum. Therefore, high rhythmic neurons were to date the most prominent neurons studied in the medial septum, giving the medial septum its suggested functional role as a 'pacemaker', particularly in shaping and coordinating cortical oscillations (Brücke *et al.*, 1959; Wang, 2002; Varga *et al.*, 2008; Hangya *et al.*, 2009). Supporting studies showed a marked reduction in cortical theta power by disrupting the MSDB (Jeffery *et al.*, 1995). In addition, these disruptions affected the spatial firing fields of entorhinal grid cells and hippocampal place cell sequences, causing deficits in spatial memory (Leutgeb and Mizumori, 1999; McNaughton, Ruan and Woodnorth, 2006; Brandon *et al.*, 2011, 2014; Wang *et al.*, 2015; Zutshi *et al.*, 2018). The importance of high rhythmic firing neurons in the MSDB raises the question about the functional role of the rest of the medial septal population, especially considering distinct cortical projections to the hippocampal formation, and GABAergic, cholinergic and glutamatergic classes of neurons within the medial septum (Kimura *et al.*, 1980; Köhler, Chan-Palay and Wu, 1984; Freund, 1989; Hajszan, Alreja and Leranth, 2004; Colom *et al.*, 2005).

Teevra cells are the most rhythmic subpopulation of mouse MSDB neurons, providing selective GABAergic input to axo-axonic cells and cholecystokinin-immunopositive GABAergic neurons in hippocampal CA3 (Joshi *et al.*, 2017; Salib, DPhil thesis 2019). In contrast,

rhythmically bursting GABAergic *Orchid* cells avoid the hippocampus and project mainly to the dorsal presubiculum and caudo-dorsal entorhinal cortex (Viney *et al.*, 2018; Salib, DPhil thesis 2019. Because rhythmicity facilitates neuronal coordination in cognition, these two kinds of high-rhythmic PV+ MSDB neurons are likely to be major contributors to the coordination of neuronal activity within and across these regions.

In rodents, CA3 principal cells preferentially fire on the descending phase of theta recorded in dorsal CA1 (CA1d) stratum pyramidale (Mizuseki *et al.*, 2009). As *Teevra* cells preferentially fire at the CA1d theta trough, and axo-axonic cells at the peak (Viney *et al.*, 2013; Joshi *et al.*, 2017), CA3 principal cells are effectively disinhibited on the descending/trough phase of each cycle. Furthermore, axo-axonic cells reduce their firing during sharp-wave associated ripple oscillations (SWRs) (Viney *et al.*, 2013), disinhibiting pyramidal cell axon initial segments, which was originally proposed as a mechanism for SWR initiation (Buzsáki, 1986).

Dentate gyrus (DG) principal cells, and hippocampal granule and mossy cells, also fire preferentially on the descending phase of theta (Mizuseki *et al.*, 2009; Lasztóczi and Klausberger, 2017; Senzai and Buzsáki, 2017), and are modulated during SWRs (Penttonen *et al.*, 1998). Intriguingly, both the *Teevra* cells and *Orchid* cells avoid the DG, an area that also receives dense innervation from the MSDB (Freund and Antal, 1988), but the firing dynamics of these afferents are unknown (Bao *et al.*, 2017). In addition to CA3 pyramidal neurons (Li *et al.*, 1994), local GABAergic interneurons (Han *et al.*, 1993; Szabo *et al.*, 2017) and SWR-suppressed MSDB neurons (Unal *et al.*, 2018) provide shared input to the DG and CA3. The MSDB also receives GABAergic input from the DG and hippocampus (Tóth, Borhegyi and Freund, 1993; Jinno *et al.*, 2007; Mattis *et al.*, 2014; Yuan *et al.*, 2017), which may contribute to septo-hippocampal coordination (Wang, 2002).

In this chapter I extend our contemporary understanding of the MSDB population by shedding light on a large group of low-rhythmic firing cortical projecting MSDB neurons (LRNs). In comparison with in *Chapter 4* discussed high-rhythmic neurons (HRNs), the *Teevra* and *Orchid* neurons, I further investigated whether LRNs contribute to septo-cortical circuits in parallel with HRNs, by extracellularly recording them in awake mice followed by juxtacellular labelling to reveal their target regions and target neurons. Therefore, by extracellularly recording LRNs in awake mice followed by juxtacellular labelling, I could address whether LRNs are GABAergic, innervate similar or different cortical regions compared to HRNs in addition to their different behaviour-related firing patterns. Thus, considering these different firing patterns I hypothesized that LRNs project to cortical regions that are distinct from those innervated by the previously defined HRNs (Joshi *et al.*, 2017; Viney *et al.*, 2018) and/or LRNs have different postsynaptic targets from those of high-rhythmic neurons. These data were also reported in (Salib *et al.*, 2019).

5.2 Results

5.2.1 Identifying low-rhythmic medial septal neurons

In the previous chapters I discussed the diversity of medial septal neurons encountered by extracellularly recording single MSDB neurons in awake head-restrained mice followed by juxtacellular labelling. Although the head-restrained condition limits the behavioural correlation to the firing patterns of single neurons to a certain extent, it does enable an in-depth analysis of the axonal projections as well as the molecular identification of a single neuron. However, to distinguish and classify neurons at a first instance based on their firing patterns I wanted to verify under head-restrained conditions the variability in firing patterns with multiple simultaneously recorded units, to rule out differences in sequentially recorded neurons or a change in firing pattern due to the technical experimental setup. Although I have recorded and

observed different single medial septal neurons within the same subjects, previous studies have reported a variability of firing patterns and degrees of rhythmicity of medial septal neurons recorded simultaneously in rats (Sweeney, Lamour and Bassant, 1992; King, Recce and O'Keefe, 1998b; Dragoi *et al.*, 1999) and mice (Joshi *et al.*, 2017; Salib *et al.*, 2019). Figure 5-1 demonstrates simultaneously firing multiple neurons using silicon probes in the MSDB of mice trained to run along a virtual linear track (n=81 isolated units, n=4 mice) recorded by Dr Abhilasha Joshi (Salib et al, 2019). Both, during immobility and locomotion, individual neurons show various degrees of rhythmicity. Based on their individual calculated rhythmicity index (RI) during locomotion, I analysed and plotted the RI distributions (Figure 5-1c). I observed a large group of LRNs defined by RI<0.1 (n=38, median RI: 0.04, interquartile range (IQR): 0.02–0.08) (Joshi *et al.*, 2017). While the HRNs were defined by RI>0.1 (n=43, median RI: 0.32, IQR: 0.19–0.45), as previously described (Joshi *et al.*, 2017). These recordings demonstrated that a large group of low-rhythmic neurons co-fire with high-rhythmic neurons in mice across different behavioural states.

Consistent with the multi-unit recordings, I encountered LRNs intermingled with HRNs during single recording sessions when lowering a glass electrode through the MSDB as the mouse moved or rested on a circular treadmill (Figure 5-1a, d-f). Thus, to reveal the identity of LRNs and compare to HRNs, I aimed to record and label low-rhythmic firing neurons. Out of 107 mice, I have successfully recorded, labelled and recovered 41 neurons in 41 mice from which 11 were classified as LRNs. Dr Tim Viney labelled further 3 LRNs (TV68a, TV77l, TV78l) that I included in this chapter to demonstrate the reproducibility of the physiological parameters calculated and molecular parameters observed. Thus, a total of 14 LRNs were used in this study (n=10/14 with RI<0.1 during movement; n=1/12 with RI=0.14, neuron MS68a; n=1/14 with qualitatively low-rhythmic firing, which lacked substantial movement, neuron TV78l; n=2/14 without RI due to low recorded running periods). In my dataset, two neurons labelled from

animals MS09 and MS53 were included and classified as LRNs as they shared many features of labelled LRN neurons, as well as neuron from MS68a with a slightly higher RI (0.14).

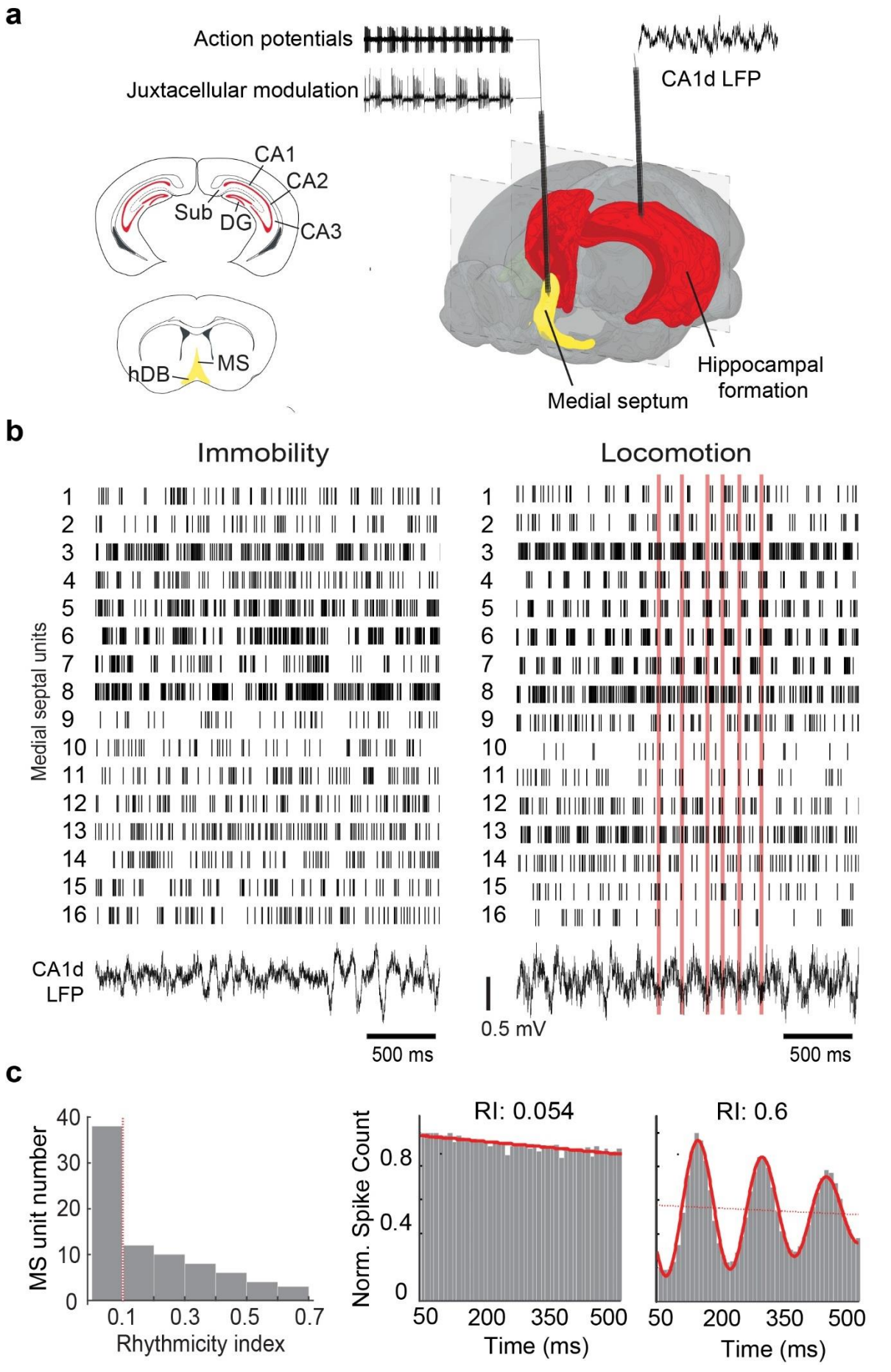

a
Action potentials
Juxtacellular modulation
CA1d LFP
CA1
CA2
Sub
DG
CA3
hDB
MS
Medial septum
Hippocampal formation
b
Immobility
Locomotion
Medial septal units
CA1d LFP
0.5 mV
500 ms
500 ms
c
MS unit number
Rhythmicity index
Norm. Spike Count
RI: 0.054
RI: 0.6
Time (ms)
Time (ms)

Figure 5-1 Co-firing of high-rhythmic and low-rhythmic medial septal neurons.

a, Schematic of recording configurations. Action potentials of single medial septal neurons were recorded extracellularly using a glass electrode followed by juxtacellular labelling. Multi-unit recordings were made using a silicon probe with 16 contacts in tetrode configuration (4 tetrodes) (Joshi et al., 2017). LFPs in CA1d, targeted to stratum pyramidale, were recorded in both configurations. Scheme adapted from the Allen Institute Brain Explorer 2. Red, hippocampal formation; yellow, MSDB. **b,** Simultaneously recorded medial septal neurons (isolated units 1-16) display diverse firing patterns during immobility and locomotion on the jet ball. During locomotion, the mouse was running along a virtual linear track towards a reward (see Methods). Red bars are aligned to the troughs of some CA1d theta cycles. Data taken from Dr Abhilasha Joshi **c**, Left, MSDB units (including those in **b**) ordered by the rhythmicity index (RI). Vertical dashed line, RI cut-off of 0.1. Middle and right, autocorrelograms of spikes during locomotion (50-500 ms, normalized counts) for two cells from **b**. Sub, subiculum; hDB, horizontal Diagonal Band.

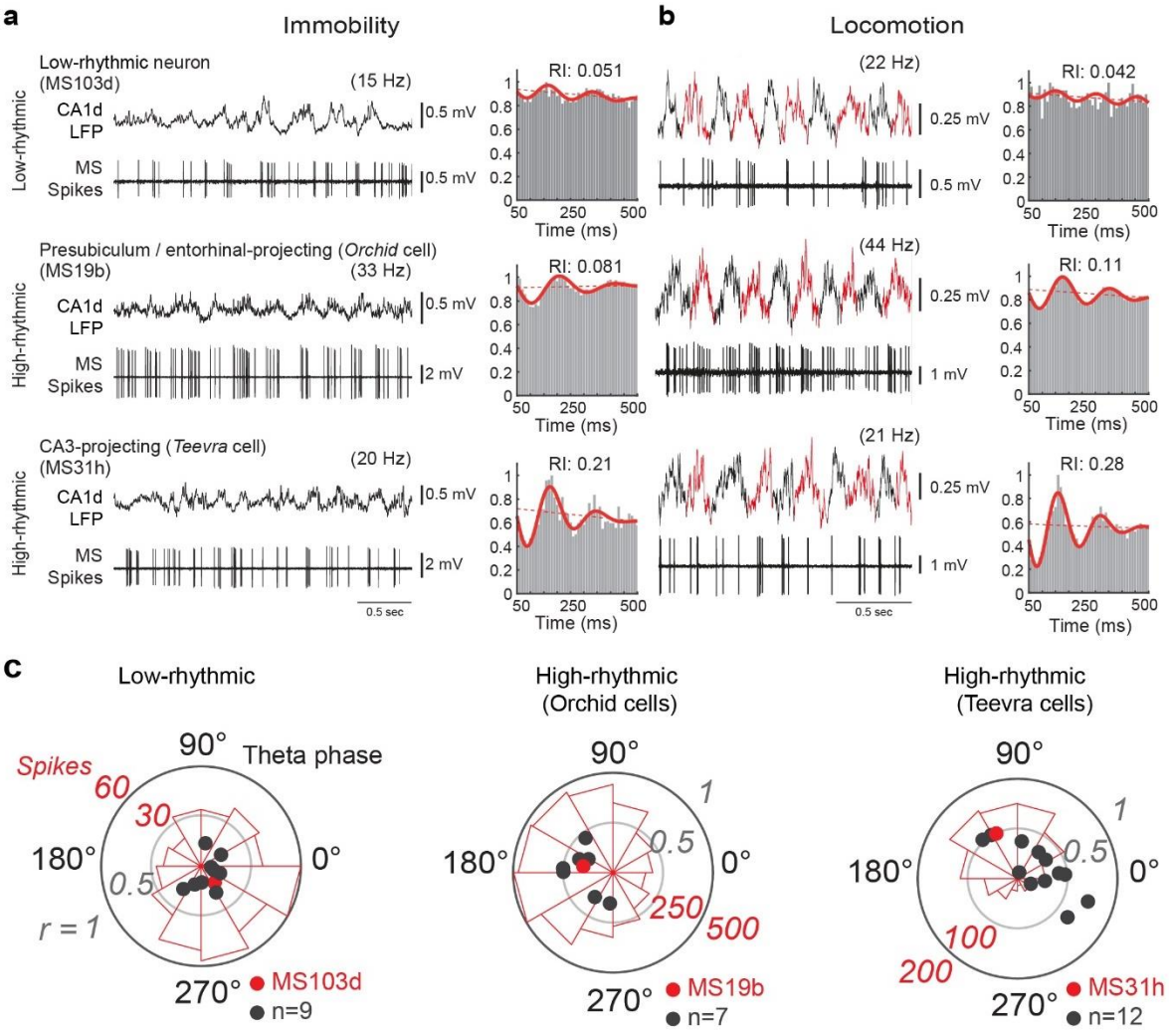

a
Immobility
b
Locomotion
Low-rhythmic neuron
(MS103d)
(15 Hz)
CA1d LFP
MS Spikes
0.5 mV
RI: 0.051
(22 Hz)
0.25 mV
RI: 0.042
Presubiculum / entorhinal-projecting (Orchid cell)
(MS19b)
(33 Hz)
2 mV
RI: 0.081
(44 Hz)
1 mV
RI: 0.11
CA3-projecting (Teevra cell)
(MS31h)
(20 Hz)
RI: 0.21
(21 Hz)
RI: 0.28
High-rhythmic
Low-rhythmic
0.5 sec
Time (ms)
c
Low-rhythmic
High-rhythmic (Orchid cells)
High-rhythmic (Teevra cells)
Theta phase
Spikes
r = 1
MS103d
n=9
MS19b
n=7
MS31h
n=12

Figure 5-2 LRNs are distinct from HRNs recorded in awake mice.

a-b, Low- and high-rhythmic neurons recorded with glass electrodes during immobility and locomotion, followed by juxtacellularly labelling. Parentheses show mean firing rates. Top row, a low-rhythmic medial septal neuron increases firing frequency from immobility to locomotion. Middle row, an entorhinal cortex-projecting high-rhythmic *Orchid* cell (Viney et al., 2018) has long-duration bursts and increases firing from immobility to locomotion. Bottom row, a CA3-projecting high-rhythmic *Teevra* cell (Joshi et al., 2017) has short-duration bursts and does not change its firing frequency from immobility to locomotion. Red bars, examples of bursts relative to CA1d theta. Autocorrelograms of spikes during immobility and locomotion reveal rhythmicity levels. **c**, Polar plots of spike counts in 30° bins (red) for the 3 neurons from **a-b** relative to CA1d pyramidal layer theta (180° is peak). Radius, vector length (r). Red points, preferred mean theta phase for each example neuron. Black points, preferred mean theta phase for other labelled neurons from each group (low-rhythmic cells, n=11; *Orchid* cells, n=8; *Teevra* cells, n=13).

5.2.2 Electrophysiological parameters of labelled low-rhythmic neurons

Medial septal LRNs were initially identified by their qualitative low rhythmicity during movement, low burst incidence and SWR inhibition during immobility, and being recorded near to HRNs in same recording session. These characteristics made them in particular distinguishable from HRNs during recording sessions. Despite their low rhythmicity, most labelled LRNs were coupled to CA1d theta oscillations (n=10/12), preferentially firing on the late descending phase (group circular mean phase ± circular s.d., 319.2 ° ± 54.2°, group mean vector length = 0.11, n=10 neurons; Figure 5-2c, Figure 5-3b, Table 5-1). Labelled high-rhythmic *Teevra* and *Orchid* cells preferentially coupled to the trough and peak of CA1d theta oscillations, neurons; Figure 5-2c, Figure 5-3b, Table 5-1). Joshi *et al.*, 2017; Viney *et al.*, 2018). The group mean theta phase of LRNs was significantly different from *Teevra* and *Orchid* cells (P=0.03 and P=0.04, respectively, permutation tests). Next, I also tested the coupling of LRNs to CA1d slow-gamma (32-39 Hz) and mid-gamma (55-80 Hz) oscillations (Lasztóczi and Klausberger, 2017), which occurred intermittently during both movement and immobility periods. For slow-gamma, individual LRNs preferentially fired on the peak and descending phases of gamma cycles (P≤0.045, r=0.08-0.16, n=4/12 neurons, Rayleigh tests). For mid-gamma, LRNs also preferentially fired on the peak and descending phases (P≤0.018, r=0.07-0.21, n=5/12 neurons, Rayleigh tests). One LRN (MS16d) showed moderate phase coupling to both frequency ranges with the same mean phase preference (214°). These data suggest, like some HRNs (Viney *et al.*, 2018), LRNs can couple to different kinds of behaviourally-contingent network oscillations.

Firing rates of LRNs (mean ± s.d., 31.9 ± 14.1 Hz during movement; 29.7 ± 15.3 Hz during immobility; n=12 LRNs; Table 5-1, Table 5-2) were distinct from ‘slow-firing’ medial septal neurons reported in freely moving rats (mean firing rates <4 Hz; Zhang, Lin and Nicolelis, 2011), which include cholinergic neurons (Simon *et al.*, 2006). I did not observe a common

change in firing patterns within the LRN group during different behavioural states. In fact, mean firing rates of LRNs were similar to HRNs during immobility (*Teevra* cells: 40.7 ± 15.8 Hz, t23=1.8, P=0.09, n = 13; *Orchid* cells: 39.8 ± 8.1 Hz during immobility, t19=1.7, P=0.11; n = 8; unpaired t-tests) and to *Teevra* HRNs during movement (*Teevra* 37.2 ± 13.5 Hz during movement, t23=0.97, P=0.34; *Orchid* cells: 55.2 ± 14.1 Hz, t19=3.6, P=0.002, n = 8; unpaired t-tests; Table 5-2). However, in contrast to high-rhythmic neurons (King, Recce and O'Keefe, 1998; Dragoi *et al.*, 1999; Borhegyi, 2004; Joshi *et al.*, 2017; Viney *et al.*, 2018), LRNs exhibited some bursting activity, but the burst incidence was lower than the HRNs across behavioural states (Table 5-2, Figure 5-3a). Indeed, high-rhythmic neurons maintained a high burst incidence during both, immobility and locomotion (Table 5-2) contributing to a high RI. Conversely, LRNs had a low-burst incidence during movement periods (Table 5-2).

Interestingly, LRNs showed variable firing patterns during theta oscillations, with 5/12 neurons not firing on 7.7-19.4% of theta cycles ('theta off'; Table 5-1). This included 'theta skipping' whereby spikes are absent from single theta cycles (Jeffery *et al.*, 1995; Brandon *et al.*, 2013). Although not as common as LRNs, some HRNs like AJ40m (recorded and labelled by Dr Abhilasha Joshi) displayed 'theta skipping' features (Figure 5-4). The variability of LRNs was also evident from the wide circular distribution of spikes around the mean preferred theta phase, measured as the mean angular deviation (circular standard deviation). The mean angular deviation of LRNs was significantly different to HRNs (median, interquartile range, LRNs: 72°, 2.5°; *Teevra* cells: 59°, 13°; U=115, P=0.00173, n=10 LRNs, n=13 *Teevra* cells; median and interquartile range *Orchid* cells: 64°, 10°; U=68, P=0.01455, n=10 LRNs, n=8 *Orchid* cells; Mann-Whitney U tests; Figure 5-3c). This suggests that LRNs fire with more variability during theta oscillations, which is reflected by their lower theta coupling (and RI) compared to HRNs (Table 5-1, Table 5-2 , Figure 5-1c).

Table 5-1 Properties of identified low-rhythmic neurons

Cell name	**MS13c***	**MS109o**	**MS83d**	**MS68a**	**MS16d**[#]	**MS09_**[##]	**MS53_**[##]	**MS103d***	**MS86b**	**MS33a**	**MS104e**	**TV78l**	**TV77q**	**TV68a**
Target hemisphere	Left	Left	Right	Left	Left	Right	Left	Left	Left	Right	Right	Left	Left	Right
Proportion of DG terminals	~99%	u	u	~90%	u	62%	~20%	u	u	u	0%	98%	30%	21%
Innervated areas	DG, u	u	u	DG, CA3	DG, u	DG, CA3	CA3, DG, CA2, CA1, SUB, MS	CA3, DG, u	u	CA3, CA1, SUBd	CA1, RSg, SUBd, PrSd	DG, CA3	CA3, DG	CA3, DG, CA2, CA1, SUB, MS
Immunoreactivity														
PV	a-	a-	x	a-	a-	a-	ad-	a+	a-	x	d+	tads-	tads-	ads+
Calbindin	a+	ads+	x	a+	a-	a-	ad-	a-	x	x	as-	d-	ad-	a-
SATB1	u	n-	x	n-	u	u	u	u	n-	x	n+	n+	n+	n+
mGluR1a	d+	x	x	d-	u	u	d+	u	ds+	x	ds+	ds+	ds+	ds+
VGAT	x	u	u	u	u	t+	x	x	u	u	t+	t+	t+	t+
VGLUT2	u	u	u	u	u	t-	u	u	u	u	u	t-	u	u
VACHT	u	u	u	u	u	t-	u	u	u	u	u	t-	u	u
NK1R	d-	u	u	u	u	u	d+	u	u	u	u	d-	ds-	s+
PCP4	d-	u	u	u	u	u	u	u	u	u	x	d+	ds+	u
Calretinin	d-	u	u	u	u	u	u	u	u	u	u	tad-	ad-	a-
ChAT	a-	u	u	u	a-	u	ad-	u	u	x	u	u	a-	u
Labeling strength	++	+	+	++	++	++	++	+	+	+	+++	+++	++	++
Firing patterns														
Rhythmicity index M	0.06	0.03	0.04	0.14	0.01	u	u	0.04	0.02	0.04	0.02	(low)	0.03	0.04
Firing rate M (Hz)	52 ± 9	50 ± 7	41 ± 8	24 ± 5	31 ± 6	u	u	19 ± 9	18 ± 10	25 ± 8	54 ± 16	23 ± 11	31 ± 13	11 ± 10
Firing rate IM (Hz)	54 ± 10	61 ± 13	38 ± 12	27 ± 9	36 ± 10	u	u	15 ± 7	16 ± 11	14 ± 6	31 ± 19	22 ± 6	16 ± 8	24 ± 12

Cell name	**MS13c***	**MS109o**	**MS83d**	**MS68a**	**MS16d#**	**MS09_##**	**MS53_##**	**MS103d***	**MS86b**	**MS33a**	**MS104e**	**TV78l**	**TV77q**	**TV68a**
Burst incidence M (Hz, 20)	4.6	4.9	2.6	1.0	1	u	u	1.8	0.4	0.3	4.7	0.3	1.5	0.5
Burst incidence IM (Hz, 20)	4.5	4.7	2.4	2.0	2.3	u	u	0.5	0.4	0.1	2.2	0.5	0.9	1.4
Burst incidence M (Hz, 40)	3.1	3.5	4.1	2.6	3	u	u	0.8	1.1	0.7	2.0	1.6	2.2	1
Burst incidence IM (Hz, 40)	2.7	2.2	3.5	2.76	3.2	u	u	1.1	1.1	0.5	2.2	1.8	1.5	2.3
Interburst interval M	226, 251	222, 206	206, 150	273, 254	252, 194	u	u	326, 347	778, 807	272, 190	362, 364	537, 413	197, 207	417, 1282
Interburst interval IM	297, 244	338, 379	246, 160	312, 220	266, 196	u	u	588, 949	563, 963	854, 1613	301, 306	394, 394	446, 616	309, 275
Intraburst frequency M	74 ± 17	68 ± 14	74 ± 19	88 ± 35	65 ± 18	u	u	75 ± 27	49 ± 8	60 ± 14	72 ± 16	68 ± 27	81 ± 26	89 ± 30
Intraburst frequency IM	73 ± 15	74 ± 22	81 ± 29	89 ± 25	72 ± 20	u	u	81 ± 31	54 ± 13	58 ± 14	77 ± 25	64 ± 16	84 ± 29	71 ± 19
CA1d SWRs (130-230 Hz)														
n SWRs	40	33	13	35	149	u	u	45	13	32	79	61	50	27
Mean rate inside (Hz)	21.71	47.44	u	15.16	9.97	u	u	10.27	u	24.78	15.61	0.65	6.2	1.73
Lambda rate outside (Hz)	53.81	61.54	u	26.84	36.66	u	u	15.16	u	8.19	31.51	21.82	15.83	24.45
SWR index	-0.43	-0.13	u	-0.28	-0.57	u	u	-0.19	u	0.5	-0.34	-0.94	-0.44	-0.87
Poisson *P*-value	<0.0001	0.01	u	0.005	<0.0001	u	u	0.05	u	<0.0001	0.001	<0.0001	0.003	<0.0001
Mean rate before ripple (Hz)	55.50	62.27	u	34.71	33.32	u	u	13.22	u	20.16	37.30	22.13	12.41	26.30
Mean rate after ripple (Hz)	59.63	65.00	u	50.00	46.81	u	u	23.22	u	21.25	45.53	30.08	46.11	36.85
Rebound index	0.04	0.02	u	0.18	0.17	u	u	0.27	u	0.03	0.10	0.15	0.58	0.17
P-value (KS-test)	0.09	0.54	u	0.002	<0.0001	u	u	<0.0001	u	0.14	<0.0001	0.002	<0.0001	0.13
CA1d theta (5-12 Hz)														
Theta cycles	419	292	448	220	429	u	u	229	165	120	517	30	374	217
Theta off %	0%	0%	0.9%	7,7%	1,6%	u	u	13,1%	18%	1,7%	0,2%	0%	14,9%	19,4%
LFP location	SP	SP	SP	SP	SP	u	u	SP	SP	SP	SP	SP	SP	SP/SR
Preferred theta phase	251°	272°	340°	290°	355°	u	u	320°	u	29°	342°	u	234°	79°
Mean vector length (*r*)	0.2	0.16	0.19	0.36	0.04	u	u	0.21	u	0.21	0.15	u	0.3	0.22
Rayleigh *P*-value	<0.0001	<0.0001	<0.0001	<0.0001	0.03	u	u	<0.0001	0.983	<0.0001	<0.0001	0.282	<0.0001	<0.0001
Total *n* spikes	2490	1785	2081	593	1674	u	u	370	276	217	3943	505	1206	522
Spikes per cycle	8.1	6.9	5.8	3.1	4.3	u	u	2.9	1.8	2.9	8.2	3.2	3.1	2.3

Table 5-1 - Properties of identified low-rhythmic neurons. Positive (+) or undetectable (–) immunoreactivity to a molecule observed within subcellular domain: s, soma; n, nucleus; d, proximal dendrite; a, axon; t, axon terminals; x, tested but inconclusive; u, unknown. *Soma was not recovered. #Labelled soma and dendrites could not be directly linked to the projection axon. ##Firing patterns could not be unequivocally matched to the labelled neuron. Firing rates are expressed as mean of 1 s bins ± s.d. M, movement (locomotion and/or small movements). IM, immobility. Bursts are defined as >3 spikes with ISIs <40 ms or <20 ms (see burst incidence). Interburst intervals are in ms (median, interquartile range). Intraburst frequency expressed as mean ± s.d (Hz). Some parameters for neurons TV78l and TV77q have been previously reported (Viney *et al.*, 2018). RSg, granular retrosplenial cortex; PrSd, dorsal presubiculum; SUBd, dorsal subiculum. Additional tests: The dendrites of TV78l and TV68a were immunopositive for SMI32.

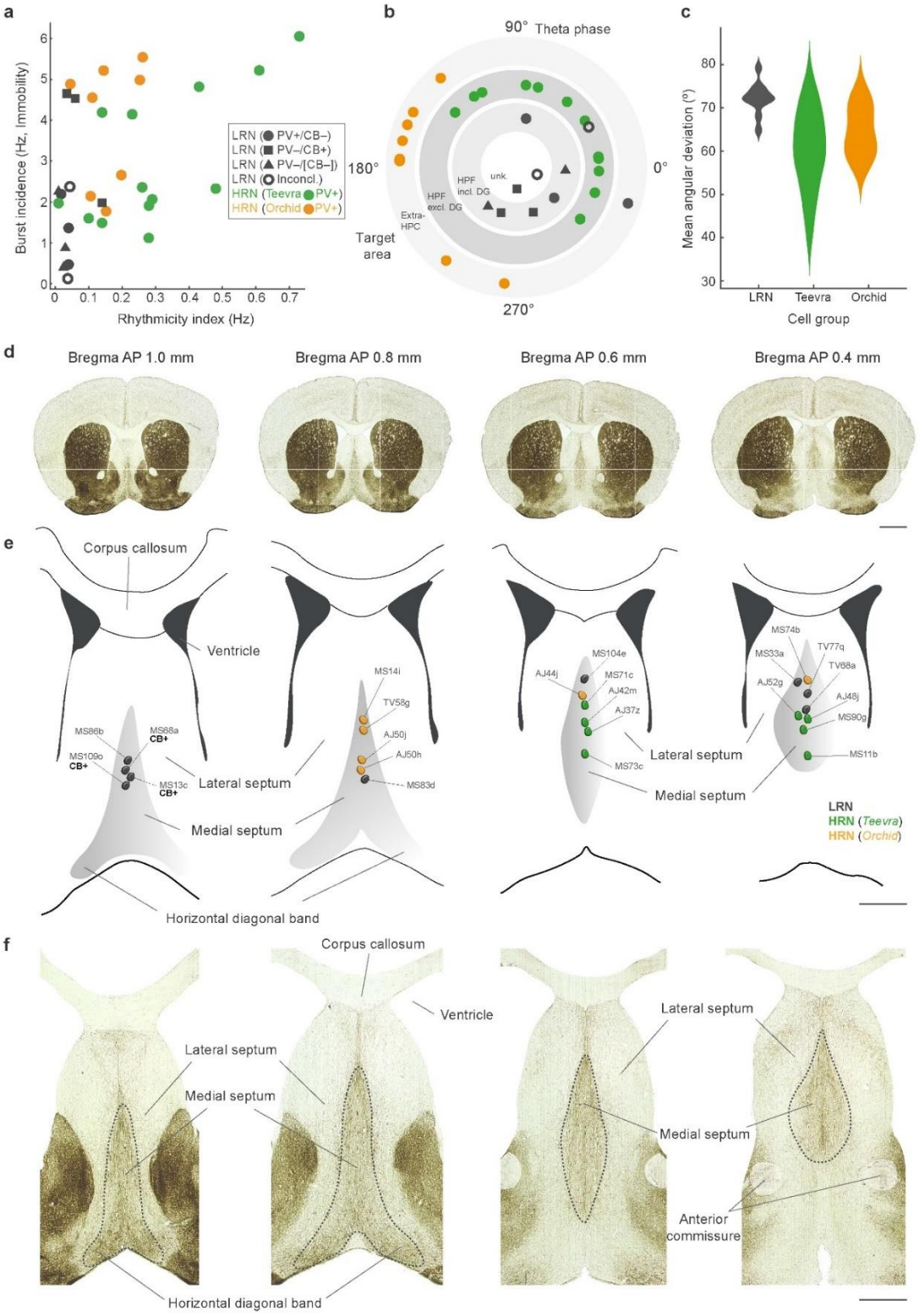

a
Burst incidence (Hz, Immobility)
Rhythmicity index (Hz)
LRN (PV+/CB–)
LRN (PV–/CB+)
LRN (PV–/[CB–])
LRN (Inconcl.)
HRN (Teevra PV+)
HRN (Orchid PV+)
b
90° Theta phase
180°
0°
270°
Target area
HPF incl. DG
HPF excl. DG
Extra-HPC
unk.
c
Mean angular deviation (°)
LRN
Teevra
Orchid
Cell group
d
Bregma AP 1.0 mm
Bregma AP 0.8 mm
Bregma AP 0.6 mm
Bregma AP 0.4 mm
e
Corpus callosum
Ventricle
MS86b
MS88a CB+
MS109o CB+
MS13c CB+
Lateral septum
Medial septum
Horizontal diagonal band
MS14i
TV58g
AJ50j
AJ50h
MS83d
MS104e
AJ44j
MS71c
AJ42m
AJ37z
MS73c
MS74b
MS33a
TV77q
TV68a
AJ52g
AJ48j
MS90g
MS11b
LRN
HRN (Teevra)
HRN (Orchid)
f
Corpus callosum
Ventricle
Lateral septum
Medial septum
Horizontal diagonal band
Anterior commissure

Figure 5-3 LRN and HRN firing patterns and their recording locations.

a, Identified low-rhythmic firing medial septal neurons (LRNs) have a low burst incidence (20 ms bursts) and a low rhythmicity index (RI) compared to identified high-rhythmic firing medial septal neurons (HRNs: green, *Teevra* cells; orange, *Orchid* cells). **b,** Polar plot of preferred mean theta phase relative to CA1d pyramidal layer theta (180° is peak) for labelled LRNs and HRNs ordered by target area(s): hippocampal formation (HPF) including dentate gyrus (DG); HPF excluding DG (i.e. cornu ammonis and subiculum); extra-HPF (presubiculum, parasubiculum, entorhinal cortex). Two had unknown target areas (see also Table 5-1). LRNs, n=11, *Orchid* cells, n=8, *Teevra* cells, n=13. **c,** Distribution chart of mean angular deviation for the 3 groups. **d,** Coronal mouse brain sections reacted for acetylcholinesterase (AChE) at 1.0 – 0.4 mm anterior-posterior (AP) relative to Bregma (left to right). **e**, Schematic coronal illustrations of the MSDB at four different AP positions according to **d** (left to right) showing the soma location of the LRNs and HRNs. The location of neuron MS13c (dashed line) is based on a proximal dendrite. **f**, Coronal AChE sections of the MSDB at the same AP positions as in **e** (left to right). Coronal AChE images were taken from (Franklin and Paxinos, 2001). Scale bars (mm): **d**, 1; **e**, **f**, 0.5Inconcl., inconclusive for PV and CB. Unk., unknown target region(s).

Table 5-2 Properties high- and low-rhythmic neurons

	HRNs (RI >0.1)		**LRNs** (RI <0.1)
CA1d theta (5 - 12 Hz)	*Teevra* cells	*Orchid* cells	
n	13	8	10
LFP location	CA1 SP	CA1 SP	CA1 SP
Preferred theta phase	37.5°±53.5°	178.6°±39.1°	319.2 ° ± 54.2°
Group Mean vector length (*r*)	0.19	0.29	0.09
Firing patterns			
n	13	8	12
Firing rate M (Hz)	37.2 ± 13.5	55.2 ± 14.1	31.9 ± 14.1
Firing rate IM (Hz)	40.7 ± 15.8	39.8 ± 8.1	29.7 ± 15.3
Burst (40ms) incidence M (Hz)	4.40 ± 1.56	4.98 ± 1.30	2.08 ± 0.88
Burst (20ms) incidence M (Hz)	3.47 ± 1.99	3.97 ± 1.42	1.97 ± 1.73
Burst (40ms) incidence IM (Hz)	3.56 ± 1.23	4.24 ± 0.74	2.14 ± 1.08
Burst (20ms) incidence IM (Hz)	3.02 ± 1.57	5.37 ± 1.54	1.82 ± 1.45

Table 5-2 - Properties high- and low-rhythmic neurons.

Firing rates are expressed as group mean of 1 s bins ± s.d. M, movement (locomotion and/or small movements), IM, immobility. Bursts are defined as >3 spikes with ISIs <40 ms or <20 ms (see burst incidence) and expressed as group mean ± s.d. Interburst intervals are in ms (median, interquartile range) and expressed as group mean ± s.d.

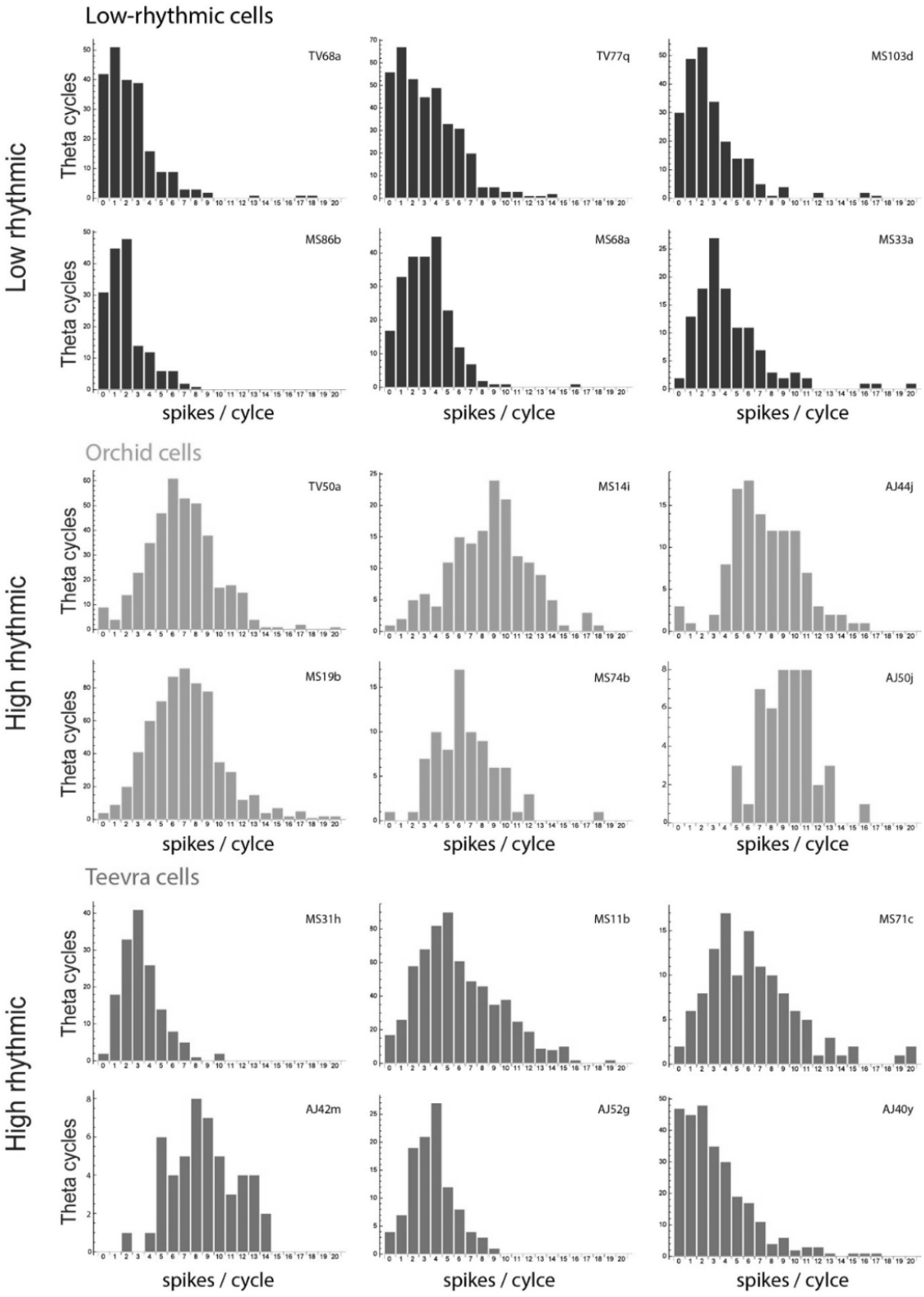

Low-rhythmic cells
Low rhythmic
TV68a
TV77q
MS103d
MS86b
MS68a
MS33a
Theta cycles
spikes / cylce
Orchid cells
High rhythmic
TV50a
MS14i
AJ44j
MS19b
MS74b
AJ50j
Teevra cells
High rhythmic
MS31h
MS11b
MS71c
AJ42m
AJ52g
AJ40y
spikes / cycle

Figure 5-4 Theta-skipping properties high- and low-rhythmic neurons.

Theta-skipping histograms comparing the firing patterns of LRNs (top) to two HRN groups (bottom, middle), *Teevra* cells and *Orchid* cells. Each group contains six recorded and labelled MSDB neurons with firing activity during locomotion. Each histogram expresses the distribution spikes recorded for each dCA1 theta cycle.

5.2.3 Low-rhythmic neurons are suppressed during sharp-wave ripples

Next, I asked whether LRNs have common firing patterns during immobility. During immobility, large amplitude irregular activity (LIA) dominates the hippocampal field potential (Vanderwolf, 1969; O'Keefe and Nadel, 1978). Firstly, I can as shown in Table 5-2 quantitatively analyze and compare the firing patterns e.g. firing rate, burst incidence, burst frequency and coupling to cortical oscillations like gamma during all non-theta states (immobility). However, during these immobility periods high-frequency local field potential activity patterns characteristic for the hippocampus also occur, the sharp wave ripples (SWR, 130 – 230 Hz). These 'awake SWRs' are implicated in memory consolidation (O'Neill et al., 2006; Carr et al., 2011), and the activity of some MSDB neurons are modulated during SWR events (Dragoi *et al.*, 1999; Borhegyi, 2004; Viney *et al.*, 2013, 2018; Unal *et al.*, 2018). Interestingly, I observed that the LRNs decreased their firing during CA1d SWRs (n=9/10 labelled LRNs with >20 recorded SWRs; firing rate distributions significantly different from a Poisson distribution, $P<0.05$; Figure 5-5, Figure 5-6, Table 5-1), contributing to their negative SWR indices (Table 5-1). Figure 5-5 shows an example of a SWR suppressed LRN, MS16d during immobility. Note how the neuron is not firing during the periods of the SWRs. Figure 5-6 shows the firing probability of further 6 LRNs during immobility. In addition, I investigated with the support of Dr. Linda Katona, the firing activity outside SWRs. LRNs fired occasional accommodating bursts outside SWRs (n=9/10 LRNs, Figure 5-6), and 6 displayed significant 'rebound firing' in the ~250 ms immediately after SWRs (Table 5-1; Figure 5-6, 2-sample KS tests, $P\leq0.002$, n=6). Thus, on average, LRNs are suppressed during SWRs, display low burst incidence during immobility and mobility and low rhythmicity during mobility. Next, I asked how these features are related to the cortical target regions of this subpopulation of MSDB neurons.

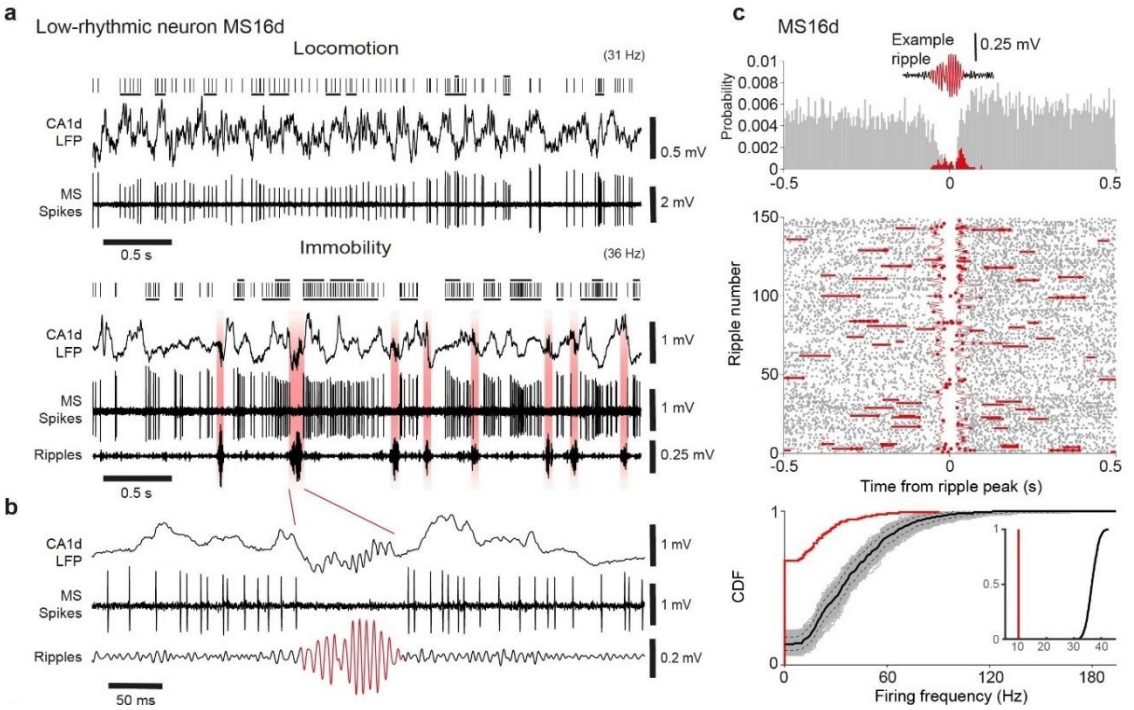


Figure 5-5 Low-rhythmic neuron is suppressed during SWRs.

a, Activity of a SWR-suppressed low-rhythmic neuron (MS16d) during locomotion (top) and immobility (bottom). Note absence of action potentials during SWRs (filtered 130–230 Hz, highlighted red). Black ticks: all detected spikes from the single neuron; top black bars: bursts of >3 spikes with ISIs <20 ms; bottom black bars: bursts of >3 spikes with ISIs <40 ms. Mean firing rates in parentheses. **b**, High time resolution of a ripple from **a**. **c**, Firing probability density (top) and raster plot (middle) relative to all detected SWRs (n=149) during immobility for neuron MS16d. Continuous staggered lines in raster delineate start and end of aligned ripples; horizontal lines delineate adjacent ripples. Red, spikes during SWRs; gray, spikes outside SWRs. Bottom, comparison of mean firing rates during SWRs and periods outside SWR events. The distribution of firing rates during individual SWRs (red), displayed as a cumulative distribution function (CDF), is shifted to the left from the distribution of a surrogate set of 1,000 firing rate-distributions during periods outside SWR events (grey; median, solid black line; 95% confidence intervals, broken lines). Inset, comparison of mean SWR-related firing rate (red) with the distribution of surrogate mean SWR-related rates (black).

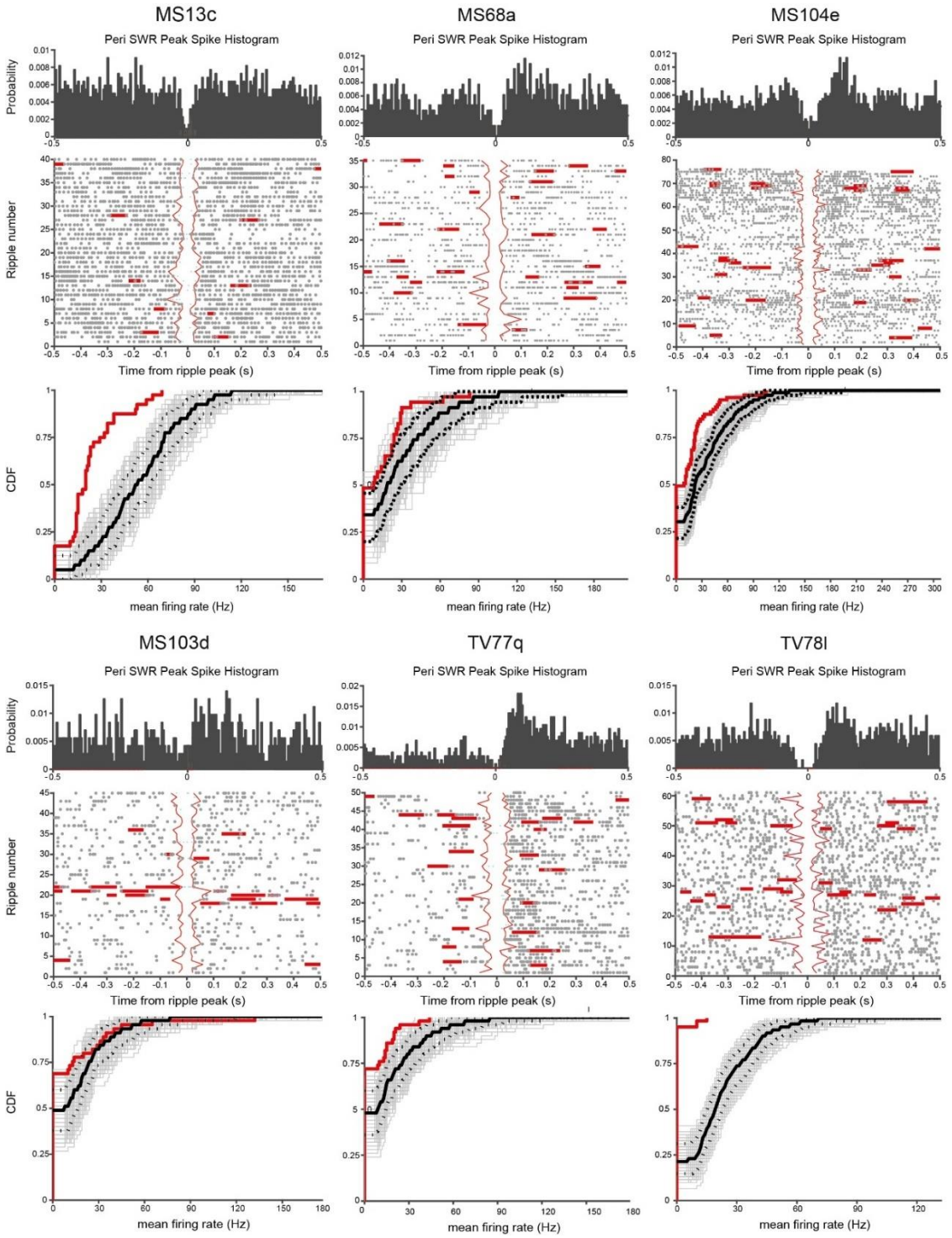

MS13c
MS68a
MS104e
MS103d
TV77q
TV78l
Peri SWR Peak Spike Histogram
Probability
Ripple number
Time from ripple peak (s)
CDF
mean firing rate (Hz)

Figure 5-6 Firing probability densities LRNs relative to SWRs during immobility.

For each of the 6 presented LRNs; firing probability density (top) and raster plot (middle) relative to all detected SWRs during immobility. Continuous staggered lines in raster delineate start and end of aligned ripples; horizontal lines delineate adjacent ripples. Red, spikes during SWRs; grey, spikes outside SWRs. Bottom, comparison of mean firing rates during SWRs and periods outside SWR events. The distribution of firing rates during individual SWRs (red), displayed as a cumulative distribution function (CDF, bottom), is shifted to the left from the distribution of a surrogate set of 1,000 firing rate-distributions during periods outside SWR events (grey; median, solid black line; 95% confidence intervals, broken lines).

5.2.4 LRNs innervate select regions of the hippocampal formation with a bias towards the DG and CA3

Recorded and labelled LRNs projected septo-temporally from the medial septum via the fimbria (n=11/12; n=1/12 via the fornix) and innervated at least one region of the hippocampal formation (n=12/12). Along the septo-temporal axis, the majority started branching within the most septal part of the hippocampus (i.e. closest to the MSDB), in CA3 (n=6/8 neurons with sufficiently labelled axon; Table 5-1). In one case, MS13c, the cell projected directly to the DG, with collaterals occupying the molecular layer of both DG blades. Another LRN (MS104e, *Chapter 3*) targeted retrosplenial cortex (RSg) via the dorsal fornix, a route shared with known *Orchid* cells. Terminals of MS104e were observed primarily in the granular retrosplenial cortex (RSg) and CA1. Michael Howarth observed in the lab an axonal branch in CA1 and ruled out any further innervation in EC, Chidinma Onyali worked for her MSc thesis project on MS104e analyzing terminals in RSg. Due to weak labelling, the remaining axons of 4 LRNs observed in the fimbria were too faint to recover branches, except for one with partial axon observed in the DG (MS16d). Unlike *Teevra* cells, that innervated only the CA3 (and in some cases CA1 as well) and extra-hippocampal projecting *Orchid* cells (Figure 5-3b), LRNs that branched in CA3 continued and additionally branched in the DG (n=5/6 neurons), or CA1d and the dorsal subiculum (SUBd) (n=1/6; MS33a). In addition, I also labelled two other neurons that innervated both CA3 and the DG (MS09_ and MS53_), but recordings could not be assigned due to >1 labelled neuron being recovered; Table 5-1). Overall, I have labelled 11 neurons that differed in their axon termination patterns from exclusively CA3-innervating Teevra cells and entorhinal cortex-projecting *Orchid* cells. The majority of LRNs had collaterals in the DG, which receives the densest MS innervation (Figure 5-7; Table 5-1). Two neurons, MS68a and TV78l, with axons observed in the DG had over

90% of terminals distributed in the septal/middle two-thirds or temporal one-third of the DG across the septo-temporal axis (MS68a and TV78l, respectively), with the remaining terminals in CA3. Only MS13c had its terminals restricted to the septal one-third of the DG. Other LRNs innervated the DG with lower proportions (62% in DG versus CA3, MS09_; 30%, Table 5-1).

So far and within the group of LRNs, I have observed neurons with mainly two restricted target areas. Nevertheless two neurons, MS53 and TV68a, exhibited a *multiple-branching pattern* originating in the fimbria within the septal one-third of the hippocampus, and innervating restricted portions of the DG (~20% of terminals), CA3, CA2, CA1, SUBd, and locally within the MSDB. further two neurons, MS103d and MS16d, were undetermined due to weak labelling, but they formed terminals in the middle septo-temporal third of the DG. Finally, I conclude that LRNs innervate select regions of the hippocampal formation, with a bias towards the DG and CA3, and are distinct from the projections of HRNs such as *Teevra* and *Orchid* cells.

The combination of firing suppression during SWRs, a low burst incidence during immobility, and low rhythmicity during locomotion yielded a strong prediction of their axonal innervation of the cortex.

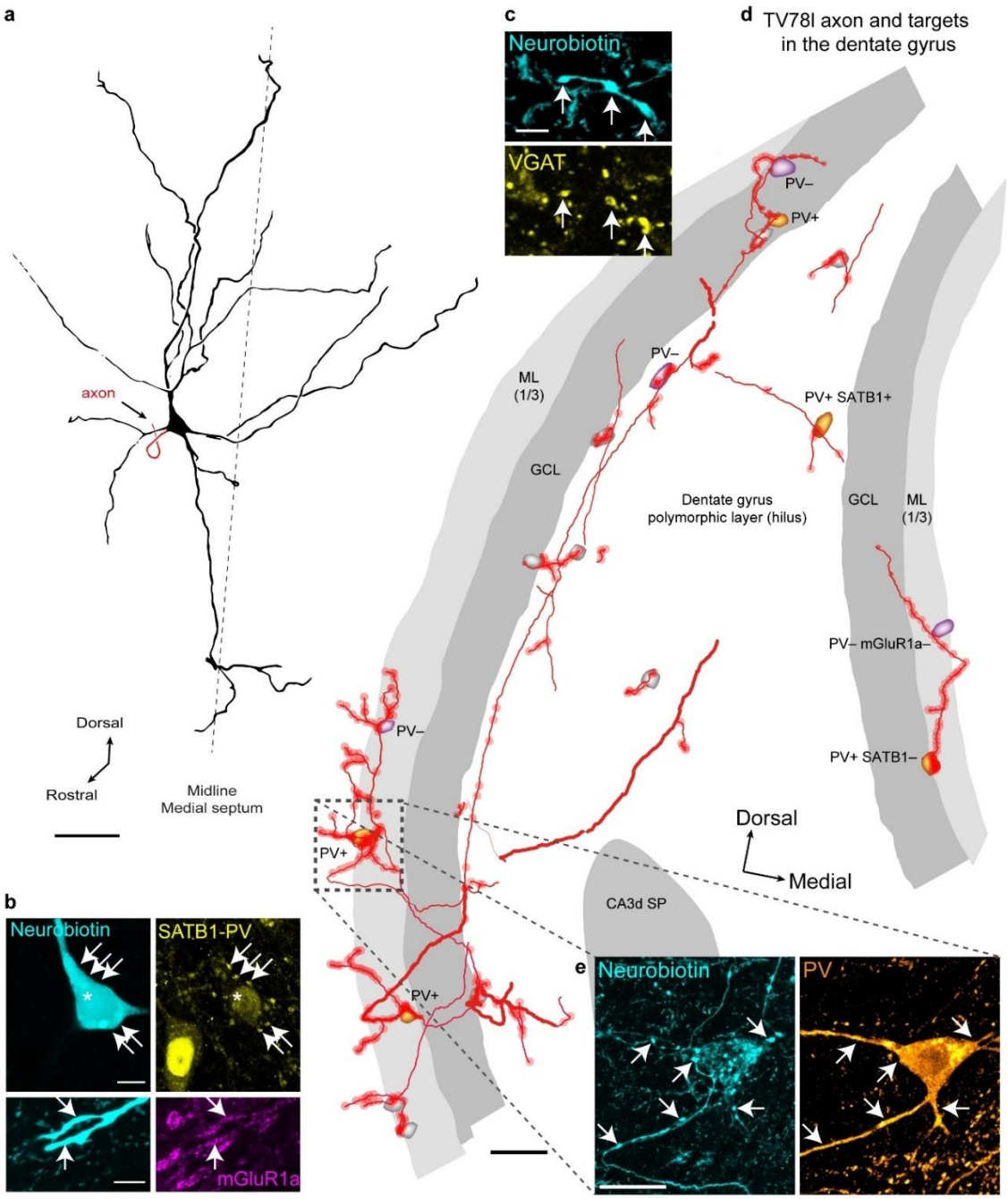

a
axon
Dorsal
Rostral
Midline
Medial septum
b
Neurobiotin
SATB1-PV
mGluR1a
c
Neurobiotin
VGAT
d
TV78l axon and targets
in the dentate gyrus
PV–
PV+
PV–
ML
(1/3)
PV+ SATB1+
GCL
Dentate gyrus
polymorphic layer (hilus)
GCL
ML
(1/3)
PV– mGluR1a–
PV+ SATB1–
PV–
PV+
Dorsal
Medial
CA3d SP
PV+
e
Neurobiotin
PV

Figure 5-7 Synaptic targets of a GABAergic LRN mainly targeting the DG.

a, Reconstruction of the soma and dendrites in the MSDB. Arrow, projection axon. Dashed line, midline (dorsal is up). **b**, Top, the soma of TV78l (cyan, neurobiotin, Nb, asterisk) was SATB1+ (yellow, nucleus) but lacked detectable cytoplasmic immunoreactivity for PV (also yellow). Some PV+ terminals were apposed to the soma and proximal dendrites (e.g. arrows). Note SATB1+/PV+ neuron at bottom left. Bottom, a dendrite (cyan, neurobiotin, arrows) was mGluR1a+ (magenta). **c**, Terminals (cyan, neurobiotin) in the dentate gyrus were VGAT+ (yellow, arrows). **d**, Partial reconstruction of the TV78l axon (red) from one 100-µm-thick section of temporal DG. Varicosities were color-coded red. Some interneuron targets could be identified: orange, PV+; magenta, PV–; gray, untested. **e**, A neuron with high mitochondrial biotin content was PV-immunoreactive (orange) in the ML (boxed region in **d**) and received extensive basket-like innervation (>37 varicosities) from TV78l (cyan, neurobiotin). Arrows highlight some terminals on the soma and proximal dendrites. Many terminals overlap the soma due to the 2D projected z-stack. Dr Tim Viney recorded the cell, planned and documented the targets, Naomi Berry processed the immunoreactions, axonal reconstruction was done by Ben Micklem and the soma and dendrites were reconstructed by Amar Sharma. Images (z-thickness in µm and z-projection type): **b**, top/bottom 3/4.2 maximum, **c**, 4.1 maximum, **e**, 9.5 standard deviation. Scale bars (µm): **a**, 100, **b**, 10 and 5 (top and bottom), **c**, 5, **d**, 50, **e**, 20. Granule cell layer, GCL; molecular layer, ML; stratum pyramidale, SP.

5.2.5 Majority of LRNs are PV- GABAergic neurons

Next, I asked whether the molecular expression profiles of the 14 labelled neurons related to their target regions and secondly, if they are different from the molecular profiles of *Teevra* and *Orchid* cells. So far, all identified HRN groups proved to be GABAergic and showed positive immunoreactivity for PV (Figure 5-3a). Unexpectedly, I found that most LRN neurons lacked detectable immunoreactivity for PV (n=9/14 tested neurons PV–; 2 inconclusive; Table 5-1**,** Figure 5-7b). However, when the terminals of 8 neurons were tested for the vesicular GABA transporter (VGAT), a marker for GABAergic neurons, I found that 5 were immunopositive (3 PV–/CB–, 2 PV+, 3 inconclusive, immunoreactivity was supported by Michael Howarth). Two PV– neurons were innervated by PV immunopositive (PV+) terminals in the MSDB (Figure 5-7b); these neurons were also immunopositive for Purkinje protein 4 (**PCP4;** Table 5-1). Of the 3 PV+ neurons, one innervated multiple regions that included the DG and CA3. The second, MS103d, was partially-labelled and small axonal branches were observed in CA3 prior to the DG. The PV+ neuron MS104e did not innervate the DG. Further, a minority of labelled neurons were CB+ (n=3/14 tested neurons, 3 inconclusive tests; Table 5-1), two of which showed strong preferential innervation of the DG, MS13c and MS68a. The axonal branching patterns of the third CB+ neuron (MS109o) could not be determined. None of the neurons were double immunopositive for PV and CB. Interestingly, the CB+ neurons were located in the most rostral part of the MSDB (Figure 5-3d-f). Other labelled LRN somata were intermingled with labelled HRNs along the midline (Figure 5-3d-f). Most neurons were also immunopositive for mGluR1a (n=7/11 tested, 3 inconclusive) and SATB1 (n=4/9 tested neurons, 2 inconclusive; Table 5-1). I conclude that LRNs comprise a diverse subpopulation of MSDB neurons based on their molecular profiles, with a majority of PV–/CB– GABAergic neurons that innervate different proportions of CA3 and the DG.

Three LRNs had similar firing patterns (MS13c, MS109o, and MS83d). I predict this group to be CB+/mGluR1+ LRNs (CB was tested but inconclusive for MS83d). These LRNs did not skip theta cycles, were coupled to the late descending/trough phase of theta, had a low RI, and exhibited a higher firing rate during movement than PV–/CB– LRNs (Table 5-1). Interestingly, CB+/GFP+ neurons were observed by Dr Katja Hartwich along the midline of the MSDB in a $VGAT^{Cre}$ mouse injected by Dr Linda Katona with a Cre-dependent AAV expressing EYFP, in the region where labelled CB+ were identified, suggesting that CB+ GABAergic MSDB neurons may also target the hippocampal formation (Fuchs et al., 2016). In comparison to HRNs, all identified *Teevra* and *Orchid* cells were immunopositive for PV (Joshi *et al.*, 2017; Viney *et al.*, 2018), suggesting a cell-type specific projection pattern linked to the molecular profile, as not one of the HRNs projected to the DG. Thus, in the next step I looked at the innervation pattern of PV- and PV+ MSDB neurons in the hippocampal formation.

5.2.6 The dentate gyrus receives less PV+ septal innervation than CA3

To investigate whether there is a different innervation pattern of MSDB PV- and PV+ projecting to the DG and CA3, I quantified brains of PV^{Cre} and $VGAT^{Cre}$ mice injected by Dr Linda Katona and processed by Dr Katja Hartwich colleagues. Based on the projections of PV–immunonegative LRNs and the lack of DG innervation by PV+ *Teevra* cells, I hypothesized that the DG receives more PV- GABAergic input than CA3. To test this, I analysed with the support of Dr. Tim Viney the proportion of PV+ axonal branches from the MSDB in the DG compared to CA3 in PV^{Cre} mice (n=4 mice). I observed a low ratio of PV+ MSDB axons in the DG versus CA3 (median, interquartile range: septal third, 0.36, 0.54; middle third, 0.27, 0.40; temporal third, 0.47, 0.66; n = 548 axons, 13 regions, 4 mice; Figure 5-8a,c). This low ratio could not be explained by the distribution

of MSDB GABAergic afferents in the DG. Further, a high ratio of GABAergic MSDB axons in the DG versus CA3 at three septo-temporal levels (septal, 1.28, 0.55; middle, 1.14, 0.25; temporal, 0.72, 0.17; n = 5216 axons, 18 regions, 3 mice; Figure 5-8b,c) was observed. Overall, there was significantly lower ratio of PV+ MSDB axons in the DG versus CA3 compared to all GABAergic MSDB axons (P=0.000057, U=16, Mann-Whitney test; n=13 and 18 regions from PV^{Cre} and $VGAT^{Cre}$ mice, respectively; Figure 5-8c,d). These data demonstrate that PV+ MSDB neurons represent a minority of the GABAergic MSDB input to the DG (Bao et al., 2017; Unal et al., 2018).

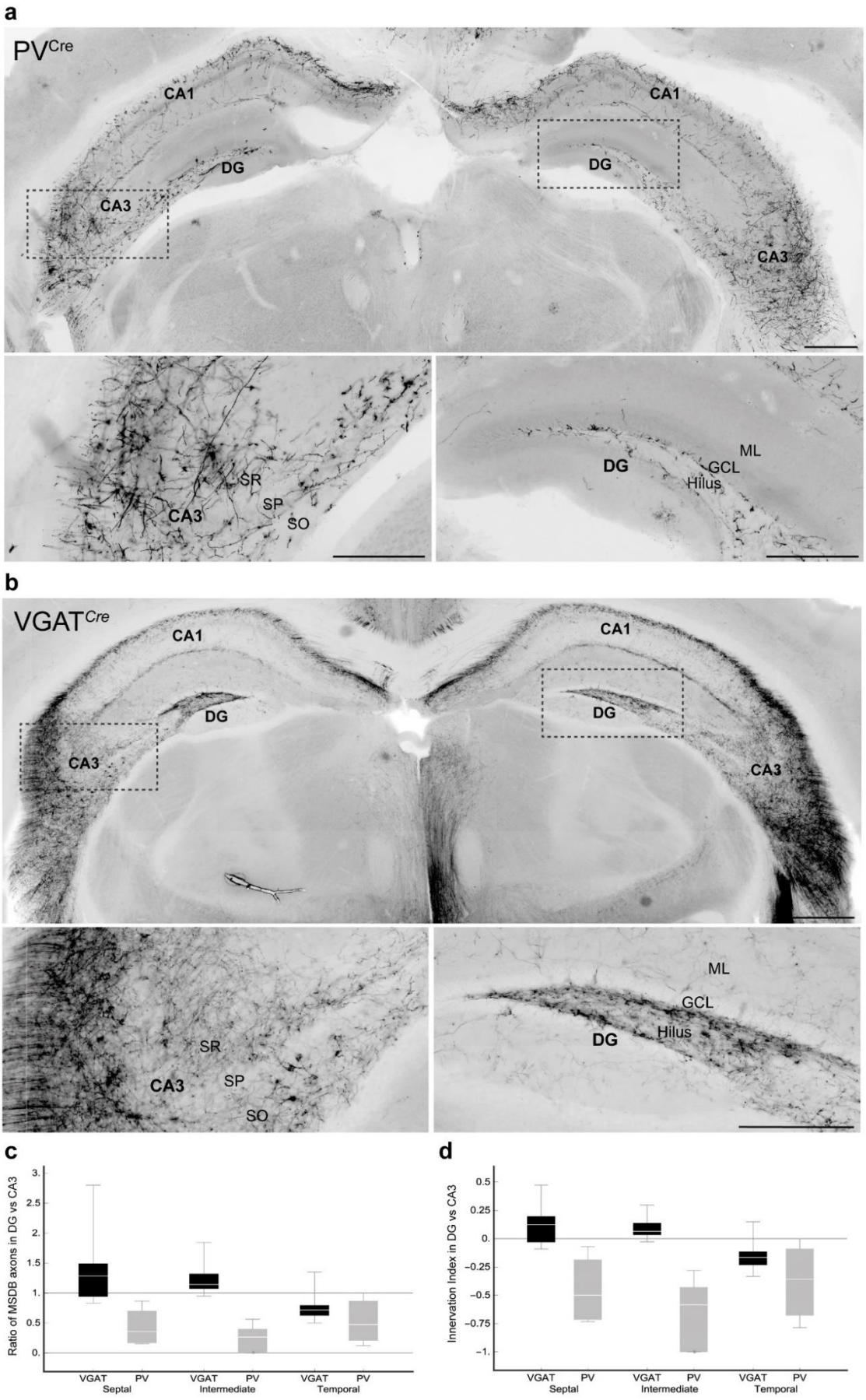

a
PVCre
CA1
CA1
DG
DG
CA3
CA3
SR
SP
SO
CA3
DG
ML
GCL
Hilus
b
VGATCre
CA1
CA1
DG
DG
CA3
CA3
SR
SP
SO
CA3
ML
GCL
Hilus
DG
c
Ratio of MSDB axons in DG vs CA3
3.
2.5
2.
1.5
1.
0.5
0.
VGAT
PV
Septal
VGAT
PV
Intermediate
VGAT
PV
Temporal
d
Innervation Index in DG vs CA3
0.5
0.25
0.
−0.25
−0.5
−0.75
−1.
VGAT
PV
Septal
VGAT
PV
Intermediate
VGAT
PV
Temporal

Figure 5-8 Differential input of DG/CA3 by GABAergic and PV+ MSDB axons.

a, Coronal section from a PV^{Cre} mouse showing MSDB innervation of the hippocampal formation (GFP, black). Below, MSDB axons in CA3 and DG, respectively, from boxed regions. **b,** Coronal section from a $VGAT^{Cre}$ mouse. Below, MSDB axons in CA3 and DG, respectively, from boxed regions. **c**, The DG receives less PV+ innervation than the CA3. Distribution chart of the ratio of MSDB axons in the DG versus CA3 in $VGAT^{Cre}$ mice (GABAergic neurons) and PV^{Cre} mice (PV+ neurons). Black, VGAT+ (GABAergic) axons; gray, PV+ axons. Boxes show median and interquartile range. **d**, Distribution chart as in **c** but plotted as an index, where -1 and +1 represent a bias towards CA3 and the DG, respectively (see Methods). All images are widefield epifluorescence montages, reverse contrast, 0.65 μm thick, at 10x magnification. Scale bars: **a,b,** top, 500 μm; bottom, 250 μm.

5.2.7 Postsynaptic targets of low rhythmic PV–/CB– septo-hippocampal neurons

Teevra cells, innervated only axo-axonic (AAC) and CCK+ cells in CA3. Thus, I further investigated the distribution of terminals and postsynaptic targets of LRNs, in particular PV–/CB– septo-hippocampal neurons across CA3 and the DG. Unfortunately, not all cells were sufficiently labelled to reveal terminals in the targeted areas. One good example is shown by Dr Tim Viney. The axon of LRN TV78l formed a single collateral in the intermediate CA3 innervating the proximal dendrites of a PV+/SATB1+/somatostatin (SOM)+ interneuron in stratum oriens (SO) (n=7 varicosities; Figure 5-9**)**, a marker combination that matches dendrite-targeting oriens lacunosum moleculare (OLM) cells and bistratified cells. The main axon in the fimbria continued to the temporal DG where multiple terminals decorated the dendrites and somata of DG interneurons (Figure 5-7). Postsynaptic targets were in the polymorphic layer (PML, hilus), granule cell layer (GCL) and molecular layer (ML) (n=815 sampled varicosities, 56% in the ML;). Most targets were PV+ (n=10/17 tested targets; Figure 5-7). By far the most extensively innervated targets were large interneurons at the GCL/ML border expressing high levels of endogenous biotin (Figure 5-7e), which resembled axo-axonic cells (Soriano, Nitsch and Frotscher, 1990). In the PML, axons were observed along the GCL border where they either targeted somata and dendrites of radially-oriented neurons, or branched superficially into the main hilar region, forming terminals on other neurons (Figure 5-7d).

Similar to LRNs TV78l , MS09_ branched in the fimbria close to CA3, with the other collateral continuing along CA3 SO to the DG. Along the septo-temporal axis, terminals were observed in CA3i and CA3d within the middle third of the hippocampus, and in the DG across the middle and temporal thirds. In the DG the majority of terminals were in

the PML (84% PML, 16% GCL), and in CA3 most were in SP (50% SP, 43% SR). MS09_ mostly formed sparse terminals along dendrites, and rarely on cell bodies. PV– targets in both CA3 and the DG (n=5/5 targets) were identified. One target was SATB1–/CR–, expressed high levels of endogenous biotin, and was located in CA3 SP; two neurons in CA3 SO were SATB1–/SOM–/CCK–; a SOM–/CCK– neuron (SATB1 inconclusive) was located in the PML (17 terminals; 9 on the soma), and finally a SATB1+/M2R– neuron (SOM inconclusive) was identified, also in the PML (7 terminals). Cortical innervation pattern of MS09_ was analysed by Dr Linda Katona. Neuron MS16d had similar firing patterns to the other PV–/CB– LRNs but was too weakly labelled to visualize targets.

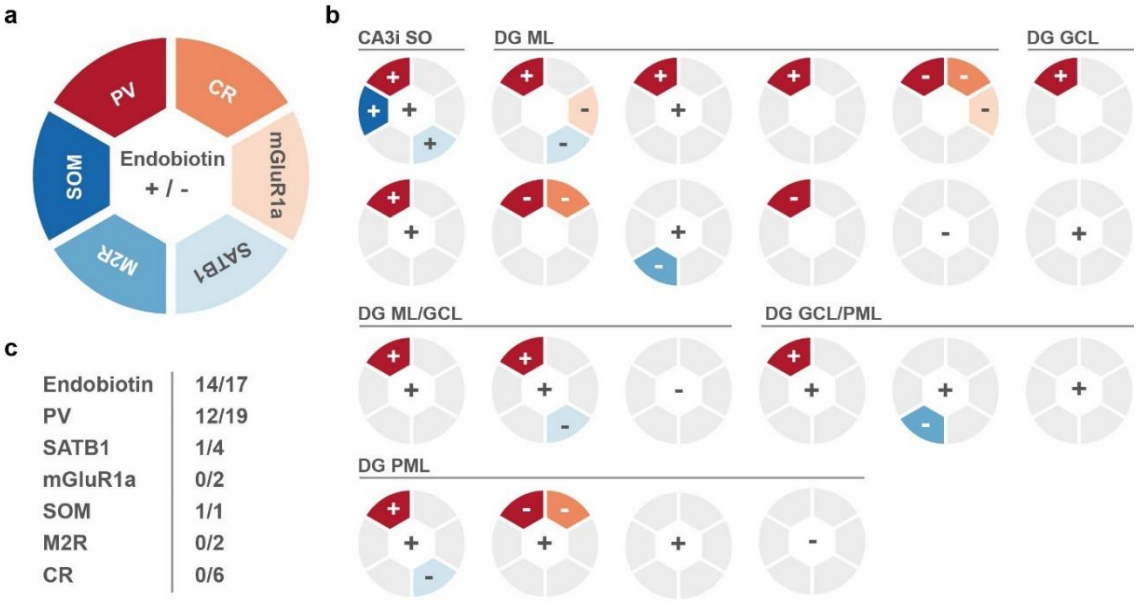


Figure 5-9 Cortical target neurons of LRN TV78l.

Molecular profiles of presumed postsynaptic neurons, based on close apposition of axon terminals; +, detectable positive immunoreactivity or signal; –, undetectable immunoreactivity or signal in vicinity of immunopositive signals.

5.3 Discussion

I report the innervation patterns and synaptic targets of the first fully characterised MSDB LRNs in awake mice. Firstly, I discovered that a majority of LRNs were GABAergic, PV-immunonegative and innervated interneurons in the dentate gyrus and CA3. Secondly, I revealed the firing dynamics of a population in the MSDB that also target an area, the DG, which receives dense innervation from the MSDB (Freund and Antal, 1988). Further, it has been shown by several studies investigating the $VGAT^{Cre}$ mouse line that PV-expressing neurons only represent a fraction of MSDB GABAergic (Freund, 1989; Fuchs *et al.*, 2016; Bao *et al.*, 2017; Unal *et al.*, 2018). The vesicular GABA transporter (VGAT) is a marker for GABAergic neurons. Intriguingly, both the PV-positive *Teevra* cells and *Orchid* cells avoid the dentate gyrus (DG). In addition, the LRN as a population, were markedly suppressed during hippocampal sharp-wave ripples and had a low burst incidence during immobility periods.

5.3.1 LRNs provide variable cortical network control

Cortical GABAergic projections from the MSDB have been shown to be area and target selective (Joshi *et al.*, 2017; Unal *et al.*, 2018; Viney *et al.*, 2018), suggesting inter-areal temporal control in functional related brain areas. Behaviour-related activity is one key characteristic of MSDB neurons for cortical computation in the areas they specifically control. These GABAergic projections from the medial septum preferentially innervate GABAergic neurons in the hippocampus in rat (Freund and Antal, 1988) and in mouse (Sun *et al.*, 2014). Following that finding, GABAergic LRNs innervated also GABAergic interneurons within the hippocampus while a majority of identified LRNs targeted the DG and CA3. Unlike the prominent constant high-rhythmic burst feature of identified HRNs (Joshi et al., 2017; Viney et al., 2018), single GABAergic LRNs show a degree of

variability in their activity patterns. My results revealed a preferred firing phase on the descending phase of CA1d theta oscillations. Within the hippocampus DG granule and CA3 pyramidal neurons fire at highest probability during the same descending theta phase (Buzsáki *et al.*, 2003; Mizuseki *et al.*, 2009; Lasztóczi and Klausberger, 2017; Senzai and Buzsáki, 2017). The observed low rhythmic firing pattern during immobility and especially during mobility suggests a strong dynamic role in time-dependent functional coordination of cortical processes. The high rhythmicity of known MSBD neurons during locomotion suggest a constant major functional role regardless any additional computational changes. In any given situation the expected rhythmicity is observed during hippocampal theta oscillations. LRNs however, provide during mobility, a temporally-distinct cycle by cycle GABAergic input. In addition, this complements the observation of frequent theta cycle skipping in labelled LRNs, as also previously shown in some rhythmic firing MSDB neurons (King, Recce and O'Keefe, 1998a). Theta cycle skipping medial septal neurons have been reported before. Interestingly, reported medial septal cells exhibited theta skipping behaviour only when the animals was running in a particular direction (King, Recce and O'Keefe, 1998a). In fact, theta cycle skipping is predominantly exhibited by neurons with significant head direction tuning (Brandon *et al.*, 2013). Inactivation of medial septum eliminated all theta cycle skipping in head direction cells despite leaving many cells with normal theta rhythmicity (Brandon *et al.*, 2013).

5.3.2 Modulation of LRNs during SWRs

SWRs are most prominent in stratum radiatum and are initiated by population bursts of groups of CA3 pyramidal cells which via their Schaffer collaterals (Csicsvari et al., 2000; Nakashiba et al., 2009) excite pyramidal cells. In addition, they also excite GABAergic

interneurons in the CA1 area. Consequently, the somatic and dendritic membranes of targeted pyramidal cells become entrained to high frequency “ripple”-like oscillations (120-230 Hz). Further, it is suggested that during SWRs, transient memories represented by assemblies of co-firing CA1 pyramidal cells are transferred to neocortex for long-term storage (Buzsáki, 1989; Hasselmo, 1999). *Do LRNs contribute to the generation of hippocampal SWR ripples?* A hypothesis might be that the drop of firing rate during SWRs in MSDB neurons (Dragoi *et al.*, 1999) allows the withdrawing of their inhibition from dentate interneurons and some types of postsynaptic CA3 interneuron, such as bistratified cells. Thus, allowing these cells to fire strongly during SWRs (Somogyi *et al.*, 2014), along with GABAergic hippocampo-septal cells. Disinhibited bistratified cells targeting pyramidal cell dendrites (Lovett-Barron *et al.*, 2012) provide ripple-frequency entrainment of reactivated neuronal assemblies. In addition, the extensive basket-like innervation of dentate interneurons, particularly those in the ML, by PV–/CB– LRN TV78l, is likely to provide a powerful inhibitory control, and would be disinhibitory during SWRs. The features of PV+ targets on the GCL/ML border resemble axo-axonic cells (Soriano, Nitsch and Frotscher, 1990; Haring, Yan and Faber, 1997). Thus, unlike their CA3 counterparts (Viney et al., 2013), dentate axo-axonic cells of the ML probably fire during SWRs. The discharge of specific granule cells during SWRs may be dependent on SWR-inhibited axo-axonic cells that target both CA3 and the DG (Han *et al.*, 1993; Szabo *et al.*, 2017), or through the interaction with mossy cells and hilar axo-axonic cells. The low-rhythmic firing of presynaptic GABAergic medial septal neurons to ML axo-axonic cells and the lack of high-rhythmic *Teevra* cell input predicts their low theta modulation. The sparse firing of granule cells during locomotion and their relatively strong theta modulation (Jung and McNaughton, 1993; Diamantaki *et al.*, 2016; Danielson *et al.*, 2017; Senzai and Buzsáki, 2017) suggests the participation of e.g.

presynaptic rhythmically-firing dendrite-targeting interneurons. Rebound firing in LRN ensures that SWR-active hippocampal neurons stop firing at the end of the sharp wave, ‘resetting’ the interneurons for successive SWR participation. The drop in firing during SWRs means that subpopulations of dentate interneurons are also disinhibited, facilitating the SWR-related discharge of granule cells (Penttonen *et al.*, 1998).

5.3.3 Specialization of medial septal low-rhythmic firing neurons

LRN’s dynamic feature is in addition reflected in their diverse immunohistochemical profile. Reported high-rhythmic neurons are shown to be PV positive and, like *Teevra* cells, form selective basket-like terminations around PV+/SATB1–axo-axonic cells and some CCK interneurons in CA3 (Viney *et al.*, 2013; Joshi *et al.*, 2017). Assuming the molecular differences of LRN are due to their target and area selectivity, can the molecular profile be linked with the innervated area? As it turned out, most LRN do not have one specific target area. In parallel to *Teevra* cells, LRNs targeted separate subpopulations of CA3 interneurons in addition to innervating other areas such as the DG. GABAergic LRN however, displayed a variety of GABAergic markers Thus, not all GABAergic MSDB neurons are PV positive. Although some identified LRNs were PV positive, the majority were either PV negative or Calbindin (CB) positive. Interestingly, previous studies have demonstrated some CB positive GABAergic septo-cortical projections (Fuchs et al., 2016, Freund, 1989), providing evidence for more than one GABAergic MSDB population projecting to the cortex. Interestingly, CB positive LRNs tend to have the DG as their major target area. In four cases, single LRNs with a multi-area innervation pattern including the DG, CA3, CA1 and Subiculum were identified. It is surprising that so far, my colleagues and I have not encountered any HRN input to the DG in mouse; out of 21 identified and published HRNs, none of them innervated the DG.

Only one rare theta-rhythmic PV+ ‘septo-dentate’ neuron was identified in rat, recorded under anaesthesia (Unal et al., 2018). This could be explained due to different recording conditions like anaesthesia and due different species. In fact, a diversity of rhythmic and non-rhythmic activity patters of MSDB neurons were observed in anaesthetised rats (Borhegyi, 2004; Simon *et al.*, 2006). However, the percentage of rhythmic bursting neurons is higher under anaesthesia than without it (Lee, Lamour and Bassant, 1991).

How are the contributions of low-rhythmically and high-rhythmically firing neurons coordinated? Due to their different activity pattern in time and space as well as target selectivity, in particular the *Teevra* cells (Joshi *et al.*, 2017), they are unlikely to interact at the level of individual cortical interneurons. Instead, in the medial septum, the multi-area innervating LRNs targeted neurons that matched the molecular profiles of other LRNs and *Orchid* cells, but not cholinergic neurons (Salib *et al.*, 2019). *Orchid* cells also have local axons in the MSDB with unknown synaptic targets. The local collaterals of *Teevra* cells, however, mostly innervated PV+/SATB1+ neurons (Joshi *et al.*, 2017), which could represent multi-area innervating LRNs or other HRNs. Both GABAergic and glutamatergic MSDB neurons are innervated by PV+ terminals (Henderson *et al.*, 2010), suggesting that PV+ LRNs may also locally modulate the activity of glutamatergic neurons (Fuhrmann *et al.*, 2015).

To conclude, I have shown that low-rhythmic firing medial septal neurons have diverse axonal outputs, including one neuron, MS104e, targeting extra-hippocampal areas. However, most of them primarily target interneurons in the DG and CA3 regions, providing variable theta-modulated input and are suppressed during SWRs, allowing the activation of some hippocampal interneurons. Rhythmic activity in the brain is implemented by specialized subcortical cell types, supporting mnemonic functions by interacting locally in the MSDB and in the cortex via inhibition of select interneurons.

Further recording and labelling experiments are needed to reveal the extent of such parallel subcortical GABAergic innervation in the cortex.

Chapter 6

General discussion

6.1 Thesis outline

Distinct types of hippocampal GABAergic interneurons target different subcellular domains of pyramidal cells and show preferred-firing phases during the theta network state. Subcortical GABAergic neurons originating in the medial septum mostly target these cortical GABAergic interneurons. During my studies, I aimed to understand how the GABAergic septal-cortical input influence the coordination of the firing of different types of interneurons within the hippocampal formation. To address this question, I have initially investigated the diversity of the medial septal population by recording the firing activity of individual neurons during different network and behavioural states, such as theta oscillations during locomotion. Based on the initial characterization in my database of 682 biologically-meaningful recorded medial septal neurons (see *Chapter 3* and *Appendix*), I have defined medial septal neurons with low- and high rhythmic firing patterns, strong and weak phase-coupling across all phases during CA1d theta oscillations and, lastly, increasing as well as decreasing mean firing rates during both immobility and locomotion.

My initial findings establishing the diversity of firing patterns from just the extracellular recordings of medial septal neurons support the hypothesis of brain-state and behaviour dependent activity of medial septal neurons as reported in anaesthetized (Petsche, Stumpf and Gogolak, 1962; Gogolák *et al.*, 1968; Borhegyi, 2004; Simon *et al.*, 2006) and unanaesthetised rodents (King, Recce and O'Keefe, 1998a; Dragoi *et al.*, 1999; Joshi *et al.*, 2017; Viney *et al.*, 2018; Salib *et al.*, 2019). These neurons have also been shown to be speed modulated (Fuhrmann *et al.*, 2015; Justus *et al.*, 2017; Tsanov, 2017). However, it has been recently demonstrated that the firing rate modulation by running speed in MEC does not depend on MSDB inputs (Dannenberg *et al.*, 2019). In rare cases (n=6/682), I have, in addition, observed so called "theta-on" and 'theta-off' cells, cells

that are only active or silent during CA1d theta oscillations (*Appendix*) (Ford, Colom and Bland, 1989). Next, by juxtacellular labelling recorded medial septal neurons, I have identified three GABAergic subpopulations of medial septal neurons targeting specific cortical areas with distinct spike train dynamics and molecular profiles. Based on their rhythmicity during locomotion, these subpopulations were grouped as high-rhythmic and low-rhythmic firing medial septal neurons, HRNs and LRNs, with two of these subpopulations, *Teevra* and *Orchid* cells, being classified as HRNs. First, I have confirmed that *Teevra* cells selectively project to the hippocampal area CA3 and innervate specific types of local GABAergic neuron. Secondly, I have demonstrated that *Orchid* cells selectively project to extra-hippocampal areas including the presubiculum and entorhinal cortex where they innervate local GABAergic neurons and largely avoid the hippocampus. Thirdly, I have demonstrated that LRNs preferentially project to the DG and CA3 and innervate local GABAergic neurons. My identified neurons match the recently reported HRN and LRN groups (Joshi *et al.*, 2017; Viney *et al.*, 2018; Salib *et al.*, 2019) and support the hypothesis of a diverse septal GABAergic population selectively targeting interneurons in specific cortical areas.

Given their target area specificity and even their selective target cell types, as shown for *Teevra* cells, what is the functional role of each identified subgroup? The distinct physiological characteristics of each subgroup, which were crucial for the classification, provide an insight in their role within cortico-cortical circuits. All of my identified *Teevra* cells are short-burst firing and strongly phase-coupled to the trough of ongoing CA1d theta oscillations, while my identified *Orchid* cells are long-burst firing and preferentially fire during the peak of theta oscillation. In contrast to HRNs, LRNs as a population are weakly phase-coupled to the descending phase of theta oscillations. However, unlike both HRN groups, LRNs are suppressed during hippocampal SWRs. Could this

distinguishable feature of LRNs indicate a different modulatory role and different targets compared to HRNs? I have summarized our current understanding of identified GABAergic septo-cortical projecting subgroups in a conceptual framework (Figure 6-1), which includes the anatomical, molecular and physiological parameters I used to classify medial septal neurons.

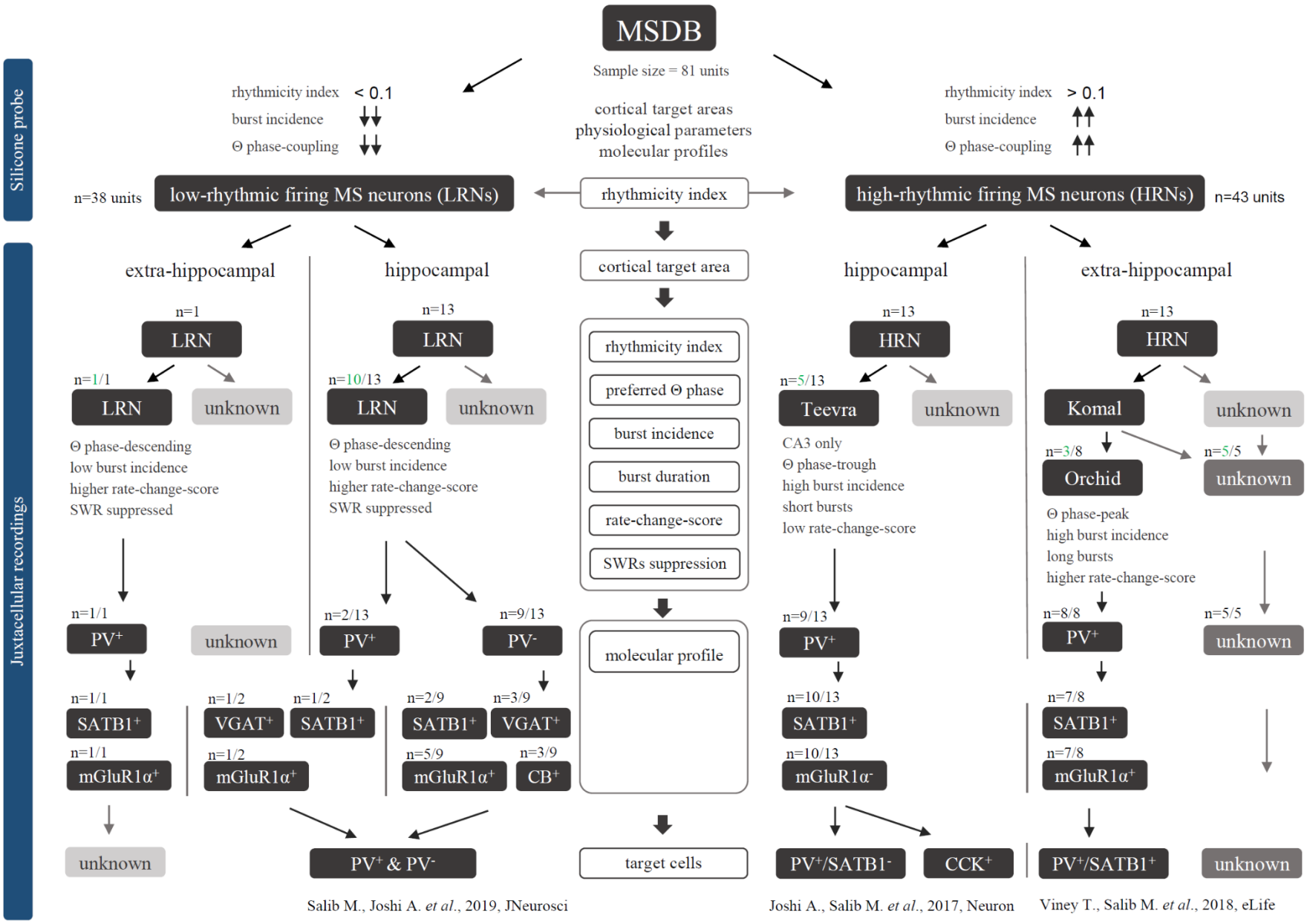

Silicone probe
Juxtacellular recordings
MSDB
Sample size = 81 units
cortical target areas
physiological parameters
molecular profiles
rhythmicity index
rhythmicity index < 0.1
burst incidence
Θ phase-coupling
rhythmicity index > 0.1
burst incidence
Θ phase-coupling
n=38 units
low-rhythmic firing MS neurons (LRNs)
high-rhythmic firing MS neurons (HRNs)
n=43 units
cortical target area
extra-hippocampal
hippocampal
hippocampal
extra-hippocampal
n=1
LRN
n=13
LRN
n=13
HRN
n=13
HRN
n=1/1
LRN
unknown
n=10/13
LRN
unknown
n=5/13
Teevra
unknown
Komal
unknown
n=3/8
Orchid
n=5/5
unknown
Θ phase-descending
low burst incidence
higher rate-change-score
SWR suppressed
Θ phase-descending
low burst incidence
higher rate-change-score
SWR suppressed
CA3 only
Θ phase-trough
high burst incidence
short bursts
low rate-change-score
Θ phase-peak
high burst incidence
long bursts
higher rate-change-score
rhythmicity index
preferred Θ phase
burst incidence
burst duration
rate-change-score
SWRs suppression
molecular profile
n=1/1
PV+
unknown
n=2/13
PV+
n=9/13
PV-
n=9/13
PV+
n=8/8
PV+
n=5/5
unknown
n=1/1
SATB1+
n=1/2
VGAT+
n=1/2
SATB1+
n=2/9
SATB1+
n=3/9
VGAT+
n=10/13
SATB1+
n=7/8
SATB1+
n=1/1
mGluR1α+
n=1/2
mGluR1α+
n=5/9
mGluR1α+
n=3/9
CB+
n=10/13
mGluR1α-
n=7/8
mGluR1α+
unknown
PV+ & PV-
target cells
PV+/SATB1-
CCK+
PV+/SATB1+
unknown
Salib M., Joshi A. et al., 2019, JNeurosci
Joshi A., Salib M. et al., 2017, Neuron
Viney T., Salib M. et al., 2018, eLife

Figure 6-1 Conceptual framework of identified subgroups of the mouse medial septum

Conceptual framework of identified (mostly GABAergic) medial septal neurons, systematically and hierarchically positioned based on their cortical target areas, physiological parameters and molecular profiles. The top part demonstrates an hierarchical clustering approach of 81 medial septal units recorded using a silicon probe in awake head-fixed mice running on a jet ball (Joshi *et al.*, 2017). Based on the calculated rhythmicity index units were arbitrarily classified as low-rhythmic firing neurons (LRN, n= 38 units, RI<0.1) and high-rhythmic firing neurons (HRN, n=43 units, RI>0.1). The bottom part demonstrates the further identification of HRN and LRN subgroups based on the extracellular recording and juxtacellular labelling method (Pinault, 1996). Considering the definition of cell types: *"Two individual neurons belong to the same cell type if they deliver the same neuroactive substances to the same range of postsynaptic targets in the same temporal patterns in a brain state-specific manner"*(Somogyi, 2010), the approach was the following: in the first instance, cells were grouped according to their cortical target area. Together with the rhythmicity index, this indicated one of the four main HRN and LRN groups. Further electrophysiological analysis, including preferred firing phase during CA1d theta oscillations, burst incidence and duration during locomotion, rate-change-score and firing activity during CA1 SWRs led to further divisions. These were accompanied by molecular characterizations of the labelled cell. Finally, post-synaptic target analysis concluded distinct cell-types and subgroups in case the same parameters were shared by several independently identified neurons. Unknown parts are given a place holder or one or more potentially exciting subgroups within each hierarchical level. Dark grey, 'unknown' subgroup indicating a putative *Komal* subgroup based on five identified unpublished HRNs. Numbers in green correspond to my recorded and labelled medial septal neurons. (Joshi *et al.*, 2017; Viney *et al.*, 2018; Salib *et al.*, 2019)

6.2 Subcortical-cortical GABAergic modulation via disinhibition

6.2.1 *Teevra* cells facilitate temporal coding in CA1

The target selectivity of the identified GABAergic neurons indicate subcortical parallel pathways to coordinate functionally-related cortical areas according to the functional requirements of their targets i.e. *Teevra* cells specifically targeting axo-axonic and CCK basket cells (Lasztoczi *et al.*, 2011; Somogyi *et al.*, 2014; Joshi *et al.*, 2017) in the CA3 region of the hippocampus. For instance, axo-axonic cells are maximally active at the peak/descending phase of hippocampal theta oscillations providing a powerful inhibitory input to the axon initial segment of pyramidal cells, while pyramidal cells preferentially fire during the trough of CA1 theta oscillations (Mizuseki *et al.*, 2009)**.** Thus, the rhythmic subcortical input of *Teevra* cells to axo-axonic cells during the trough of CA1 theta oscillations (Viney *et al.*, 2013; Joshi *et al.*, 2017) coordinates precisely the output of CA3 pyramidal cells to CA1 via disinhibition on the descending theta phase (Mizuseki *et al.*, 2009). This mechanism could link a coordination role of *Teevra* cells with a proposed model of encoding and retrieval of memories during theta oscillations. According to that model, the hippocampal theta rhythm contributes to encoding and retrieval of memories, by separating encoding and retrieval of memories into different functional cycles (Hasselmo, Bodelón and Wyble, 2002). At the trough of hippocampal theta cycle (recorded at the hippocampal fissure), during encoding the hippocampal region receives stronger input from the entorhinal cortex whereas efferents from CA3 pyramidal cells to CA1, and hippocampal output are relatively weak. This allows long-term potentiation to take place within the hippocampus by strengthening connections among the principal cells. At the peak of hippocampal theta cycle, during the retrieval phase, the entorhinal input is reduced while intraregional, hippocampal transmission and

hippocampal output are at their maximum (Hasselmo, Bodelón and Wyble, 2002; Kunec, Hasselmo and Kopell, 2005). Thus, septal *Teevra* cells allow CA3 pyramidal cells the temporal coding of CA1 ensemble via their output at the trough of the theta cycle (Borhegyi, 2004; Middleton and McHugh, 2016; Joshi *et al.*, 2017).

6.2.2 Orchid cells participate in the rhythmic entrainment of spatially-modulated projection neurons in the PrSd and EC via disinhibition

Orchid cells, firing counter-phased to *Teevra* cells, could have a key role in coordinating hippocampal CA1 and CA3 input from the entorhinal cortex. During the peak of CA1d theta oscillations *Orchid* cells provide powerful inhibition to extra-hippocampal target interneurons such as in the PrS and EC (Gonzalez-Sulser *et al.*, 2014; Viney *et al.*, 2018), allowing the modulation of local principal cells via disinhibition. The GABAergic population of both areas are not as well defined as within the hippocampus (Klausberger and Somogyi, 2008), thus the disinhibitory effect could be modulated in several ways according to the somato-dendritc input of those cells onto postsynaptic local principal cells. However, as *Orchid* cells terminate in the entorhinal cortex, I predict, interneurons and principal cells with strong theta modulation (Beed *et al.*, 2013). Presubicular afferent, innervate several extra-hippocampal areas including the entorhinal cortex where they terminate on cells in layer II (ECII) and III (ECIII) (van Groen and Wyss, 1990; Caballero-Bleda -Menno *et al.*, 1994). Especially ECII contains as large population of hippocampal projecting interneurons (Germroth, Schwerdtfeger and Buhl, 1989; Jones and Bühl, 1993). Moreover, a dense inhibitory circuitry onto ECII stellate cells and principal cells in the entorhinal cortex was shown to be mostly mediated by parvalbumin positive interneurons (Buetfering, Allen and Monyer, 2014). Grid cells in ECII showed hippocampal independent phase precession, whereas grid cells in ECII fired at a fixed

phase relative to the theta rhythm (Hafting *et al.*, 2008; Mizuseki *et al.*, 2009). However, a following study has shown that these phase precessing cells represent only a minority of ECII principal cell, in fact, the majority of EC2 cells fired at a relatively low rate and were strongly phase-locked to the theta cycle (Mizuseki *et al.*, 2009). Further, ECII principal cells mainly project to the DG and CA3 (Steward, 1976) whereas EC projections to CA1 originate mainly in ECIII (Steward and Scoville, 1976; Amaral and Witter, 1989). Accordingly, head-direction cells, were identified in the dorsal portion of the rat PrS to be tuned (Taube, Muller and Ranck, 1990), including 'fast spiking' PV+ neurons including 'theta cells' (Preston-Ferrer *et al.*, 2016). Thus, I propose that the septal high-rhythmic and long bursting GABAergic input of *Orchid* cells to extra-hippocampal areas is coordinating spatially modulated cells, including principal cells in ECII and ECIII, via disinhibition, while coordinating the entorhinal input to DG/CA3 and CA1. In support, medial septal inactivation was established to reversibly abolish theta frequency oscillations and grid cell firing patterns (Mitchell *et al.*, 1982; Brandon *et al.*, 2011, 2013; Koenig *et al.*, 2011). In conclusion, both groups of HRNs are likely to coordinate the temporal dynamics of CA3 and EC glutamatergic inputs to CA1 (Kajiwara *et al.*, 2008).

6.2.3 LRNs participate in memory discrimination on select theta cycles

LRNs show a degree of variability in their activity patterns compared to the consistently high rhythmic firing feature of both HRN cell types. Most LRNs preferentially fired on the descending phase of CA1d theta oscillations when DG granule and CA3 pyramidal neurons fire at highest probability (Buzsáki *et al.*, 2003; Mizuseki *et al.*, 2009; Lasztóczi and Klausberger, 2017; Senzai and Buzsáki, 2017). In CA1, GABAergic OLM and bistratified cells modulate pyramidal neuron dendrites mainly during the theta trough, when pyramidal cells as a population fire with highest probability (Mizuseki *et al.*, 2009;

Varga, Golshani and Soltesz, 2012; Katona *et al.*, 2014; Varga *et al.*, 2014). Due to the temporal redistribution of inhibition across subcellular domains of principal neurons during each oscillatory cycle (Somogyi *et al.*, 2013; Varga *et al.*, 2014), the axon initial segment is disinhibited at the same time as the dendrites are maximally modulated. Thus, I suggest that LRNs participate in changing the firing mode of DG and CA3 principal cells by inhibiting dendrite-targeting interneurons (Lovett-Barron *et al.*, 2012; Szabo *et al.*, 2017).

The DG has been proposed to contribute to memory discrimination (Wills *et al.*, 2005; Leutgeb *et al.*, 2007; Colgin, Moser and Moser, 2008). The storage and recall of associative memory rely on two complementary processes: pattern separation and pattern completion. Pattern separation allows the network to reduce the overlap between similar input patterns before they are stored to reduce interference in memory recall. Pattern completion refers to retrieve stored output patterns when presented with similar input patterns. The DG has been proposed as a pre-processing area that performs pattern separation on entorhinal cortex inputs (Neunuebel and Knierim, 2014). The CA3 network in contrast performs pattern completion when input representations are similar to stored memories or pattern separation when input representations are more distinct (Guzowski, Knierim and Moser, 2004). A recent study has shown dentate place cells and interneurons transiently increase their firing activity at times when mice are most likely to be making memory discriminations that required the DG, suggesting a powerful dynamic coordination by a local interneuron network. Here, LRNs could play a major role during dentate-dependent memory discriminations providing such a subcortical interneuron-driven control on select theta cycles (Lopes-dos-Santos *et al.*, 2018; van Dijk and Fenton, 2018).

6.3 Rhythmic activity in the basal forebrain

Subcortical input to the hippocampus has not only been shown from the medial septum and diagonal band but across the entire basal forebrain (Petsche, Stumpf and Gogolak, 1962; Gogolák *et al.*, 1968; Détári and Vanderwolf, 1987; Détári, Rasmusson and Semba, 1999; Zaborszky *et al.*, 1999, 2015; Duque *et al.*, 2000; Manns, Alonso and Jones, 2000, 2003; Kang *et al.*, 2017). The basal forebrain serves as a major extra-thalamic relay from the brainstem to the cerebral cortex and is involved in arousal, learning and memory (Rye *et al.*, 1984; Buzsaki *et al.*, 1988; Gritti *et al.*, 1997; Jones, 2004; Adamantidis, Carter and de Lecea, 2010; Han *et al.*, 2014; Shi *et al.*, 2015). There is no consensus regarding the generation of hippocampal theta oscillations and the question of which of the subcortical structures are responsible for pacing hippocampal oscillations. Theta frequency oscillations are thought to be generated in the brainstem and midbrain then relayed to cortex through the basal forebrain including the medial septum (Vertes and Kocsis, 1997; Orzeł-Gryglewska, Matulewicz and Jurkowlaniec, 2015) rather than generated locally in the medial septum (Brücke *et al.*, 1959; Wang, 2002; Varga *et al.*, 2008; Hangya *et al.*, 2009). For instance, areas such as the supramammillary nucleus contain rhythmically firing neurons in synchrony with hippocampal theta rhythm is thought to generate theta rhythm (Kocsis and Kaminski, 2006). However, the effect of the supramammillary nucleus on hippocampal theta was suggested to be most likely mediated by the medial septum (Vertes, 1988), due to the interconnections between the three structures. In *Chapter 3*, I have demonstrated in my reported viral hippocampal DG/CA3 retrograde tracing studies such interconnectivity between the DG/CA3, SuM and MSDB. Also MSDB cells containing calretinin, calbindin or both projecting to the SuM have been reported (Borhegyi and Freund, 1998) as well as SuM-hippocampal projecting neurons selectively innervating hippocampal CA2 and DG areas (Vertes,

2015). Interestingly, brainstem stimulation induced theta rhythmic firing the supramammillary nucleus even after elimination of hippocampal theta by medial septal inactivation (Kirk and McNaughton, 1991; Kirk *et al.*, 1996). Within the basal forebrain, behaviour state-dependent cholinergic neurons were identified in the nucleus basalis and the horizontal limb of the diagonal band to exhibit fast, precise, and reliable responses to natural reinforcers such as water reward and air-puff punishment (Hangya, Sachin P Ranade, *et al.*, 2015). This could support my pilot study in *Chapter 3* showing a DG projecting medial septal calbindin positive and air-puff stimulus reacting high rate firing LRN (MS13c). Based on my results, I suggest that the concept of target-specific and area selective cortical innervation by rhythmic subcortical neurons likely applies to the entire basal forebrain and hypothalamic nuclei.

6.4 Technical limitations

Recording and juxtacellular labelling of single neurons deep in the awake brain comes with its challenges, risks and technical limitations. To identify the contribution of single medial septal cells to cortico-cortical circuits requires electrophysiological recordings of single cells during distinct brain and behavioural states and successful juxtacellular labelling of the recorded cell to reveal its cortical projection patterns including postsynaptic target analyses and enable molecular characterizations. Each of the aforementioned steps has its own challenges, thus the yield is expected to be low. However, succeeding across all steps provides valuable insights into the functional role of these cells. Nevertheless, to identify a pattern to finally conclude (a subgroup) requires reproducible results, a challenge in itself among a proven diverse population. Starting from the surgical procedures where recording locations and head-plate implantation must be precisely accurate in order to target the medial septum in a head-fixed configuration to acquiring the technique of breaking suitable glass pipettes for capturing meaningful

signals during intracortical recordings, I had to adapt and optimize several processes during my studies. Labelling was only attempted after sufficient periods of immobility and locomotion were captured, thus, stabilizing a single active cell in the awake moving brain led to many failed labelling attempts. During labelling attempts, high current injections could cause cell damage or cell death leading to unrecoverable cells after perfusions. Perfusions and sectioning the brain and tissue processing including DAB processing were further risk factors in the process of recovering the recorded and labelled cell. I have attempted to replace the degradable neurotracer, neurobiotin, with and non-degradable tracer, BDA (see Methods), to increase the visualization of distal axonal processes including terminals in the targeted areas with limited success. However, successful cases were the strongest labelling attempts, revealing the entire axonal arborizations till the most caudal part of the brain.

6.5 Concluding remarks

This work demonstrates the existence of a diverse population of the medial septal neurons with three identified GABAergic cortical projecting subpopulations, Teevra and Orchid cells (HRNs) and LRNs, suggesting distinct functional roles during cortico-cortical circuits. All identified cells were systematically analyzed based on their physiological, anatomical and molecular parameters and hierarchically positioned with cells that share parameters across all criteria. Each subpopulation demonstrated distinct brain state and behaviour dependent firing activity, cortical target areas and in one case, *Teevra* cells, with cell-type specific targets. Understanding the GABAergic system is crucial for our understanding of various pathological conditions. Dysfunctions in the GABAergic system is associated with several conditions including epilepsy, Parkinson's disease, Alzheimer's disease and mental illness such as anxiety and depression (Kalueff and Nutt, 2007; Schmidt and Mirnics, 2015; Fogaça and Duman, 2019). In addition, in Alzheimer's disease the GABAergic system undergoes significant remodelling at an early stage (Govindpani *et al.*, 2017) and thus, becomes a promising therapeutic target for AD (Calvo-Flores Guzmán *et al.*, 2018).

6.6 Outlook

Despite the fact that matching firing patterns and theta phase-coupling support the proposed functions of identified HRNs and LRNs, other GABAergic septal neurons with different firing patterns may target hippocampal or extra-hippocampal areas i.e. high-rhythmic firing and theta-trough coupled hippocampal targeting GABAergic medial septal neurons, as I have pointed out in my framework (Figure 6-1). In rat, type 1a and 1b rhythmically-bursting medial septal neurons (Gaztelu and Buño, 1982; King, Recce and O'Keefe, 1998) match the profiles of mouse *Komal* and *Teevra* cells, respectively. LRNs match rat type 2 'non-rhythmic' medial septal cells coupled to the descending theta phase (King, Recce and O'Keefe, 1998b), taking into account theta recording site within the hippocampus (Gaztelu and Buño, 1982; Dragoi *et al.*, 1999). The initial silicon probe clustering of medial septal neurons (*Chapter 4*, Joshi *et al.*, 2017) has further shown four major clusters of highly rhythmic medial septal neurons. Only two, the *Teevra* and *Komal* cluster, has been identified so far with *Orchid* cells representing a distinct subpopulation of *Komal* cells (Figure 6-1). For instance, one of the remaining clusters indicated a group of CA1d theta-trough firing HRNs (Joshi *et al.*, 2017). Nevertheless, as indicated in *Chapter 3*, I have already identified an additional group of five medial septal neurons (Table 3-1, Figure 6-1), proposed to be putative new subpopulation of extra-hippocampal projecting HRNs. These five neurons require further analysis including post-synaptic target analysis as most of them are strongly labelled with recovered axon terminals in extra-hippocampal areas such as the medial entorhinal cortex or ventral subiculum. The LRN subgroup revealed three calbindin positive neurons with the majority of their projecting axons terminating in the DG. All identified cells happen to be located in the most rostral part of the medial septum (*Chapter 5*, Figure 5-3). Could that part of the medial septum indicate a location for a specific calbindin positive subgroup targeting the

DG? However, it should be noted that only two of the three calbindin positive medial septal neurons displayed positive immunoreactivity for mGluR1a. Further studies are necessary to shed light on the topographic organization of identified and unidentified subgroups of the medial septum. Finally, the more we disclose the firing patterns of medial septal subgroups with known cortical targets and projection patterns the more it becomes feasible to investigate these patterns in chronic feely moving behaving models to gain a greater insight of their role during behavioural tasks including learning and memory or sleep.

References

Acsády, L., Kamondi, A., Sík, A., Freund, T. and Buzsáki, G. (1998) GABAergic cells are the major postsynaptic targets of mossy fibers in the rat hippocampus., *The Journal of Neuroscience*, 18(9), pp. 3386–403.

Adamantidis, A., Carter, M. C. and de Lecea, L. (2010) Optogenetic deconstruction of sleep-wake circuitry in the brain, *Frontiers in Molecular Neuroscience*, 2, p. 31.

Agostinelli, L. J., Geerling, J. C. and Scammell, T. E. (2019) Basal forebrain subcortical projections, *Brain Structure and Function*.

Albert, M. S. and Moss, M. B. (1999) Early Features of Alzheimer's Disease, in. Springer, Boston, MA, pp. 461–474.

Alexander, M. P. and Freedman, M. (1984) Amnesia after anterior communicating artery aneurysm rupture., *Neurology*, 34(6), pp. 752–7.

Amaral, D. G. and Cowan, W. M. (1980) Subcortical afferents to the hippocampal formation in the monkey, *The Journal of Comparative Neurology*, 189(4), pp. 573–591.

Amaral, D. G. and Kurz, J. (1985) An analysis of the origins of the cholinergic and noncholinergic septal projections to the hippocampal formation of the rat, *The Journal of Comparative Neurology*, 240(1), pp. 37–59.

Amaral, D. G. and Witter, M. P. (1989) The three-dimensional organization of the hippocampal formation: A review of anatomical data, *Neuroscience*. Pergamon, 31(3), pp. 571–591.

Andersen, P. (2007) *The hippocampus book*. Oxford University Press.

Andy, O. J. and Stephan, H. (1968) The septum in the human brain, *The Journal of Comparative Neurology*, 133(3), pp. 383–409.

Aston-Jones, G. and Bloom, F. E. (1981) Activity of norepinephrine-containing locus coeruleus neurons in behaving rats anticipates fluctuations in the sleep-waking cycle., *The Journal of neuroscience : the official journal of the Society for Neuroscience*, 1(8), pp. 876–86.

Bao, H., Asrican, B., Li, W., Gu, B., Wen, Z., Lim, S. A., Haniff, I., Ramakrishnan, C., Deisseroth, K., Philpot, B., *et al.* (2017) Long-Range GABAergic Inputs Regulate Neural Stem Cell Quiescence and Control Adult Hippocampal Neurogenesis, *Cell Stem Cell*, 21(5), pp. 604-617 e5.

Beed, P., Gundlfinger, A., Schneiderbauer, S., Song, J., Böhm, C., Burgalossi, A., Brecht, M., Vida, I. and Schmitz, D. (2013) Inhibitory gradient along the dorsoventral axis in the medial entorhinal cortex, *Neuron*. Cell Press, 79(6), pp. 1197–1207.

Berry, S. D. and Seager, M. A. (2001) Hippocampal Theta Oscillations and Classical Conditioning, *Neurobiology of Learning and Memory*, 76(3), pp. 298–313.

Berry, S. D. and Thompson, R. F. (1978) Prediction of learning rate from the hippocampal electroencephalogram., *Science*, 200(4347), pp. 1298–300.

Bieri, K. W., Bobbitt, K. N. and Colgin, L. L. (2014) Slow and Fast Gamma Rhythms Coordinate

Different Spatial Coding Modes in Hippocampal Place Cells, *Neuron*, 82(3), pp. 670–681.

Bland, B. H., Konopacki, J., Kirk, I. J., Oddie, S. D. and Dickson, C. T. (1995) Discharge patterns of hippocampal theta-related cells in the caudal diencephalon of the urethan-anesthetized rat, *Journal of Neurophysiology*, 74(1), pp. 322–333.

Bland, B. H., Oddie, S. D., Colom, L. V. and Vertes, R. P. (1994) Extrinsic modulation of medial septal cell discharges by the ascending brainstem hippocampal synchronizing pathway, *Hippocampus*, 4(6), pp. 649–660.

Boissard, R., Fort, P., Gervasoni, D., Barbagli, B. and Luppi, P.-H. (2003) Localization of the GABAergic and non-GABAergic neurons projecting to the sublaterodorsal nucleus and potentially gating paradoxical sleep onset., *The European journal of neuroscience*, 18(6), pp. 1627–39.

Borhegyi, Z. (2004) Phase Segregation of Medial Septal GABAergic Neurons during Hippocampal Theta Activity, *Journal of Neuroscience*. Society for Neuroscience, 24(39), pp. 8470–8479.

Borhegyi, Z. and Freund, T. F. (1998) Dual projection from the medial septum to the supramammillary nucleus in the rat., *Brain research bulletin*, 46(5), pp. 453–9.

Borhegyi, Z., Maglóczky, Z., Acsády, L. and Freund, T. F. (1998) The supramammillary nucleus innervates cholinergic and GABAergic neurons in the medial septum-diagonal band of Broca complex., *Neuroscience*, 82(4), pp. 1053–65.

Boyce, R., Glasgow, S. D., Williams, S. and Adamantidis, A. (2016) Causal evidence for the role of REM sleep theta rhythm in contextual memory consolidation, *Science*, 352(6287), pp. 812–816.

Bragin, A., Jandó, G., Nádasdy, Z., Hetke, J., Wise, K. and Buzsáki, G. (1995) Gamma (40-100 Hz) oscillation in the hippocampus of the behaving rat., *The Journal of neuroscience : the official journal of the Society for Neuroscience*, 15(1 Pt 1), pp. 47–60.

Bramham, C. R. and Srebro, B. (1989) Synaptic plasticity in the hippocampus is modulated by behavioral state, *Brain Research*. Elsevier, 493(1), pp. 74–86.

Brandon, M. P., Bogaard, A. R., Libby, C. P., Connerney, M. A., Gupta, K. and Hasselmo, M. E. (2011) Reduction of theta rhythm dissociates grid cell spatial periodicity from directional tuning., *Science*. NIH Public Access, 332(6029), pp. 595–9.

Brandon, M. P., Bogaard, A. R., Schultheiss, N. W. and Hasselmo, M. E. (2013) Segregation of cortical head direction cell assemblies on alternating theta cycles, *Nature Neuroscience*. Nature Publishing Group, 16(6), pp. 739–748.

Brandon, M. P., Koenig, J., Leutgeb, J. K. and Leutgeb, S. (2014) New and Distinct Hippocampal Place Codes Are Generated in a New Environment during Septal Inactivation, *Neuron*. Cell Press, 82(4), pp. 789–796.

Brashear, H. R., Zaborszky, L. and Heimer, L. (1986) Distribution of gabaergic and cholinergic neurons in the rat diagonal band, *Neuroscience*. Pergamon, 17(2), pp. 439–451.

Brown, R. E., Basheer, R., McKenna, J. T., Strecker, R. E. and McCarley, R. W. (2012) Control of Sleep and Wakefulness, *Physiological Reviews*. American Physiological Society Bethesda, MD, 92(3), pp. 1087–1187.

Brücke, F., Petsche, H., Pillat, B. and Deisenhammer, E. (1959) Ein Schrittmacher in der medialen Septumregion des Kaninchengehirnes, *Pflügers Archiv für die Gesamte Physiologie des Menschen und der Tiere*. Springer-Verlag, 269(2), pp. 135–140.

Buetfering, C., Allen, K. and Monyer, H. (2014) Parvalbumin interneurons provide grid cell–driven recurrent inhibition in the medial entorhinal cortex, *Nature Neuroscience*, 17(5), pp. 710–718.

Buhl, E. H., Han, Z. S., Lorinczi, Z., Stezhka, V. V., Karnup, S. V. and Somogyi, P. (1994) Physiological properties of anatomically identified axo-axonic cells in the rat hippocampus, *Journal of Neurophysiology*, 71(4), pp. 1289–1307.

Burgalossi, A., von Heimendahl, M. and Brecht, M. (2014) Deep layer neurons in the rat medial entorhinal cortex fire sparsely irrespective of spatial novelty, *Frontiers in Neural Circuits*. Frontiers, 8, p. 74.

Burgess, N., Maguire, E. A. and O'Keefe, J. (2002) The human hippocampus and spatial and episodic memory, *Neuron*. 2002/08/27, 35(4), pp. 625–641. 2002/08/27.

Butler, T., Zaborszky, L., Pirraglia, E., Li, J., Wang, X. H., Li, Y., Tsui, W., Talos, D., Devinsky, O., Kuchna, I., *et al.* (2014) Comparison of human septal nuclei MRI measurements using automated segmentation and a new manual protocol based on histology., *NeuroImage*. NIH Public Access, 97, pp. 245–51.

Buzsáki, G. (1986) Hippocampal sharp waves: Their origin and significance, *Brain Research*. 1986/11/29. Elsevier, 398(2), pp. 242–252. 1986/11/29.

Buzsáki, G. (2002) Theta oscillations in the hippocampus., *Neuron*, 33(3), pp. 325–40.

Buzsáki, G., Anastassiou, C. A. and Koch, C. (2012) The origin of extracellular fields and currents-EEG, ECoG, LFP and spikes, *Nature Reviews Neuroscience*. 2012/05/19, 13(6), pp. 407–420. 2012/05/19.

Buzsaki, G., Bickford, R. G., Ponomareff, G., Thal, L. J., Mandel, R. and Gage, F. H. (1988) Nucleus basalis and thalamic control of neocortical activity in the freely moving rat., *The Journal of Neuroscience*, 8(11), pp. 4007–26.

Buzsáki, G., Buhl, D. L., Harris, K. D., Csicsvari, J., Czéh, B. and Morozov, A. (2003) Hippocampal network patterns of activity in the mouse, *Neuroscience*. Pergamon, 116(1), pp. 201–211.

Buzsáki, G., Czopf, J., Kondákor, I. and Kellényi, L. (1986) Laminar distribution of hippocampal rhythmic slow activity (RSA) in the behaving rat: Current-source density analysis, effects of urethane and atropine, *Brain Research*. Elsevier, 365(1), pp. 125–137.

Buzsáki, G. and Draguhn, A. (2004) Neuronal olscillations in cortical networks, *Science*, 304(5679), pp. 1926–1929.

Buzsáki, G., Lai-Wo S., L. and Vanderwolf, C. H. (1983) Cellular bases of hippocampal EEG in the behaving rat, *Brain Research Reviews*. 1983/10/01, 6(2), pp. 139–171. 1983/10/01.

Caballero-Bleda -Menno, M., Witter, P., Caballero-Bleda, M. and Witter, M. P. (1994) *Projections from the presubiculum and the parasubiculum to morphologically characterized entorhinal-hippocampal projection neurons in the rat*, *Exp Brain Res*. Springer-Verlag.

Calvo-Flores Guzmán, B., Vinnakota, C., Govindpani, K., Waldvogel, H. J., Faull, R. L. M. and Kwakowsky, A. (2018) The GABAergic system as a therapeutic target for Alzheimer's disease, *Journal of Neurochemistry*. John Wiley & Sons, Ltd (10.1111), 146(6), pp. 649–669.

Canolty, R. T., Edwards, E., Dalal, S. S., Soltani, M., Nagarajan, S. S., Kirsch, H. E., Berger, M. S., Barbaro, N. M. and Knight, R. T. (2006) High Gamma Power Is Phase-Locked to Theta Oscillations in Human Neocortex, *Science*, 313(5793), pp. 1626–1628.

Chrobak, J. J., Stackman, R. W. and Walsh, T. J. (1989) Intraseptal administration of muscimol produces dose-dependent memory impairments in the rat., *Behavioral and neural biology*, 52(3), pp. 357–69.

Cobb, S. R., Buhl, E. H., Halasy, K., Paulsen, O. and Somogyi, P. (1995) Synchronization of neuronal activity in hippocampus by individual GABAergic interneurons, *Nature*. Nature Publishing Group, 378(6552), pp. 75–78.

Colgin, L. L., Denninger, T., Fyhn, M., Hafting, T., Bonnevie, T., Jensen, O., Moser, M.-B. B. and Moser, E. I. (2009) Frequency of gamma oscillations routes flow of information in the hippocampus, *Nature*. Nature Publishing Group, 462(7271), pp. 353–357.

Colgin, L. L. and Moser, E. I. (2010) Gamma Oscillations in the Hippocampus, *Physiology*. American Physiological Society Bethesda, MD, 25(5), pp. 319–329.

Colgin, L. L., Moser, E. I. and Moser, M.-B. (2008) Understanding memory through hippocampal remapping, *Trends in Neurosciences*. Elsevier Current Trends, 31(9), pp. 469–477.

Colom, L. V., Castaneda, M. T., Reyna, T., Hernandez, S. and Garrido-Sanabria, E. (2005) Characterization of medial septal glutamatergic neurons and their projection to the hippocampus, *Synapse*. 2005/08/19, 58(3), pp. 151–164. 2005/08/19.

Czurko, A., Huxter, J., Li, Y., Hangya, B. and Muller, R. U. (2011) Theta Phase Classification of Interneurons in the Hippocampal Formation of Freely Moving Rats, *Journal of Neuroscience*. 2011/03/19, 31(8), pp. 2938–2947. 2011/03/19.

Danielson, N. B., Turi, G. F., Ladow, M., Chavlis, S., Petrantonakis, P. C., Poirazi, P. and Losonczy, A. (2017) In Vivo Imaging of Dentate Gyrus Mossy Cells in Behaving Mice, *Neuron*, 93(3), pp. 552-559.e4.

Dannenberg, H., Kelley, C., Hoyland, A., Monaghan, C. K. and Hasselmo, M. E. (2019) The firing rate speed code of entorhinal speed cells differs across behaviorally relevant time scales and does not depend on medial septum inputs, *The Journal of Neuroscience*, pp. 1450–18.

Détári, L., Rasmusson, D. D. and Semba, K. (1999) The role of basal forebrain neurons in tonic and phasic activation of the cerebral cortex., *Progress in Neurobiology*, 58(3), pp. 249–77.

Détári, L. and Vanderwolf, C. H. (1987) Activity of identified cortically projecting and other basal forebrain neurones during large slow waves and cortical activation in anaesthetized rats., *Brain Research*, 437(1), pp. 1–8.

Dhikav, V. and Anand, K. (2011) Potential Predictors of Hippocampal Atrophy in Alzheimer's Disease, *Drugs & Aging*, 28(1), pp. 1–11.

Diamantaki, M., Frey, M., Berens, P., Preston-Ferrer, P. and Burgalossi, A. (2016) Sparse activity

of identified dentate granule cells during spatial exploration, *eLife*, 5.

Diekelmann, S. and Born, J. (2010) The memory function of sleep, *Nature Reviews Neuroscience*. Nature Publishing Group, 11(2), pp. 114–126.

van Dijk, M. T. and Fenton, A. A. (2018) On How the Dentate Gyrus Contributes to Memory Discrimination, *Neuron*, 98(4), pp. 832-845.e5.

Dragoi, G. and Buzsáki, G. (2006) Temporal Encoding of Place Sequences by Hippocampal Cell Assemblies, *Neuron*, 50(1), pp. 145–157.

Dragoi, G., Carpi, D., Recce, M., Csicsvari, J. and Buzsáki, G. (1999) Interactions between hippocampus and medial septum during sharp waves and theta oscillation in the behaving rat., *The Journal of neuroscience*. Society for Neuroscience, 19(14), pp. 6191–6199.

Duque, A., Balatoni, B., Detari, L. and Zaborszky, L. (2000) EEG Correlation of the Discharge Properties of Identified Neurons in the Basal Forebrain, *Journal of Neurophysiology*, 84(3), pp. 1627–1635.

Duque, A. and Zaborszky, L. (2006) Juxtacellular Labeling of Individual Neurons In Vivo: From Electrophysiology to Synaptology, in *Neuroanatomical Tract-Tracing 3*. Springer US, pp. 197–236.

Ego-Stengel, V. and Wilson, M. A. (2007) Spatial selectivity and theta phase precession in CA1 interneurons, *Hippocampus*. 2006/12/22, 17(2), pp. 161–174. 2006/12/22.

Eichenbaum, H. (2014) Time cells in the hippocampus: a new dimension for mapping memories, *Nature Reviews Neuroscience*, 15(11), pp. 732–744.

Faisal, A. A., Selen, L. P. J. and Wolpert, D. M. (2008) Noise in the nervous system, *Nature Reviews Neuroscience*. Nature Publishing Group, 9(4), pp. 292–303.

Fernández-Ruiz, A., Oliva, A., Nagy, G. A., Maurer, A. P., Berényi, A. and Buzsáki, G. (2017) Entorhinal-CA3 Dual-Input Control of Spike Timing in the Hippocampus by Theta-Gamma Coupling, *Neuron*, 93(5), pp. 1213-1226.e5.

Fiáth, R., Márton, A. L., Mátyás, F., Pinke, D., Márton, G., Tóth, K. and Ulbert, I. (2019) Slow insertion of silicon probes improves the quality of acute neuronal recordings, *Scientific Reports*. Nature Publishing Group, 9(1), p. 111.

Fogaça, M. V. and Duman, R. S. (2019) Cortical GABAergic Dysfunction in Stress and Depression: New Insights for Therapeutic Interventions, *Frontiers in Cellular Neuroscience*. Frontiers, 13, p. 87.

Fonseca, L. C., Tedrus, G. M. A. S., Prandi, L. R., Almeida, A. M. and Furlanetto, D. S. (2011) Alzheimer's disease: relationship between cognitive aspects and power and coherence EEG measures., *Arquivos de neuro-psiquiatria*. 2012/02/03, 69(6), pp. 875–881. 2012/02/03.

Ford, R. D., Colom, L. V and Bland, B. H. (1989) The classification of medial septum-diagonal band cells as theta-on or theta-off in relation to hippocampal EEG states., *Brain Research*, 493(2), pp. 269–82.

Franklin, K. B. J. and Paxinos, G. (2001) *Paxinos and Franklin's The mouse brain in stereotaxic coordinates*. second edi. second edi.

Freund, T. F. (1989) GABAergic septohippocampal neurons contain parvalbumin, *Brain Research*, 478(2), pp. 375–381.

Freund, T. F. and Antal, M. (1988) GABA-containing neurons in the septum control inhibitory interneurons in the hippocampus, *Nature*. Nature Publishing Group, 336(6195), pp. 170–173.

Freund, T. F. and Buzsáki, G. (1998) Interneurons of the hippocampus, *Hippocampus*. John Wiley & Sons, Ltd, 6(4), pp. 347–470.

Fries, P. (2005) A mechanism for cognitive dynamics: Neuronal communication through neuronal coherence, *Trends in Cognitive Sciences*, 9(10), pp. 474–480.

Fuchs, E. C. C., Neitz, A., Pinna, R., Melzer, S., Caputi, A. and Monyer, H. (2016) Local and Distant Input Controlling Excitation in Layer II of the Medial Entorhinal Cortex, *Neuron*. Cell Press, 89(1), pp. 194–208.

Fuhrmann, F., Justus, D., Sosulina, L., Kaneko, H., Beutel, T., Friedrichs, D., Schoch, S., Schwarz, M. K., Fuhrmann, M. and Remy, S. (2015) Locomotion, Theta Oscillations, and the Speed-Correlated Firing of Hippocampal Neurons Are Controlled by a Medial Septal Glutamatergic Circuit, *Neuron*. 2015/05/20. Cell Press, 86(5), pp. 1253–1264. 2015/05/20.

Fujii, T., Okuda, J., Tsukiura, T., Ohtake, H., Miura, R., Fukatsu, R., Suzuki, K., Kawashima, R., Itoh, M., Fukuda, H., *et al.* (2002) The Role of the Basal Forebrain in Episodic Memory Retrieval: A Positron Emission Tomography Study, *NeuroImage*, 15(3), pp. 501–508.

Ganter, P., Szücs, P., Paulsen, O. and Somogyi, P. (2004) Properties of horizontal axo-axonic cells in stratum oriens of the hippocampal CA1 area of rats in vitro, *Hippocampus*, 14(2), pp. 232–243.

Gaztelu, J. M. and Buño, W. (1982) Septo-hippocampal relationship during EEG theta rhythm, *Electroencephalography and Clinical Neurophysiology*. Elsevier, 54(4), pp. 375–387.

Germroth, P., Schwerdtfeger, W. K. and Buhl, E. H. (1989) GABAergic neurons in the entorhinal cortex project to the hippocampus, *Brain Research*. Elsevier, 494(1), pp. 187–192.

Givens, B. S. and Olton, D. S. (1990) Cholinergic and GABAergic modulation of medial septal area: Effect on working memory., *Behavioral Neuroscience*, 104(6), pp. 849–855.

Gogolák, G., Stumpf, C., Petsche, H. and Sterc, J. (1968) The firing pattern of septal neurons and the form of the hippocampal theta wave., *Brain Research*, 7(2), pp. 201–7.

Gonzalez-Sulser, A., Parthier, D., Candela, A., McClure, C., Pastoll, H., Garden, D., Surmeli, G. and Nolan, M. F. (2014) GABAergic Projections from the Medial Septum Selectively Inhibit Interneurons in the Medial Entorhinal Cortex, *Journal of Neuroscience*. Society for Neuroscience, 34(50), pp. 16739–16743.

Good, P. (1994) *Permutation Tests*. New York, NY: Springer New York (Springer Series in Statistics).

Govindpani, K., Guzmán, B. C.-F., Vinnakota, C., Waldvogel, H. J., Faull, R. L., Kwakowsky, A., Govindpani, K., Calvo-Flores Guzmán, B., Vinnakota, C., Waldvogel, H. J., *et al.* (2017) Towards a Better Understanding of GABAergic Remodeling in Alzheimer's Disease, *International Journal of Molecular Sciences*. Multidisciplinary Digital Publishing Institute, 18(8), p. 1813.

Gritti, I., Mainville, L., Mancia, M. and Jones, B. E. (1997) GABAergic and other noncholinergic basal forebrain neurons, together with cholinergic neurons, project to the mesocortex and isocortex in the rat., *The Journal of comparative neurology*, 383(2), pp. 163–77.

van Groen, T. and Wyss, J. M. (1990) The postsubicular cortex in the rat: characterization of the fourth region of the subicular cortex and its connections, *Brain Research*. Elsevier, 529(1–2), pp. 165–177.

Guzowski, J. F., Knierim, J. J. and Moser, E. I. (2004) Ensemble Dynamics of Hippocampal Regions CA3 and CA1, *Neuron*, 44(4), pp. 581–584.

Hafting, T., Fyhn, M., Bonnevie, T., Moser, M.-B. and Moser, E. I. (2008) Hippocampus-independent phase precession in entorhinal grid cells, *Nature*, 453(7199), pp. 1248–1252.

Hafting, T., Fyhn, M., Molden, S., Moser, M.-B. B. and Moser, E. I. (2005) Microstructure of a spatial map in the entorhinal cortex, *Nature*. Nature Publishing Group, 436(7052), pp. 801–806.

Haglund, L., Swanson, L. W. and Köhler, C. (1984) The projection of the supramammillary nucleus to the hippocampal formation: An immunohistochemical and anterograde transport study with the lectin PHA-L in the rat, *Journal of Comparative Neurology*, 229(2), pp. 171–185.

Hajszan, T., Alreja, M. and Leranth, C. (2004) Intrinsic vesicular glutamate transporter 2-immunoreactive input to septohippocampal parvalbumin-containing neurons: Novel glutamatergic local circuit cells, *Hippocampus*, 14(4), pp. 499–509.

Han, Y., Shi, Y., Xi, W., Zhou, R., Tan, Z., Wang, H., Li, X., Chen, Z., Feng, G., Luo, M., *et al.* (2014) Selective Activation of Cholinergic Basal Forebrain Neurons Induces Immediate Sleep-wake Transitions, *Current Biology*, 24(6), pp. 693–698.

Han, Z. S., Buhl, E. H., Lörinczi, Z. and Somogyi, P. (1993) A high degree of spatial selectivity in the axonal and dendritic domains of physiologically identified local-circuit neurons in the dentate gyrus of the rat hippocampus., *The European journal of neuroscience*, 5(5), pp. 395–410.

Hangya, B., Borhegyi, Z., Szilagyi, N., Freund, T. F. and Varga, V. (2009) GABAergic Neurons of the Medial Septum Lead the Hippocampal Network during Theta Activity, *Journal of Neuroscience*, 29(25), pp. 8094–8102.

Hangya, B., Li, Y., Muller, R. U. and Czurkó, A. (2010) Complementary spatial firing in place cell-interneuron pairs, *Journal of Physiology*. 2010/09/08, 588(21), pp. 4165–4175. 2010/09/08.

Hangya, B., Ranade, Sachin P., Lorenc, M. and Kepecs, A. (2015) Central Cholinergic Neurons Are Rapidly Recruited by Reinforcement Feedback, *Cell*. Cell Press, 162(5), pp. 1155–1168.

Haring, J. H., Yan, W. and Faber, K. M. (1997) Neuronal dye coupling in the developing rat fascia dentata., *Brain research. Developmental brain research*, 103(2), pp. 205–8.

Harris, K. D., Csicsvari, J., Hirase, H., Dragoi, G. and Buzsáki, G. (2003) Organization of cell assemblies in the hippocampus, *Nature*. Nature Publishing Group, 424(6948), pp. 552–556.

Hasselmo, M. E. (2005) What is the function of hippocampal theta rhythm?—Linking behavioral

data to phasic properties of field potential and unit recording data, *Hippocampus*. John Wiley & Sons, Ltd, 15(7), pp. 936–949.

Hasselmo, M. E., Bodelón, C. and Wyble, B. P. (2002) A Proposed Function for Hippocampal Theta Rhythm: Separate Phases of Encoding and Retrieval Enhance Reversal of Prior Learning, *Neural Computation*, 14(4), pp. 793–817.

Hebb, D. O. (Donald O. (1949) *The organization of behavior a neuropsychological theory*. L. Erlbaum Associates.

Henderson, Z., Lu, C. B., Janzsó, G., Matto, N., McKinley, C. E., Yanagawa, Y. and Halasy, K. (2010) Distribution and role of Kv3.1b in neurons in the medial septum diagonal band complex, *Neuroscience*, 166(3), pp. 952–969.

Henriksen, E. J., Colgin, L. L., Barnes, C. A., Witter, M. P., Moser, M. B. and Moser, E. I. (2010) Spatial representation along the proximodistal axis of CA1, *Neuron*. Cell Press, 68(1), pp. 127–137.

Hobson, J., McCarley, R. and Wyzinski, P. (1975) Sleep cycle oscillation: reciprocal discharge by two brainstem neuronal groups, *Science*, 189(4196), pp. 55–58.

Huerta, P. T. and Lisman, J. E. (1993) Heightened synaptic plasticity of hippocampal CA1 neurons during a Cholinergically induced rhythmic state, *Nature*. 1993/08/19, 364(6439), pp. 723–725. 1993/08/19.

Huerta, P. T. and Lisman, J. E. (1995) Bidirectional synaptic plasticity induced by a single burst during cholinergic theta oscillation in CA1 in vitro, *Neuron*. Cell Press, 15(5), pp. 1053–1063.

Jadhav, S. P., Kemere, C., German, P. W. and Frank, L. M. (2012) Awake Hippocampal Sharp-Wave Ripples Support Spatial Memory, *Science*, 336(6087), pp. 1454–1458.

Jeffery, K. J., Donnett, J. G., O'keefe, J. and O'Keefe, J. (1995) Medial septal control of theta-correlated unit firing in the entorhinal cortex of awake rats, *NeuroReport*, 6(16), pp. 2166–2170.

Jensen, O. and Lisman, J. E. (2005) Hippocampal sequence-encoding driven by a cortical multi-item working memory buffer, *Trends in Neurosciences*. Elsevier Current Trends, 28(2), pp. 67–72.

Jinno, S., Klausberger, T., Marton, L. F., Dalezios, Y., Roberts, J. D. B., Fuentealba, P., Bushong, E. A., Henze, D., Buzsáki, G., Somogyi, P., *et al.* (2007) Neuronal Diversity in GABAergic Long-Range Projections from the Hippocampus, *Journal of Neuroscience*. Society for Neuroscience, 27(33), pp. 8790–8804.

Jinno, S. and Kosaka, T. (2002) Patterns of expression of calcium binding proteins and neuronal nitric oxide synthase in different populations of hippocampal GABAergic neurons in mice, *Journal of Comparative Neurology*, 449(1), pp. 1–25.

Jones, B. E. (2004) Activity, modulation and role of basal forebrain cholinergic neurons innervating the cerebral cortex, in *Progress in Brain Research*, pp. 157–169.

Jones, R. S. G. and Bühl, E. H. (1993) Basket-like interneurones in layer II of the entorhinal cortex exhibit a powerful NMDA-mediated synaptic excitation, *Neuroscience Letters*. Elsevier, 149(1), pp. 35–39.

Joshi, A., Salib, M., Viney, T. J., Dupret, D. and Somogyi, P. (2017) Behavior-Dependent Activity and Synaptic Organization of Septo-hippocampal GABAergic Neurons Selectively Targeting the Hippocampal CA3 Area, *Neuron*. Cell Press, 96(6), pp. 1342-1357.e5.

Jung, M. W. and McNaughton, B. L. (1993) Spatial selectivity of unit activity in the hippocampal granular layer, *Hippocampus*, 3(2), pp. 165–182.

Justus, D., Dalügge, D., Bothe, S., Fuhrmann, F., Hannes, C., Kaneko, H., Friedrichs, D., Sosulina, L., Schwarz, I., Elliott, D. A., *et al.* (2017) Glutamatergic synaptic integration of locomotion speed via septoentorhinal projections, *Nature Neuroscience*. Nature Publishing Group, 20(1), pp. 16–19.

Jyoti, A., Plano, A., Riedel, G. and Platt, B. (2010) EEG, Activity, and Sleep Architecture in a Transgenic AβPPswe/PSEN1A246E Alzheimer's Disease Mouse, *Journal of Alzheimer's Disease*. 2010/09/23, 22(3), pp. 873–887. 2010/09/23.

Kajiwara, R., Wouterlood, F. G., Sah, A., Boekel, A. J., Baks-te Bulte, L. T. G. and Witter, M. P. (2008) Convergence of entorhinal and CA3 inputs onto pyramidal neurons and interneurons in hippocampal area CA1—An anatomical study in the rat, *Hippocampus*, 18(3), pp. 266–280.

Kalueff, A. V. and Nutt, D. J. (2007) Role of GABA in anxiety and depression, *Depression and Anxiety*. John Wiley & Sons, Ltd, 24(7), pp. 495–517.

Kang, D., Ding, M., Topchiy, I. and Kocsis, B. (2017) Reciprocal Interactions between Medial Septum and Hippocampus in Theta Generation: Granger Causality Decomposition of Mixed Spike-Field Recordings, *Frontiers in Neuroanatomy*, 11.

Katona, L., Lapray, D., Viney, T. J., Oulhaj, A., Borhegyi, Z., Micklem, B. R., Klausberger, T. and Somogyi, P. (2014) Sleep and Movement Differentiates Actions of Two Types of Somatostatin-Expressing GABAergic Interneuron in Rat Hippocampus, *Neuron*. Cell Press, 82(4), pp. 872–886.

Kim, J.-S., Lee, S.-H., Park, G., Kim, S., Bae, S.-M., Kim, D.-W. and Im, C.-H. (2012) Clinical Implications of Quantitative Electroencephalography and Current Source Density in Patients with Alzheimer's Disease, *Brain Topography*. 2012/06/28, 25(4), pp. 461–474. 2012/06/28.

Kimura, H., McGeer, P. L., Peng, F. and McGeer, E. G. (1980) Choline acetyltransferase-containing neurons in rodent brain demonstrated by immunohistochemistry., *Science*, 208(4447), pp. 1057–9.

King, C., Recce, M. and O'Keefe, J. (1998a) The rhythmicity of cells of the medial septum/diagonal band of Broca in the awake freely moving rat: Relationships with behaviour and hippocampal theta, *European Journal of Neuroscience*, 10(2), pp. 464–477.

Kirk, I. J. (1998) Frequency modulation of hippocampal theta by the supramammillary nucleus, and other hypothalamo-hippocampal interactions: mechanisms and functional implications., *Neuroscience & Biobehavioral Reviews*, 22(2), pp. 291–302.

Kirk, I. J. and McNaughton, N. (1991) Supramammillary cell firing and hippocampal rhythmical slow activity., *Neuroreport*, 2(11), pp. 723–5.

Kirk, I. J. and McNaughton, N. (1993) Mapping the differential effects of procaine on frequency and amplitude of reticularly elicited hippocampal rhythmical slow activity, *Hippocampus*,

3(4), pp. 517–525.

Kirk, I. J., Oddie, S. D., Konopacki, J. and Bland, B. H. (1996) Evidence for differential control of posterior hypothalamic, supramammillary, and medial mammillary theta-related cellular discharge by ascending and descending pathways., *The Journal of Neuroscience*, 16(17), pp. 5547–54.

Kiss, J., Patel, A. J., Baimbridge, K. G. and Freund, T. F. (1990) Topographical localization of neurons containing parvalbumin and choline acetyltransferase in the medial septum-diagonal band region of the rat, *Neuroscience*, 36(1), pp. 61–72.

Klausberger, T., Magill, P. J., Márton, L. F., Roberts, J. D. B., Cobden, P. M., Buzsáki, G. and Somogyi, P. (2003) Brain-state- and cell-type-specific firing of hippocampal interneurons in vivo, *Nature*, 421(6925), pp. 844–848.

Klausberger, T., Márton, L. F., Baude, A., Roberts, J. D. B., Magill, P. J. and Somogyi, P. (2004) Spike timing of dendrite-targeting bistratified cells during hippocampal network oscillations in vivo, *Nature Neuroscience*. Nature Publishing Group, 7(1), pp. 41–47.

Klausberger, T. and Somogyi, P. (2008) Neuronal diversity and temporal dynamics: The unity of hippocampal circuit operations, *Science*, 321(5885), pp. 53–57.

Kocsis, B. and Kaminski, M. (2006) Dynamic changes in the direction of the theta rhythmic drive between supramammillary nucleus and the septohippocampal system, *Hippocampus*, 16(6), pp. 531–540.

Kocsis, B. and Vertes, R. P. (1994) Characterization of neurons of the supramammillary nucleus and mammillary body that discharge rhythmically with the hippocampal theta rhythm in the rat., *The Journal of Neuroscience*, 14(11 Pt 2), pp. 7040–52.

Koenig, J., Linder, A. N., Leutgeb, J. K. and Leutgeb, S. (2011) The spatial periodicity of grid cells is not sustained during reduced theta oscillations, *Science*. American Association for the Advancement of Science, 332(6029), pp. 592–595.

Köhler, C., Chan-Palay, V. and Wu, J. Y. (1984) Septal neurons containing glutamic acid decarboxylase immunoreactivity project to the hippocampal region in the rat brain, *Anatomy and Embryology*, 169(1), pp. 41–44.

Korotkova, T., Ponomarenko, A., Monaghan, C. K., Poulter, S. L., Cacucci, F., Wills, T., Hasselmo, M. E. and Lever, C. (2018) Reconciling the different faces of hippocampal theta: The role of theta oscillations in cognitive, emotional and innate behaviors, *Neuroscience & Biobehavioral Reviews*, 85, pp. 65–80.

Kosaka, T. (1980) The axon initial segment as a synaptic site: Ultrastructure and synaptology of the initial segment of the pyramidal cell in the rat hippocampus (CA3 region), *Journal of Neurocytology*. Kluwer Academic Publishers, 9(6), pp. 861–882.

Kramis, R., Vanderwolf, C. H. and Bland, B. H. (1975) Two types of hippocampal rhythmical slow activity in both the rabbit and the rat: Relations to behavior and effects of atropine, diethyl ether, urethane, and pentobarbital, *Experimental Neurology*. Academic Press, 49(1), pp. 58–85.

Kunec, S., Hasselmo, M. E. and Kopell, N. (2005) Encoding and Retrieval in the CA3 Region of the Hippocampus: A Model of Theta-Phase Separation, *Journal of Neurophysiology*. American Physiological Society, 94(1), pp. 70–82.

Lapray, D., Lasztoczi, B., Lagler, M., Viney, T. J., Katona, L., Valenti, O., Hartwich, K., Borhegyi, Z., Somogyi, P. and Klausberger, T. (2012) Behavior-dependent specialization of identified hippocampal interneurons, *Nature Neuroscience*. 2012/08/07, 15(9), pp. 1265–1271. 2012/08/07.

Lasztóczi, B. and Klausberger, T. (2016) Hippocampal Place Cells Couple to Three Different Gamma Oscillations during Place Field Traversal, *Neuron*. Cell Press, 91(1), pp. 34–40.

Lasztóczi, B. and Klausberger, T. (2017) Distinct gamma oscillations in the distal dendritic fields of the dentate gyrus and the CA1 area of mouse hippocampus, *Brain Structure and Function*.

Lasztoczi, B., Tukker, J. J., Somogyi, P. and Klausberger, T. (2011) Terminal Field and Firing Selectivity of Cholecystokinin-Expressing Interneurons in the Hippocampal CA3 Area, *Journal of Neuroscience*, 31(49), pp. 18073–18093.

Lecourtier, L., de Vasconcelos, A. P., Leroux, E., Cosquer, B., Geiger, K., Lithfous, S. and Cassel, J. C. (2011) Septohippocampal pathways contribute to system consolidation of a spatial memory: Sequential implication of gabaergic and cholinergic neurons, *Hippocampus*. 2010/07/14, 21(12), pp. 1277–1289. 2010/07/14.

Lee, B. H., Lamour, Y. and Bassant, M. H. (1991) Iontophoretic study of medial septal neurons in the unanesthetized rat, *Neuroscience Letters*. Elsevier, 128(1), pp. 29–32.

Leranth, C., Carpi, D., Buzsaki, G. and Kiss, J. (1999) The entorhino-septo-supramammillary nucleus connection in the rat: morphological basis of a feedback mechanism regulating hippocampal theta rhythm., *Neuroscience*, 88(3), pp. 701–18.

Leranth, C. and Kiss, J. (1996) A population of supramammillary area calretinin neurons terminating on medial septal area cholinergic and lateral septal area calbindin-containing cells are aspartate/glutamatergic., *The Journal of Neuroscience*, 16(23), pp. 7699–710.

Leung, L. S. (1992) Fast (beta) rhythms in the hippocampus: A review, *Hippocampus*, 2(2), pp. 93–98.

Leung, L. W., Lopes da Silva, F. H. and Wadman, W. J. (1982) Spectral characteristics of the hippocampal EEG in the freely moving rat., *Electroencephalography and clinical neurophysiology*, 54(2), pp. 203–19.

Leutgeb, J. K., Leutgeb, S., Moser, M.-B. and Moser, E. I. (2007) Pattern Separation in the Dentate Gyrus and CA3 of the Hippocampus, *Science*, 315(5814), pp. 961–966.

Leutgeb, S. and Mizumori, S. J. (1999) Excitotoxic septal lesions result in spatial memory deficits and altered flexibility of hippocampal single-unit representations., *The Journal of Neuroscience*, 19(15), pp. 6661–72.

Li, X.-G., Somogyi, P., Ylinen, A. and Buzsáki, G. (1994) The hippocampal CA3 network: An in vivo intracellular labeling study, *Journal of Comparative Neurology*, 339(2), pp. 181–208.

Llinas, R. (1988) The intrinsic electrophysiological properties of mammalian neurons: insights into central nervous system function, *Science*, 242(4886), pp. 1654–1664.

Lopes-dos-Santos, V., van de Ven, G. M., Morley, A., Trouche, S., Campo-Urriza, N. and Dupret, D. (2018) Parsing Hippocampal Theta Oscillations by Nested Spectral Components during

Spatial Exploration and Memory-Guided Behavior, *Neuron*, 100(4), pp. 940-952.e7.

Louie, K. and Wilson, M. A. (2001) Temporally structured replay of awake hippocampal ensemble activity during rapid eye movement sleep., *Neuron*, 29(1), pp. 145–56.

Lovett-Barron, M., Turi, G. F., Kaifosh, P., Lee, P. H., Bolze, F., Sun, X.-H., Nicoud, J.-F., Zemelman, B. V, Sternson, S. M. and Losonczy, A. (2012) Regulation of neuronal input transformations by tunable dendritic inhibition, *Nature Neuroscience*, 15(3), pp. 423–430.

Lu, J., Sherman, D., Devor, M. and Saper, C. B. (2006) A putative flip–flop switch for control of REM sleep, *Nature*, 441(7093), pp. 589–594.

Lubenov, E. and Siapas, a (2009) Hippocampal theta oscillations are travelling waves, *Nature*, 459(7246), pp. 534–9.

Manns, I. D., Alonso, A. and Jones, B. E. (2000) Discharge profiles of juxtacellularly labeled and immunohistochemically identified GABAergic basal forebrain neurons recorded in association with the electroencephalogram in anesthetized rats., *The Journal of Neuroscience*, 20(24), pp. 9252–63.

Manns, I. D., Alonso, A. and Jones, B. E. (2003) Rhythmically Discharging Basal Forebrain Units Comprise Cholinergic, GABAergic, and Putative Glutamatergic Cells, *Journal of Neurophysiology*, 89(2), pp. 1057–1066.

Manns, J. R., Zilli, E. A., Ong, K. C., Hasselmo, M. E. and Eichenbaum, H. (2007) Hippocampal CA1 spiking during encoding and retrieval: Relation to theta phase, *Neurobiology of Learning and Memory*. Academic Press, 87(1), pp. 9–20.

Mattis, J., Brill, J., Evans, S., Lerner, T. N., Davidson, T. J., Hyun, M., Ramakrishnan, C., Deisseroth, K. and Huguenard, J. R. (2014) Frequency-Dependent, Cell Type-Divergent Signaling in the Hippocamposeptal Projection, *Journal of Neuroscience*, 34(35), pp. 11769–11780.

Maurer, A. P., Cowen, S. L., Burke, S. N., Barnes, C. A. and McNaughton, B. L. (2006) Phase Precession in Hippocampal Interneurons Showing Strong Functional Coupling to Individual Pyramidal Cells, *Journal of Neuroscience*. 2006/12/29, 26(52), pp. 13485–13492. 2006/12/29.

McCarley, R. and Hobson, J. (1975) Neuronal excitability modulation over the sleep cycle: a structural and mathematical model, *Science*, 189(4196), pp. 58–60.

McGinty, D. J. and Harper, R. M. (1976) Dorsal raphe neurons: depression of firing during sleep in cats, *Brain Research*, 101(3), pp. 569–575.

McNaughton, N., Ruan, M. and Woodnorth, M.-A. A. (2006) Restoring theta-like rythmicity in rats restores initial learning in the Morris water maze, *Hippocampus*. Wiley-Blackwell, 16(12), pp. 1102–1110.

Melzer, S., Michael, M., Caputi, A., Eliava, M., Fuchs, E. C., Whittington, M. A. and Monyer, H. (2012) Long-Range-Projecting GABAergic Neurons Modulate Inhibition in Hippocampus and Entorhinal Cortex, *Science*, 335(6075), pp. 1506–1510.

Middleton, S. J. and McHugh, T. J. (2016) Silencing CA3 disrupts temporal coding in the CA1 ensemble., *Nature neuroscience*, 19(7), pp. 945–51.

Mitchell, S., Rawlins, J., Steward, O. and Olton, D. (1982) Medial septal area lesions disrupt theta rhythm and cholinergic staining in medial entorhinal cortex and produce impaired radial arm maze behavior in rats, *Journal of Neuroscience*. Society for Neuroscience, 2(3), pp. 292–302.

Mizuseki, K., Sirota, A., Pastalkova, E. and Buzsáki, G. (2009) Theta Oscillations Provide Temporal Windows for Local Circuit Computation in the Entorhinal-Hippocampal Loop, *Neuron*. 2009/10/31. Cell Press, 64(2), pp. 267–280. 2009/10/31.

Morris, R. G. M., Garrud, P., Rawlins, J. N. P. and O'Keefe, J. (1982) Place navigation impaired in rats with hippocampal lesions, *Nature*. 1982/06/24, 297(5868), pp. 681–683. 1982/06/24.

Nerad, L. and McNaughton, N. (2006) The septal EEG suggests a distributed organization of the pacemaker of hippocampal theta in the rat, *European Journal of Neuroscience*. Wiley/Blackwell (10.1111), 24(1), pp. 155–166.

Neunuebel, J. P. and Knierim, J. J. (2014) CA3 Retrieves Coherent Representations from Degraded Input: Direct Evidence for CA3 Pattern Completion and Dentate Gyrus Pattern Separation, *Neuron*. Cell Press, 81(2), pp. 416–427.

O'Keefe, J. and Burgess, N. (2005) Dual phase and rate coding in hippocampal place cells: Theoretical significance and relationship to entorhinal grid cells, *Hippocampus*. John Wiley & Sons, Ltd, 15(7), pp. 853–866.

O'Keefe, J. and Dostrovsky, J. (1971) The hippocampus as a spatial map. Preliminary evidence from unit activity in the freely-moving rat, *Brain Research*. 1971/11/01. Elsevier, 34(1), pp. 171–175. 1971/11/01.

O'Keefe, J. and Nadel, L. (1978) *The hippocampus as a cognitive map*. OxfordNew York: Clarendon Press ;Oxford University Press.

O'Keefe, J. and Recce, M. L. (1993) Phase relationship between hippocampal place units and the EEG theta rhythm, *Hippocampus*. 1993/07/01, 3(3), pp. 317–330. 1993/07/01.

Oddie, S. D., Bland, B. H., Colom, L. V. and Vertes, R. P. (1994) The midline posterior hypothalamic region comprises a critical part of the ascending brainstem hippocampal synchronizing pathway, *Hippocampus*, 4(4), pp. 454–473.

Orzeł-Gryglewska, J., Matulewicz, P. and Jurkowlaniec, E. (2015) Brainstem system of hippocampal theta induction: The role of the ventral tegmental area, *Synapse*, 69(11), pp. 553–575.

Oyibo, H. K., Znamenskiy, P., Oviedo, H. V., Enquist, L. W. and Zador, A. M. (2014) Long-term Cre-mediated retrograde tagging of neurons using a novel recombinant pseudorabies virus, *Frontiers in Neuroanatomy*. Frontiers, 8, p. 86.

Pace-Schott, E. F. and Hobson, J. A. (2002) The Neurobiology of Sleep: Genetics, cellular physiology and subcortical networks, *Nature Reviews Neuroscience*, 3(8), pp. 591–605.

Pang, K. C. H., Jiao, X., Sinha, S., Beck, K. D. and Servatius, R. J. (2010) Damage of GABAergic neurons in the medial septum impairs spatial working memory and extinction of active avoidance: Effects on proactive interference, *Hippocampus*, 21(8), p. n/a-n/a.

Pastalkova, E., Itskov, V., Amarasingham, A., Buzsaki, G. and Buzsáki, G. (2008) Internally generated cell assembly sequences in the rat hippocampus, *Science*, 321(5894), pp. 1322–

1327.

Pavlides, C., Greenstein, Y. J., Grudman, M. and Winson, J. (1988) Long-term potentiation in the dentate gyrus is induced preferentially on the positive phase of θ-rhythm, *Brain Research*. 1988/01/26, 439(1–2), pp. 383–387. 1988/01/26.

Penttonen, M., Kamondi, A., Sik, A., Acsády, L. and Buzsáki, G. (1998) Feed-forward and feed-back activation of the dentate gyrus in vivo during dentate spikes and sharp wave bursts, *Hippocampus*. Wiley-Blackwell, 7(4), pp. 437–450.

Pepeu, G. and Blandina, P. (1998) The acetylcholine, GABA, glutamate triangle in the rat forebrain, *Journal of Physiology-Paris*, 92(5–6), pp. 351–355.

Perrenoud, Q., Geoffroy, H., Gauthier, B., Rancillac, A., Alfonsi, F., Kessaris, N., Rossier, J., Vitalis, T. and Gallopin, T. (2012) Characterization of Type I and Type II nNOS-Expressing Interneurons in the Barrel Cortex of Mouse, *Frontiers in Neural Circuits*, 6, p. 36.

Petsche, H., Stumpf, C. and Gogolak, G. (1962) The significance of the rabbit's septum as a relay station between the midbrain and the hippocampus I. The control of hippocampus arousal activity by the septum cells, *Electroencephalography and Clinical Neurophysiology*. 1962/04/01. Elsevier, 14(2), pp. 202–211. 1962/04/01.

Pinault, D. (1996) A novel single-cell staining procedure performed in vivo under electrophysiological control: Morpho-functional features of juxtacellularly labeled thalamic cells and other central neurons with biocytin or Neurobiotin, *Journal of Neuroscience Methods*. 1996/04/01. Elsevier, 65(2), pp. 113–136. 1996/04/01.

Preilowski, B. (2009) Erinnerung an einen Amnestiker (und ein halbes Jahrhundert Gedächtnisforschung), *Fortschritte der Neurologie · Psychiatrie*, 77(10), pp. 568–576.

Preston-Ferrer, P., Coletta, S., Frey, M. and Burgalossi, A. (2016) Anatomical organization of presubicular head-direction circuits, *eLife*. eLife Sciences Publications Limited, 5(JUNE2016), p. e14592.

Raisman, G. (1966) The connexions of the septum, *Brain*. 1966/06/01, 89(2), pp. 317–348. 1966/06/01.

Rawlins, J. N. P., Feldon, J. and Gray, J. A. (1979) Septo-hippocampal connections and the hippocampal theta rhythm, *Experimental Brain Research*. Springer-Verlag, 37(1), pp. 49–63.

Risold, P. . and Swanson, L. . (1997) Chemoarchitecture of the rat lateral septal nucleus, *Brain Research Reviews*. Elsevier, 24(2–3), pp. 91–113.

Rubio, S. E., Vega-Flores, G., Martínez, A., Bosch, C., Pérez-Mediavilla, A., del Río, J., Gruart, A., Delgado-García, J. M., Soriano, E. and Pascual, M. (2012) Accelerated aging of the GABAergic septohippocampal pathway and decreased hippocampal rhythms in a mouse model of Alzheimer's disease, *The FASEB Journal*, 26(11), pp. 4458–4467.

Rye, D. B., Wainer, B. H., Mesulam, M. M., Mufson, E. J. and Saper, C. B. (1984) Cortical projections arising from the basal forebrain: a study of cholinergic and noncholinergic components employing combined retrograde tracing and immunohistochemical localization of choline acetyltransferase., *Neuroscience*, 13(3), pp. 627–43.

Salib, M. (2015) *Firing patterns and postsynaptic cortical targets of medial septal neurons*

recorded and labelled in behaving mice. MSc Thesis (University of Oxford).

Salib, M., Joshi, A., Katona, L., Howarth, M., Somogyi, P. and Viney, T. J. (2019) GABAergic medial septal neurons with low-rhythmic firing innervating the dentate gyrus and hippocampal area CA3, *The Journal of Neuroscience*.

Saper, C. B. (1985) Organization of cerebral cortical afferent systems in the rat. II. Hypothalamocortical projections, *The Journal of Comparative Neurology*, 237(1), pp. 21–46.

Saper, C. B., Fuller, P. M., Pedersen, N. P., Lu, J. and Scammell, T. E. (2010) Sleep State Switching, *Neuron*, 68(6), pp. 1023–1042.

Sapin, E., Lapray, D., Bérod, A., Goutagny, R., Léger, L., Ravassard, P., Clément, O., Hanriot, L., Fort, P. and Luppi, P.-H. (2009) Localization of the Brainstem GABAergic Neurons Controlling Paradoxical (REM) Sleep, *PLoS ONE*. Edited by P. A. Bartell, 4(1), p. e4272.

Scharfman, H. E. and Myers, C. E. (2013) Hilar mossy cells of the dentate gyrus: a historical perspective, *Frontiers in Neural Circuits*. Frontiers, 6, p. 106.

Schlesiger, M. I., Cannova, C. C., Boublil, B. L., Hales, J. B., Mankin, E. A., Brandon, M. P., Leutgeb, J. K., Leibold, C. and Leutgeb, S. (2015) The medial entorhinal cortex is necessary for temporal organization of hippocampal neuronal activity, *Nature Neuroscience*. Nature Publishing Group, 18(8), pp. 1123–1132.

Schmidt, M. J. and Mirnics, K. (2015) Neurodevelopment, GABA system dysfunction, and schizophrenia., *Neuropsychopharmacology : official publication of the American College of Neuropsychopharmacology*. Nature Publishing Group, 40(1), pp. 190–206.

Schomburg, E. W., Fernández-Ruiz, A., Mizuseki, K., Berényi, A., Anastassiou, C. A., Koch, C. and Buzsáki, G. (2014) Theta Phase Segregation of Input-Specific Gamma Patterns in Entorhinal-Hippocampal Networks, *Neuron*. 2014/09/30. Cell Press, 84(2), pp. 470–485. 2014/09/30.

Senzai, Y. and Buzsáki, G. (2017) Physiological Properties and Behavioral Correlates of Hippocampal Granule Cells and Mossy Cells, *Neuron*, 93(3), pp. 691–70400000.

Shadlen, M. N. and Newsome, W. T. (1994) Noise, neural codes and cortical organization., *Current opinion in neurobiology*, 4(4), pp. 569–79.

Shi, Y.-F., Han, Y., Su, Y.-T., Yang, J.-H. and Yu, Y.-Q. (2015) Silencing of Cholinergic Basal Forebrain Neurons Using Archaerhodopsin Prolongs Slow-Wave Sleep in Mice, *PLoS ONE*. Edited by G. F. Gilestro, 10(7), p. e0130130.

Sik, A., Penttonen, M., Ylinen, A. and Buzsáki, G. (1995) Hippocampal CA1 interneurons: an in vivo intracellular labeling study, *The Journal of Neuroscience*. 1995/10/01, 15(10), pp. 6651–6665. 1995/10/01.

Simon, A. P., Poindessous-Jazat, F., Dutar, P., Epelbaum, J., Bassant, M. H. and Pascale Simon, A. (2006) Firing properties of anatomically identified neurons in the medial septum of anesthetized and unanesthetized restrained rats, *J Neurosci*. Society for Neuroscience, 26(35), pp. 9038–9046.

Sirota, A., Montgomery, S., Fujisawa, S., Isomura, Y., Zugaro, M. and Buzsáki, G. (2008) Entrainment of Neocortical Neurons and Gamma Oscillations by the Hippocampal Theta

Rhythm, *Neuron*, 60(4), pp. 683–697.

Skaggs, W. E., McNaughton, B. L., Wilson, M. A. and Barnes, C. A. (1996) Theta phase precession in hippocampal neuronal populations and the compression of temporal sequences., *Hippocampus*, 6(2), pp. 149–72.

Solstad, T. (2008) Representation of Geometric Bordersin the Entorhinal Cortex, *Science*. American Association for the Advancement of Science, 1865(5909), pp. 1–5.

Soltesz, I., Deschênes, M. and Deschenes, M. (1993) Low- and high-frequency membrane potential oscillations during theta activity in CA1 and CA3 pyramidal neurons of the rat hippocampus under ketamine-xylazine anesthesia, *Journal of neurophysiology*. American Physiological Society Bethesda, MD , 70(1), pp. 97–116.

Somogyi, P. (2010) Hippocampus: Intrinsic Organization, in *Handbook of Brain Microcircuits*. Oxford University Press, pp. 148–164.

Somogyi, P., Katona, L., Klausberger, T., Lasztóczi, B. and Viney, T. J. (2014) Temporal redistribution of inhibition over neuronal subcellular domains underlies state-dependent rhythmic change of excitability in the hippocampus, *Philosophical transactions of the Royal Society of London. Series B, Biological sciences*, 369(1635), p. 20120518.

Somogyi, P. and Klausberger, T. (2005) Defined types of cortical interneurone structure space and spike timing in the hippocampus, *Journal of Physiology*, 562(1), pp. 9–26.

Somogyi, P. and Klausberger, T. (2018) Hippocampus: Intrinsic Organization Chapter: Hippocampus: Intrinsic Organization Oxford Medicine Online Hippocampus: Intrinsic Organization.

Somogyi, P., Nunzi, M. G., Gorio, A. and Smith, A. D. (1983) A new type of specific interneuron in the monkey hippocampus forming synapses exclusively with the axon initial segments of pyramidal cells, *Brain Research*. Elsevier, 259(1), pp. 137–142.

Soriano, E., Nitsch, R. and Frotscher, M. (1990) Axo-axonic chandelier cells in the rat fascia dentata: Golgi-electron microscopy and immunocytochemical studies, *The Journal of Comparative Neurology*, 293(1), pp. 1–25.

Stein, R. B., Gossen, E. R. and Jones, K. E. (2005) Neuronal variability: noise or part of the signal?, *Nature Reviews Neuroscience*, 6(5), pp. 389–397.

Steward, O. (1976) Topographic organization of the projections from the entorhinal area to the hippocampal formation of the rat, *The Journal of Comparative Neurology*. John Wiley & Sons, Ltd, 167(3), pp. 285–314.

Steward, O. and Scoville, S. A. (1976) Cells of origin of entorhinal cortical afferents to the hippocampus and fascia dentata of the rat, *The Journal of Comparative Neurology*. John Wiley & Sons, Ltd, 169(3), pp. 347–370.

Stewart, M. and Fox, S. E. (1990) Firing relations of lateral septal neurons to the hippocampal theta rhythm in urethane anesthetized rats, *Experimental Brain Research*. Springer-Verlag, 79(1), pp. 92–96.

Stickgold, R. and Walker, M. P. (2005) Sleep and Memory: The Ongoing Debate, *Sleep*, 28(10), pp. 1225–1227.

van Strien, N. M., Cappaert, N. L. M. and Witter, M. P. (2009) The anatomy of memory: an interactive overview of the parahippocampal–hippocampal network, *Nature Reviews Neuroscience*, 10(4), pp. 272–282.

Sun, Y., Nguyen, A. Q., Nguyen, J. P., Le, L., Saur, D., Choi, J., Callaway, E. M. and Xu, X. (2014) Cell-Type-Specific Circuit Connectivity of Hippocampal CA1 Revealed through Cre-Dependent Rabies Tracing, *Cell Reports*. Cell Press, 7(1), pp. 269–280.

Swanson, L. W. (2018) Brain maps 4.0-Structure of the rat brain: An open access atlas with global nervous system nomenclature ontology and flatmaps., *The Journal of comparative neurology*. Wiley-Blackwell, 526(6), pp. 935–943.

Swanson, L. W. and Cowan, W. M. (1977) An autoradiographic study of the organization of the efferet connections of the hippocampal formation in the rat, *The Journal of Comparative Neurology*, 172(1), pp. 49–84.

Sweeney, J. E. E., Lamour, Y. and Bassant, M. H. H. (1992) Arousal-dependent properties of medial septal neurons in the unanesthetized rat, *Neuroscience*. Pergamon, 48(2), pp. 353–362.

Szabo, G. G., Du, X., Oijala, M., Varga, C., Parent, J. M. and Soltesz, I. (2017) Extended Interneuronal Network of the Dentate Gyrus., *Cell reports*, 20(6), pp. 1262–1268.

Takács, V. T., Cserép, C., Schlingloff, D., Pósfai, B., Szőnyi, A., Sos, K. E., Környei, Z., Dénes, Á., Gulyás, A. I., Freund, T. F., *et al.* (2018) Co-transmission of acetylcholine and GABA regulates hippocampal states, *Nature Communications*. Nature Publishing Group, 9(1), p. 2848.

Takács, V. T., Freund, T. F. and Gulyás, A. I. (2008) Types and synaptic connections of hippocampal inhibitory neurons reciprocally connected with the medial septum, *European Journal of Neuroscience*. 2008/07/30, 28(1), pp. 148–164. 2008/07/30.

Taube, J. S., Muller, R. U. and Ranck, J. B. (1990) Head-direction cells recorded from the postsubiculum in freely moving rats. I. Description and quantitative analysis., *The Journal of Neuroscience*, 10(2), pp. 420–35.

Tóth, K., Borhegyi, Z. and Freund, T. F. (1993) Postsynaptic targets of GABAergic hippocampal neurons in the medial septum-diagonal band of broca complex., *The Journal of Neuroscience*. 1993/09/01. Society for Neuroscience, 13(9), pp. 3712–3724. 1993/09/01.

Tóth, K, Freund, T. F. and Miles, R. (1997) Disinhibition of rat hippocampal pyramidal cells by GABAergic afferents from the septum., *The Journal of Physiology*, 500(2), pp. 463–474.

Tsanov, M. (2017) Speed and Oscillations: Medial Septum Integration of Attention and Navigation, *Frontiers in Systems Neuroscience*. Frontiers, 11, p. 67.

Tsanov, M. (2018) Differential and complementary roles of medial and lateral septum in the orchestration of limbic oscillations and signal integration, *European Journal of Neuroscience*. John Wiley & Sons, Ltd (10.1111), 48(8), pp. 2783–2794.

Tukker, J. J., Fuentealba, P., Hartwich, K., Somogyi, P. and Klausberger, T. (2007) Cell Type-Specific Tuning of Hippocampal Interneuron Firing during Gamma Oscillations In Vivo, *Journal of Neuroscience*, 27(31), pp. 8184–8189.

Tukker, J. J., Tang, Q., Burgalossi, A. and Brecht, M. (2015) Head-Directional Tuning and Theta

Modulation of Anatomically Identified Neurons in the Presubiculum, *Journal of Neuroscience*. Society for Neuroscience, 35(46), pp. 15391–15395.

Uhlhaas, P. J. and Singer, W. (2012) Neuronal Dynamics and Neuropsychiatric Disorders: Toward a Translational Paradigm for Dysfunctional Large-Scale Networks, *Neuron*. 2012/09/25, 75(6), pp. 963–980. 2012/09/25.

Unal, G., Crump, M. G., Viney, T. J., Éltes, T., Katona, L., Klausberger, T., Somogyi, P., Eltes, T., Katona, L., Klausberger, T., *et al.* (2018) Spatio-temporal specialization of GABAergic septo-hippocampal neurons for rhythmic network activity, *Brain Structure and Function*.

Unal, G., Joshi, A., Viney, T. J., Kis, V. and Somogyi, P. (2015) Synaptic Targets of Medial Septal Projections in the Hippocampus and Extrahippocampal Cortices of the Mouse, *The Journal of Neuroscience*. Society for Neuroscience, 35(48), pp. 15812–15826.

Vanderwolf, C. . (1969) Hippocampal electrical activity and voluntary movement in the rat, *Electroencephalography and Clinical Neurophysiology*. 1969/04/01. Elsevier, 26(4), pp. 407–418. 1969/04/01.

Varga, C., Golshani, P. and Soltesz, I. (2012) Frequency-invariant temporal ordering of interneuronal discharges during hippocampal oscillations in awake mice, *Proceedings of the National Academy of Sciences*. National Academy of Sciences, 109(40), pp. E2726–E2734.

Varga, C., Oijala, M., Lish, J., Szabo, G. G., Bezaire, M., Marchionni, I., Golshani, P. and Soltesz, I. (2014) Functional fission of parvalbumin interneuron classes during fast network events, *eLife*, 3.

Varga, V., Hangya, B., Kránitz, K., Ludányi, A., Zemankovics, R., Katona, I., Shigemoto, R., Freund, T. F. and Borhegyi, Z. (2008) The presence of pacemaker HCN channels identifies theta rhythmic GABAergic neurons in the medial septum, *Journal of Physiology*. Wiley/Blackwell (10.1111), 586(16), pp. 3893–3915.

Verret, L., Fort, P., Gervasoni, D., Léger, L. and Luppi, P.-H. (2006) Localization of the neurons active during paradoxical (REM) sleep and projecting to the locus coeruleus noradrenergic neurons in the rat, *The Journal of Comparative Neurology*, 495(5), pp. 573–586.

Vertes, R. P. (1986) Brainstem Modulation of the Hippocampus, in *The Hippocampus*. Boston, MA: Springer US, pp. 41–75.

Vertes, R. P. (1988) Brainstem afferents to the basal forebrain in the rat, *Neuroscience*. Pergamon, 24(3), pp. 907–935.

Vertes, R. P. (1992) PHA-L analysis of projections from the supramammillary nucleus in the rat, *The Journal of Comparative Neurology*, 326(4), pp. 595–622.

Vertes, R. P. (2015) Major diencephalic inputs to the hippocampus: supramammillary nucleus and nucleus reuniens. Circuitry and function., *Progress in brain research*. NIH Public Access, 219, pp. 121–44.

Vertes, R. P. and Kocsis, B. (1997) Brainstem-diencephalo-septohippocampal systems controlling the theta rhythm of the hippocampus, *Neuroscience*, 81(4), pp. 893–926.

Vertes, R. P. and McKenna, J. T. (2000) Collateral projections from the supramammillary nucleus to the medial septum and hippocampus, *Synapse*. John Wiley & Sons, Ltd, 38(3), pp. 281–

293.

Villette, V., Poindessous-Jazat, F., Simon, A., Lena, C., Roullot, E., Bellessort, B., Epelbaum, J., Dutar, P. and Stephan, A. (2010) Decreased Rhythmic GABAergic Septal Activity and Memory-Associated Oscillations after Hippocampal Amyloid- Pathology in the Rat, *Journal of Neuroscience*. 2010/08/20, 30(33), pp. 10991–11003. 2010/08/20.

Viney, T. J., Lasztoczi, B., Katona, L., Crump, M. G., Tukker, J. J., Klausberger, T. and Somogyi, P. (2013) Network state-dependent inhibition of identified hippocampal CA3 axo-axonic cells in vivo, *Nature Neuroscience*. Nature Publishing Group, 16(12), pp. 1802–1811.

Viney, T. J., Salib, M., Joshi, A., Unal, G., Berry, N. and Somogyi, P. (2018) Shared rhythmic subcortical GABAergic input to the entorhinal cortex and presubiculum, *eLife*. eLife Sciences Publications Limited, 7, p. e34395.

Wang, X.-J. (2002) Pacemaker Neurons for the Theta Rhythm and Their Synchronization in the Septohippocampal Reciprocal Loop, *Journal of Neurophysiology*, 87(2), pp. 889–900.

Wang, Y., Romani, S., Lustig, B., Leonardo, A. and Pastalkova, E. (2015) Theta sequences are essential for internally generated hippocampal firing fields, *Nature Neuroscience*. Nature Publishing Group, 18(2), pp. 282–288.

Wei, B., Huang, Z., He, S., Sun, C., You, Y., Liu, F. and Yang, Z. (2012) The onion skin-like organization of the septum arises from multiple embryonic origins to form multiple adult neuronal fates, *Neuroscience*. Pergamon, 222, pp. 110–123.

Whitehouse, P. J., Price, D. L., Struble, R. G., Clark, A. W., Coyle, J. T. and DeLong, M. R. (1982) Alzheimer's disease and senile dementia: Loss of neurons in the basal forebrain, *Science*. 1982/03/05, 215(4537), pp. 1237–1239. 1982/03/05.

Wills, T. J., Lever, C., Cacucci, F., Burgess, N. and O'Keefe, J. (2005) Attractor dynamics in the hippocampal representation of the local environment., *Science*. American Association for the Advancement of Science, 308(5723), pp. 873–6.

Wilson, M. A. and McNaughton, B. L. (1993) Dynamics of the hippocampal ensemble code for space., *Science*, 261(5124), pp. 1055–8.

Winson, J. (1978) Loss of hippocampal theta rhythm results in spatial memory deficit in the rat., *Science*. American Association for the Advancement of Science, 201(4351), pp. 160–3.

Wyss, J. M., Swanson, L. W. and Cowan, W. M. (1979) Evidence for an input to the molecular layer and the stratum granulosum of the dentate gyrus from the supramammillary region of the hypothalamus., *Anatomy and Embryology*, 156(2), pp. 165–76.

Ylinen, A., Soltész, I., Bragin, A., Penttonen, M., Sik, A. and Buzsáki, G. (1995) Intracellular correlates of hippocampal theta rhythm in identified pyramidal cells, granule cells, and basket cells, *Hippocampus*. Wiley-Blackwell, 5(1), pp. 78–90.

Yuan, M., Meyer, T., Benkowitz, C., Savanthrapadian, S., Ansel-Bollepalli, L., Foggetti, A., Wulff, P., Alcami, P., Elgueta, C. and Bartos, M. (2017) Somatostatin-positive interneurons in the dentate gyrus of mice provide local- and long-range septal synaptic inhibition., *eLife*, 6.

Zaborszky, L., Csordas, A., Mosca, K., Kim, J., Gielow, M. R., Vadasz, C. and Nadasdy, Z. (2015) Neurons in the Basal Forebrain Project to the Cortex in a Complex Topographic

Organization that Reflects Corticocortical Connectivity Patterns: An Experimental Study Based on Retrograde Tracing and 3D Reconstruction, *Cerebral Cortex*. Oxford University Press, 25(1).

Zaborszky, L., Pang, K., Somogyi, J., NADASDY, Z. and Kallo, I. (1999) The Basal Forebrain Corticopetal System Revisited, *Annals of the New York Academy of Sciences*. John Wiley & Sons, Ltd (10.1111), 877(1 ADVANCING FRO), pp. 339–367.

Zar, J. H. (1999) *Biostatistical analysis*. Prentice Hall.

Zhang, H., Lin, S.-C. C. and Nicolelis, M. A. (2011) A distinctive subpopulation of medial septal slow-firing neurons promote hippocampal activation and theta oscillations, *Journal of neurophysiology*, 106(5), pp. 2749–2763.

Zhang, K., Ginzburg, I., McNaughton, B. L. and Sejnowski, T. J. (1998) Interpreting Neuronal Population Activity by Reconstruction: Unified Framework With Application to Hippocampal Place Cells, *Journal of Neurophysiology*, 79(2), pp. 1017–1044.

Zutshi, I., Brandon, M. P., Fu, M. L., Donegan, M. L., Leutgeb, J. K. and Leutgeb, S. (2018) Hippocampal Neural Circuits Respond to Optogenetic Pacing of Theta Frequencies by Generating Accelerated Oscillation Frequencies, *Current Biology*, 28(8), pp. 1179-1188.e3.

APPENDIX

Table 8-1 Single recorded medial septal neurons

Animal	Labelling	Region	Identified	Recording Date	Day	Approx. depth	Pipette trackt
MS01							
a	-	HPC	-	26/02/2015	III	767 µm	u
b	-	HPC	-	26/02/2015	III	1082 µm	u
c	-	HPC	-	26/02/2015	III	832 µm	u
d	-	HPC	-	26/02/2015	III	877 µm	u
e	-	HPC	-	26/02/2015	III	764 µm	u
f	-	HPC	-	26/02/2015	III	779 µm	u
g	attempt	HPC	-	02/03/2015	IV	972 µm	u
h	attempt	HPC	-	02/03/2015	IV	1300 µm	u
i	-	HPC	-	03/03/2015	V	1242 µm	u
j	attempt	HPC	-	03/03/2015	V	1276 µm	u
k	-	HPC	-	03/03/2015	V	1931 µm	u
l	-	HPC	-	03/03/2015	V	2061 µm	u
m	attempt	HPC	-	03/03/2015	V	1960 µm	u
MS02							
a	-	MS	-	09/03/2015	I	1171 µm	u
b	-	MS	-	09/03/2015	I	2059 µm	u
c	-	MS	-	09/03/2015	I	2195 µm	u
d	-	MS	-	09/03/2015	I	1884 µm	u
e1	-	MS	-	09/03/2015	I	1751 µm	u
e2	-	MS	-	09/03/2015	I	1765 µm	u
f	-	MS	-	09/03/2015	I	1681 µm	u
g	attempt	MS	-	09/03/2015	I	2336 µm	u
h	-	MS	-	09/03/2015	I	1800 µm	u
i	-	MS	-	09/03/2015	I	1996 µm	u
j	-	MS	-	09/03/2015	I	1848 µm	u
k	-	MS	-	11/03/2015	III	2095 µm	u
l	-	MS	-	12/03/2015	IV	1825 µm	u
m	-	MS	-	12/03/2015	IV	3034 µm	u
n	-	MS	-	12/03/2015	IV	2868 µm	u
o	-	MS	-	13/03/2015	V	3613 µm	u
p	-	MS	-	13/03/2015	V	2507 µm	u
q	-	MS	-	16/03/2015	V	2108 µm	u
MS03							
a	-	MS	-	18/03/2015	I	2516 µm	u
b	-	MS	-	18/03/2015	I	3136 µm	u
c	-	MS	-	18/03/2015	I	3828 µm	u
d	-	MS	-	18/03/2015	I	3814 µm	u
e	-	MS	-	18/03/2015	I	4030 µm	u
f	-	MS	-	18/03/2015	I	3128 µm	u
g	-	MS	-	19/03/2015	II	3019 µm	u
h	-	MS	-	19/03/2015	II	2273 µm	u
i	-	MS	-	19/03/2015	II	3282 µm	u
j	-	MS	-	19/03/2015	II	4008 µm	u
k	-	MS	-	19/03/2015	II	3663 µm	u
l	-	MS	-	19/03/2015	II	3015 µm	u
m	attempt	MS	-	19/03/2015	II	3388 µm	u
n	-	MS	-	19/03/2015	II	3565 µm	u
o	attempt	MS	-	20/03/2015	III	3571 µm	u
p	attempt	MS	-	20/03/2015	III	2410 µm	u
q	-	MS	-	20/03/2015	III	2852 µm	u
r	attempt	MS	-	23/03/2015	IV	2999 µm	u
MS04							
a	attempt	MS	-	26/03/2015	I	1278 µm	u
b	attempt	MS	-	26/03/2015	I	1398 µm	u
c	-	MS	-	26/03/2015	I	3432 µm	u
d	-	MS	-	26/03/2015	I	3538 µm	u
e	-	MS	-	26/03/2015	I	2199 µm	u
f	labelled	MS	-	26/03/2015	I	3283 µm	u
MS05							
a	-	MS	-	01/04/2015	II	2583 µm	same
b	-	MS	-	01/04/2015	II	2762 µm	same
c1	attempt	MS	-	01/04/2015	II	3082 µm	same 1
c2	attempt	MS	-	01/04/2015	II	3100 µm	same 1
d	-	MS	-	01/04/2015	II	3588 µm	same 1
e	-	MS	-	01/04/2015	II	3160 µm	same 1
f	-	MS	-	01/04/2015	II	3202 µm	same 1
g	-	MS	-	01/04/2015	II	3400 µm	same 1
h	-	MS	-	02/04/2015	III	3387 µm	same 2
i	labelled	MS	+	02/04/2015	III	3455 µm	same 2
MS06							
a	-	MS	-	02/05/2015	I	2844 µm	same
b	-	MS	-	03/05/2015	II	3989 µm	same 1
c	-	MS	-	11/05/2015	VI	3152 µm	same 2
d	-	MS	-	11/05/2015	VI	3312 µm	same 2
e	-	MS	-	11/05/2015	VI	3554 µm	same 2
MS07							
a	-	MS	-	14/05/2015	II	2975 µm	same
b	-	MS	-	14/05/2015	II	2400 µm	same
c	-	MS	-	14/05/2015	II	3617 µm	same
d	-	MS	-	18/05/2015	III	3639 µm	same 1
e	-	MS	-	18/05/2015	III	3667 µm	same 1
f	-	MS	-	18/05/2015	III	4090 µm	same 1
g	-	MS	-	18/05/2015	III	3741 µm	same 1
h	attempt	MS	+	18/05/2015	III	3310 µm	same 1
i	-	MS	-	18/05/2015	III	3344 µm	same 1
j1	attempt	MS	-	18/05/2015	III	3568 µm	same 1
j2	attempt	MS	-	18/05/2015	III	3571 µm	same 1
k	attempt	MS	-	18/05/2015	III	3636 µm	same 1
l	-	MS	-	18/05/2015	III	3800 µm	same 1
m	attempt	MS	-	18/05/2015	III	3816 µm	same 1
MS08							
a	attempt	MS	-	02/06/2015	I	3822 µm	same
b	-	MS	-	05/06/2015	III	3315 µm	same
c	-	MS	-	05/06/2015	III	3583 µm	same
d	-	MS	-	05/06/2015	III	4378 µm	same
e	-	MS	-	09/06/2015	IV	4207 µm	same
f	-	MS	-	09/06/2015	IV	3130 µm	same
g	attempt	MS	-	09/06/2015	IV	3224 µm	same
i	attempt	MS	+	09/06/2015	IV	4086 µm	same
MS09	8 hours to p						
a	labelled	MS	+	15/10/2015	II	2828 µm	same
MS10	7 hours to p						
a	-	MS		23/10/2015	II	3571 µm	same
b	labelled	MS	weak	23/10/2015	II	3452 µm	same

MS11	4 hours to p						
a	-	MS		06/11/2015	I	3165 µm	same
b	labelled	MS	+	06/11/2015	I	3461 µm	same
MS12	5 hours to p						
a	-	-		11/11/2015	I	3631 µm	same
b	-	-		11/11/2015	I	3420 µm	same
c	-	MS		11/11/2015	I	2739 µm	same
d	-	MS		11/11/2015	I	2912 µm	same
e	labelled	MS	+	11/11/2015	I	2718 µm	same
MS13	6 hours to p						
a	-	MS		19/11/2015	I	3199 µm	same
b	-	MS		19/11/2015	I	3580 µm	same
c	labelled	MS	+	19/11/2015	I	3476 µm	same
MS14	6 hours to p						
a	-			24/11/2015	I	3292 µm	same
b	-			24/11/2015	I	3611 µm	same 1
c	-			24/11/2015	I	3786 µm	same 1
d	-			24/11/2015	I	3591 µm	same 1
e	labelled		no	24/11/2015	I	3618 µm	same 1
f	-	MS		25/11/2015	II	2859 µm	same 2
g	-	MS		25/11/2015	II	2927 µm	same 2
h	-	MS		25/11/2015	II	3029 µm	same 2
i	labelled	MS	+	25/11/2015	II	3154 µm	same 2
MS15	perfused without labelling						
a	-	-		08/12/2015	I	4239 µm	same 1
b	-	-		09/12/2015	II	3998 µm	same 2
c	-	-		10/12/2015	III	4482 µm	same 3
d	-	-		11/12/2015	IV	3624 µm	same 4
MS16	6 hours to p						
a	-	LS?		13/01/2016	I	2388 µm	
b	-	MS		13/01/2016	I	3308 µm	same
c	-	MS		13/01/2016	I	3290 µm	same
d	labelled	MS	+	13/01/2016	I	3303 µm	same
MS17	6 hours to p						
a	labelled	MS		15/01/2016	I	3803 µm	
b	-	MS		17/01/2016	II	3325 µm	same
c	-	MS		17/01/2016	II	4061 µm	same
d	-	MS		17/01/2016	II	4125 µm	same
e	-	MS		17/01/2016	II	3201 µm	same
f	-	MS		17/01/2016	II	2702 µm	
g	-	MS		17/01/2016	II	3306 µm	same 1
h	-	MS		17/01/2016	II	3488 µm	same 1
i	-	MS		17/01/2016	II	3607 µm	same 1
j	-	MS		17/01/2016	II	3292 µm	same 2
k	labelled	MS	+	17/01/2016	II	3292 µm	same 2
MS18	5 hours to p						
a	-	MS		20/01/2016	I	3482 µm	
b	-	MS		20/01/2016	I	2988 µm	same
c	labelled	MS	-	20/01/2016	I	3200 µm	same
MS19	5 hours to p						
a	-	MS		21/01/2016	I	2998 µm	same
b	labelled	MS	+	21/01/2016	I	2996 µm	same
MS20	4 hours to p						
a	-	MS		27/01/2016	I	3471 µm	
b	-	MS		27/01/2016	I	3621 µm	same
c	-	MS		27/01/2016	I	4286 µm	same
d	-	MS		27/01/2016	I	3506 µm	same 1
e	labelled	MS	-	27/01/2016	I	3615 µm	same 1
MS21	no labelling						
a	-	MS	-	27/01/2016	I	3920 µm	
MS22	6 hours to p						
a	-	MS		04/02/2016	I	3242 µm	same
b	-	MS		04/02/2016	I	2741 µm	same
c	attempt	MS		04/02/2016	I	3395 µm	same
d	attempt	MS		04/02/2016	I	3106 µm	same
e	attempt	MS		04/02/2016	I	3322 µm	same
f	attempt	MS		04/02/2016	I	3642 µm	same
g	-	MS		05/02/2016	II	3413 µm	same 1
h	-	MS		05/02/2016	II	3437 µm	same 1
i	-	MS		05/02/2016	II	3471 µm	same 1
j	labelled	MS	+	05/02/2016	II	3540 µm	same 1
MS23	4 hours to p						
a	labelled	MS	-	05/02/2016	I	3800 µm	
MS24							
a	-	MS	-	09/02/2016	I	3377 µm	same
b	labelled	MS	-	09/02/2016	I	3656 µm	same
MS25	no labelling						
a	-	MS	-	10/02/2016	II	3809 µm	not
b	-	MS	-	10/02/2016	II	3680 µm	not
c	-	MS	-	10/02/2016	II	3339 µm	not
MS26	no labelling						
a	-	MS	-	16/02/2016	I	3718 µm	
b	-	MS	-	16/02/2016	I	3621 µm	
c	-	MS	-	17/02/2016	II	3025 µm	same
d	-	MS	-	17/02/2016	II	3513 µm	same
e	-	MS	-	17/02/2016	II	3603 µm	same
f	-	MS	-	17/02/2016	II	3594 µm	same
g	-	MS	-	17/02/2016	II	3274 µm	same
h	-	MS	-	17/02/2016	II	3161 µm	
MS27	no labelling						
MS28	*PRV/AAV injection*						
MS29	*PRV/AAV injection*						
MS30	no labelling						
MS31	hours to p						
a	-	MS	-	26/02/2016	I	2753 µm	same
b	-	MS	-	26/02/2016	I	3420 µm	same
c	-	MS	-	26/02/2016	I	3550 µm	same
d	-	MS	-	26/02/2016	I	3845 µm	same
e	-	MS	-	26/02/2016	I	3360 µm	same
f	-	MS	-	26/02/2016	I	3273 µm	same
g	-	MS	-	26/02/2016	I	3283 µm	same
h	labelled	MS	+	26/02/2016	I	3270 µm	same
MS32	cell died						
a	-	MS	-	02/03/2016	I	2817 µm	same
b	-	MS	-	02/03/2016	I	2950 µm	same
c	-	MS	-	02/03/2016	I	2953 µm	same

d	-	MS	-	02/03/2016	I	3118 µm	same
e	-	MS	-	02/03/2016	I	3429 µm	same
f	-	MS	-	02/03/2016	I	3478 µm	same
g	-	MS	-	02/03/2016	I	3441 µm	same
h	-	MS	-	02/03/2016	I	3179 µm	same
i	-	MS	-	02/03/2016	I	3365 µm	same
j	labelled	MS	+	02/03/2016	I	3408 µm	same

MS33 8 hours to p

a	labelled	MS	+	02/03/2016	I	3603 µm	

MS34 no labelling

a	-	MS	-	10/03/2016	I	3514 µm	same
b	-	MS	-	10/03/2016	I	4430 µm	same
c	-	MS	-	10/03/2016	I	4503 µm	same
d	-	MS	-	10/03/2016	I	4234 µm	same
e	labelled	MS	-	10/03/2016	I	3949 µm	same 1
f	-	MS	-	10/03/2016	I	4329 µm	same 1
g	-	MS	-	10/03/2016	I	3293 µm	same 2
h	-	MS	-	10/03/2016	I	4402 µm	same 2
i	-	MS	-	13/03/2016	II	4359 µm	same 3
j	labelled	MS	-	13/03/2016	II	4574 µm	same 3

MS35 no labelling

MS36 8 hours to p

a	-	MS	-	15/03/2016	I	3320 µm	same
b	-	MS	-	15/03/2016	I	3071 µm	same
c	-	MS	-	15/03/2016	I	3161 µm	same
d	-	MS	-	15/03/2016	I	3512 µm	same
e	-	MS	-	15/03/2016	I	3728 µm	same
f	labelled	MS	-	15/03/2016	I	4296 µm	same
g	-	MS	-	15/03/2016	I	4261 µm	same

MS37 no labelling

a	-	MS	-	15/03/2016	I	2851 µm	same

MS38 perfused immediately

a	-	MS	-	07/04/2016	I	3505 µm	same
b	-	MS	-	07/04/2016	I	3572 µm	same
c	-	MS	-	07/04/2016	I	3757 µm	same
d	-	MS	-	07/04/2016	I	4109 µm	same
e	-	MS	-	07/04/2016	I	3859 µm	same
f	-	MS	-	07/04/2016	I	4060 µm	same
g	-	MS	-	07/04/2016	I	3037 µm	same 1
h	-	MS	-	07/04/2016	I	3698 µm	same 2
i	-	MS	-	07/04/2016	I	3589 µm	same 2
j	-	MS	-	08/04/2016	II	3677 µm	same 3
k	labelled	MS	-	08/04/2016	II	4577 µm	same 3

MS39 6 hours to p

				06/04/2016	I	4703 µm	same
a	-	MS	-	06/04/2016	I	4438 µm	same
b	-	MS	-	06/04/2016	I	4484 µm	same
c	-	MS	-	06/04/2016	I	4276 µm	same
d	-	MS	-	06/04/2016	I	4785 µm	same
e	-	MS	-	07/04/2016	II	4785 µm	same 1
f	-	MS	-	07/04/2016	II	4721 µm	same 2
g	-	MS	-	07/04/2016	II	3052 µm	same 2
h	-	MS	-	07/04/2016	II	3198 µm	same 2
i	-	MS	-	07/04/2016	II	4214 µm	same 2
j	-	MS	-	07/04/2016	II	4549 µm	same 3
k	-	MS	-	07/04/2016	II	3925 µm	same 4
l	-	MS	-	07/04/2016	II	4784 µm	same 4
m	labelled	MS	+	07/04/2016	II	3791 µm	same 4

MS40 *PRV/AAV injection*

a	-	MS	-	19/04/2016	I	2919 µm	same
b	-	MS	-	19/04/2016	I	2933 µm	same
c	-	MS	-	19/04/2016	I	3424 µm	same 1
d	-	MS	-	19/04/2016	I	3677 µm	same 2
e	labelled	MS	+	19/04/2016	I	3152 µm	same 2

MS41 *PRV/AAV injection*

a	labelled	MS	-	21/04/2016	I	4175 µm	same
b	labelled	MS	-	21/04/2016	I	4133 µm	same
c	labelled	MS	-	21/04/2016	I	3700 µm	same
d	-	MS	-	22/04/2016	II	3600 µm	same 1
e	-	MS	-	22/04/2016	II	3786 µm	same 1
f	labelled	MS	-	22/04/2016	II	4122 µm	same 1
g	-	MS	-	22/04/2016	II	4322 µm	same 1
h	labelled	MS	-	22/04/2016	II	3764 µm	same 1
i	labelled	MS	-	22/04/2016	II	4115 µm	same 1
j	-	MS	-	25/04/2016	III	4309 µm	same 2
k	-	MS	-	25/04/2016	III	3809 µm	same 2
l	-	MS	-	25/04/2016	III	4269 µm	same 2
m	-	MS	-	25/04/2016	III	4191 µm	same 2
n	-	MS	-	25/04/2016	III	4232 µm	same 2
o	-	MS	-	25/04/2016	III	3967 µm	same 2
p	labelled	MS	-	25/04/2016	III	3822 µm	same 2

MS42 6 hours to p

a	-	MS	-	19/04/2016	I	3569 µm	same 1
b	labelled	MS	-	19/04/2016	I	3844 µm	same 2
c	labelled	MS	-	19/04/2016	I	3525 µm	same 3
d	labelled	MS	-	19/04/2016	I	4001 µm	same 3
e	labelled	MS	-	25/04/2016	II	4180 µm	same

MS43 6 hours to p

a	-	MS	-	17/05/2016	I	2836 µm	same
b	-	MS	-	17/05/2016	I	2869 µm	same
c	-	MS	-	17/05/2016	I	3019 µm	same 1
d	-	MS	-	17/05/2016	I	3174 µm	same 1
e	-	MS	-	17/05/2016	I	3353 µm	same 2
f	-	MS	-	18/04/2016	II	3524 µm	same 3
g	-	MS	-	18/04/2016	II	3121 µm	same 4
h	-	MS	-	18/04/2016	II	3526 µm	same 4
i	-	MS	-	18/04/2016	II	3858 µm	same 5
j	-	MS	-	18/04/2016	II	3720 µm	same 5
k	labelled	MS	-	18/04/2016	II	3812 µm	same 6
l	-	MS	-	18/04/2016	II	3546 µm	same 6

MS44 perfused immediately

a	-	MS	-	09/05/2016	I	3033 µm	same
b	-	MS	-	09/05/2016	I	3345 µm	same
c	-	MS	-	10/05/2016	II	3878 µm	same 1
d	-	MS	-	10/05/2016	II	3901 µm	same 1
e	labelled	MS	?	10/05/2016	II	3619 µm	same 2

MS45 8 hours to p

a	-	MS	-	13/05/2016	I	3529 µm	same
b	-	MS	-	13/05/2016	I	3912 µm	same 1
c	-	MS	-	13/05/2016	I	3995 µm	same 1
d	-	MS	-	13/05/2016	I	4598 µm	same 1

e	-	MS	-	13/05/2016	I	4992 µm	same 1
f	labelled	MS	-	13/05/2016	I	4031 µm	same 2

MS46 *PRV/AAV injection*

a	-	MS	-	17/06/2016	I	3671 µm	same
b	-	MS	-	17/06/2016	I	4336 µm	same 1
c	-	MS	-	21/06/2016	II	4031 µm	same 2
d	-	MS	-	21/06/2016	II	4301 µm	same 2
e	-	MS	-	21/06/2016	II	4425 µm	same 2
f	-	MS	-	21/06/2016	II	4682 µm	same 2
g	-	MS	-	21/06/2016	II	4500 µm	same 2
h	-	MS	-	21/06/2016	II	4910 µm	same 2
i	-	MS	-	21/06/2016	II	5013 µm	same 2
j	-	MS	-	21/06/2016	II	4276 µm	same 3
k	labelled	MS	?	21/06/2016	II	4337 µm	same 3

MS47 *PRV/AAV injection*

a	-	MS	-	08/07/2016	I	3532 µm	same
b	labelled	MS	?	08/07/2016	I	3077 µm	same

MS48 6 hours to p

a	-	MS	-	25/05/2016	I	3080 µm	same
b	-	MS	-	25/05/2016	I	3140 µm	same 1
c	-	MS	-	25/05/2016	I	3202 µm	same 1
d	-	MS	-	25/05/2016	I	4021 µm	same 2
e	-	MS	-	25/05/2016	I	4060 µm	same 2
f	labelled	MS	-	25/05/2016	I	4189 µm	same 2
g	-	MS	-	25/05/2016	I	3890 µm	same 3
h	-	MS	-	25/05/2016	I	3897 µm	same 3
i	labelled	MS	-	25/05/2016	I	4000 µm	same 3
j	-	MS	-	27/05/2016	II	4085 µm	same 4
k	-	MS	-	27/05/2016	II	4050 µm	same 4
l	labelled	MS	-	27/05/2016	II	4555 µm	same 4
m	-	MS	-	27/05/2016	II	4466 µm	same 4
n	-	MS	-	27/05/2016	II	4641 µm	same 4
o	-	MS	-	27/05/2016	II	4686 µm	same 5
p	-	MS	-	27/05/2016	II	3937 µm	same 5
q	-	MS	-	27/05/2016	II	4156 µm	same 5
r	-	MS	-	27/05/2016	II	3432 µm	same 6
s	-	MS	-	27/05/2016	II	3698 µm	same 6
t	-	MS	-	27/05/2016	II	3800 µm	same 6
u	-	MS	-	27/05/2016	II	4000 µm	same 6
v	-	MS	-	27/05/2016	II	4128 µm	same 6
w	-	MS	-	27/05/2016	II	3919 µm	same 6
x	-	MS	-	27/05/2016	II	3989 µm	same 6
y	labelled	MS	-	27/05/2016	II	4181 µm	same 6
z	-	MS	-	27/05/2016	II	4200 µm	same 6
ab	labelled	MS	-	27/05/2016	II	4300 µm	same 6
ac	-	MS	-	31/05/2016	III	3364 µm	same 7
ad	-	MS	-	31/05/2016	III	3751 µm	same 7
ae	-	MS	-	31/05/2016	III	3557 µm	same 7
af	-	MS	-	31/05/2016	III	3532 µm	same 7
ag	labelled	MS	-	31/05/2016	III	3267 µm	same 7

MS49 6 hours to p

a	-	MS	-	13/07/2016	I	3200 µm	same
b	-	MS	-	13/07/2016	I	3957 µm	same 1
c	-	MS	-	13/07/2016	I	4000 µm	same 1
d	-	MS	-	13/07/2016	I	3200 µm	same 1
e	-	MS	-	13/07/2016	I	3400 µm	same 2
f	-	MS	-	13/07/2016	I	3552 µm	same 2
g	-	MS	-	13/07/2016	I	3592 µm	same 2
h	-	MS	-	13/07/2016	I	3753 µm	same 2
i	-	MS	-	13/07/2016	I	4294 µm	same 3
j	-	MS	-	13/07/2016	I	3755 µm	same 3
k	-	MS	-	13/07/2016	I	3844 µm	same 4
l	-	MS	-	13/07/2016	I	4348 µm	same 4
m	-	MS	-	13/07/2016	I	4226 µm	same 4
n	-	MS	-	13/07/2016	I	3737 µm	same 4
o	-	MS	-	14/07/2016	II	3505 µm	same 5
p	-	MS	-	14/07/2016	II	4120 µm	same 6
q	-	MS	-	14/07/2016	II	3388 µm	same 6
r	-	MS	-	14/07/2016	II	3516 µm	same 6
s	-	MS	-	14/07/2016	II	3590 µm	same 6
t	-	MS	-	14/07/2016	II	3650 µm	same 6
u	-	MS	-	14/07/2016	II	4279 µm	same 6
v	-	MS	-	14/07/2016	II	3856 µm	same 7
w	labelled	MS	?	14/07/2016	II	3600 µm	same 7

MS50 8 hours to p

a	-	MS	-	28/07/2016	I	3789 µm	same
b	-	MS	-	28/07/2016	I	4000 µm	same
c	-	MS	-	28/07/2016	I	4320 µm	same
d	labelled	MS	-	28/07/2016	I	4015 µm	same 1
e	-	MS	-	28/07/2016	I	4122 µm	same 1
f		MS	-	28/07/2016	II	4290 µm	same 1
g	-	MS	-	28/07/2016	II	3208 µm	same 2
h	-	MS	-	28/07/2016	II	3870 µm	same 2
i	-	MS	-	28/07/2016	II	3692 µm	same 2
j	-	MS	-	28/07/2016	II	3400 µm	same 3
k	-	MS	-	28/07/2016	II	3466 µm	same 3
l	-	MS	-	28/07/2016	II	3700 µm	same 3
m	labelled	MS	-	28/07/2016	II	4000 µm	same 3
n	labelled	MS	-	28/07/2016	II	3411 µm	same 3
o	-	MS	-	28/07/2016	II	3880 µm	same 3
p	-	MS	-	28/07/2016	III	3575 µm	same 4
q	-	MS	-	28/07/2016	III	3367 µm	same 4
r	-	MS	-	28/07/2016	III	3432 µm	same 4
s	-	MS	-	28/07/2016	III	3445 µm	same 4
t	-	MS	-	28/07/2016	III	3700 µm	same 4
u	labelled	MS	-	28/07/2016	III	3469 µm	same 4
v	-	MS	-	28/07/2016	III	3497 µm	same 5
w	-	MS	-	28/07/2016	III	4000 µm	same 5
x	labelled	MS	?	28/07/2016	III	3442 µm	same 5

MS52 perfused

a	-	MS	-	25/08/2016	I	3621 µm	same
b	-	MS	-	25/08/2016	I	3700 µm	same 1
c	-	MS	-	27/08/2016	II	4127 µm	same 2
d	-	MS	-	27/08/2016	II	4198 µm	same 3
e	-	MS	-	28/08/2016	III	5014 µm	same 4
f		MS	-	28/08/2016	III	4754 µm	same 5
g	-	MS	-	28/08/2016	III	3448 µm	same 5
h	-	MS	-	28/08/2016	III	3571 µm	same 5

MS53 8 hours to p

a	-	MS	-	31/08/2016	I	u	u

b	-	MS	-	31/08/2016	I	u	u
c	-	MS	-	31/08/2016	I	u	u
d	-	MS	-	31/08/2016	I	u	u
e	-	MS	-	31/08/2016	I	u	u
f	-	MS	-	31/08/2016	I	u	u
g	-	MS	-	31/08/2016	I	u	u
h	-	MS	-	31/08/2016	I	u	u
i	-	MS	-	31/08/2016	I	u	u
j	-	MS	-	04/09/2016	II	u	u
k	-	MS	-	04/09/2016	II	u	u
l	-	MS	-	04/09/2016	II	u	u
m	-	MS	-	04/09/2016	II	u	u
n	-	MS	-	04/09/2016	II	u	u
o	-	MS	-	04/09/2016	II	u	u
p	-	MS	-	05/09/2016	III	u	u
q	-	MS	-	05/09/2016	III	u	u
r	-	MS	-	05/09/2016	III	u	u
s	-	MS	-	05/09/2016	III	u	u
t	-	MS	-	05/09/2016	III	u	u
u	-	MS	-	05/09/2016	III	u	u
v	-	MS	-	05/09/2016	III	u	u
w	-	MS	-	05/09/2016	III	u	u
x	-	MS	-	05/09/2016	III	u	u
y	labelled	MS	+	05/09/2016	III	u	u

MS54 8 hours to p

a	-	MS	-	24/11/2016	I	u	u
b	-	MS	-	24/11/2016	I	u	u
c	labelled	MS	+	24/11/2016	I	u	u

MS55 8 hours to p

a	-	MS	-	01/12/2016	I	4379 µm	same
b	-	MS	-	02/12/2016	II	4257 µm	same 1
c	-	MS	-	02/12/2016	II	3660 µm	same 1
d	-	MS	-	02/12/2016	II	4419 µm	same 1

MS56 S1 (haemorrage)

MS57 8 hours to p

a	-	MS		u	u	u	u
b	-	MS		u	u	u	u
c	-	MS		u	u	u	u
d	-	MS		u	u	u	u
e	-	MS		u	u	u	u
f	-	MS		u	u	u	u
g	-	MS		u	u	u	u
h	-	MS		u	u	u	u
i	-	MS		u	u	u	u
j	-	MS		u	u	u	u
k	-	MS		u	u	u	u
l	-	MS		u	u	u	u
m	-	MS		u	u	u	u
n	-	MS		u	u	u	u
o	-	MS		u	u	u	u
p	-	MS		u	u	u	u
q	-	MS		u	u	u	u
r	-	MS		u	u	u	u
s	-	MS		u	u	u	u
t	-	MS		u	u	u	u
u	-	MS		u	u	u	u
v	-	MS		u	u	u	u
w	-	MS		u	u	u	u
x	-	MS		u	u	u	u
y	-	MS		u	u	u	u
z	-	MS		u	u	u	u

MS58 8 hours to p

a	-	MS	-	u	u	u	u
b	-	MS	-	u	u	u	u
c	-	MS	-	u	u	u	u
d	-	MS	-	u	u	u	u
e	-	MS	-	u	u	u	u
f	-	MS	-	u	u	u	u
g	-	MS	-	u	u	u	u
h	-	MS	-	u	u	u	u
i	labelled	MS	-	u	u	u	u

MS59 died during surgery (Heatplate not working)

MS60 *PRV (LEC) + AAV (MS) injections*

MS61 *PRV (LEC) + AAV (MS) injections*

MS62 S1 after many recording days

a	-	MS	-	14/02/2017	IV	3869 µm	same
b	-	MS	-	14/02/2017	IV	3518 µm	same
c	-	MS	-	15/02/2017	V	4360 µm	same 1
d	-	MS	-	15/02/2017	V	3908 µm	same 1
e	attempt	MS	-	15/02/2017	V	4181 µm	same 1
f	-	MS	-	16/02/2017	VI	3466 µm	same 2
g	-	MS	-	16/02/2017	VI	4120 µm	same 2
h	attempt	MS	-	16/02/2017	VI	3536 µm	same 2
i	-	MS	-	16/02/2017	VI	3050 µm	same 2
j	attempt	MS	-	16/02/2017	VI	3201 µm	same 2
k	-	MS	-	17/02/2017	VII	4165 µm	same 3
l	attempt	MS	-	17/02/2017	VII	4071 µm	same 3

MS63 S1 after many recording days

a	-	MS	-	22/02/2017	II	4700 µm	same
b	-	MS	-	22/02/2017	II	4536 µm	same
c	-	MS	-	22/02/2017	II	4824 µm	same
d	attempt	MS	-	22/02/2017	II	4993 µm	same
e	attempt	MS	-	22/02/2017	II	4981 µm	same

MS64 S1 after many recording days

a	attempt	MS	-	28/02/2017	V	3888 µm	same
b	-	MS	-	01/03/2017	VII	3541 µm	same 1
c	attempt	MS	-	01/03/2017	VII	3905 µm	same 1
d	attempt	MS	-	01/03/2017	VII	3920 µm	same 1
f	-	MS	-	01/03/2017	VII	4358 µm	same 1
g	-	MS	-	02/03/2017	VIII	4406 µm	same 2
h	attempt	MS	-	02/03/2017	VIII	4951 µm	same 2
i	attempt	MS	-	02/03/2017	VIII	4950 µm	same 2

MS65 S1

MS66 *PRV (LEC) + AAV (MS) injections*

MS67 S1

MS68

a	labelled	MS	+	09/03/2017	I	3600 µm	same

MS69 S1

MS70 S1 after many recording days

a	-	MS	-	16/03/2017	I	3748 µm	same
b	-	MS	-	16/03/2017	I	4332 µm	same

MS71 S1 after many recording days

a	-	MS	-	15/03/2017	I	3461 µm	same
b	-	MS	-	15/03/2017	I	4100 µm	same
c	labelled	MS	+	15/03/2017	I	4100 µm	same

MS72 S1 after many recording days

a	-	MS	-	15/03/2017	I	3971 µm	same
b	-	MS	-	15/03/2017	I	4160 µm	same
c	-	MS	?	15/03/2017	I	4099 µm	same

MS73

a	attempt	MS	-	28/03/2017	I	4110 µm	same
b	attempt	MS	-	28/03/2017	I	4123 µm	same
c	labelled	MS	+	28/03/2017	I	4330 µm	same

MS74

a	-	MS	-	28/03/2017	I	4300 µm	same
b	labelled	MS	+	28/03/2017	I	4200 µm	same

MS75

a	labelled	MS	?	05/04/2017	I	3200 µm	same

MS76 *PRV (LEC) + AAV (MS) injections*

MS77 *PRV (LEC) + AAV (MS /*

MS78 *PRV (LEC) + AAV (MS) injections*

MS79

a	-	MS	-	22/04/2017	I	4700 µm	same
b	attempt	MS	-	22/04/2017	I	4318 µm	same
c	-	MS	-	22/04/2017	I	4630 µm	same
d	attempt	MS	-	25/04/2017	III	3500 µm	same 1
e	-	MS	-	25/04/2017	III	3630 µm	same 1
f	attempt	MS	-	25/04/2017	III	3465 µm	same 1
g	attempt	MS	-	26/04/2017	IV	4280 µm	same 2
h	labelled	MS	+	26/04/2017	IV	3298 µm	same 2

MS80 perfused after 8 h

a	labelled	MS	-	21/04/2017	I	3480 µm	same

MS81 perfused without labelling

MS82 perfused without labelling

a	-	MS	-	04/05/2017	I	3922 µm	same
b	-	MS	-	04/05/2017	I	4293 µm	same
c	-	MS	-	04/05/2017	I	4118 µm	same
d	-	MS	-	04/05/2017	I	3921 µm	same
e	attempt	MS	-	04/05/2017	I	3782 µm	same
f	labelled	MS	-	04/05/2017	I	3800 µm	same
g	-	MS	-	10/05/2017	IV	8002 µm	same 1
h	-	MS	-	10/05/2017	IV	4070 µm	same 1

MS83 10% BDA, perfused after 20 h

a	-	MS	-	12/05/2017	I	4800 µm	same
b	-	MS	-	13/05/2017	II	4500 µm	same 1
c				13/05/2017	II	4471 µm	same 1
d	labelled	MS	+	13/05/2017	II	4805 µm	same 1

MS84 10% BDA, perfused after 20 h

a	-	MS	-	17/05/2017	I	3689 µm	same
b	-	MS	-	17/05/2017	I	4285 µm	same
c	-	MS	-	17/05/2017	I	4952 µm	same
d	-	MS	-	17/05/2017	I	4192 µm	same
e	-	MS	-	17/05/2017	I	4194 µm	same
f	-	MS	-	18/05/2017	II	#######	same 1
g	-	MS	-	18/05/2017	II	6066 µm	same 1
h	-	MS	-	18/05/2017	II	3302 µm	same 1
i	-	MS	-	18/05/2017	II	3158 µm	same 1
j	-	MS	-	18/05/2017	II	3665 µm	same 1
k	-	MS	-	18/05/2017	II	3084 µm	same 1
l	-	MS	-	18/05/2017	II	3461 µm	same 1
m	-	MS	-	18/05/2017	II	3724 µm	same 1
n	-	MS	-	18/05/2017	II	3821 µm	same 1
o	-	MS	-	18/05/2017	II	3927 µm	same 1
p	-	MS	-	18/05/2017	II	3691 µm	same 1
q	-	MS	-	18/05/2017	II	3623 µm	same 1
r	attempt	MS	-	18/05/2017	II	3192 µm	same 1
s	attempt	MS	-	18/05/2017	II	3552 µm	same 2
t	labelled	MS	-	18/05/2017	II	3887 µm	same 2

MS85 10 % BDA, perfused after 2 days

a	-	MS	-	23/05/2017	I	3819 µm	same
b	attempt	MS	-	23/05/2017	I	3836 µm	same
c	attempt	MS	-	23/05/2017	I	3836 µm	same
d	-	MS	-	23/05/2017	I	3664 µm	same
e	-	MS	-	23/05/2017	I	3754 µm	same
f	-	MS	-	23/05/2017	I	3370 µm	same
g	-	MS	-	23/05/2017	I	3551 µm	same
h	labelled	MS	+	23/05/2017	I	3802 µm	same

MS86

a	-	MS	-	31/05/2017	I	3680 µm	same
b	labelled	MS	+	31/05/2017	I	3934 µm	same

MS87 bleeeding, perfused without labelling

a	-	MS	-	03/06/2017	I	3800 µm	same
b	-	MS	-	03/06/2017	I	3470 µm	same 1
c	-	MS	-	03/06/2017	I	4830 µm	same 1

MS88 5% BDA, perfused after 1 day

a	-	MS	-	03/06/2017	I	4002 µm	same
b	-	MS	-	03/06/2017	I	3995 µm	same
c	labelled	MS	-	03/06/2017	I	3888 µm	same 1
d	labelled	MS	-	03/06/2017	I	4204 µm	same 1
e	labelled	MS	-	03/06/2017	I	3570 µm	same 1

MS89 perfused without labelling

MS90 5% BDA, perfused after 2 days

a	-	MS	-	08/06/2017	I	3224 µm	same
b	-	MS	-	11/06/2017	IV	3880 µm	same 1
c	-	MS	-	11/06/2017	IV	3633 µm	same 1
d	attempt	MS	-	11/06/2017	IV	3761 µm	same 1

e	attempt	MS	-	11/06/2017	IV	3347 µm	same 1
f	-	MS	-	11/06/2017	IV	3388 µm	same 1
g	labelled	MS	+	11/06/2017	IV	3308 µm	same 1

MS91 5% BDA, perfused after 1 day

a	-	MS	-	16/06/2017	I	3891 µm	same
b	labelled	MS	+	16/06/2017	I	4100 µm	same

MS92 5% BDA, perfused after 1 day

a	-	MS	-	29/06/2017	I	3782 µm	same
b	attempt	MS	-	29/06/2017	I	3788 µm	same
c	labelled	MS	-	29/06/2017	I	3441 µm	same

MS93 5% BDA, perfused after 1 day

a	-	MS	-	30/06/2017	I	3171 µm	same
b	attempt	MS	-	30/06/2017	I	4273 µm	same 1
c	labelled	MS	-	30/06/2017	I	3720 µm	same 1

MS94 5% BDA, perfused after 1 day

a	-	MS	-	01/07/2017	I	3571 µm	same
b	-	MS	-	01/07/2017	I	3821 µm	same
c	-	MS	-	01/07/2017	I	3898 µm	same
d	labelled	MS	+	01/07/2017	I	3842 µm	same
e	-	MS	-	03/07/2017	II	3620 µm	same 1
f	-	MS	-	03/07/2017	II	3578 µm	same 1
g	-	MS	-	03/07/2017	II	3791 µm	same 1
h	labelled	MS	+	03/07/2017	II	3562 µm	same 1

MS95 long 5% BDA labelling

a	labelled	MS	-	16/08/2017	I	3152 µm	same

MS96 perfused without labelling

MS97 surgery --> S1

MS98 5% BDA labelling, 3 labelling attempts

a	-	MS	-	31/08/2017	I	4216 µm	same
b	-	MS	-	31/08/2017	I	4121 µm	same
c	attempt	MS	-	31/08/2017	I	3924 µm	same
d	labelled	MS	+	31/08/2017	I	3479 µm	same
e	attempt	MS	-	31/08/2017	I	3477 µm	same

MS99 5% BDA labelling

a	-	MS	-	29/08/2017	I	4318 µm	same
b	-	MS	-	29/08/2017	I	3140 µm	same
c	labelled	MS	+	29/08/2017	I	3556 µm	same

MS100 5% BDA labelling, 10 degree angle

a	-	MS	-	06/09/2017	I	4030 µm	same
b	-	MS	-	06/09/2017	I	4196 µm	same
c	-	MS	-	06/09/2017	I	3610 µm	same
d	labelled	MS	-	06/09/2017	I	4190 µm	same

MS101 5% BDA labelling (perfused after after 20 hours)

a	-	MS	-	29/09/2017	I	3602 µm	same
b	labelled	MS	+	29/09/2017	I	3700 µm	same

MS102 5% BDA labelling (perfused after after 20 hours)

a	-	MS	-	30/09/2017	I	3902 µm	same
b	-	MS	-	30/09/2017	I	3861 µm	same
c	-	MS	-	30/09/2017	I	3958 µm	same
d	-	MS	-	30/09/2017	I	4214 µm	same
e	-	MS	-	30/09/2017	I	3111 µm	same
f	-	MS	-	30/09/2017	I	3288 µm	same
g	attempt	MS	-	30/09/2017	I	3546 µm	same
h	-	MS	-	30/09/2017	I	3524 µm	same
i	labelled	MS	-	30/09/2017	I	3200 µm	same
j	-	MS	-	01/10/2017	II	3326 µm	same 1
k	-	MS	-	01/10/2017	II	3436 µm	same 1
l	-	MS	-	01/10/2017	II	3795 µm	same 1
m	-	MS	-	01/10/2017	II	3713 µm	same 1
n	labelled	MS	-	01/10/2017	II	3480 µm	same 1

MS103 5% BDA labelling (perfused after after 20 hours)

a	-	MS	-	07/10/2017	I	3472 µm	same
b	-	MS	-	07/10/2017	I	3294 µm	same
c	-	MS	-	07/10/2017	I	3061 µm	same
d	labelled	MS	+	07/10/2017	I	3370 µm	same

MS104 10% BDA labelling (p SEE ON LONGEST LABELLING!

a	-	MS	-	17/10/2017	I	3628 µm	same
b	-	MS	-	17/10/2017	I	3655 µm	same
c	-	MS	-	17/10/2017	I	4028 µm	same
d	attempt	MS	-	17/10/2017	I	4113 µm	same
e	labelled	MS	+	17/10/2017	I	3519 µm	same 1

MS105 10% BDA labelling (perfused after after 24hours)

a	-	MS	-	19/10/2017	I	4289 µm	same
b	labelled	MS	-	19/10/2017	I	3742 µm	same

MS106 10% BDA labelling (perfused after after 24hours)

a	attempt	MS	-	30/10/2017	I	2295 µm	same
b	-	MS	-	30/10/2017	I	3150 µm	same 1
c	labelled	MS	-	30/10/2017	I	3081 µm	same 1

MS107 10% BDA labelling (perfused after after 24hours)

a	-	MS	-	11/12/2017	I	3226 µm	same
b	-	MS	-	11/12/2017	I	3774 µm	same
c	-	MS	-	11/12/2017	I	3516 µm	same
d	-	MS	-	11/12/2017	I	3946 µm	same
e	-	MS	-	11/12/2017	I	3255 µm	same
f	attempt	MS	-	11/12/2017	I	3322 µm	same
g	-	MS	-	11/12/2017	I	3443 µm	same
h	labelled	MS	+	12/12/2017	II	3943 µm	same 1
i	labelled	MS	-	12/12/2017	II	1264 µm	same 1

MS108 10% BDA labelling (perfused after after 24hours)

a	-	MS	-	14/12/2017	I	3324 µm	same
b	-	MS	-	14/12/2017	I	3789 µm	same
c	-	MS	-	14/12/2017	I	3809 µm	same 1
d	-	MS	-	14/12/2017	I	3715 µm	same 1
e	-	MS	-	14/12/2017	I	3636 µm	same 1
f	-	MS	-	14/12/2017	I	4082 µm	same 1
g	labelled	MS	-	14/12/2017	I	3542 µm	same 1

MS109

a	-	MS	-	20/12/2017	I	3312 µm	same
b	-	MS	-	20/12/2017	I	3313 µm	same
c	-	MS	-	20/12/2017	I	3569 µm	same

d	-	MS	-	20/12/2017	I	2939 µm	same
e	-	MS	-	20/12/2017	I	3672 µm	same
f	-	MS	-	20/12/2017	I	3748 µm	same
g	-	MS	-	20/12/2017	I	3031 µm	same
h	-	MS	-	20/12/2017	I	3039 µm	same
i	-	MS	-	20/12/2017	I	3772 µm	same
j	-	MS	-	20/12/2017	I	3081 µm	same
k	-	MS	-	21/12/2017	II	3443 µm	same 1
l	-	MS	-	21/12/2017	II	3723 µm	same 1
m	-	MS	-	21/12/2017	II	3620 µm	same 1
n	-	MS	-	21/12/2017	II	1780 µm	same 1
o	labelled	MS	+	21/12/2017	II	3600 µm	same 1

MS110 *Virus injections PRV (MS) + AAV (DG-CA3) injections 25/*

a	-	MS	-	21/11/2017	I	3571 µm	same
b	-	MS	-	21/11/2017	I	3180 µm	same
c	-	MS	-	21/11/2017	I	3453 µm	same
d	-	MS	-	21/11/2017	I	3400 µm	same 1
e	-	MS	-	21/11/2017	I	3283 µm	same 1
f	-	MS	-	21/11/2017	I	3656 µm	same 1
g	-	MS	-	21/11/2017	I	3149 µm	same 1
h	-	MS	-	21/11/2017	I	3249 µm	same 1
i	labelled	MS	-	21/11/2017	I	3078 µm	same 1

MS111 *Virus injections PRV (MS) + AAV (DG-CA3) injections 25/*

a	-	MS	-	23/11/2017	I	2972 µm	same
b	labelled	MS	-	23/11/2017	I	2847 µm	same

MS112 *Virus injections PRV (MS) + AAV (DG-CA3) injections 25/*

a	-	MS	-	19/12/2017	I	3045 µm	same
b	-	MS	-	19/12/2017	I	3036 µm	same
c	attempt	MS	-	19/12/2017	I	3321 µm	same
d	-	MS	-	19/12/2017	I	3449 µm	same
e	-	MS	-	19/12/2017	I	3918 µm	same
f	-	MS	-	19/12/2017	I	3642 µm	same
g	-	MS	-	19/12/2017	I	3288 µm	same
h	-	MS	-	20/12/2017	II	3893 µm	same 1
i	-	MS	-	20/12/2017	II	3779 µm	same 1
j	-	MS	-	20/12/2017	II	3314 µm	same 1
k	-	MS	-	20/12/2017	II	3942 µm	same 1
l	labelled	MS	+	20/12/2017	II	3062 µm	same 1

MS113 3% Neurobiotin Labelling, 60sec, perfused after 6 h

a	-	MS	-	13/03/2018	I	3350 µm	same
b	attempt	MS	-	13/03/2018	I	3782 µm	same
c	-	MS	-	13/03/2018	I	3399 µm	same
d	-	MS	-	14/03/2018	II	3818 µm	same 1
e	labelled	MS	+	14/03/2018	II	3659 µm	same 1

MS114 3% Neurobiotin Labelling, perfused after 6 h

a	-	MS	-	13/03/2018	I	2873 µm	same
b	-	MS	-	14/03/2018	II	3381 µm	same 1
c	-	MS	-	14/03/2018	II	3416 µm	same 1
d	-	MS	-	14/03/2018	II	3068 µm	same 1
e	-	MS	-	15/03/2018	III	3488 µm	same 2
f	-	MS	-	15/03/2018	III	3531 µm	same 2
g	-	MS	-	15/03/2018	III	3221 µm	same 2
h	labelled	MS	-	16/03/2018	IV	3700 µm	same 3

MS115 3% Neurobiotin Labelling 70 sec, perfused after 6 h

a	-	MS	-	21/03/2018	I	3392 µm	same
b	-	MS	-	22/03/2018	II	3195 µm	same 1
c	-	MS	-	22/03/2018	II	3513 µm	same 1
d	-	MS	-	22/03/2018	II	4500 µm	same 1
e	-	MS	-	22/03/2018	II	3910 µm	same 1
f	-	MS	-	22/03/2018	II	4041 µm	same 1
g	-	MS	-	22/03/2018	II	4450 µm	same 1
h	-	MS	-	22/03/2018	II	3787 µm	same 1
i	-	MS	-	22/03/2018	II	3776 µm	same 1
j	-	MS	-	22/03/2018	II	3642 µm	same 1
k	labelled	MS	-	22/03/2018	II	3715 µm	same 1

MS116 *chronic polytrode freely moving recordings*

MS117 *chronic polytrode freely moving recordings*

MS118 *chronic polytrode freely moving recordings*

MS119 *chronic polytrode freely moving recordings*